

# Sub-Regional Modelling Case Study 2005-2006 Status Report

NWMO TR-2007-07

November 2007

**S.D. Normani**

**Y.-J. Park**

**J.F. Sykes**

**E.A. Sudicky**

University of Waterloo

**nwmo**

NUCLEAR WASTE  
MANAGEMENT  
ORGANIZATION

SOCIÉTÉ DE GESTION  
DES DÉCHETS  
NUCLÉAIRES



**Nuclear Waste Management Organization**

22 St. Clair Avenue East, 6<sup>th</sup> Floor

Toronto, Ontario

M4T 2S3

Canada

Tel: 416-934-9814

Web: [www.nwmo.ca](http://www.nwmo.ca)

**Sub-Regional Modelling Case Study 2005-2006 Status Report**

**NWMO TR-2007-07**

November 2007

**S.D. Normani**  
**Y.-J. Park**  
**J.F. Sykes**  
**E.A. Sudicky**  
University of Waterloo

---

Disclaimer:

This report does not necessarily reflect the views or position of the Nuclear Waste Management Organization, its directors, officers, employees and agents (the "NWMO") and unless otherwise specifically stated, is made available to the public by the NWMO for information only. The contents of this report reflect the views of the author(s) who are solely responsible for the text and its conclusions as well as the accuracy of any data used in its creation. The NWMO does not make any warranty, express or implied, or assume any legal liability or responsibility for the accuracy, completeness, or usefulness of any information disclosed, or represent that the use of any information would not infringe privately owned rights. Any reference to a specific commercial product, process or service by trade name, trademark, manufacturer, or otherwise, does not constitute or imply its endorsement, recommendation, or preference by NWMO.

---

## ABSTRACT

**Title:** Sub-Regional Modelling Case Study 2005-2006 Status Report  
**Report No.:** NWMO TR-2007-07  
**Author(s):** S.D. Normani, Y.-J. Park, J.F. Sykes, and E.A. Sudicky  
**Company:** University of Waterloo  
**Date:** November 2007

### Abstract

The Phase-II sub-regional model presented in this report is an improvement upon the Phase-I model developed in Sykes et al. (2004). Although the Phase-I sub-regional flow system case study provided valuable insight into the behaviour of flow domains characterized by complex, 3-dimensional, curve-planar fracture zones, a number of modelling scenarios relevant to a deep geologic repository and the impact of long-term climate change were considered a logical extension of the program. Boundary conditions, matrix and fracture zone parameters were modified and a statistical model of fracture zone permeability was developed, providing a depth varying probability density function (PDF).

Mean life expectancy (MLE) is shown to be an excellent tool for determining the most relevant and dominant geosphere parameters and processes that influence groundwater flow system characteristics in fractured, crystalline rock settings typical of the Canadian Shield. Mean life expectancy represents the average time for any subsurface location to discharge to the biosphere, while honouring both advective and diffusive dispersion processes (unlike particle tracking which can only honour advection). Since life expectancy is characterized by a probability density function, its mean may not represent earliest arrival or least dose, and hence, must be used with this caveat in mind.

The presence of brines at depth is shown to enhance the stability of deep groundwater flow systems since denser pore fluids at depth essentially reduce the topographic gradient (and driving forces) by requiring a greater energy potential to displace them. Mean life expectancy increases with increasing brine density at depth. It should be noted that the presence of brines at depth have a greater influence on the MLE of fluids in fractures than they do on fluids in the matrix.

MLE was used to assess the impact of fracture zone permeability, width, and porosity on travel time. The most significant of these is permeability, followed by width, and finally porosity. Decreasing fracture zone permeability can significantly increase MLE by several orders of magnitude at depth. The effects of fracture zone permeability assumptions on flow and transport are significant. Using a fracture zone permeability characteristic of near surface conditions at depth can significantly reduce the MLE, even in the adjacent matrix domain, especially if this higher permeability is used for fracture zones at depth.

For the cold-based (NN2008) and warm-based (NN2778) climate scenarios, sub-regional simulations illustrated that meltwater produced underneath the ice sheet is able to penetrate deeper in the warm-based scenario. This is primarily due to the absence of permafrost, which in the case of NN2008, acts to seal the near surface and greatly reduces, by several orders of magnitude, the hydraulic connection with the fracture zone network.



**TABLE OF CONTENTS**

	<u>Page</u>
<b>ABSTRACT</b> . . . . .	<b>v</b>
<b>1. INTRODUCTION</b> . . . . .	<b>1</b>
<b>1.1 BACKGROUND</b> . . . . .	<b>1</b>
1.1.1 Regional Case Study . . . . .	2
1.1.2 Phase-I Sub-Regional Case Study . . . . .	2
<b>1.2 SCOPE AND OBJECTIVES</b> . . . . .	<b>3</b>
1.2.1 Paleoclimate . . . . .	3
1.2.2 FRAC3DVS and FRAC3DVS-OPG . . . . .	4
<b>2. PHASE-II SUB-REGIONAL MODEL DEVELOPMENT</b> . . . . .	<b>5</b>
<b>2.1 MODELLING DOMAIN</b> . . . . .	<b>5</b>
<b>2.2 SURFACE BOUNDARY CONDITIONS</b> . . . . .	<b>5</b>
<b>2.3 MATRIX PROPERTIES</b> . . . . .	<b>8</b>
<b>2.4 FRACTURE ZONE GEOMETRY</b> . . . . .	<b>9</b>
<b>2.5 FRACTURE ZONE PERMEABILITY</b> . . . . .	<b>11</b>
<b>2.6 FRACTURE ZONE WIDTH</b> . . . . .	<b>16</b>
<b>2.7 FRACTURE ZONE POROSITY</b> . . . . .	<b>18</b>
<b>3. METHODOLOGY</b> . . . . .	<b>19</b>
<b>3.1 DENSITY DEPENDENT FLOW AND TRANSPORT</b> . . . . .	<b>19</b>
3.1.1 Characterizing Brine Solutions . . . . .	19
3.1.2 Governing Equations . . . . .	19
3.1.3 Numerical Implementation . . . . .	21
3.1.4 Vertically Hydrostatic Initial Condition . . . . .	22
<b>3.2 CLIMATE AND SURFACE BOUNDARY CONDITIONS</b> . . . . .	<b>23</b>
<b>3.3 LIFETIME EXPECTANCY AS A SAFETY INDICATOR</b> . . . . .	<b>24</b>
3.3.1 Contaminant Transport in Groundwater . . . . .	25
3.3.2 The Lifetime Expectancy of Radionuclides . . . . .	26
3.3.3 Mean Lifetime Expectancy as a Safety Indicator . . . . .	27
3.3.4 Mass Loads at the Biosphere and Risk Assessment . . . . .	27
3.3.5 Lifetime Expectancy in Fractured Porous Media . . . . .	28
<b>3.4 STATISTICAL ANALYSIS</b> . . . . .	<b>31</b>
3.4.1 Parametric Statistics . . . . .	31
3.4.2 Non-Parametric Statistics . . . . .	32
3.4.3 Advantages and Disadvantages . . . . .	33
<b>4. GROUNDWATER FLOW AND LIFETIME EXPECTANCY IN A SINGLE SUB-REGIONAL MODEL REALIZATION</b> . . . . .	<b>34</b>
<b>4.1 HYDRAULIC PROPERTIES</b> . . . . .	<b>34</b>
<b>4.2 GROUNDWATER FLOW</b> . . . . .	<b>36</b>
<b>4.3 BRINE DISTRIBUTION</b> . . . . .	<b>36</b>

continued ...

**TABLE OF CONTENTS (concluded)**

	<b><u>Page</u></b>
4.3.1	Initial and Boundary Conditions . . . . . 36
4.3.2	Illustrative Examples . . . . . 36
4.3.3	Brine Distribution and Groundwater Flow in the Sub-Regional Domain . . . 46
<b>4.4</b>	<b>LONG-TERM CLIMATE CHANGE . . . . . 50</b>
4.4.1	Simulation Results . . . . . 55
<b>4.5</b>	<b>LIFETIME EXPECTANCY . . . . . 58</b>
4.5.1	Illustrative Examples . . . . . 58
4.5.1.1	Model Layout and Proof-of-Concept . . . . . 60
4.5.1.2	Effects of Fracture Zone Geometry . . . . . 61
4.5.2	Mean Lifetime Expectancy - Sub-Regional Domain . . . . . 64
4.5.3	Probability Density for Lifetime Expectancy - Sub-Regional Domain . . . . . 67
4.5.4	Effects of Shield Brine - Sub-Regional Domain . . . . . 69
<b>5.</b>	<b>SUB-REGIONAL MODEL UNCERTAINTY AND SENSITIVITY ANALYSIS 76</b>
<b>5.1</b>	<b>PARAMETER UNCERTAINTY . . . . . 76</b>
5.1.1	Fracture Zone Permeability . . . . . 76
5.1.2	Fracture Zone Porosity . . . . . 85
5.1.3	Fracture Zone Width . . . . . 87
5.1.4	Diffusion and Tortuosity . . . . . 88
<b>5.2</b>	<b>FRACTURE ZONE NETWORK GEOMETRY . . . . . 91</b>
5.2.1	Probabilistic Characteristics . . . . . 94
5.2.2	Effects on Groundwater Flow . . . . . 96
5.2.3	Effects on Lifetime Expectancy . . . . . 98
<b>6.</b>	<b>SUMMARY AND CONCLUSIONS . . . . . 112</b>
<b>REFERENCES</b>	<b>. . . . . 114</b>
<b>APPENDIX A: FORWARD AND BACKWARD ADVECTION-DISPERSION EQUATIONS EQUIVALENT TO STOCHASTIC DIFFERENTIAL EQUATIONS</b>	<b>. . . . . 117</b>

**LIST OF TABLES**

	<b><u>Page</u></b>
Table 1: Sub-Regional Phase–II model matrix permeability by layer and depth . . . . .	9

**LIST OF FIGURES**

	<b><u>Page</u></b>
Figure 1: Vertical Darcy flux at ground surface for Case 1, 2, and 3 of the Phase-I sub-regional model . . . . .	6
Figure 2: Expanded sub-regional modelling domain (black line) and aerial photo draped on the TIN derived DEM . . . . .	7
Figure 3: Vertical Darcy flux at ground surface for Phase-II sub-regional model . . . . .	7
Figure 4: Horizontal and vertical matrix permeabilities as a function of depth for the Phase-II sub-regional model . . . . .	8
Figure 5: Phase-I sub-regional model with water features and fractures that intersect ground surface . . . . .	10
Figure 6: Lateral extents and boundaries of Phase-I modelling domain (red line), Phase-II modelling domain (dotted yellow line), DEM (dashed cyan line), Phase-I fracture zone network model (boxed red line), and Phase-II fracture zone network model (green line) . . . . .	12
Figure 7: Fracture zone log <sub>10</sub> permeability data for the Finnish Olkiluoto site and the Whiteshell Research Area (WRA) . . . . .	13
Figure 8: Log <sub>10</sub> permeability percentiles with depth for a 100 m depth range . . . . .	13
Figure 9: Log <sub>10</sub> permeability percentiles with depth for a 200 m depth range . . . . .	14
Figure 10: Log <sub>10</sub> permeability percentile with depth for a 200 m depth range and best-fit cubic splines . . . . .	14
Figure 11: Cumulative density function for log <sub>10</sub> of fracture permeability . . . . .	15
Figure 12: Probability density function for log <sub>10</sub> of fracture permeability . . . . .	15
Figure 13: 3-D view of the probability density function for log <sub>10</sub> of fracture permeability . . . . .	16
Figure 14: Inverse cumulative density function for log <sub>10</sub> of fracture permeability . . . . .	17
Figure 15: Fracture zone width histogram and log-normal PDF . . . . .	17
Figure 16: Figure 7 from Adams and Bachu (2002) showing brine density versus mass fraction for 4854 formation water analyses . . . . .	20
Figure 17: Examples for vertically hydrostatic initial conditions for equivalent freshwater head distributions . . . . .	23
Figure 18: Schematics for a set of parallel vertical fractures and matrix block system, to derive analytical solutions for temporal moments for lifetime expectancy . . . . .	29
Figure 19: Mean lifetime expectancy solutions for a set of parallel fractures and matrix block system in Figure 18 . . . . .	30
Figure 20: (a) Mean ( $E_f$ : solid line) and standard deviation ( $\sigma_f$ : dashed line) in lifetime expectancy, and (b) the coefficient of variation ( $\sigma_f/E_f$ ) with depth for the fracture domain . . . . .	31
Figure 21: Fracture zone permeability for reference case . . . . .	34
Figure 22: Fracture zone porosity for reference case . . . . .	35
Figure 23: Fracture zone width for reference case . . . . .	35
Figure 24: Piezometric head for steady-state flow in the (a) matrix, and (b) fracture zones . . . . .	37
Figure 25: Darcy flux distribution for reference case . . . . .	38
Figure 26: Initial concentration distribution for viscous buoyancy-driven flow and transport simulations . . . . .	38
Figure 27: Initial equivalent freshwater head for maximum relative brine density of 1.2 . . . . .	39

**continued ...**

**LIST OF FIGURES (continued)**

	<u>Page</u>
Figure 28: Hydraulic head distribution in steady state . . . . .	40
Figure 29: Initial relative brine concentration . . . . .	40
Figure 30: Illustrative initial equivalent freshwater head for a relative brine density of: (a) 1.03, (b) 1.1, and (c) 1.2 . . . . .	41
Figure 31: Relative brine concentration at 20 000 years for relative brine densities of: (a) 1.0, (b) 1.03, (c) 1.1, and (d) 1.2 . . . . .	42
Figure 32: Linear velocity at 20 000 years for relative brine densities of: (a) 1.0, (b) 1.03, (c) 1.1, and (d) 1.2 . . . . .	43
Figure 33: Streamlines at 20 000 years for relative brine densities of: (a) 1.0, (b) 1.03, (c) 1.1, and (d) 1.2 . . . . .	44
Figure 34: Relative brine concentration at 20 000 years for a relative brine density of 1.2 and with maximum relative viscosities of: (a) 2.0, and (b) 4.0 . . . . .	45
Figure 35: Linear velocity at 20 000 years for a relative brine density of 1.2 and with maximum relative viscosities of: (a) 2.0, and (b) 4.0 . . . . .	46
Figure 36: Streamlines at 20 000 years for a relative brine density of 1.2 and with maximum relative viscosities of: (a) 2.0, and (b) 4.0 . . . . .	47
Figure 37: Magnitude of linear fluid velocity at 20 000 years for maximum relative brine densities of: (a) 1.0, (b) 1.03, (c) 1.1, and (d) 1.2 . . . . .	48
Figure 38: Magnitude of linear fluid velocity at 20 000 years for a relative brine density of 1.2 and with maximum relative viscosities of: (a) 2.0, and (b) 4.0 . . . . .	49
Figure 39: Relative brine concentration without density and viscosity effects. Plane view at -200 masl . . . . .	49
Figure 40: Relative brine concentration without density and viscosity effects. Plane view at 0 masl . . . . .	50
Figure 41: Relative brine concentration at 20 000 years for maximum relative brine densities of: (a) 1.03, (b) 1.1, and (c) 1.2. Plane view at -200 masl . . . . .	51
Figure 42: Darcy flux distribution at 20 000 years for maximum relative brine densities of: (a) 1.0, (b) 1.03, (c) 1.1, and (d) 1.2. Plane view at -200 masl . . . . .	52
Figure 43: Darcy velocity vectors along with relative brine concentration in a cross section of the sub-regional domain at 20 000 years for maximum relative brine densities of: (a) 1.0, (b) 1.03, (c) 1.1, and (d) 1.2 . . . . .	54
Figure 44: Time series plots of (a) permafrost depth, and (b) ice load in equivalent metres of water for climate simulation NN2008 (cold-based glaciation) . . . . .	55
Figure 45: Time series plots of (a) permafrost depth, and (b) ice load in equivalent metres of water for climate simulation NN2778 (warm-based glaciation) . . . . .	56
Figure 46: Piezometric heads for north-south cross-section at 12 000 years before present. The red dot represents a location in the rock matrix, while the green dot represents a location within a fracture. . . . .	56
Figure 47: Vertical Darcy velocities within the rock matrix and a fracture as indicated in Figure 46, for climate simulation NN2008 (cold-based glaciation) . . . . .	57
Figure 48: Vertical Darcy velocities within the rock matrix and a fracture as indicated in Figure 46, for climate simulation NN2778 (warm-based glaciation) . . . . .	57

**continued ...**

**LIST OF FIGURES (continued)**

	<u>Page</u>
Figure 49: Iso-surface of 5% recharge water at the end of a 121 000 year simulation for the NN2008 climate simulation (red iso-surface) and for the NN2778 climate simulation (blue iso-surface) . . . . .	58
Figure 50: East-west and north-south trending fences showing 5% recharge water at the end of a 121 000 year simulation for the NN2008 climate simulation (red lines) and for the NN2778 climate simulation (blue lines) . . . . .	59
Figure 51: Schematics of the vertical cross-sections used to model mean and probability density for lifetime expectancy: (a) hydraulic head distribution in a homogeneous matrix system under given flow boundary conditions; (b)-(d) variation cases with different fracture networks (thick lines). . . . .	59
Figure 52: Lifetime expectancy solutions for the case in Figure 51. (a) Mean lifetime expectancy distribution in years, (b) lifetime expectancy probability density at nine observation points in (a), and (c) vertical logs of mean lifetime expectancy passing through the observation points. . . . .	60
Figure 53: Lifetime expectancy solutions for the case in Figure 51b. (a) Mean lifetime expectancy distribution in years, (b) lifetime expectancy probability density at nine observation points in (a), and (c) vertical logs of mean lifetime expectancy passing through the observation points. . . . .	62
Figure 54: Lifetime expectancy solutions for different fracture network geometries. (a) and (c) show lifetime expectancy probability density at nine observation points for Figure 51c and Figure 51d, respectively. (b) and (d) are vertical logs of mean lifetime expectancy passing through the observation points for Figure 51c and Figure 51d . . . . .	63
Figure 55: Mean lifetime expectancy distribution in (a) matrix, and (b) fracture domains. Plane view at -415 masl . . . . .	65
Figure 56: Mean lifetime expectancy at four different elevations in the sub-region . . . . .	66
Figure 57: Isosurface for $10^6$ years of mean lifetime expectancy . . . . .	66
Figure 58: Frequency plots for mean lifetime expectancy at four different elevations . . . . .	67
Figure 59: Cumulative frequency plots for mean lifetime expectancy at four different elevations . . . . .	68
Figure 60: Mass flux to biosphere from sources at four different elevations . . . . .	69
Figure 61: Mean lifetime expectancy distributions for maximum relative brine densities of: (a) 1.0, (b) 1.03, (c) 1.1, and (d) 1.2 . . . . .	70
Figure 62: Mean lifetime expectancy at four elevations in the sub-region with maximum relative brine density of: (a) 1.0, (b) 1.03, (c) 1.1, and (d) 1.2 . . . . .	71
Figure 63: Isosurface for $10^6$ years of mean lifetime expectancy in the sub-region with maximum relative brine density of: (a) 1.0, and (b) 1.2 . . . . .	74
Figure 64: Comparison of cumulative frequency plots for mean lifetime expectancy at four different elevations in the sub-region with (red lines) and without brine effects (black lines) . . . . .	75
Figure 65: Darcy flux (a) and MLE distributions (b) for $k_F = 10^{-13} \text{ m}^2$ . . . . .	77
Figure 66: Frequency plots for mean lifetime expectancy at four different elevations for $k_F = 10^{-13} \text{ m}^2$ . . . . .	78

**continued ...**

**LIST OF FIGURES (continued)**

	<u>Page</u>
Figure 67: Comparison of cumulative frequency plots for mean lifetime expectancy at four different elevations: Reference case (black lines) and $k_F = 10^{-13} \text{ m}^2$ (red lines) . . . . .	79
Figure 68: Darcy flux and MLE distributions for $k_F = 10^{-12} \text{ m}^2$ . . . . .	80
Figure 69: Darcy flux and MLE distributions for $k_F = 10^{-14} \text{ m}^2$ . . . . .	81
Figure 70: Darcy flux and MLE distributions for $k_F = 10^{-16} \text{ m}^2$ . . . . .	82
Figure 71: Comparison of cumulative frequency plots for mean lifetime expectancy at four different elevations: Reference case (black lines), and $k_F = 10^{-12} \text{ m}^2$ (red lines), $k_F = 10^{-14} \text{ m}^2$ (purple lines), and $k_F = 10^{-16} \text{ m}^2$ (blue lines) . . . . .	83
Figure 72: Darcy flux and MLE distributions with probabilistic $k_F$ and depth relationship . . . . .	84
Figure 73: Comparison of cumulative frequency plots for mean lifetime expectancy at four different elevations: Reference case (black lines) and a probabilistic $k_F$ distribution (red lines) . . . . .	85
Figure 74: MLE distributions for constant fracture zone porosity of (a) 0.3 %, and (b) 3 % . . . . .	86
Figure 75: Comparison of cumulative frequency plots for mean lifetime expectancy at four different elevations: Reference case (circles), and uniform fracture zone porosity ( $n_F$ ) of 0.3 % (red lines) and 3.0 % (blue lines) . . . . .	87
Figure 76: Darcy flux and MLE distributions for a fracture zone width of 1 m . . . . .	89
Figure 77: Darcy flux and MLE distributions for a fracture zone width of 10 m . . . . .	90
Figure 78: Comparison of cumulative frequency plots for mean lifetime expectancy at four different elevations: Reference case (black lines) and uniform fracture zone widths ( $w_F$ ) of 1 m (red lines) and 10 m (blue lines) . . . . .	91
Figure 79: MLE Distributions for Different Tortuosity Values of (a) 0.01 and (b) 1 . . . . .	92
Figure 80: Comparison of cumulative frequency plots for mean lifetime expectancy at four different depths: Reference case (black lines) and tortuosity values of 0.01 (red lines) and 1.0 (blue lines) . . . . .	93
Figure 81: Fracture zone probability at ground surface . . . . .	94
Figure 82: Propagation of fracture zone probability with depth . . . . .	95
Figure 83: Fracture zone probability in the subsurface. Plane elevation at -200 masl . . . . .	95
Figure 84: Distribution of (a) mean, and (b) standard deviation for 100 head values at each node computed for 100 fracture zone network realizations . . . . .	97
Figure 85: Distribution of (a) median, and (b) quartile deviation for 100 head values at each node computed for 100 fracture zone network realizations . . . . .	99
Figure 86: Four representative statistics for 100 Darcy flux values at each element computed for 100 fracture zone realizations: (a) arithmetic mean, (b) geometric mean, (c) median, and (d) midrange . . . . .	100
Figure 87: Four different measures for uncertainty in representative statistics for Darcy flux: standard deviations in (a) linear and (b) log-scale, (c) quartile deviation, and (d) half-range . . . . .	102
Figure 88: Measures for relative uncertainty in representative statistics for Darcy flux: (a) coefficient of variation, and (b) quartile coefficient of variation . . . . .	104

continued ...

**LIST OF FIGURES (concluded)**

	<b><u>Page</u></b>
Figure 89: Representative statistics for mean lifetime expectancy computed for 100 fracture zone realizations: (a) arithmetic mean, (b) geometric mean, (c) median, and (d) midrange . . . . .	105
Figure 90: Degree of scattering in representative statistics for mean lifetime expectancy: standard deviations in (a) linear and (b) log-scale, (c) quartile deviation, and (d) half-range . . . . .	107
Figure 91: Measures for relative uncertainty in representative statistics for mean lifetime expectancy: (a) coefficient of variation, and (b) quartile coefficient of variation	109
Figure 92: Worst case estimates for mean lifetime expectancy in terms of 2.5 percentage points in (a) linear and (b) log-scale . . . . .	110
Figure 93: Worst case estimates for mean lifetime expectancy in terms of (a) minimum, (b) 5 <sup>th</sup> percentile, and (c) $Q2 - 2QD$ . . . . .	111

## 1. INTRODUCTION

As part of the Nuclear Waste Management Organization (NWMO) Technical Program, activities have been undertaken to further the understanding of groundwater flow system evolution and dynamics within Canadian Shield settings. In conducting such studies, a principal focus has been on developing field and numerical geoscience tools and methods to assess groundwater flow system dynamics during the Quaternary (2–0 Ma). In this capacity, numerical methods are being pursued to:

- i) serve as a systematic framework to assemble and test descriptive conceptual geosphere models derived from integration of multi-disciplinary data sets;
- ii) improve the fidelity with which site characterisation data may be input and realised within numerical simulations;
- iii) develop methodologies to assess and quantify robustness in numerical flow and transport predictions as a consequence of site characterisation uncertainty typical of large Shield flow systems; and
- iv) to improve the utility of numerical codes to allow transfer of vetted site characterisation models to Safety Assessment, thereby improving Safety Case transparency.

This study further demonstrates the application of the flow and transport code FRAC3DVS through its application in a case study of Shield groundwater flow system evolution as affected by long-term climate change, and represents a logical extension of work completed during previous modelling activities, which included preliminary sensitivity analyses of deep-seated groundwater flow within a hypothetical regional domain, and the Phase-I sub-regional flow domain as described by Sykes et al. (2003, 2004).

### 1.1 BACKGROUND

The NWMO's Technical Program is developing various tools and methods, as well as multiple geoscientific lines-of-reasoning, to convey a sense of understanding of Shield flow system evolution as it affects the siting and safety case of a Deep Geologic Repository. Specific aspects include the development of probabilistic 3-dimensional curve-planar field constrained Fracture Zone Network (FZN) models (Srivastava, 2002), the simulation of climate driven Laurentide glacial ice-sheet history including the influence of permafrost (Peltier, 2002, 2003a), the paleohydrogeologic assessment of WRA Lac du Bonnet batholith fracture infill mineralogy relevant to fracture fluid evolution and redox front migration (Gascoyne et al., 2004), the hydrogeochemical characterisation of deep-seated crystalline flow domains affected by long-term climate change (Frape et al., 2004), and application of virtual reality technology for multi-disciplinary data integration and communication of a site-specific conceptual geosphere model(s) (Cotesta and Kaiser, 2004). These developments provide a basis for:

- i) further demonstrating modelling approaches that are commensurate with and take into account realistic observations and uncertainties arising from field characterisation studies;
- ii) illustrating aspects of gradual and/or episodic flow system response to cyclic climate change/glacial events;

- iii) providing an illustrative example to site characterisation programs as to site-specific flow system attributes most influencing confidence in predicted outcomes; and
- iv) demonstrating to broader audiences alternative geoscience lines-of-evidence regarding flow domain stability at nominal repository depths that contribute to confidence in the repository Safety Case.

### **1.1.1 Regional Case Study**

The regional groundwater flow system case study considered a typical 5700 km<sup>2</sup> Shield watershed in which groundwater flow to a depth of 1500 m was simulated (Sykes et al., 2003). These numerical simulations or flow system scenarios were purposely designed to illustrate the influence of:

- i) variable groundwater salinity distributions;
- ii) spatially variable permeability fields;
- iii) assumed flow system dimensionality; and
- iv) residual glacial over-pressures, on groundwater flow paths, flow rates and residence times.

This case study provides insight into Shield flow systems, which as a consequence of glacial cycles may remain in a transient state and that flow system dimensionality coupled with salinity/permeability distributions creates a deep-seated, sluggish flow system in which solute transport may be diffusion dominated (Sykes et al., 2003). These modelling results further provide a basis to query historical concepts of regional Shield groundwater flow and to explore the applicability of flow boundaries assigned to internal sub-regional flow domains, at scales relevant to repository siting.

### **1.1.2 Phase-I Sub-Regional Case Study**

The sub-regional groundwater flow system case study undertook a detailed flow analysis of an 84 km<sup>2</sup> portion of the regional Shield watershed (Sykes et al., 2004). Surface water features and a Digital Elevation Model (DEM) were applied in a GIS framework to delineate the sub-watershed and to populate a FRAC3DVS model grid. One realization of a complex, 3-dimensional, geostatistical Fracture Zone Network (FZN) model, constrained by measured surface lineaments, was superimposed onto a 600 000 element flow domain mesh. A methodology was developed to assign orthogonal fracture faces (between adjacent finite element blocks) to best represent the over 540 irregular, fracture zones within the sub-region (Srivastava, 2002). These fracture zones were assigned a fixed hydraulic conductivity and the rock mass between the discontinuities was assigned a range of depth-dependent hydraulic conductivities considered representative of sparsely and moderately fractured rock of the Shield. All simulations indicated that estimated Darcy velocities within the bulk rock mass at depths below 600 m were indicative of diffusion-dominant transport regimes. Interconnectivity of permeable fracture zones at depth was required to create discrete pathways for advective flow.

## 1.2 SCOPE AND OBJECTIVES

Although the Phase–I sub-regional flow system case study provided valuable insight into the behaviour of flow domains characterized by complex, 3-dimensional, curve-planar fracture zones, a number of modelling scenarios relevant to a deep geologic repository and the impact of long-term climate change were considered a logical extension of the program.

This study addresses the following additional scenarios:

- i) the incorporation of multiple realizations (up to 100) of the FZN models, each constrained to measured surface lineaments,
- ii) an investigation into the role of variable-density groundwaters (salinity),
- iii) the exploration of the impact of more realistic, spatially-correlated, permeability fields in the fracture zones and matrix continua,
- iv) the inclusion of transient analyses governed by the time history of pore pressure responses associated with glacial cycles.

The goal of undertaking such modelling tasks is to illustrate whether the flow system at repository depth remains stagnant and diffusion-dominated regardless of the uncertainty in fracture zone geometry, interconnectivity, flow and transport parameters, as well as the domain being subjected to extreme changes in boundary conditions associated with glaciation. Insight modelling is also undertaken to explore whether glacial, oxygenated waters could migrate to typical repository depth as a result of significant changes in surface boundary conditions associated with future and past glaciation events.

### 1.2.1 Paleoclimate

Based on the work of Peltier (2002, 2003a), it is clear that to credibly address the long-term safety of a deep geologic repository, long-term climate change and in particular a glaciation scenario, must be incorporated into performance assessment modelling activities. In addition, by simulating flow system responses to the last Laurentide (North American) glacial episode, insight is gained into the role of significant past stresses (mechanical, thermal and hydrological) on determining the nature of present flow system conditions, and by extension, the likely impact of similar, future boundary condition changes on long-term flow system stability. The Laurentide glacial episode was characterized by the following:

- i) occurred over a 120 000 year time period,
- ii) included at least three cycles of glacial advance and retreat, with maximum ice thickness over a typical Northern Ontario Shield site reaching nearly 3 km,
- iii) included extensive periods of transient, peri-glacial conditions during which permafrost could impact the subsurface to several hundreds of metres, and
- iv) was accompanied by significant basal meltwater production near the end of the glacial episode.

### 1.2.2 FRAC3DVS and FRAC3DVS-OPG

To undertake the Phase-II modelling activities, the following improvements to FRAC3DVS have been undertaken since 2004:

- i) the treatment of flow system/water compressibility;
- ii) the treatment of variably dense groundwater distributions in fracture and matrix continua;
- iii) the improvement of execution time by upgrading the solver in FRAC3DVS to accommodate faster solution techniques;
- iv) the implementation of multi-grid and asynchronous time stepping techniques to improve model applicability for various scale flow and transport simulations;
- v) the implementation of a methodology to facilitate multiple realisations of probabilistic curve-planar FZN models; and
- vi) the implementation of an approach to allow assignment of field constrained permeability fields based on both parameter and spatial distribution uncertainty.

While FRAC3DVS is used for all modelling tasks in this report, FRAC3DVS-OPG is to be used for all current and future modelling tasks beginning August 2007. FRAC3DVS-OPG is currently being developed as a branch of HydroGeoSphere (which itself was developed from FRAC3DVS), but excluding the surface water flow and transport components. This approach has allowed FRAC3DVS-OPG to benefit from code developments and improvements made to HydroGeoSphere at the University of Waterloo. Development during 2005/2006 has included:

- i) the implementation of backward-in-time (BIT) and mean life expectancy (MLE) algorithms for computing groundwater age, especially important for diffusion dominated flow systems, characteristic of Shield environments;
- ii) the implementation of variable and uncertain fracture zone widths, fracture zone porosity, and spatially variable fracture zone permeability;
- iii) the implementation of a simplified vertical one-dimensional hydro-mechanical coupling as described by Neuzil (2003)
- iv) the implementation of temperature and thermo-haline processes, and subsequent coupling of temperature, density, and viscosity terms;
- v) the development and implementation of a data interchange standard from FRAC3DVS-OPG to GoCAD; and
- vi) the development of a platform independent build environment using Python and SCons to compile the FRAC3DVS-OPG source code for execution on Microsoft Windows operating systems (32-bit and 64-bit), and Linux based operating systems using various optimizing Fortran95 compilers.

## **2. PHASE-II SUB-REGIONAL MODEL DEVELOPMENT**

The Phase-II sub-regional model development is based on the Phase-I model developed in Sykes et al. (2004). As part of the continuing refinement of the sub-regional model, the modelling domain, various model parameters, and boundary conditions were modified from the Phase-I work. The following sections describe the changes made to the Phase-I model as well as the spatial extents, boundary conditions, and parameters used for the Phase-II model.

### **2.1 MODELLING DOMAIN**

Due to the choice of Dirichlet boundary conditions for the top surface, and the use of a DEM which was quantized to integer elevation values, a stair-step effect was noticed when plotting the Darcy flux. The relatively abrupt step change in elevation from one plateau to the next lead to seepage faces forming along contour lines (see Figure 1). This modelling outcome is due to artifacts in the DEM, and is not related to any physical groundwater phenomenon.

A new DEM was constructed using the following GIS vector data: contour lines, rivers, wetlands, and lakes. The paper NTS maps for the area were used to define elevations for the wetlands and lakes based on their position relative to nearby contours, as well as their hydrologic relationship to connected rivers, lakes, and wetland features within the same contour interval. River elevations were then linearly interpolated along their length, honouring any contour which crossed the rivers, as well as the elevations which were previously specified for lakes and wetlands.

The eastern extent of the Phase-I sub-regional modelling domain was defined along a divide described by a river. A number of the generated FZN fractures also follow rivers, leading to the situation where a fracture could be partially inside the modelling domain, and partially outside the domain, thereby violating its connectedness. The sub-regional modelling domain was extended laterally to surface water divides along topographic highs for the eastern and western portions of the modelling domain. The large river to the south would remain, as would the topographic divide to the north. Figure 2 shows the expanded sub-regional modelling domain outlined in black, with the aerial photograph draped over the new DEM.

ArcView GIS 3.2a was used to create a triangular irregular network (TIN) using the contour lines, lakes, wetlands, and sloping rivers for the revised modelling boundary plus a 1 km buffer. From the TIN, a 10 m square DEM ASCII grid was created. Since some of the FZN fractures extend beyond the revised modelling boundary and 1 km buffer, a 20 m square DEM was generated using the NRCAN 1:250 000 DEM converted to a Lambert Conformal Conic projection. Both DEMs are used when calculating the elevation of fractures; any triangular fracture face vertices within the modelling boundary (and buffer) use the TIN derived DEM, while all other vertices use the NRCAN derived DEM.

### **2.2 SURFACE BOUNDARY CONDITIONS**

The Dirichlet surface boundary condition that was previously applied to the entire top surface of the model was subsequently applied only at nodes that were within lakes or wetlands, or within

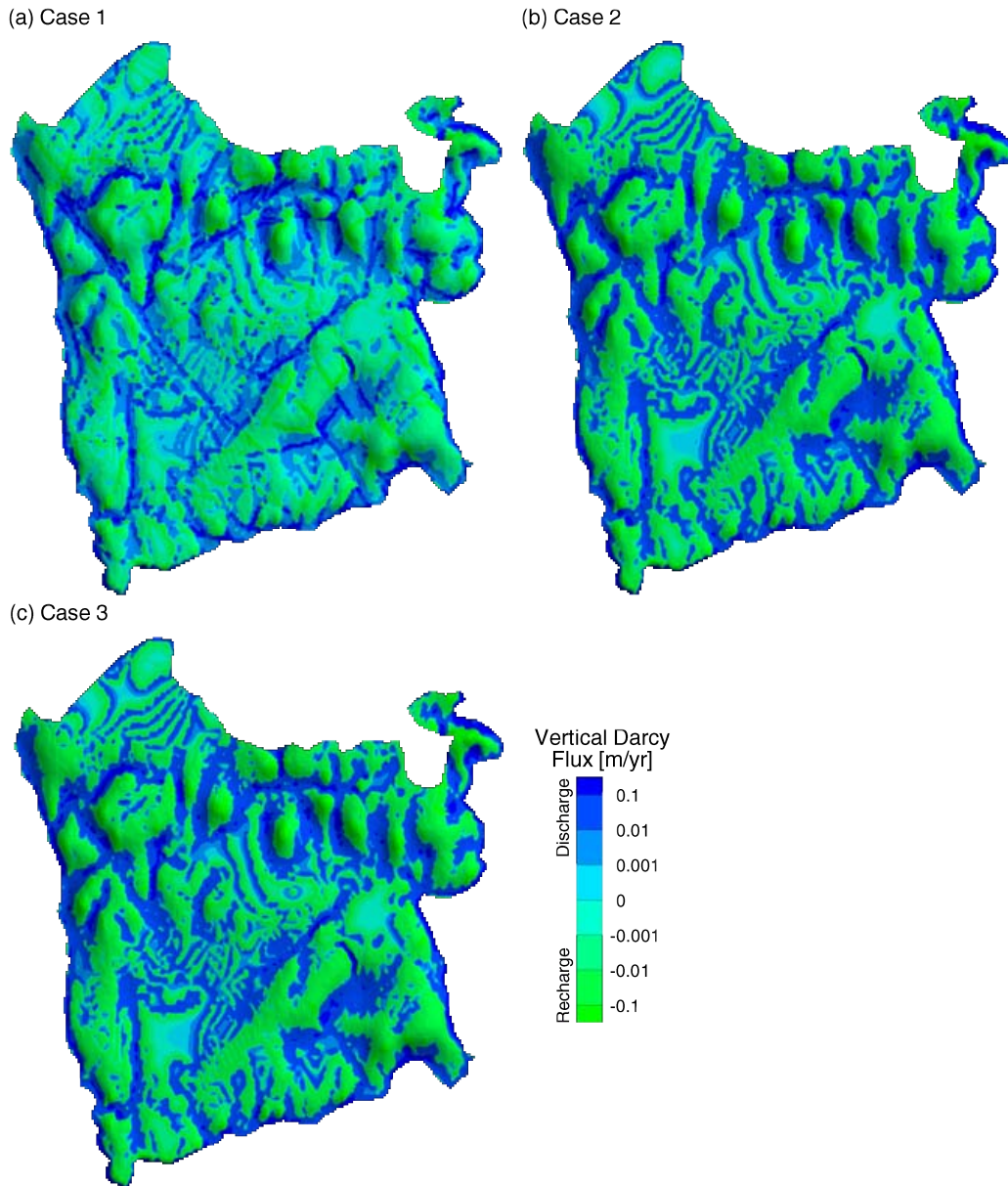


**Figure 1: Vertical Darcy flux at ground surface for Case 1, 2, and 3 of the Phase-I sub-regional model**

36 m of a river (approximately  $\frac{50\sqrt{2}}{2}$ , where a grid block is 50 m per side). This ensured that rivers would be continuous while considering the grid discretization. A recharge boundary condition was applied to the top surface of the model at a rate of 1.0 mm/year.

The vertical surface Darcy flux is shown in Figure 3. As can be clearly seen, the anomalous banding evident in Figure 1 has been eliminated and the resulting surface discharge coincides with actual locations of water features such as wetlands, lakes or rivers.

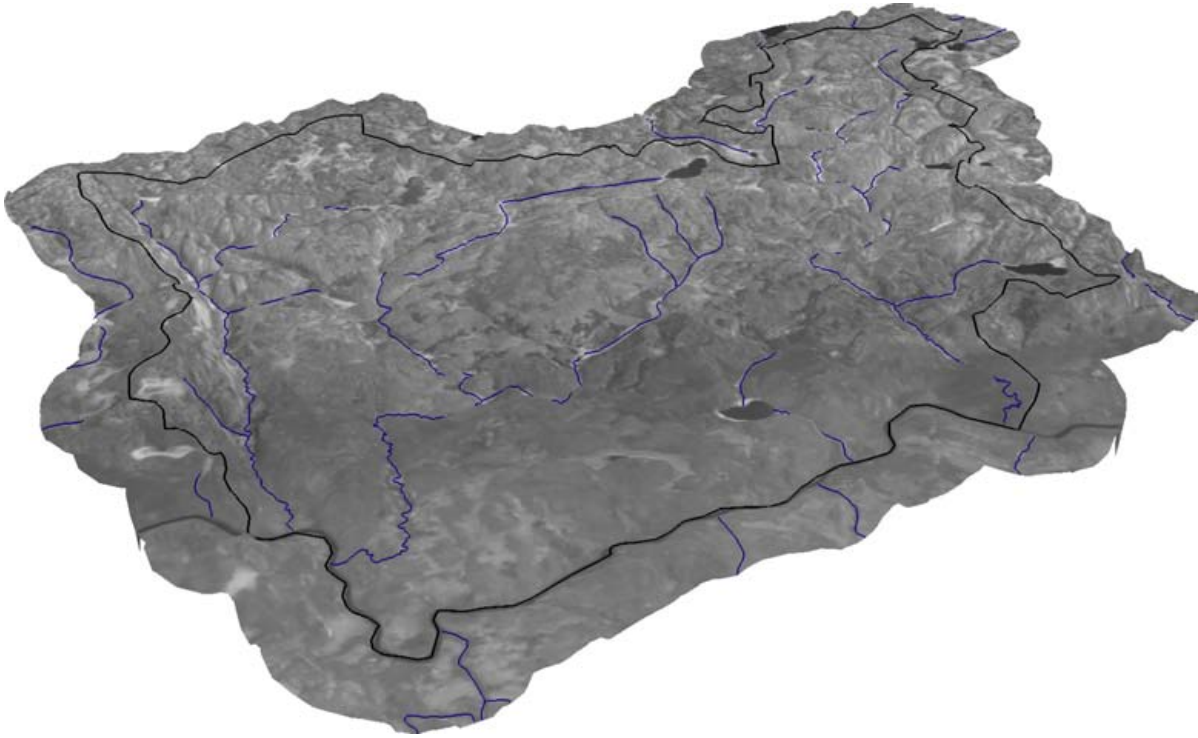


Figure 2: Expanded sub-regional modelling domain (black line) and aerial photo draped on the TIN derived DEM

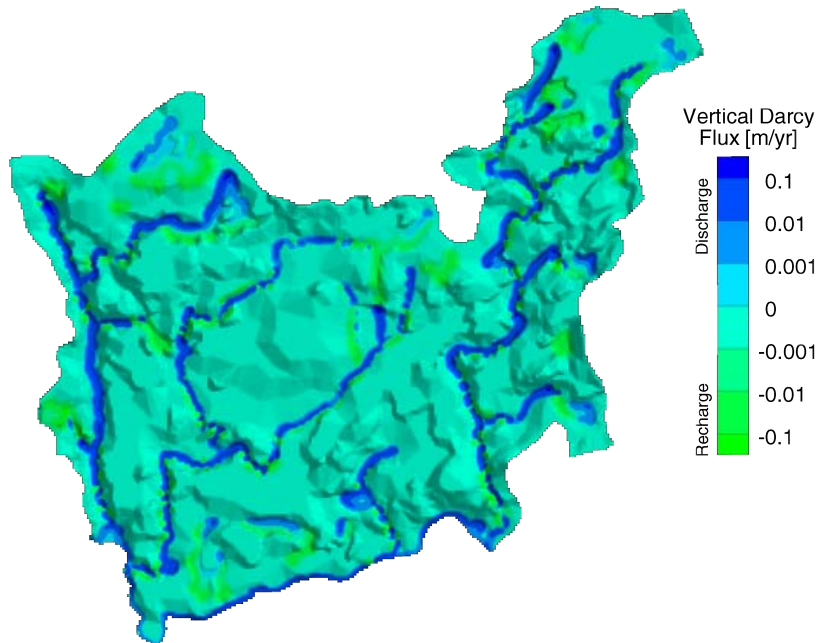


Figure 3: Vertical Darcy flux at ground surface for Phase-II sub-regional model

### 2.3 MATRIX PROPERTIES

The Phase–I sub-regional hydraulic conductivities were based on the original regional scale modelling of 10 vertical layers (Sykes et al., 2003). Due to the need to account for variations in hydraulic conductivity due to changes in fluid density and viscosity within the Phase–II model, permeabilities are used instead. The matrix permeabilities listed in Table 1 provide a smoother permeability transition from layer to layer, exponentially decreasing with increasing depth from ground surface, and accounting for the presence of Moderately Fractured Rock (MFR) near surface, and Sparsely Fractured Rock (SFR) at depth. The distribution of anisotropy ratios in Table 1 are those used in the conceptual model of Stevenson et al. (1996). The permeability relationships with depth are:

$$k_H = 10^{-14.5-4.5(1-e^{-0.002469d})} \quad (1)$$

$$k_V = \begin{cases} 10k_H, & \text{for } d \leq 300 \text{ m;} \\ [0.09(400 - d) + 1]k_H, & \text{for } 300 < d \leq 400 \text{ m;} \\ k_H, & \text{for } d > 400 \text{ m.} \end{cases} \quad (2)$$

where  $k_H$  is horizontal permeability;  $k_V$  is the vertical permeability; and  $d$  is the average depth below ground surface for a given layer. Both the horizontal and vertical permeabilities as a function of depth from ground surface are plotted in Figure 4.

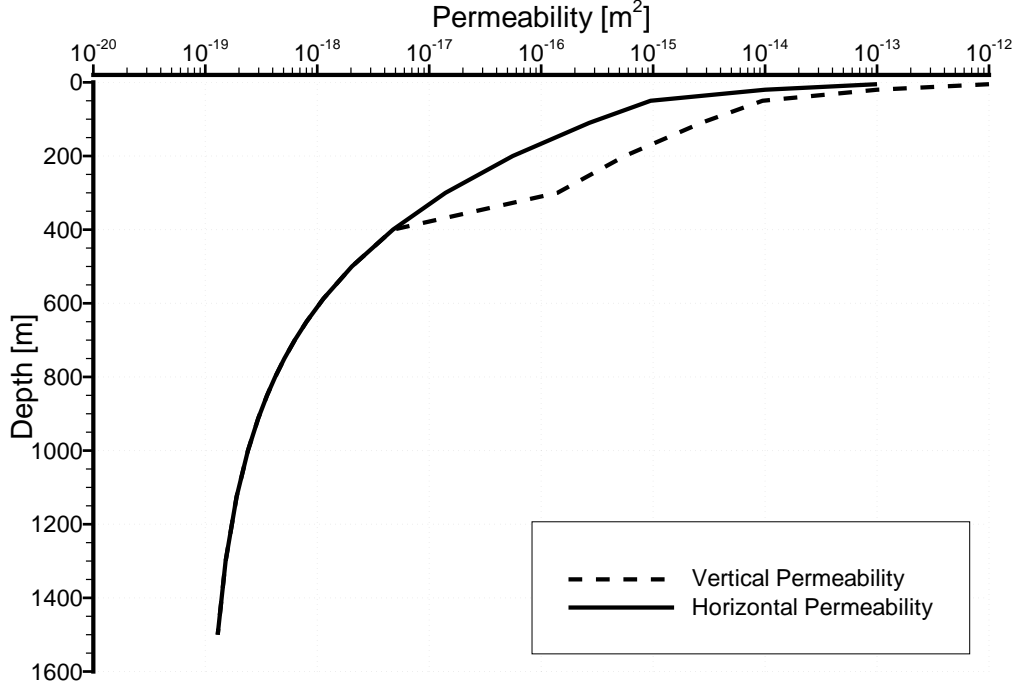


**Figure 4: Horizontal and vertical matrix permeabilities as a function of depth for the Phase–II sub-regional model**

A matrix porosity of 0.003 was chosen based on the work of Stevenson et al. (1996). Matrix and fracture properties for solute transport include a longitudinal dispersivity of 50 m, a transverse horizontal dispersivity of 5 m and a transverse vertical dispersivity of 0.5 m. A matrix bulk density of 2642.05 kg/m<sup>3</sup> (2650 kg/m<sup>3</sup> × (1 – 0.003)) is also used.

## 2.4 FRACTURE ZONE GEOMETRY

In the Phase–I sub-regional model case study of Sykes et al. (2004), aerial photography served as the basis for developing the fracture zone network model. A surface lineament analysis was conducted by Srivastava (2002) to define the major fracture features. These fracture features are mainly coincident with surface drainage features that exhibit linearity. Additional surface lineaments were created to account for the extension of existing major lineaments, and to increase the fracture density in areas where overburden cover obscured the surface lineaments. The resulting surface fracture features are shown in Figure 5. The fracture generation procedure is based on the lineament and fracture statistics for the Lac du Bonnet region of the Whiteshell Research Area and preserves the fracture zone orientation, fracture zone length, and area density distribution statistics. It represents both sensible and geomechanically plausible fracture behaviour (Srivastava, 2002).

**Table 1: Sub-Regional Phase–II model matrix permeability by layer and depth**

Layer	Depth [m]	Average Depth [m]	Anisotropy Ratio $k_V:k_H$	Permeability [m <sup>2</sup> ]	
				$k_H$	$k_V$
19	0–10	5	10	$1.0 \times 10^{-13}\dagger$	$1.0 \times 10^{-12}$
18	10–30	20	10	$1.0 \times 10^{-14}\dagger$	$1.0 \times 10^{-13}$
17	30–70	50	10	$9.5 \times 10^{-16}$	$9.5 \times 10^{-15}$
16	70–150	110	10	$2.7 \times 10^{-16}$	$2.7 \times 10^{-15}$
15	150–250	200	10	$5.6 \times 10^{-17}$	$5.6 \times 10^{-16}$
14	250–350	300	10	$1.4 \times 10^{-17}$	$1.4 \times 10^{-16}$
13	350–450	400	1	$4.7 \times 10^{-18}$	$4.7 \times 10^{-18}$
12	450–550	500	1	$2.0 \times 10^{-18}$	$2.0 \times 10^{-18}$
11	550–625	587.5	1	$1.1 \times 10^{-18}$	$1.1 \times 10^{-18}$
10	625–675	650	1	$8.0 \times 10^{-19}$	$8.0 \times 10^{-19}$
9	675–725	700	1	$6.3 \times 10^{-19}$	$6.3 \times 10^{-19}$
8	725–775	750	1	$5.1 \times 10^{-19}$	$5.1 \times 10^{-19}$
7	775–825	800	1	$4.2 \times 10^{-19}$	$4.2 \times 10^{-19}$
6	825–875	850	1	$3.6 \times 10^{-19}$	$3.6 \times 10^{-19}$
5	875–950	912.5	1	$3.0 \times 10^{-19}$	$3.0 \times 10^{-19}$
4	950–1050	1000	1	$2.4 \times 10^{-19}$	$2.4 \times 10^{-19}$
3	1050–1200	1125	1	$1.9 \times 10^{-19}$	$1.9 \times 10^{-19}$
2	1200–1400	1300	1	$1.5 \times 10^{-19}$	$1.5 \times 10^{-19}$
1	1400–1600	1500	1	$1.3 \times 10^{-19}$	$1.3 \times 10^{-19}$

Note: †Permeability manually set.

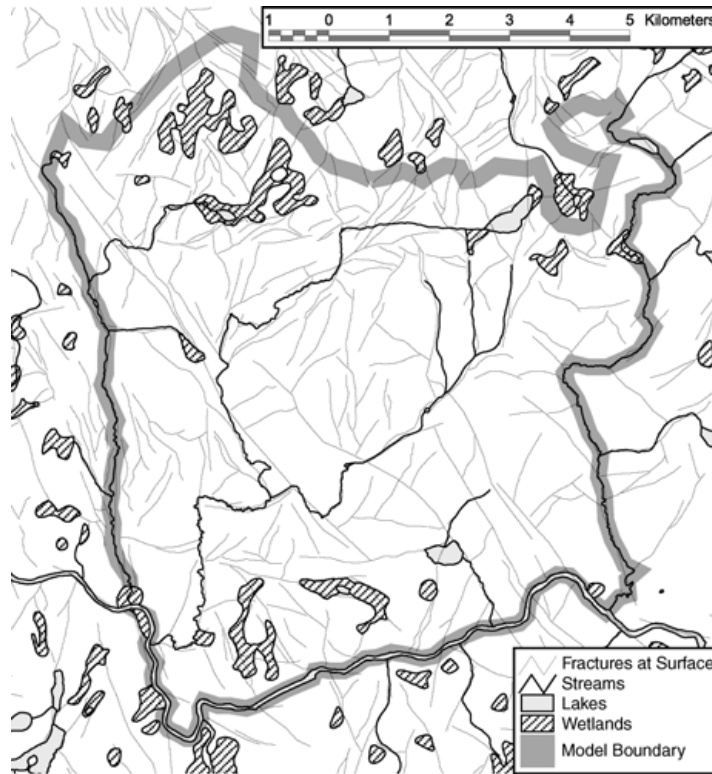


**Figure 5: Phase-I sub-regional model with water features and fractures that intersect ground surface**

To create 3-dimensional curve-planar fracture zones, the surface lineaments shown in Figure 5 are propagated to depth until one of the following conditions are met:

- the fracture zone's down-dip width reaches the prescribed length to width ratio;
- the fracture zone truncates against an existing fracture zone; or
- the fracture zone reaches the edge or bottom of the modelled domain.

A network of 548 discrete curve-planar fractures representing fracture zones was generated by Srivastava (2002) for the Phase-I sub-regional domain. The generated network is one stochastic realization of many possible fracture zone networks that could be generated for the sub-regional domain. Fracture network density decreases with increasing depth; minor fracture features are shallower than major fracture features. The resulting fracture network model contains a high degree of realism that honours many geological, statistical, and geomechanical constraints (Srivastava, 2002).

Since the Phase-II sub-regional model was extended both eastward and westward, the boundary of the generated fracture zone network also needs to be extended. A visual comparison of the Phase-I and Phase-II modelling extents, DEM boundary, and fracture zone network model generation boundaries is shown in Figure 6. Due to the stochastic nature of the fracture generation procedure (for both surface lineaments and fracture zone propagation to depth), multiple fracture zone network realizations can be produced to investigate the role of fracture

zone geometry on various performance measures of interest. A total of 100 equally probable fracture zone networks were generated by Srivastava for use within the Phase-II sub-regional model.

## 2.5 FRACTURE ZONE PERMEABILITY

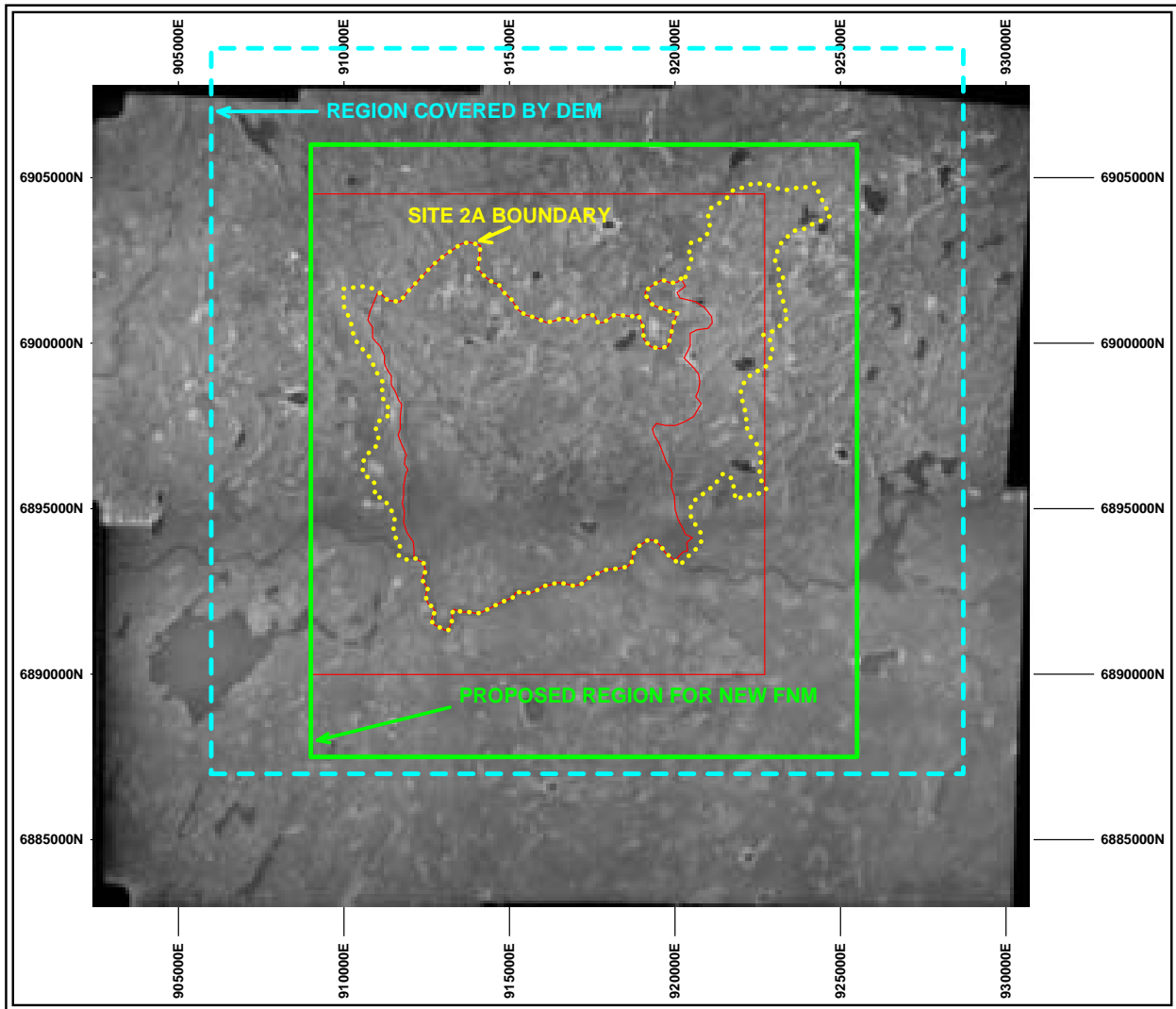
Fracture zone permeabilities (or conductivity), which were constant in the Phase-I work, are now defined on both a stochastic and a depth dependent basis. A plot of fracture zone permeability versus depth for the Whiteshell Research Area (Stevenson et al., 1996) and the Finnish Olkiluoto site (Hellä et al., 2004; Vaittinen et al., 2003) representing fracture zones is shown in Figure 7. As can be seen, it can be quite difficult to determine a depth trend from the wide permeability scatter in the data.

A depth trend was noticeable when rank statistics were used to calculate the 5<sup>th</sup>, 25<sup>th</sup>, 50<sup>th</sup>, 75<sup>th</sup>, and 95<sup>th</sup> percentiles. A total of eight depth ranges  $r$  of 50 m, 100 m, 150 m, 200 m, 250 m, 300 m, 350 m, and 400 m were selected. Percentiles were calculated for all permeability values within  $r/2$  metres of a specified depth  $d$ . Permeability percentile plots for  $r = 100$  m and  $r = 200$  m are shown in Figure 8 and Figure 9 respectively.

The various percentile curves can be quite “noisy”, although they do get smoother when selecting a larger  $r$  or depth range. Figure 9 was used as the basis for calculating cubic splines to best fit the various percentiles. The splines were interactively fit using Microsoft Excel™ for visualization, writing the necessary spline routines in Visual Basic for Applications (VBA) and linking the VBA code to the Excel spreadsheet. The resulting splines and the percentile curves from Figure 9 are shown in Figure 10.

Once the percentile cubic spline curves were created, another cubic spline interpolation was required to determine intermediate percentile values for a given depth. An additional spline curve representing the 1.4<sup>th</sup> percentile was necessary in order to ensure that the cumulative density function (CDF) was always increasing, and its slope was always greater than zero. The slope or first derivative of a CDF is the probability density function (PDF). The final CDF for fracture permeability is shown in Figure 11, while the PDF is shown in Figure 12. A 3-dimensional view of the PDF is shown in Figure 13. Although the CDF is quite smooth, the locations chosen for the cubic splines in Figure 10 greatly influenced the shape of the PDF. Multi-modal as well as negative values for the PDF were discovered during the creation of the CDF. As a result, the locations of the cubic splines were somewhat influenced by the PDF, thereby ensuring that the PDF was unimodal throughout the entire depth range of interest. The PDF for fracture permeabilities at depths below 700 m are nearly identical, primarily due to the lack of supporting fracture permeability data. Figure 13 clearly shows the depth dependent nature of the fracture permeability, in that the greatest expectation (PDF peaks) varies from approximately  $10^{-13} \text{ m}^2$  to  $10^{-16} \text{ m}^2$ .

A random fracture permeability variate can be calculated from the depth dependent PDF by using the inverse CDF (see Figure 14). Given a depth and a uniform random variate, the  $\log_{10}$  permeability random variate can be calculated by bi-linearly interpolating the inverse CDF



<b>ONTARIO</b> GENERATION	<i>froidaveaux</i> <i>srivastava</i> <i>scholfield</i>
DEEP GEOLOGIC REPOSITORY TECHNICAL PROGRAM GS42 GEOSTATISTICS STUDIES REGIONAL FLOW MODEL SITE 2A STUDY AREA BOUNDARIES	
0 5000 10000 m	
DATE: SEPT. 3, 2004	PROJ. FIG. NO.: 1001
DRAWN BY: RMS	CHECKED BY:

**Figure 6: Lateral extents and boundaries of Phase-I modelling domain (red line), Phase-II modelling domain (dotted yellow line), DEM (dashed cyan line), Phase-I fracture zone network model (boxed red line), and Phase-II fracture zone network model (green line)**

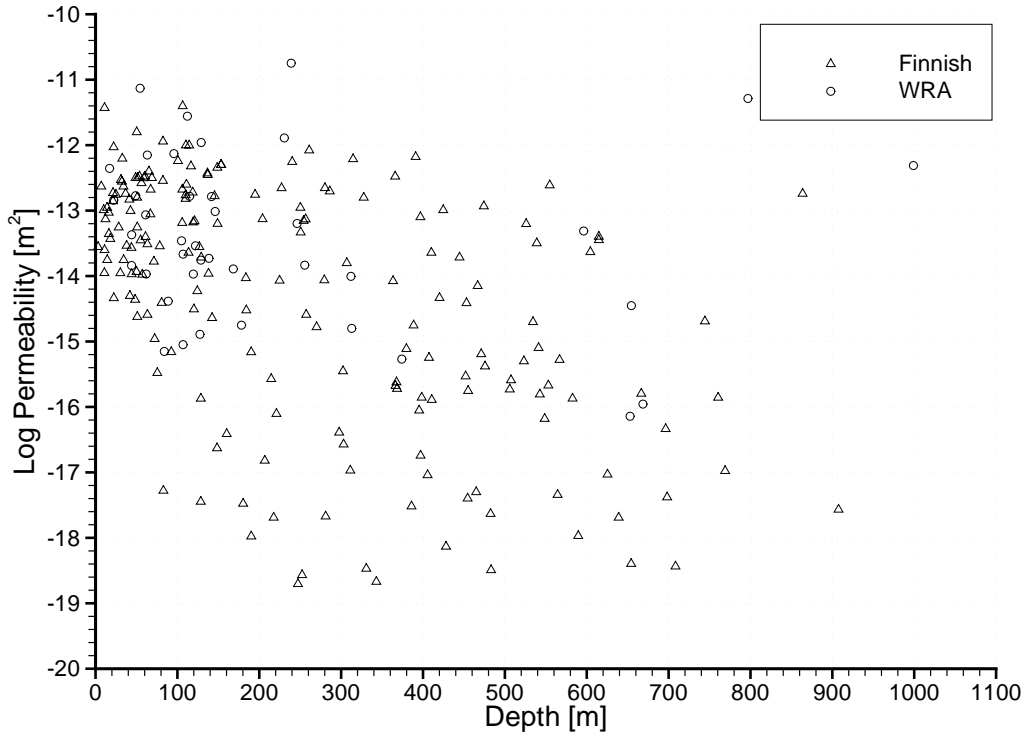


Figure 7: Fracture zone log<sub>10</sub> permeability data for the Finnish Olkiluoto site and the White-shell Research Area (WRA)

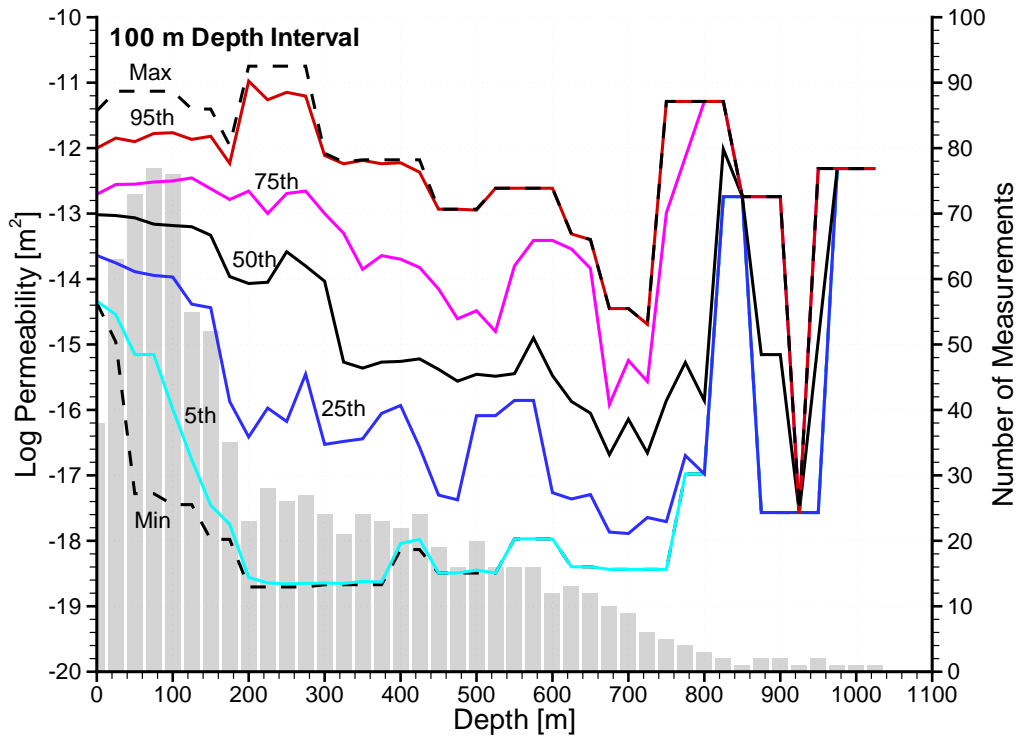


Figure 8: Log<sub>10</sub> permeability percentiles with depth for a 100 m depth range

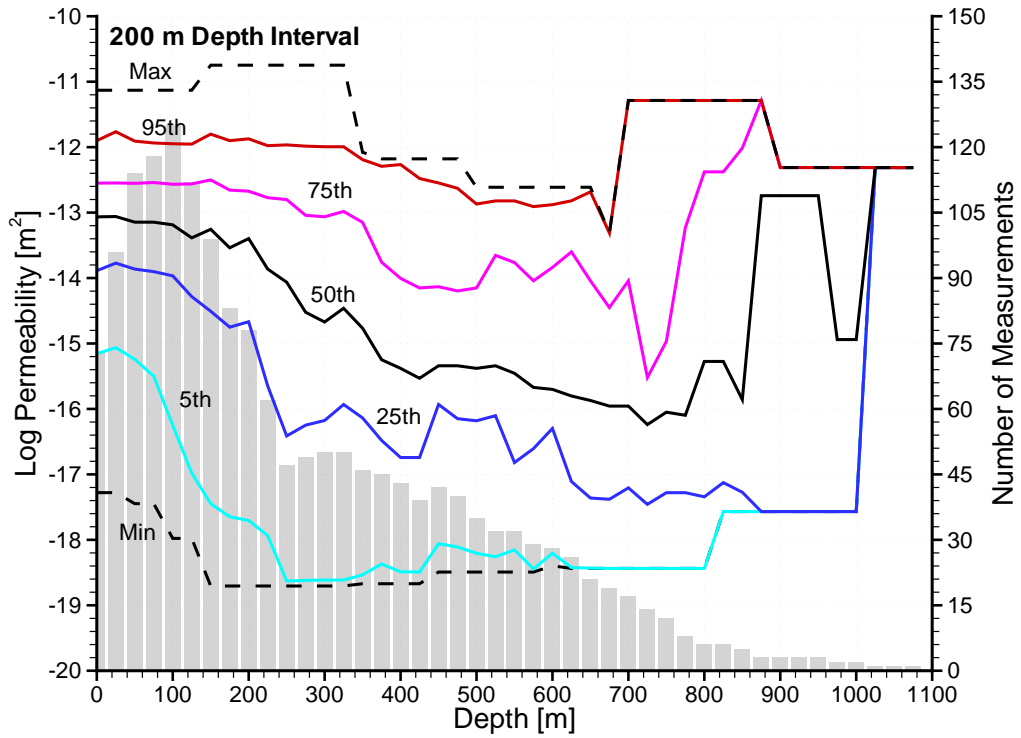


Figure 9:  $\text{Log}_{10}$  permeability percentiles with depth for a 200 m depth range

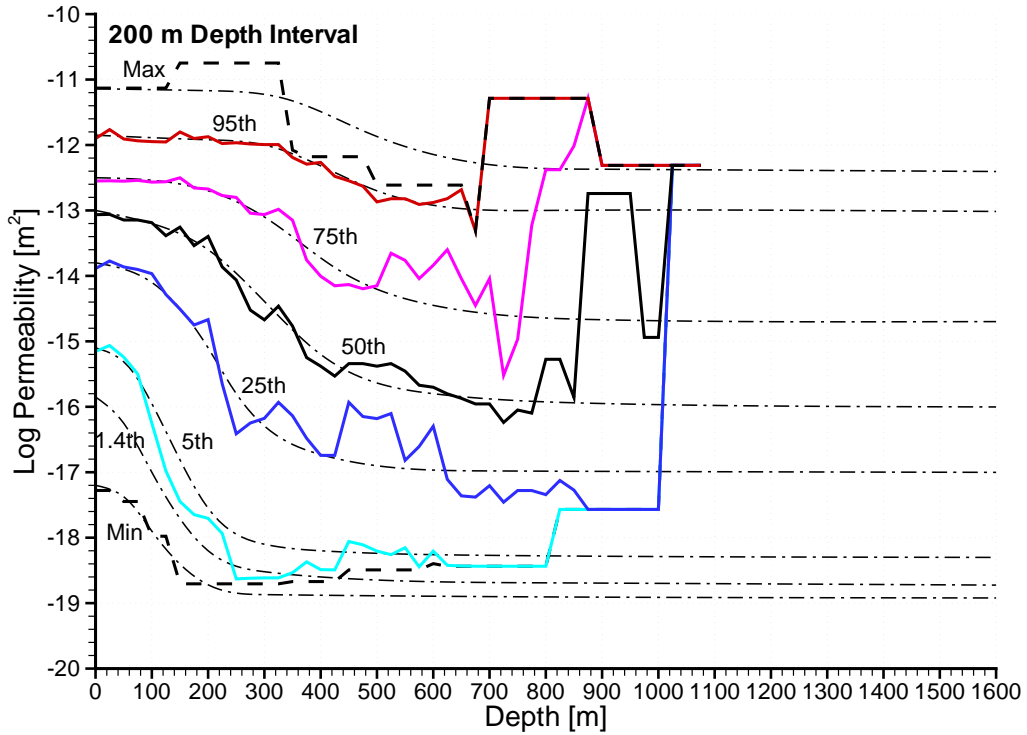


Figure 10:  $\text{Log}_{10}$  permeability percentile with depth for a 200 m depth range and best-fit cubic splines

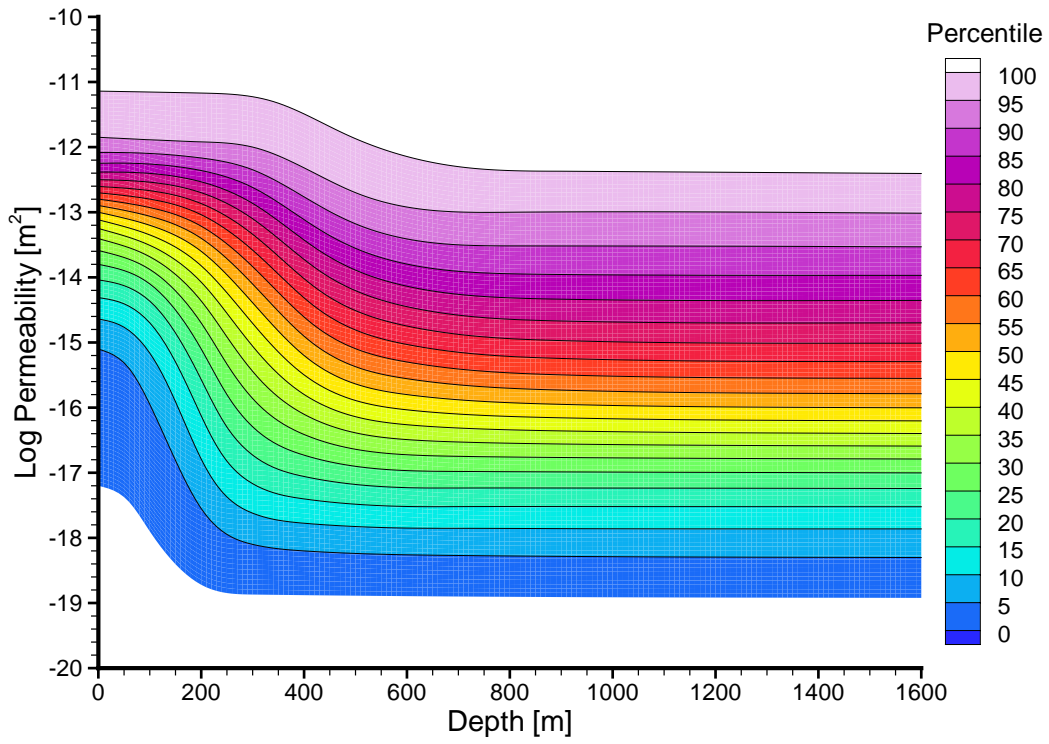


Figure 11: Cumulative density function for log<sub>10</sub> of fracture permeability

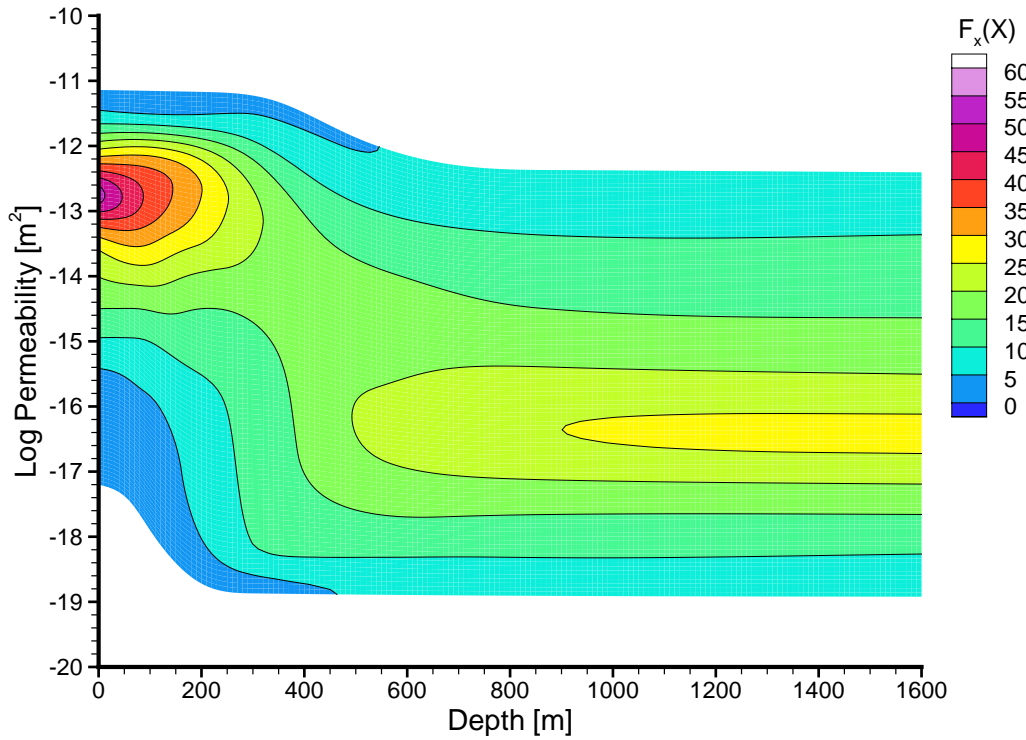
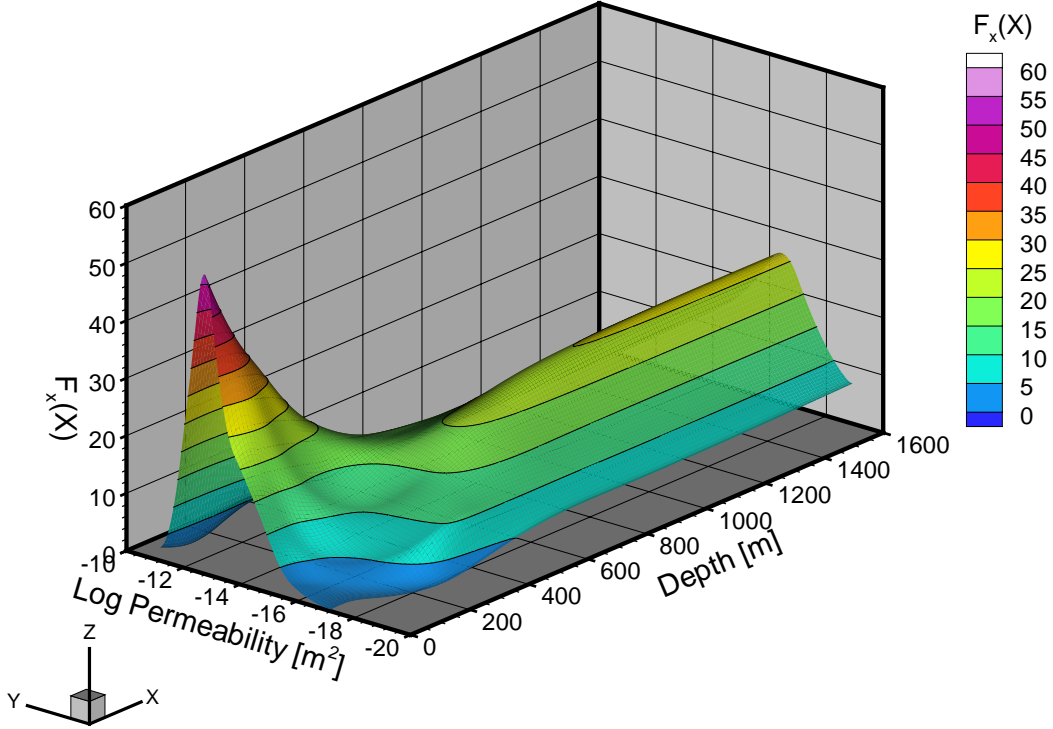


Figure 12: Probability density function for log<sub>10</sub> of fracture permeability



**Figure 13: 3-D view of the probability density function for  $\log_{10}$  of fracture permeability**

surface. The fracture permeability  $k_F$  is therefore calculated as:

$$k_F = 10^{CDF(d, U[0,100])^{-1}} \quad (3)$$

where  $d$  is the depth;  $U[0, 100]$  is a uniform random variate between 0 and 100; and  $CDF()^{-1}$  is the inverse CDF. A correlated random fracture permeability field can then be calculated using a correlated random uniform variate field.

## 2.6 FRACTURE ZONE WIDTH

In the Phase-I model, fracture zone width was represented as a constant width of 1.0 m. Since a probability density function for fracture zone width is also desired, the WRA data in Figure 7 from Stevenson et al. (1996), where the fracture interval width is indicated for each estimated fracture zone permeability, was plotted as a histogram and a minimum error log-normal probability distribution was developed:

$$F_X(x) = \frac{1}{x\sigma\sqrt{2\pi}} e^{-\frac{1}{2}\left(\frac{\ln(x/m)}{\sigma}\right)^2} \quad (4)$$

where  $\sigma = 0.48289$  and  $m = 3.26841$ . The log-normal PDF and WRA fracture width histogram are shown in Figure 15.

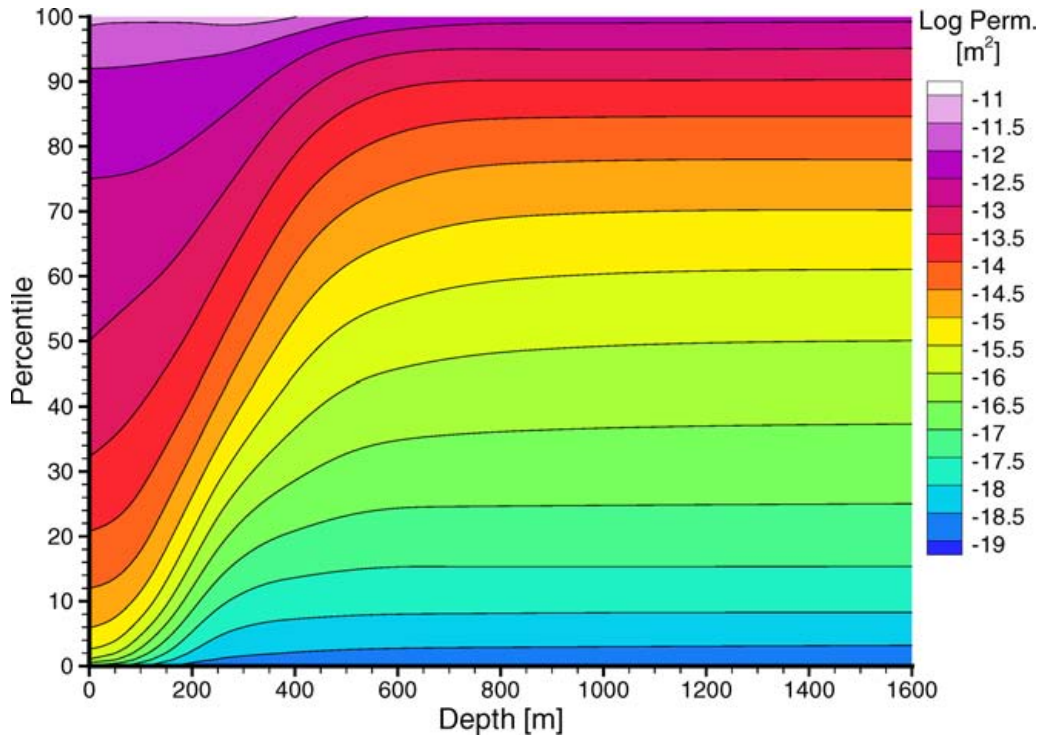


Figure 14: Inverse cumulative density function for log<sub>10</sub> of fracture permeability

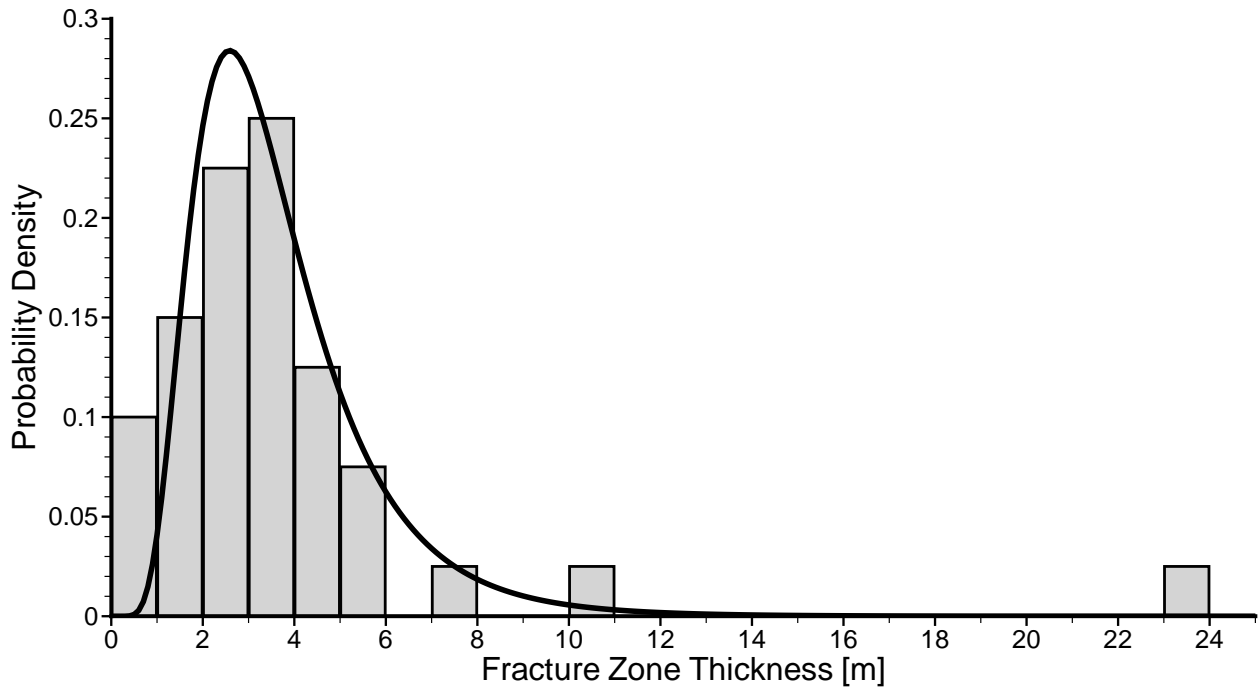


Figure 15: Fracture zone width histogram and log-normal PDF

## 2.7 FRACTURE ZONE POROSITY

A fracture zone porosity can be calculated from the fracture zone permeability and a given fracture frequency (Bear, 1988; Chen et al., 1999; Snow, 1968, 1969). The bulk fracture zone permeability tensor and bulk fracture zone porosity are defined as:

$$k_{F_{ij}}^{bulk} = \sum_{i=1}^n k_{F,i} (\mathbf{I} - \mathbf{n}_i \otimes \mathbf{n}_i) + (1 - \phi_F) k_{M_{ij}} \quad (5)$$

$$\phi_F^{bulk} = \phi_F + (1 - \phi_F)\phi \quad (6)$$

where  $k_{F,i}$  is the single fracture permeability in direction  $i$  [ $L^2$ ];  $\mathbf{I}$  is the identity matrix [/];  $\mathbf{n}_i$  is the unit vector normal to fracture plane  $i$  [/];  $\phi_F$  is the volumetric fracture fraction [/];  $k_{M_{ij}}$  is the porous matrix permeability tensor [ $L^2$ ]; and  $\phi$  is the porous matrix porosity [/].  $k_{F,i}$  and  $\phi_F$  are then defined as:

$$k_{F,i} = \frac{\gamma_i a_i^3}{12} \quad (7)$$

$$\phi_F = \sum_{i=1}^n \gamma_i a_i \quad (8)$$

where  $\gamma_i$  is the fracture density in direction  $i$  [fractures/L]; and  $a_i$  is the fracture aperture in direction  $i$  [L]. For the case of three sets of orthogonal fractures with identical apertures and fracture spacing,  $k_{F_{ij}}^{bulk}$  and  $\phi_F^{bulk}$  become:

$$k_{F_{ij}}^{bulk} = \frac{\gamma a^3}{6} + (1 - 3\gamma a) k_{M_{ij}} \quad (9)$$

$$\phi_F^{bulk} = 3\gamma a + (1 - 3\gamma a)\phi \quad (10)$$

Hence, given a fracture permeability from Equation (3), a fracture aperture,  $a$ , can be calculated using Equation (9), and then substituted into Equation (10) to determine the fracture zone porosity.

### 3. METHODOLOGY

#### 3.1 DENSITY DEPENDENT FLOW AND TRANSPORT

The physical properties of groundwater in a Shield environment can vary by greater than 25 % for density and by one order of magnitude for viscosity, although the relationship between fluid properties and TDS, temperature, or pressure is not yet completely understood. Density and viscosity changes may retard or enhance fluid flow or contaminant transport driven by other mechanisms: flow and transport is dependent on fluid density and viscosity as well as media properties such as permeability, porosity, and dispersivity. Thus, variations in fluid density and viscosity may have significant impacts on the flow system with consequences for various relevant processes (Adams and Bachu, 2002).

##### 3.1.1 Characterizing Brine Solutions

The relationship between TDS, solution density, and mass fraction in characterizing solutes in water is as follows:

$$\rho = \frac{M}{V} \quad (11a)$$

$$TDS = \frac{m}{V} \quad (11b)$$

$$X = \frac{m}{M} \quad (11c)$$

where  $\rho$  is the solution density,  $M$  is the mass of solution,  $V$  is the volume of solution,  $m$  is the mass of solute (salts such as  $NaCl$  or  $CaCl_2$ ), and  $X$  is the mass fraction. By combining these equations, a new relationship for TDS can be determined as:

$$TDS = m \cdot \frac{1}{V} = XM \cdot \frac{\rho}{M} = X\rho \quad (12)$$

Adams and Bachu (2002) present a study of brine density and viscosity for the Alberta Basin, consisting primarily of Na-Cl waters. The data and analyses of their paper can be used to illustrate the relationship between brine concentration given as mass fraction and fluid density. Figure 7 in their paper presents a plot of brine density versus mass fraction for 4854 formation water analyses and is presented as Figure 16 below.

We see that a mass fraction of 0.25 matches a density of approximately  $1200 \text{ kg/m}^3$  or  $1.2 \text{ kg/L}$ . Using Equation (12) results in a TDS of  $300 \text{ kg/m}^3 = 300 \text{ g/L} = 300\,000 \text{ mg/L}$ .

##### 3.1.2 Governing Equations

The equations governing density-dependent flow and transport are the Darcy equation, the continuity equation for the fluid, the continuity equation for the solute, and the constitutive

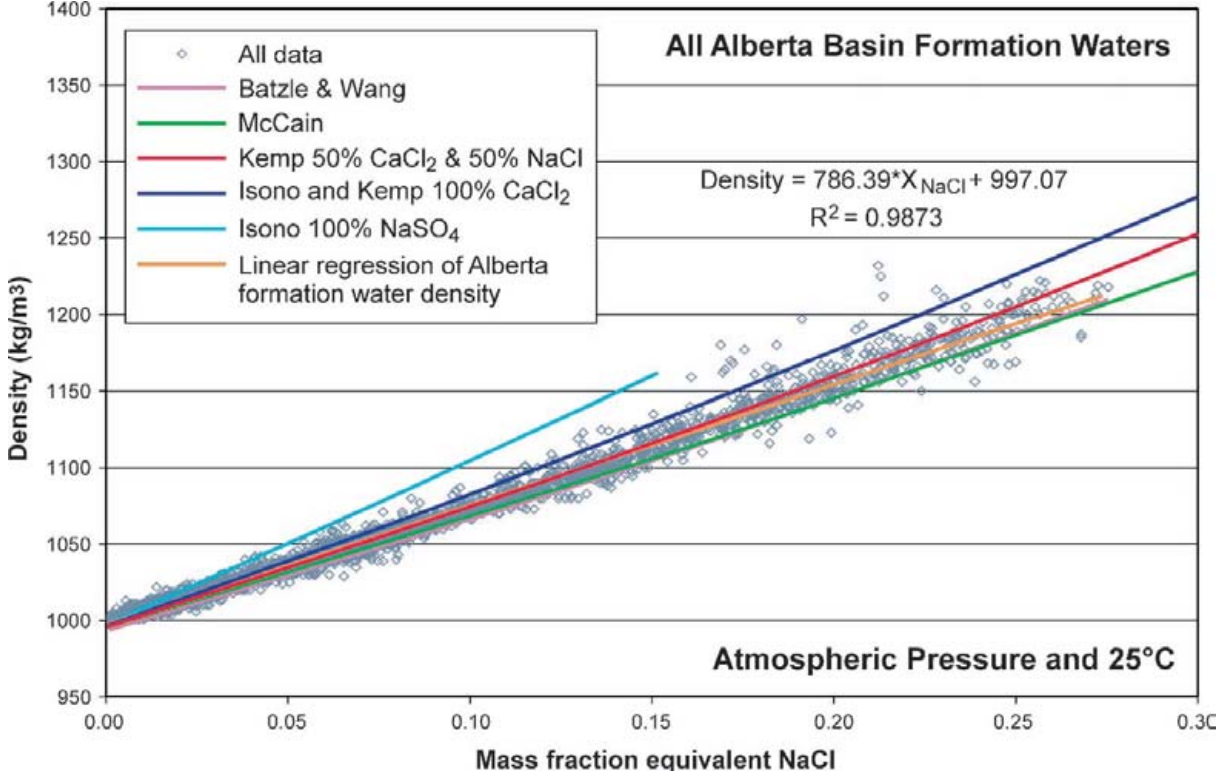


**Figure 16: Figure 7 from Adams and Bachu (2002) showing brine density versus mass fraction for 4854 formation water analyses**

equation relating fluid density to concentration (Frind, 1982). The general Darcy equation for density-dependent flow is:

$$q_i = -\frac{k_{ij}}{\mu} \left( \frac{\partial p}{\partial x_j} + \rho g \eta_j \right) \quad (13)$$

where  $q_i$  is the flux in the  $i$  th direction,  $k_{ij}$  is the permeability tensor,  $\mu$  is the dynamic viscosity,  $p$  is the pressure,  $\rho$  is the density, and  $\eta_j = 1$  for the vertical direction ( $z$ ) while  $\eta_j = 0$  for the horizontal directions ( $x, y$ ). The general Darcy equation can be re-written in terms of equivalent fresh water head, defined as  $h = p/\rho_0 g + z$ :

$$q_i = -\frac{k_{ij}}{\mu g} \left( \frac{\partial h}{\partial x_j} + \rho_r \eta_j \right) \quad (14)$$

where  $\rho_r$  is the relative density given as  $(\rho/\rho_0 - 1)$  and  $\rho_0$  is the reference (freshwater) density. For an elastic solution (fluid), its density is a function of fluid pressure and solute concentration:

$$\rho = \rho_0 [1 + c_w (\rho - \rho_0) + \gamma C] \quad (15)$$

where  $\rho_0$  represents the freshwater density at reference pressure  $p_0$ ,  $c_w$  is the compressibility of water,  $\gamma$  is a constant derived from the maximum density of the fluid,  $\rho_{max}$ , and is defined as  $\gamma = (\rho_{max}/\rho_0 - 1)$ , and  $C$  is the relative concentration.

Viscosity ( $\mu$ ) is a function of concentration under isothermal conditions. It is reasonable to assume a linear relationship with  $C$  as far as the maximum change in viscosity is insignificant in isothermal conditions.

$$\mu = \mu_0(1 + \gamma_\mu C) \quad (16)$$

where  $\mu_0$  is the viscosity of pure water, and  $\gamma_\mu = (\mu_{max}/\mu_0 - 1)$ . The general Darcy equation for visco-elastic solutions is then given as the following:

$$q_i = -\frac{k_{ij}}{\mu_0 g} \cdot \frac{1}{1 + \gamma_\mu C} \cdot \left( \frac{\partial h}{\partial x_j} + [c_w(p - p_0) + \gamma C] \eta_j \right) \quad (17)$$

By applying the continuity principle, the groundwater flow equation can be derived for visco-elastic solutions:

$$\frac{\partial}{\partial x_i} \left[ K_{ij}^0 \cdot \frac{1}{1 + \gamma_\mu C} \left( \frac{\partial h}{\partial x_j} + [c_w(p - p_0) + \gamma C] \eta_j \right) \right] = S_s \frac{\partial h}{\partial t} \quad (18)$$

where  $K_{ij}^0 = k_{ij}/\mu_0 g$  and  $S_s$  is the specific storage. The solute continuity equation is written in terms of the relative concentration as:

$$\frac{\partial}{\partial x_i} \left( \phi D_{ij} \frac{\partial C}{\partial x_j} \right) - \frac{\partial}{\partial x_i} (q_i C) = \theta \frac{\partial C}{\partial t} \quad (19)$$

where the Darcy flux  $q_i$  is computed by solving Equation (18),  $\phi$  is the porosity, and  $D_{ij}$  is the hydrodynamic dispersion tensor as defined by Bear (1988):

$$\phi D_{ij} = (\alpha_l - \alpha_t) \frac{q_i q_j}{|q|} + \alpha_t |q| \delta_{ij} + \phi \tau D_{free} \delta_{ij} \quad (20)$$

where  $\alpha_l$  and  $\alpha_t$  are the longitudinal and transverse dispersivities, respectively,  $|q|$  is the magnitude of the Darcy flux,  $\tau$  is the tortuosity,  $D_{free}$  is the free-solution diffusion coefficient and  $\delta_{ij}$  is the Kronecker delta. The product  $\tau D_{free}$  represents an effective diffusion coefficient.

Note that the density-dependent flow and transport problem is nonlinear because the solution of Equation (18) (flow equation) requires fluid densities which depend on the solute concentration from Equation (19), and the solution for Equation (19) requires the Darcy flux calculated from Equation (18).

### 3.1.3 Numerical Implementation

Equation (18) can be re-written by using a differential operator as:

$$L(h) = \frac{\partial}{\partial x_i} \left[ K_{ij}^0 \cdot \frac{1}{1 + \gamma_\mu C} \left( \frac{\partial h}{\partial x_j} + [c_w(p - p_0) + \gamma C] \eta_j \right) \right] - S_s \frac{\partial h}{\partial t} = 0 \quad (21)$$

The Galerkin finite element formulation using a trial solution  $\hat{h} = \sum_j w_j h_j$  (where  $w_j$  is a shape function) was applied to Equation (21) over the solution domain  $\Omega$ .

$$\int_{\Omega} L(\hat{h}) w_i d\Omega = 0 \quad (22)$$

and the discrete equation for Equation (21) can be derived as:

$$\begin{aligned} & \sum_{j=1}^n h_j \left\{ \sum_e \int_{\Omega^e} \left( K_{kl}^0 \frac{\partial w_i}{\partial x_k} \frac{\partial w_j}{\partial x_l} \right) \cdot \frac{1}{1+\gamma_\mu \bar{C}} \cdot d\Omega^e \right\} + \\ & \sum_{j=1}^n \frac{\partial h_j}{\partial t} \left\{ \sum_e \int_{\Omega^e} S_s \delta_j w_j' d\Omega^e \right\} + \\ & \sum_{\Omega^e} \int_{\Omega^e} K_{zz}^0 [c_w(\bar{p} - p_0) + \gamma \bar{C}] \frac{\partial w_i}{\partial z} \cdot \frac{1}{1+\gamma_\mu \bar{C}} d\Omega^e - \sum_e \int_{\delta\Omega^e} q_n w_i d(\delta\Omega^e) = 0 \end{aligned} \quad (23)$$

where  $\sum_e$  indicates summation over the elements joining at node  $j$ ,  $\Omega^e$  and  $\delta\Omega$  are the elemental domain and the elemental boundary, respectively,  $\bar{p}$  and  $\bar{C}$  are the average elemental fluid pressure and relative concentration in the element, respectively, and  $q_n$  is the flux normal to  $\delta\Omega$ .

Equation (19) is identical to the equation for transport in freshwater. Numerical discretization for Equation (19) and solution strategies are detailed in Therrien et al. (2004). Nonlinear flow and transport equations are solved by using Picard iteration in each time step, until the changes in equivalent freshwater head and relative concentration are negligible for convergence.

### 3.1.4 Vertically Hydrostatic Initial Condition

Hydrostatic equilibrium in the vertical direction can be applied to the domain as an initial condition for density-dependent flow and transport simulations. A vertically hydrostatic equilibrium condition is expressed as:

$$q_z = -\frac{k_{zz}}{\mu_0 g} \cdot \frac{1}{1 + \gamma_\mu C} \cdot \left( \frac{\partial h}{\partial z} + [c_w(p - p_0) + \gamma C] \right) = 0 \quad (24)$$

where  $z$  represents the vertical direction. By integrating Equation (24) from  $z_{ref}$  to  $z$ , where  $z_{ref}$  is the reference elevation at which the equivalent freshwater head  $h(z_{ref})$  is prescribed, the equivalent freshwater head at  $z$  in an equilibrium condition can be derived:

$$h(z) = h(z_{ref}) - \int_{z=z_{ref}}^z [c_w(p - p_0) + \gamma C] dz \quad (25)$$

Numerical integration of  $N$  vertically aligned nodes is given by:

$$h_i^{it} = h_{ref,N} + \sum_{k=i}^N [c_w(\bar{p}_k^{it-1} - p_0) + \gamma \bar{C}_k] \Delta z_k \quad (26)$$

where superscript  $it$  represents the nonlinear iteration count and summation is implied over elements between node  $i$  and the top reference node  $N$  of reference head  $h_{ref}$ .

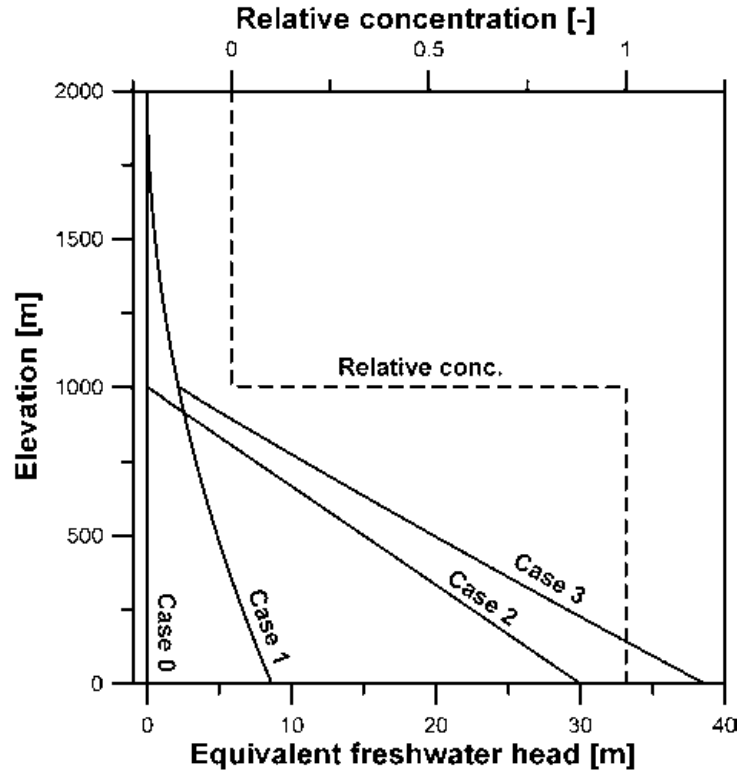


**Figure 17: Examples for vertically hydrostatic initial conditions for equivalent freshwater head distributions. Case 0: reference head; Case 1: compressible fluid without density effects; Case 2: incompressible fluid with a maximum density of 1.03 kg/L; Case 3: compressible fluid with a maximum density of 1.03 kg/L**

The initial vertically hydrostatic equilibrium condition was tested for a vertical 1-dimensional domain of 2 km depth where the fluid is considered to be either compressible or incompressible, while considering or neglecting density effects (see Figure 17).

### 3.2 CLIMATE AND SURFACE BOUNDARY CONDITIONS

The climate and surface boundary conditions are provided by Peltier (2003a, 2006). Two parameters are used in this study: permafrost depth ( $d_{PF}$ ), and the normal stress ( $\sigma_{ice}$ ) at ground surface due to the presence of ice. Both of these parameters are used in FRAC3DVS, with some assumptions. First, the ice load is applied as equivalent freshwater head using a Dirichlet boundary condition across all surface nodes, and second, the permafrost depth modifies the porous media and fracture zone permeabilities, depending on whether the entire grid block or fracture face is completely frozen, or partially frozen. Since both permafrost depth and normal stress vary in time (1000 year time steps), their values are linearly interpolated in time with respect to the simulation time. As FRAC3DVS can vary time steps to suit groundwater flow and solute transport maximum change criteria ( $\Delta h$ ,  $\Delta C$ ), the permafrost depth and normal stress are recalculated for the current simulation time.

The hydraulic conductivity of frozen porous media is assigned the value of  $K_{PF} = 0.4102488 \times 10^{-4}$  m/year and is assumed to be isotropic. This value is similar to the permeability for the deepest units in Table 1. For grid blocks and fracture faces that are partially frozen, the following equation is used:

$$K_{H(PF)} = \frac{K_H \Delta Z_{unfrozen} + K_{PF} \Delta Z_{frozen}}{\Delta Z_{unfrozen} + \Delta Z_{frozen}} \quad (27a)$$

$$K_{V(PF)} = \frac{\frac{\Delta Z_{unfrozen}}{K_V} + \frac{\Delta Z_{frozen}}{K_{PF}}}{\frac{\Delta Z_{unfrozen}}{K_V} + \frac{\Delta Z_{frozen}}{K_{PF}}} \quad (27b)$$

where  $K_H$  is the horizontal hydraulic conductivity,  $\Delta Z_{unfrozen}$  is the unfrozen height of a grid block or vertical fracture face,  $\Delta Z_{frozen}$  is the frozen height of a grid block or vertical fracture face, and  $K_V$  is the vertical hydraulic conductivity. The total height of the grid block or vertical fracture face is  $\Delta Z_{unfrozen} + \Delta Z_{frozen}$ . Equation (27a) represents the arithmetic mean for horizontal hydraulic conductivity, while Equation (27b) represents the harmonic mean for vertical hydraulic conductivity.

The normal stress due to the weight of ice on the domain is used to calculate an equivalent freshwater head which is applied at all surface nodes as a Dirichlet boundary condition,  $h_{ice}$  according to:

$$h_{ice} = \begin{cases} \frac{\sigma_{ice}}{\rho g} + z, & \text{for } d_{PF} > 0 \text{ and } \sigma_{ice} > 0; \\ z, & \text{otherwise} \end{cases} \quad (28)$$

where  $\rho$  is freshwater density,  $g$  is the gravitational constant,  $z$  is ground surface elevation and  $d_{PF}$  is the depth of permafrost. For the situation where  $\sigma_{ice} = 0$  and  $d_{PF} = 0$  (no ice load or permafrost), only surface nodes associated with water features, such as rivers, lakes, and wetlands, are selected as Dirichlet nodes, allowing recharge to occur across the modelling domain. Once either permafrost or an ice load are present, all surface nodes are selected as Dirichlet nodes and the appropriate  $h_{ice}$  is applied. Assigning Dirichlet nodes across the entire surface prevents recharge from entering the system if surface permeability is too low (in the case of permafrost) or in the case of the presence of ice, which would not allow recharge to take place. A meltwater production rate is not used for the ice-sheet.

### 3.3 LIFETIME EXPECTANCY AS A SAFETY INDICATOR

The classical criteria used to determine the optimal location of a deep geologic repository (DGR) are:

- i) the longest travel time from the waste site to the biosphere,
- ii) the least dose (or maximum dilution) to the biosphere; and
- iii) the minimal prediction uncertainty.

In the following sections, we mainly focus on points (i) and (ii). In this report, we first recall the equivalence between the standard advection-dispersion equation (ADE) and standard diffusion

theory which relates the dynamics of a diffusion process to the Fokker-Planck equation. The lifetime expectancy of water molecules is then defined by introducing the formal adjoint of the forward equation. Various sources of uncertainty for the sub-regional domain are discussed in Chapter 5.

### 3.3.1 Contaminant Transport in Groundwater

The stochastic motion of particles in dynamic systems has been studied intensively in the theory of stochastic differential equations. The spreading of a contaminant mass can be described by the random motion of solute particles, and the ADE is assimilated to the forward Fokker-Planck (or forward Kolmogorov) equation. Therefore, it is possible to derive an Itô stochastic differential equation as a random walk model for the movement of a contaminant particle that is exactly consistent with the advection-dispersion model. Two alternative differential equations have been developed (see Gardiner (1983)): the forward Fokker-Planck equation (FPE) and the backward-in-time Kolmogorov equation (BKE) (Kolmogorov, 1931). The FPE describes the future state of a system, given its initial situation, while the BKE provides information about the state of the system in the past. Both equations are formulated in terms of probabilities. With the FPE, one can see that, under certain conditions, the probability densities can be interpreted as solute concentrations and the expected resident concentration of a conservative tracer conforms to the probability density for the location of a particle, at any time after having entered the system.

A Lagrangian approach for solute transport describes the spreading of a contaminant in a flow system as follows: in a bounded domain  $\Omega$  in  $R^d$  ( $d = 1, 2, \text{ or } 3$ ) with boundary  $d\Omega$ , the position of the contaminant particle at time  $t$ ,  $X_{x_0 t_0}(t)$ , released at time  $t_0$  at  $X_{x_0 t_0} = x_0$  is determined by means of the Itô stochastic differential equation, as detailed in Appendix A. The transition probability density  $p(x, t | x_0, t_0)$  to find a particle at position  $x$  at time  $t$ , given that it was released at position  $x_0$  at time  $t_0$ , can be obtained by solving the FPE:

$$\frac{\partial p}{\partial t} = -\frac{\partial a_i p}{\partial x_i} + \frac{\partial^2 b_{ij} p}{\partial x_i \partial x_j} \quad (29)$$

where the terms  $a_i = a_i(x, t)$  and  $b_{ij} = b_{ij}(x, t)$  denote the drift vector and noise tensor, respectively, and the Einstein summation convention is used. The solution of the FPE is subject to the initial condition  $p(x, t_0 | x_0, t_0) = \delta(x - x_0)$  and any appropriate boundary conditions (Gardiner, 1983). The change of variable  $p(x, t)$  to  $\phi(x)C(x, t)$ , where  $\phi$  is the porosity or mobile water content, and  $C$  is the solute residence concentration, leads to the definitions of  $a_i$  and  $b_{ij}$  as follows:

$$a_i(x, t) = v_i(x, t) + \phi(x)^{-1} \frac{\partial}{\partial x_j} (\phi(x) D_{ij}(x, t)) \quad (30a)$$

$$b_{ij}(x, t) = D_{ij}(x, t) \quad (30b)$$

where the  $v_i$  is the pore velocity component and  $D_{ij}$  is the dispersion tensor as defined by Bear (1988). One can show that Equation (29) becomes equivalent to the following classical forward ADE (LaBolle et al., 1998, 2000):

$$\frac{\partial \phi C}{\partial t} = -\frac{\partial}{\partial x_i} (q_i C) + \frac{\partial}{\partial x_i} \phi D_{ij} \frac{\partial C}{\partial x_j} \quad (31)$$

where  $q_i = \phi v_i$  is the water flux vector. This result implies that the particle model equation (Equation (A.1)) with  $a_i$  and  $b_{ij}$  defined as in Equation (30) are exactly consistent with the ADE. Consequently, a particle concentration that is obtained by simulating Equation (A.1) for many particles is an approximation of the solution for Equation (31).

### 3.3.2 The Lifetime Expectancy of Radionuclides

The use of forward and backward models for location and travel time probability has become a classical mathematical approach for contaminant transport characterization and prediction (LaBolle et al., 1998; Uffink, 1989; Neupauer and Wilson, 1999; Spivakovskaya et al., 2005). The forward version of the Fokker-Planck equation points to the future and the transformation from probabilities and particle densities to a physical concept of a solute concentration is straightforward. In the backward formulation, the correspondence between probability and concentration is lost. When a particle is observed at a certain time and position, its possible location at an earlier time covers an area that increases in size as we look further back in time (Uffink, 1989). Assuming that the flow field is divergence-free and at steady-state, the BKE can be expressed by the following (see Appendix A):

$$\frac{\partial \rho}{\partial \tau} = -\frac{\partial a_i^* \rho}{\partial x_i} + \frac{\partial^2 b_{ij} \rho}{\partial x_i \partial x_j} \quad (32)$$

where  $\tau = t_0 - t$  is backward (or reverse) time, and the drift vector  $a_i^*$  and noise tensor  $b_{ij}$  are defined as follows:

$$a_i^*(x) = -v_i(x) + \phi(x)^{-1} \frac{\partial}{\partial x_j} (\phi(x) b_{ij}(x)) \quad (33a)$$

$$b_{ij}(x) = D_{ij}(x) \quad (33b)$$

Equation (32) has the form of a forward equation, showing that the FPE and the BKE are equivalent to each other. Only the drift coefficient differs from its original definition: velocity presents a reversed sign to handle the backward-in-time evolution. Equation (32) is often called the formal adjoint of the FPE (Garabedian, 1964; Arnold, 1974). Suppose that a particle is found at position  $x_0$  at time  $t_0$ . To evaluate the probability that this particle was at an upstream position at an earlier time, one can solve the BKE as expressed by Equation (32), with the initial condition  $\rho(x, t_0 | x_0, t_0) = \delta(x - x_0)$ . Solutions of the FPE, subject to such an initial condition and any appropriate boundary conditions, yield solutions of the BKE as well. For the FPE, solutions exist for  $t \geq t_0$  with  $(x_0, t_0)$  fixed, while, for the BKE, solutions exist for  $t \leq t_0$ , so that the backward equation expresses the development in  $t_0$ , and  $\rho(x, t_0 | x_0, t_0) = \delta(x - x_0)$  is rather termed as the final condition (Gardiner, 1983). The forward equation gives more directly the values of measurable quantities (such as concentration  $C$ ) as a function of the observed time  $t$ . The backward equation is most applicable in the study of first passage time or exit problems, in which we find the probability that a particle leaves a region in a given time. Using the definitions Equation (33), and replacing  $\rho = \phi g$  in Equation (32), one obtains:

$$\frac{\partial \phi g}{\partial \tau} = \frac{\partial}{\partial x_i} (q_i g) + \frac{\partial}{\partial x_i} \phi D_{ij} \frac{\partial g}{\partial x_j} \quad (34)$$

where  $g = g(x, t)$  is a backward-in-time probability density for the particle location. Equation (34) corresponds to the so-called "backward-in-time" ADE (Uffink, 1989; Van Kooten, 1995; Wilson and Liu, 1997; Neupauer and Wilson, 1999; Weissmann et al., 2002; Cornaton and Perrochet, 2006a,b). The probability density function (PDF) for lifetime expectancy can be obtained by solving Equation (34) when a unit pulse flux input is uniformly applied over the discharging areas of the reservoir. Specific details concerning the numerical implementation of the lifetime expectancy boundary value problem can be found in Cornaton and Perrochet (2006a). In the current problem of safety analysis of a DGR, one can consider that the target is known (e.g., the biosphere), and this target can be taken as the union of all the outlets for the region of concern. The source is a priori unknown since we are investigating potentially acceptable repository locations.

### 3.3.3 Mean Lifetime Expectancy as a Safety Indicator

Lifetime expectancy is given as a PDF for an appropriate representative volume and the mean lifetime expectancy, its first temporal moment, is an average expected lifetime for the volume and a representative statistic for the PDF. Since this statistic can be more comparable to radiometric data and can be computed with relative ease, it may be used for preliminary safety analysis in evaluating possible repository locations. It could also be used as a tool to compare the influence of relevant physical processes and parameters. Note, however, that a longer mean lifetime expectancy does not always guarantee the least dose, or the later arrival of risks at the biosphere, as the averaged travel time of contaminants can be much longer than first or peak arrivals in multiple pathway reactive systems, even though it might indicate so.

Suppose that  $g(x, t)$  is a solution of Equation (34), given that  $g(x, 0) = \delta(x - x_b)$ , for all  $x_b$  on the outlet boundary. The density function  $g(x, t)$  is equivalent to the lifetime expectancy of a water molecule at the location  $x$ , prior to exiting the reservoir. The mean lifetime expectancy  $E(x)$  is defined as the first temporal moment of the function  $g(x, t)$ :

$$E(x) = \langle g(x, t) \rangle = \int_0^{\infty} t g(x, t) dt \quad (35)$$

The function  $E(x)$  is the solution of the first moment form of Equation (34), given that  $E(x_b) = 0$ :

$$\frac{\partial}{\partial x_i} (q_i E) + \frac{\partial}{\partial x_i} \phi D_{ij} \frac{\partial E}{\partial x_j} + \phi = 0 \quad (36)$$

In Equation (36), mean lifetime expectancy is continuously generated during groundwater flow, since porosity  $\phi(x)$  acts as a source term. This source term indicates that groundwater is aging one unit per unit time, on average. The mean lifetime expectancy equation can be easily handled by numerical codes that solve ADEs, by distributing a source term equal to porosity, and by reversing the velocity field.

### 3.3.4 Mass Loads at the Biosphere and Risk Assessment

In order to simulate the transient history of a contaminant release with a relatively low computational burden, we again make use of the backward-in-time equation. The solution of

Equation (36),  $g(x, t)$ , is the PDF for the lifetime expectancy of water molecules. It can be shown that the total net mass flux  $j_b$  at the biosphere, resulting from a transient input of intensity  $m^*(x, t)$  [ $MT^{-1}$ ] at the repository site location, can be evaluated by the following equation (Cornaton, 2003):

$$j_b(t) = \int_{\Omega} \left( \int_0^t m^*(x, t-u)g(x, u)du \right) \delta(x - x_r)dx \quad (37)$$

where the  $x_r$  indicate the coordinates over the repository locations. Equation (37) is similar to the one presented in Rubin (2003), but it presents the considerable advantage that, since  $g(x, t)$  needs to be solved only once, the mass outflux  $j_b(t)$  (and thus the associated risk) can be post-processed for a series of different repository locations. The flux averaged concentration at the biosphere can be obtained by normalizing  $j_b(t)$  with the outflow discharge rate. A decay process can easily be added in the formulation Equation (37) by substituting the lifetime expectancy density  $g(x, t)$  by the defective density  $g_d(x, t) = \exp(-\frac{\ln 2}{\omega}t)g(x, t)$ , where  $\omega$  is the radionuclide half-life (Andričević et al., 1994). Equation (37) can then be applied to a series of specific radionuclides with different half-lives.

### 3.3.5 Lifetime Expectancy in Fractured Porous Media

In a crystalline geologic environment, interconnected permeable fracture networks have attracted concern since they could act as pathways for rapid contaminant migration. In this section, analytical solutions are derived for the first and second temporal moments of lifetime expectancy in a semi-infinite domain with a set of parallel vertical fractures in a porous matrix block, which could represent a typical fractured crystalline environment as shown in Figure 18 (Sudicky and Frind, 1982).

To derive analytical solutions for lifetime expectancy, fractures with a constant aperture  $2b$  are distributed with equal spacing  $L$ , as shown in Figure 18. Fluid flow is assumed to be upward-directional with a constant flow rate  $q_f$  in each fracture. Transport in fractures is assumed to be 1-dimensional advective-dispersive along the fracture axis, while diffusion is the dominant transport process in the matrix block perpendicular to the fracture axis. Under these conditions, the following boundary value problem can be derived from Equation (36) for mean life expectancy in the fracture and matrix domains:

$$-q_f \frac{\partial E_f}{\partial z} + n_f D_f \frac{\partial^2 E_f}{\partial z^2} + n_f = -\frac{n_m D_m}{b} \frac{\partial E_m}{\partial x} \Big|_{x=0} \quad (38)$$

$$n_m D_m \frac{\partial^2 E_m}{\partial x^2} + n_m = 0 \quad (39)$$

where  $x$  ( $[0, \infty)$ ) and  $z$  ( $[0, L]$ ) are spatial coordinates along and perpendicular to the fracture axis, respectively,  $E$  is the mean lifetime expectancy,  $n$  is porosity,  $D$  is the effective dispersion coefficient, and subscripts  $f$  and  $m$  denote fracture and matrix respectively. Symmetry and continuity constrain the boundary conditions as follows:

$$E_f(z = 0) = 0 \quad (40a)$$

$$\lim_{z \rightarrow \infty} E_f(z) \rightarrow \infty \quad (40b)$$

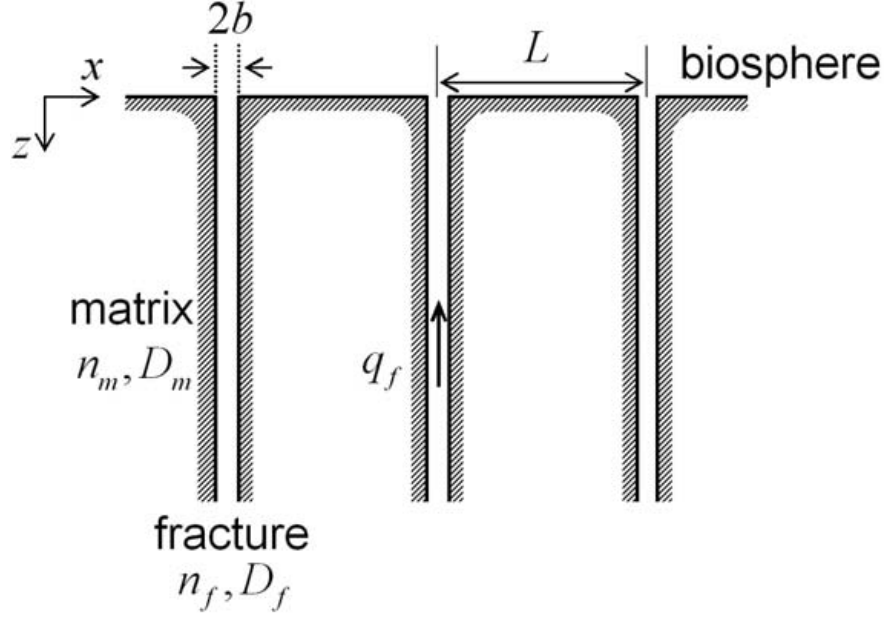


**Figure 18: Schematics for a set of parallel vertical fractures and matrix block system, to derive analytical solutions for temporal moments for lifetime expectancy**

$$E_m(x = 0, z) = E(x = L, z) = E_f(z) \quad (40c)$$

$$\left. \frac{\partial E_m}{\partial x} \right|_{x=L/2} = 0 \quad (40d)$$

The solution for Equation (38) with Equation (40) is given by

$$E_f(z) = \frac{z}{2bq_f} (n_m L + 2bn_f) = \frac{z}{v_f} \left( \frac{n_m L}{2bn_f} + 1 \right) \quad (41)$$

where  $v_f = q_f/n_f$  is the pore velocity in the fractures. The resulting mean lifetime expectancy in the fractures is a linear function of depth  $z$  and it becomes longer as the volume of water in the matrix block ( $n_m L$ ) becomes larger than the volume of water in the fractures ( $2bn_f$ ) due to matrix diffusion. On the other hand, when the matrix porosity is negligible ( $n_m L \ll 2bn_f$ ), the mean lifetime expectancy at depth  $z$  becomes the trivial piston-flow solution  $z/v_f$ . The mean lifetime expectancy in the matrix block is also given by:

$$E_m(x, z) = -\frac{1}{2D_m} x(x - L) + E_f(z) \quad (42)$$

Equation (42) shows that the mean lifetime expectancy is parabolic across the matrix block constrained by the solution in the bounding fractures  $E_f(z)$ . Maximum mean lifetime expectancy is obtained in the midpoint of the block ( $x = L/2$ ) as  $L^2/8D_m + E_f(z)$ , indicating that it becomes larger as the block gets bigger with smaller effective matrix diffusion (see Figure 19).

As solute travels longer, it spreads wider, and the variance of lifetime expectancy becomes larger as the mean lifetime expectancy becomes longer. The variance represents the uncertainty of the

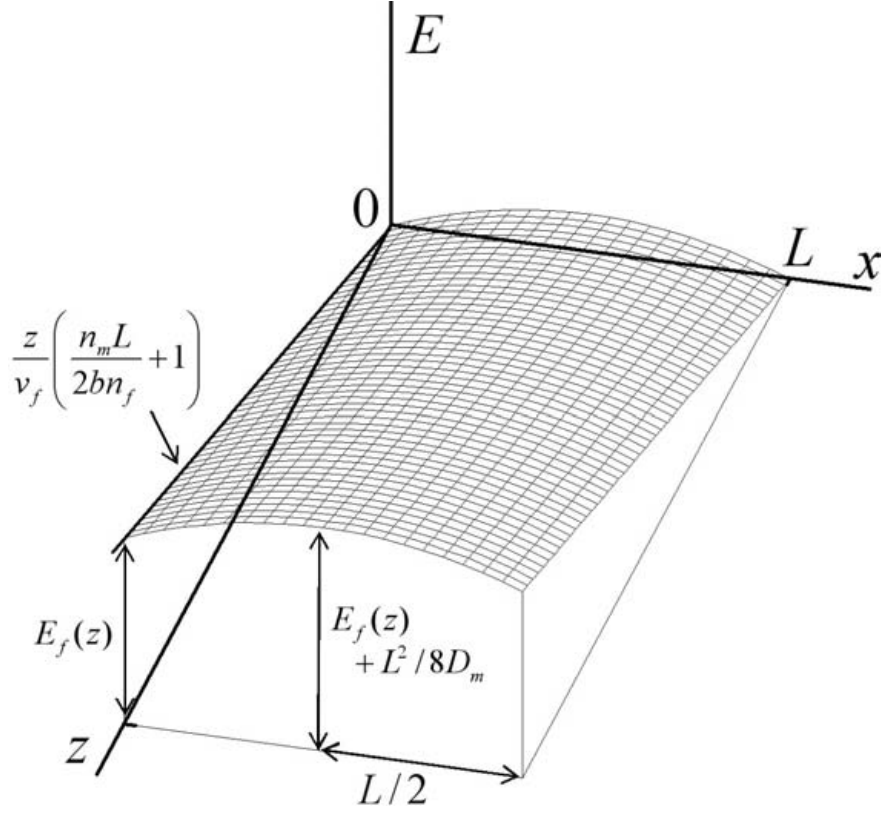


**Figure 19: Mean lifetime expectancy solutions for a set of parallel fractures and matrix block system in Figure 18**

mean as a safety indicator for repositories: for instance, if the mean of the lifetime expectancy is large and its variance is small for a certain point, it could be considered to be a safe location, while if the variance is large compared to the mean, a long lifetime expectancy may not adequately represent safety. In this context, we derive the variance of lifetime expectancy for a fracture as:

$$\sigma_f^2(z) = V_f(z) - E_f^2(z) = \int_0^\infty (t - E_f(z))^2 g(z, t) dt \quad (43)$$

A second moment equation similar to Equation (38) and Equation (39) can be derived from Equation (36) as follows:

$$-q_f \frac{\partial V_f}{\partial z} + n_f D_f \frac{\partial^2 V_f}{\partial z^2} + 2n_f E_f = -\frac{n_m D_m}{b} \frac{\partial V_m}{\partial x} \Big|_{y=b} \quad (44)$$

$$n_m D_m \frac{\partial^2 V_m}{\partial x^2} + 2n_m E_m = 0 \quad (45)$$

The solution for the variance of lifetime expectancy in fractures  $\sigma_f^2(z)$  has a form of  $\alpha z^2 + \beta z$ , where the coefficients  $\alpha$  and  $\beta$  are functions of  $b$ ,  $L$ ,  $n$ ,  $D$  and  $q_f$ . To avoid the redundancy but for illustrative purposes, the solutions  $E_f(z)$ ,  $\sigma_f(z)$ , and  $\sigma_f/E_f$  are plotted with depth for the case where  $L = 150$  m,  $b = 20$  m,  $n_f = 0.01$ ,  $n_m = 0.001$ ,  $q_f = 10$  m/year,  $D_f = D_m = 0.00725$  m<sup>2</sup>/year

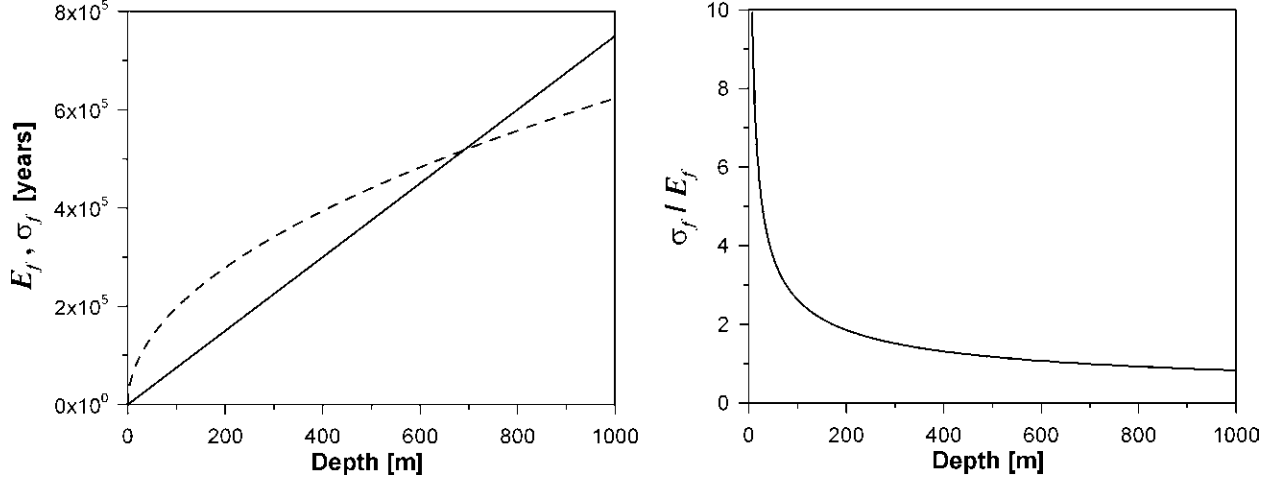


**Figure 20: (a) Mean ( $E_f$ : solid line) and standard deviation ( $\sigma_f$ : dashed line) in lifetime expectancy, and (b) the coefficient of variation ( $\sigma_f/E_f$ ) with depth for the fracture domain**

as shown in Figure 20. Figure 20a shows that the mean and standard deviation for lifetime expectancy become larger with depth. Note that increasing mean and variance in lifetime expectancy has positive and negative effects for a repository location as we can expect longer travel time from that location, but with a higher uncertainty. Interestingly, although both statistics increase with depth, the rates of increase are different and their ratio actually decreases, causing the relative uncertainty to get smaller with depth in Figure 20b. From these results, it could be concluded that, with careful uncertainty analysis, the mean lifetime expectancy could be used as a safety indicator for potential repository locations at depth in a fractured crystalline environment.

### 3.4 STATISTICAL ANALYSIS

In order to compare spatially and temporally distributed data such as hydraulic head, concentration, and lifetime expectancy, etc., parametric statistics such as mean and standard deviation, and non-parametric rank statistics such as percentiles, quartiles, quartile deviation, and range are utilized. In this section, various statistics used for this study, and their advantages and disadvantages, are summarized.

#### 3.4.1 Parametric Statistics

The mean,  $\mu = E(x)$ , and standard deviation,  $\sigma(x)$ , of variable  $x$  are the first and second central moments for a given number of samples,  $n$ :

$$E(x) = \frac{1}{n} \sum_{i=1}^n x_i \quad (46a)$$

$$\sigma(x) = \sqrt{\frac{1}{n} \sum_{i=1}^n [x_i - E(x)]^2} \quad (46b)$$

The mean and standard deviation for a given probability density function  $f(x)$  are defined as:

$$E(x) = \int x f(x) dx \quad (47a)$$

$$\sigma(x) = \sqrt{\int [x - E(x)]^2 f(x) dx} \quad (47b)$$

The mean is a representative statistic for a given sample or an expectation and the standard deviation represents the uncertainty of the mean or the degree of scattering about the mean. When the random variable  $x$  follows a certain specified probability density function such as a normal distribution, then the characteristics of the random variable can be characterized solely by its mean and standard deviation; the statistical inferences based on those statistics will be accurate and unbiased.

When the random variable  $\log(x)$  follows a known distribution function, then statistical inferences can be performed based on  $E(\log(x))$  and  $\sigma(\log(x))$ . In general, if samples of a random variable have orders of magnitude range and have only positive (or negative) values (for example, concentration or travel time), then the analysis with log-transformed values could be more appropriate. A representative value as  $\mu_g = 10^{E(\log(x))}$  is often called a geometric mean, to distinguish from an arithmetic mean  $\mu_a$ . An interesting characteristic for  $\sigma(\log(x))$  is its magnitude-independence; because the difference between sample value and the mean can be transformed as their ratio  $\log(x) - \log(\mu) = \log(x/\mu)$ , standard deviation (or root mean squared difference) in log-scale represents the relative degree of scattering. For a random variable following a normal distribution with a standard deviation value of 1, one can expect about 68 % of samples to range between  $E(x) - 1$  and  $E(x) + 1$ , and thus if  $\sigma(x) = 1$ , then 68 % of samples can range between 0 and 2, while if  $E(x) = 100$ , then 68 % of samples can range between 99 and 101. Therefore, uncertainty for the expectation is relatively higher for a smaller mean and lower for a larger mean. For a random variable following a log-normal distribution with a standard deviation of unity in log-scale,  $\sigma(\log(x)) = 1$ , if  $E(\log(x)) = 0$ , then 68 % of samples can range between 0.1 and 10, and if  $E(\log(x)) = 2$ , then they range between 10 and 1000.

In order to measure the uncertainty associated with the mean or expectation, the coefficient of variation (CV), defined as the ratio between standard deviation and mean  $CV = \sigma(x)/E(x)$ , can be used. When  $CV = 1$  with  $E(x) = 1$ , then 68 % of samples can range between 0 and 2, and in the case that  $E(x) = 100$ , they range between 0 and 200.

In safety analysis, certain worst case values need to be considered to ensure that the risk is minimal. In parametric statistics, statistics such as  $\mu - 2\sigma$  ( $\mu + 2\sigma$  if a larger value is considered to be safer) can be worst case values, because one can expect less than 2.5 % of samples to be smaller than  $\mu - 2\sigma$ .

### 3.4.2 Non-Parametric Statistics

When the population statistics are unknown for the random variable  $x$ , statistical inferences based on parametric statistics such as the mean, standard deviation, and CV could lead to inappropriate conclusions. Nonparametric rank statistics utilize the statistical rank of samples (ordinal number

of a sample in a list arranged in increasing or decreasing order) and thus they are independent of population statistics. For a given number of samples,  $n$ , ordered as  $Y_1 < Y_2 < \dots < Y_n$ , the statistical rank of  $Y_k$  is  $k$ . Important rank statistics include: minimum, maximum, midrange, range (or half range), percentiles, quartiles, quartile deviation, quartile coefficient of variation, etc.

Minimum and maximum are  $Y_1$  and  $Y_n$ , and represent the smallest and largest sample values. Midrange ( $MR$ ) is a representative value for the sample and is defined as  $MR = (Y_1 + Y_n)/2$ . The half range is defined as  $HR = (Y_n - Y_1)/2$  and is a measure of a degree of scattering or variability.

A  $k^{\text{th}}$  percentile ( $P_k$ ) is defined as  $\hat{Y}_{(k/100)n}$ , where  $\hat{Y}$  is an estimate for non-integer  $(k/100)n$  and one can expect  $k\%$  number of samples less than  $P_k$ .  $P_{25}$ ,  $P_{50}$ , and  $P_{75}$  are often termed as the first, second, and third quartiles ( $Q_1$ ,  $Q_2$ , and  $Q_3$ ). The second quartile is specifically termed as the median due to its representativeness of a sample. Quartile deviation ( $QD$ ) is defined as  $QD = (Q_3 - Q_1)/2$  to indicate the degree of scattering. Quartile coefficient of variation ( $QCV$ ) is a relative measure of the degree of scattering and it is defined as  $QCV = (Q_3 - Q_1)/(Q_3 + Q_1)$ .

Worst case values can be represented by minimum,  $P_1$ ,  $P_5$ ,  $Q_2 - 2QD$ , etc., in rank statistics as most samples are expected to be greater than the worst case values.

### 3.4.3 Advantages and Disadvantages

For given samples, arithmetic and geometric means ( $\mu_a$  and  $\mu_g$ ), midrange ( $MR$ ), and median ( $P_{50}$ ) can be used as a representative value.  $MR$  was derived from extreme samples (minimum and maximum) and thus is most sensitive to samples of extreme values (or outliers). If most sample values are different from minimum or maximum, then  $MR$  may not be representative for the general sample characteristics. Thus,  $MR$  can only be representative for average extreme characteristics. The median,  $P_{50}$ , is least influenced by samples with extreme values as it is independent of the distribution characteristics of the sample. Arithmetic or geometric mean considers all sample values with the same weighting of  $1/n$  and thus they can be influenced by extreme values (or outliers) but it becomes negligible when the number of samples increases.

Standard deviation, half range, and quartile deviation are measures of the degree of scattering around the representative value of the sample. Range is most sensitive to outliers and quartile deviation is least influenced by extreme values or outliers. Relative uncertainty of representative values can be measured by coefficient of variation in parametric statistics and by quartile coefficient of variation in rank statistics, as they are independent from magnitude of sample values. The ratio between half range and midrange  $HR/MR$  can be used as a measure of the relative uncertainty when samples of extreme value are considered to be important.

A worst case can be represented by  $\mu - 2\sigma$ , the minimum,  $P_1$ ,  $P_5$ , or  $Q_2 - 2QD$ . The minimum is most sensitive to outliers while the percentiles can be easily interpreted from their definition.

Both parametric and non-parametric statistics will be used in subsequent sections to explore their relative merits in visualizing and comparing some of the very complex flow and transport simulation results completed for the sub-regional modelling case study.

## 4. GROUNDWATER FLOW AND LIFETIME EXPECTANCY IN A SINGLE SUB-REGIONAL MODEL REALIZATION

### 4.1 HYDRAULIC PROPERTIES

In order to better understand the evolution and the dynamics of groundwater flow in the sub-regional domain, a reference case using fracture zone network realization 1 was selected and embedded in the domain as described in Chapter 2. Matrix hydraulic properties are given in Table 1.

The distribution of hydraulic properties in the fracture domain is critical to groundwater flow and solute transport, but these properties are somewhat uncertain as described in Chapter 2. As a reference simulation, the fracture zone permeability is assumed to decrease with depth following the median trend (50<sup>th</sup> percentile) in Figure 12; the fracture zone porosity is given as a function of the permeability (Equation (10)) with, for illustrative purposes, an assumed fracture density of  $10 \text{ m}^{-1}$  and matrix porosity of 0.003; the fracture zone width is assumed to follow a log-normal distribution as given by Equation (4) (see Figure 21, Figure 22, and Figure 23). The uncertainty related to fracture zone hydraulic properties will be discussed later.

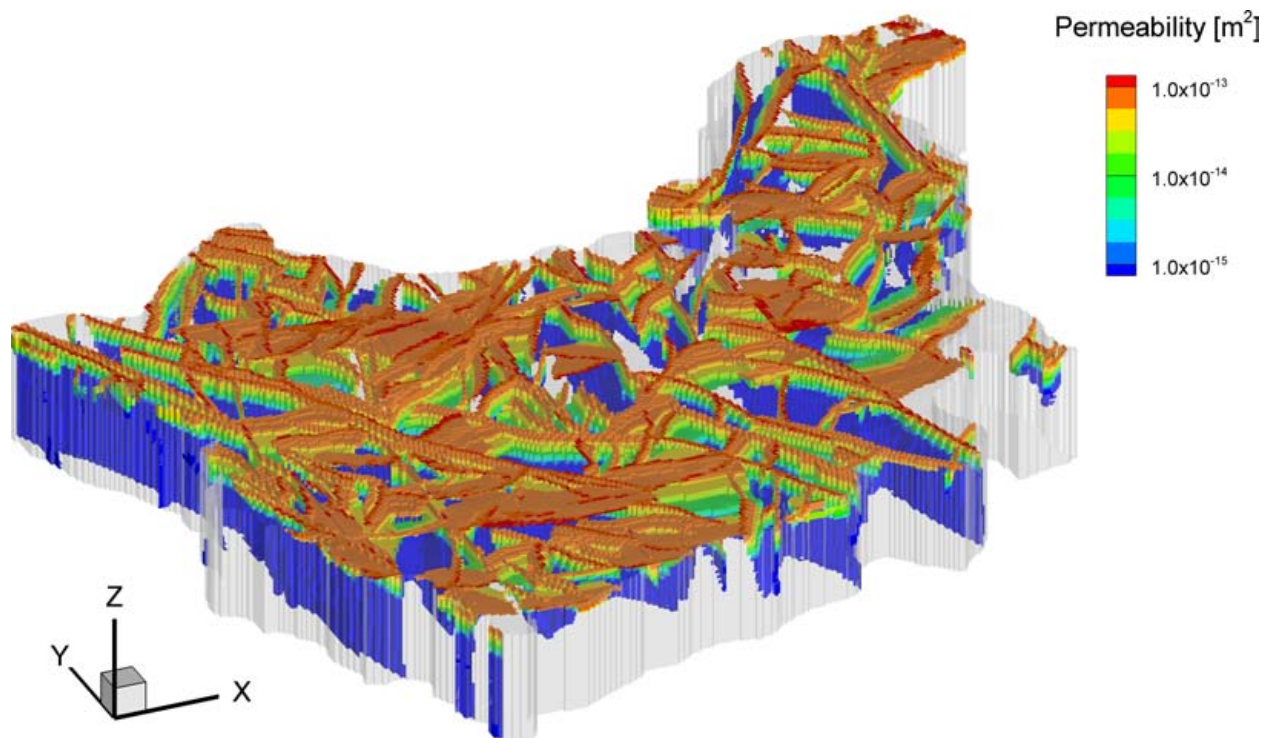


Figure 21: Fracture zone permeability for reference case

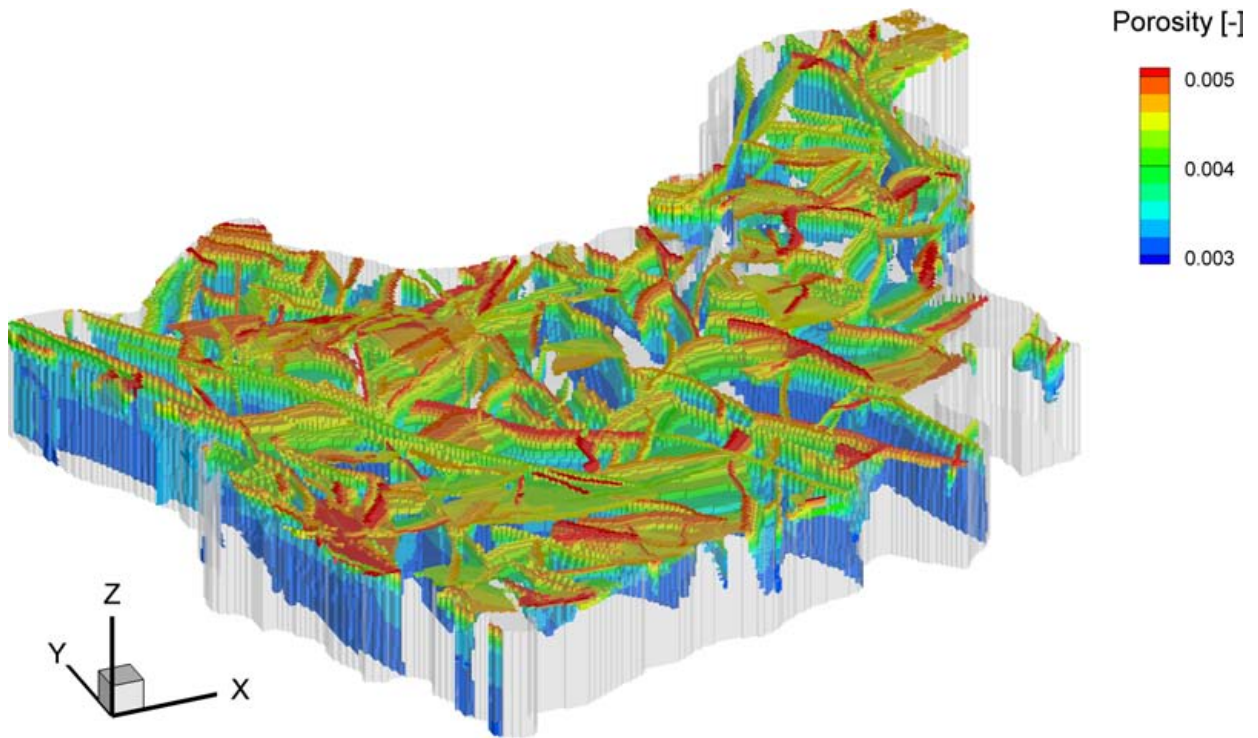


Figure 22: Fracture zone porosity for reference case

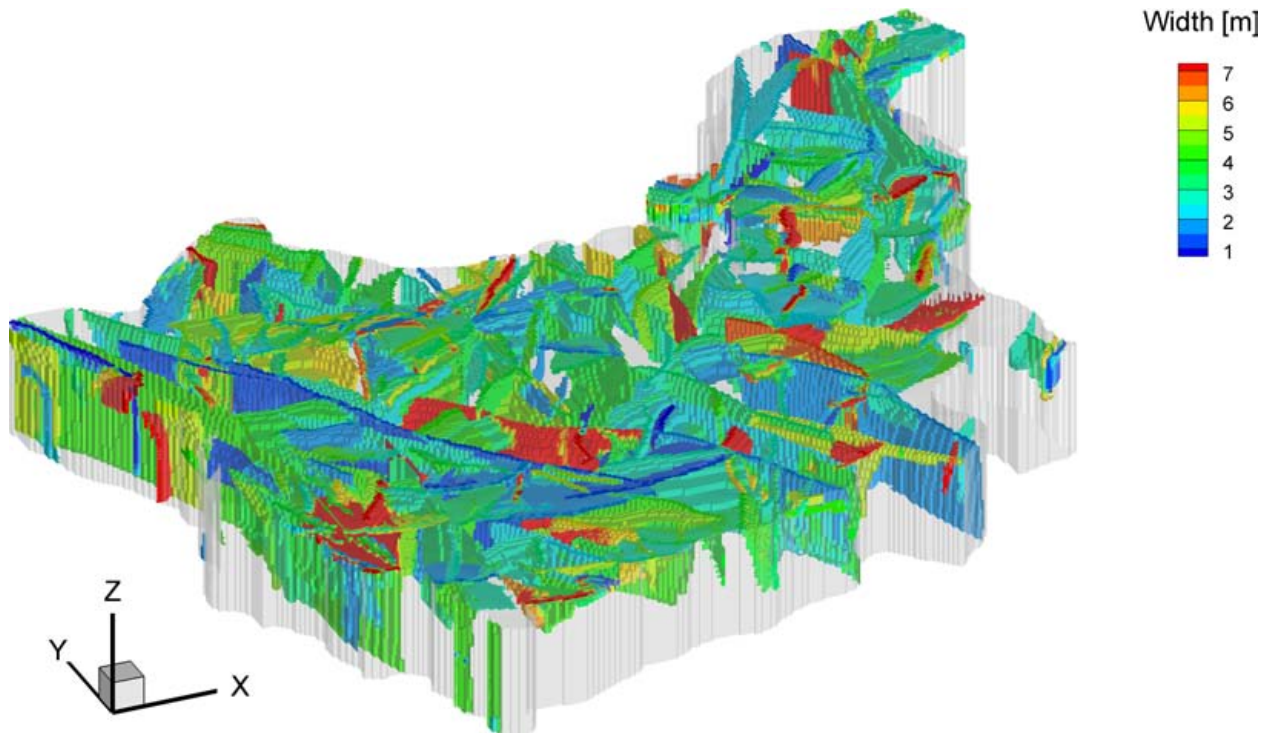


Figure 23: Fracture zone width for reference case

## 4.2 GROUNDWATER FLOW

With the boundary conditions specified as described in Chapter 2, steady-state flow was simulated. As a first step, density effects were not considered for the simulations. Figure 24 shows the head distributions in the matrix and fracture domains. The results show that the hydraulic head near ground surface is influenced by the surface boundary conditions (due to topography) and fracture zone geometry. Hydraulic head tends to become smoother at depth, as suggested by Tóth and Sheng (1996) and shown by Sykes et al. (2003).

The fluid flux distribution (Figure 25) confirms that fracture zones could act as permeable pathways for fluid flow and contaminant migration even at depths of 870 m ( $z = -500$  m), although the flux decreases approximately an order of magnitude, or more, as compared to near surface fluxes. Note that groundwater flow is more active near surface than at depth as fracture zones and matrix permeabilities are higher and the hydraulic driving force is stronger near surface. Likewise, with increasing depth, fracture zones become sparser and less permeable, matrix permeabilities decrease, and the resulting flows can become stagnant, except within major fracture zones.

## 4.3 BRINE DISTRIBUTION

### 4.3.1 Initial and Boundary Conditions

In order to examine the effects of Shield brine on the sub-regional flow system, a series of simulations were completed assuming a simple linear relationship between density or viscosity and TDS concentration with the maximum density (see Section 3.1.1) of 1.0 kg/L (TDS: 3500 mg/L), 1.03 kg/L (TDS: 35 000 mg/L), 1.1 kg/L (TDS: 150 000 mg/L), or 1.2 kg/L (TDS: 300 000 mg/L), and a maximum viscosity (relative to fresh water) of 1.0, 2.0, or 4.0.

For the initial condition of 20 000 years of viscous buoyancy-driven flow and transport simulations, the following steps were followed:

- i) a steady flow field was obtained without density and viscosity effects (Figure 24),
- ii) initial relative concentration was set to 1.0 below an elevation of  $-250$  masl and 0.0 elsewhere (Figure 26), and
- iii) hydraulic head in brine region is modified to accommodate vertical hydrostatic condition with given maximum brine density (for example, see Figure 27).

The bottom of the domain was set as a specified concentration boundary assuming that the brine always exists, zero mass flux condition was applied for surface recharge areas, and zero dispersive flux boundary condition was applied for discharge areas.

### 4.3.2 Illustrative Examples

In order to check the validity of the numerical simulator for density-dependent flow and transport and also to demonstrate the effects of brine on groundwater flow system behaviours, simplified simulations were carried out for illustrative purposes. For this example, a 10 km wide and 1.6 km

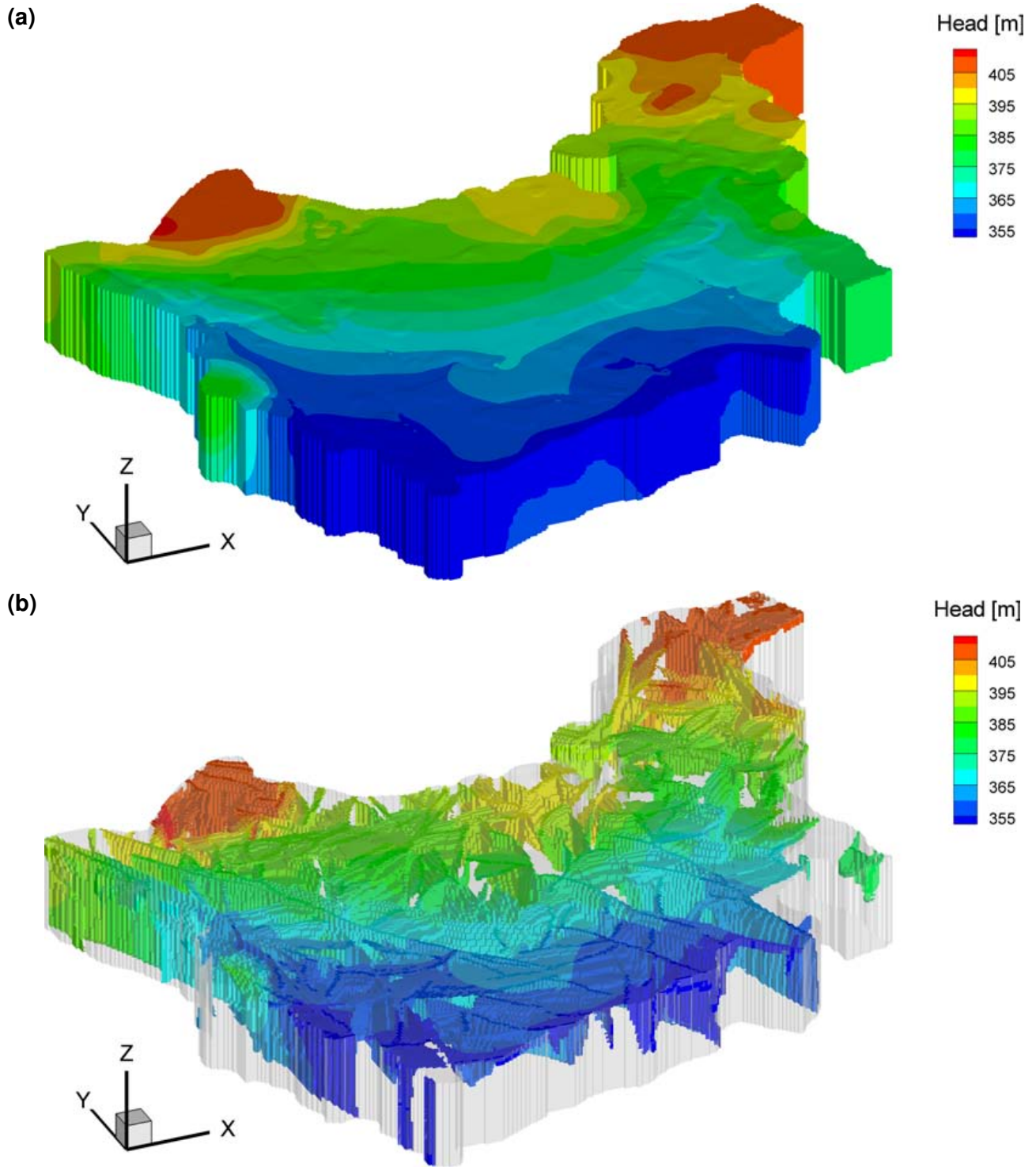


Figure 24: Piezometric head for steady-state flow in the (a) matrix, and (b) fracture zones

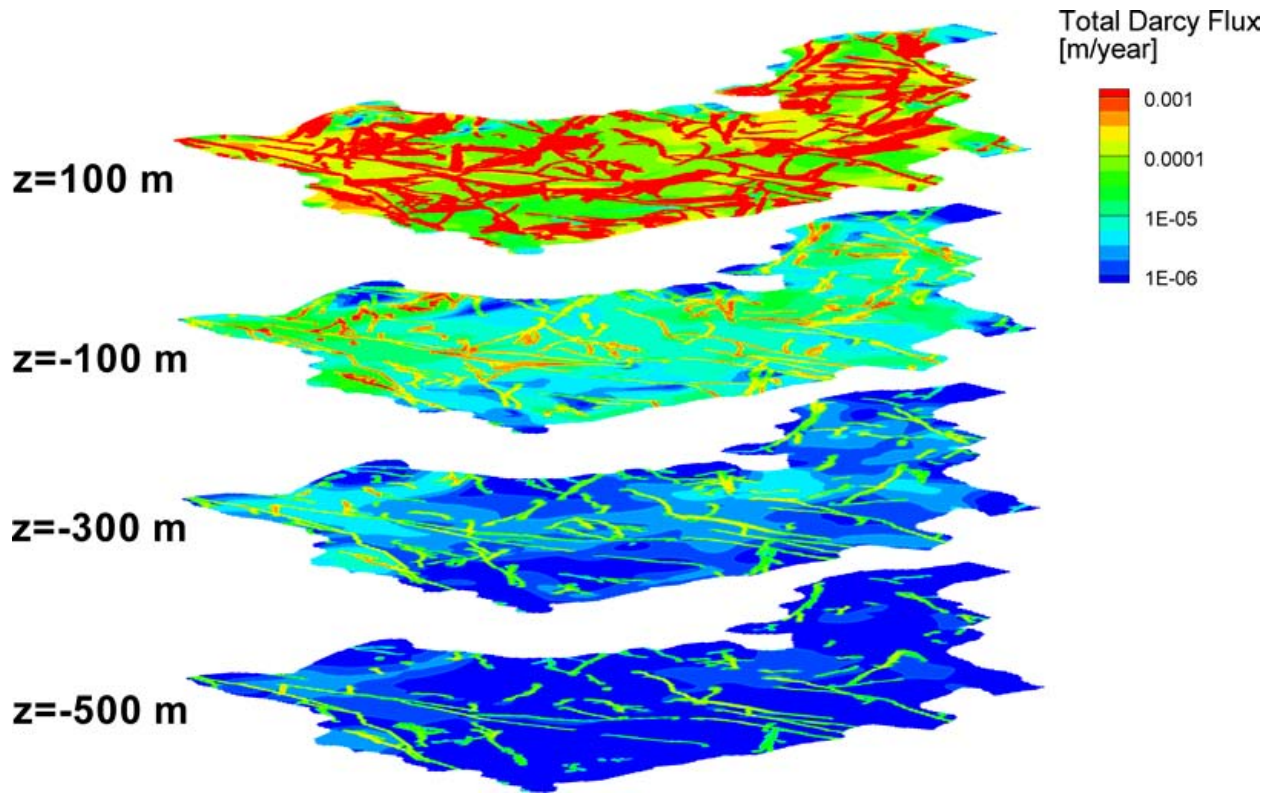


Figure 25: Darcy flux distribution for reference case

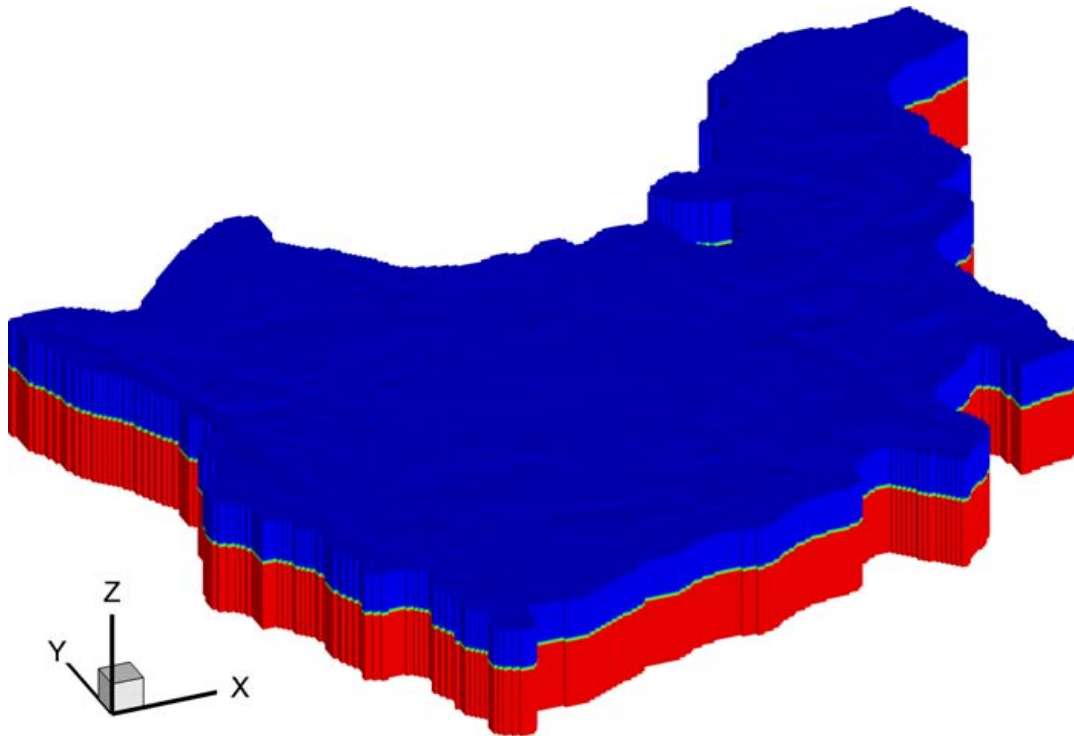
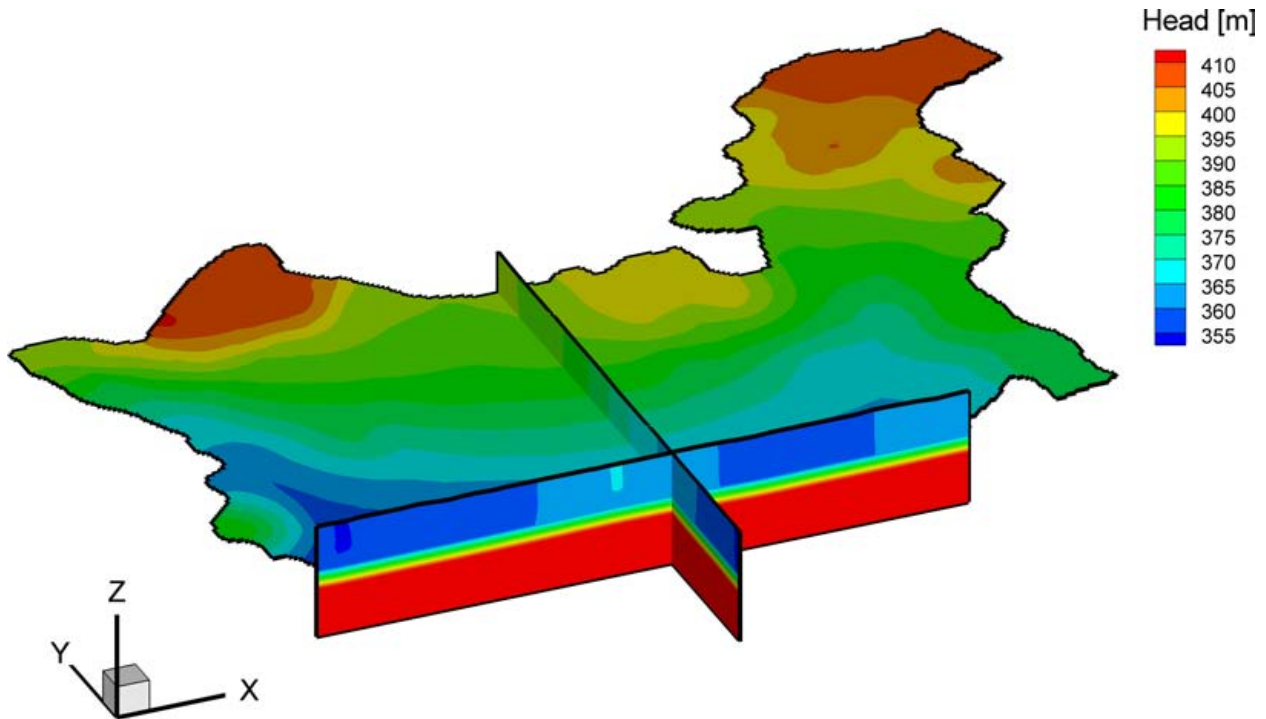


Figure 26: Initial concentration distribution for viscous buoyancy-driven flow and transport simulations



**Figure 27: Initial equivalent freshwater head for maximum relative brine density of 1.2**

deep rectangular domain was considered. The domain was discretized similarly to the sub-region; each element being 50 m wide with variable thickness as described in Chapter 2. The domain was assumed to be homogeneous with a hydraulic conductivity of 0.01 m/year. Hydraulic head was specified at the top of the domain to linearly vary from 420 m (roughly the highest ground surface elevation in the subregion) in the left top corner to 350 m (the lowest ground surface elevation in the subregion) in the right top corner. Steady flow was simulated first without brine (Figure 28) and then brine was assumed to exist initially below  $-250$  masl (Figure 29). The initial head distribution for vertical hydrostatic equilibrium was modified for given maximum relative density values (Figure 30). The increase in the maximum relative density results in an increase in head in the lower portion of the domain. Horizontal, transverse horizontal and transverse vertical dispersivities are 50 m, 5 m, and 0.5 m respectively with a diffusion coefficient of  $0.000725 \text{ m}^2/\text{year}$  and a tortuosity of 1.0 (i.e., not considered).

Density-dependent flow and transport was simulated for 20 000 years for a maximum relative brine density of 1.0 (no brine effect), 1.03 (saline), 1.1 (brackish), and 1.2 (brine). Figure 31 shows the relative brine concentration distributions for given maximum brine density values. Results in Figure 31 clearly demonstrate the effects of brine density: as the fluid becomes denser, upward migration is retarded in the discharge area, as noted by the varying concentration contours near the top right corner of the domain. A similar effect is notable in the recharge area near the top left corner of the domain; the increased density impedes downward recharge, visible in the variation in the concentration contours.

Brine distributions in Figure 31 influences the groundwater flow field and Figure 32 shows the change in groundwater linear velocity fields for different values of maximum brine density. In

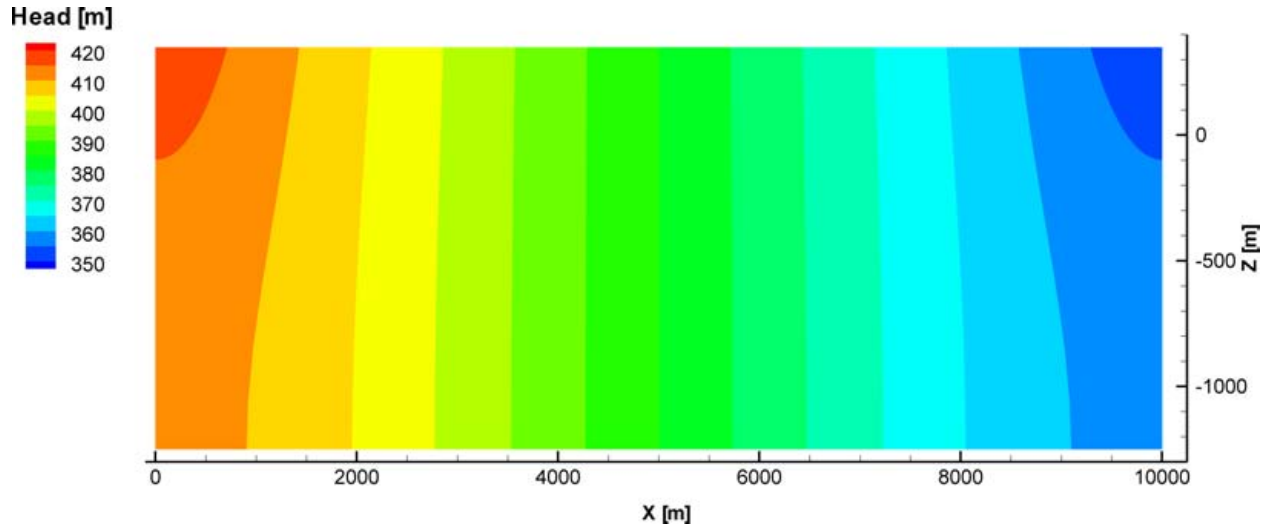


**Figure 28: Hydraulic head distribution in steady state**

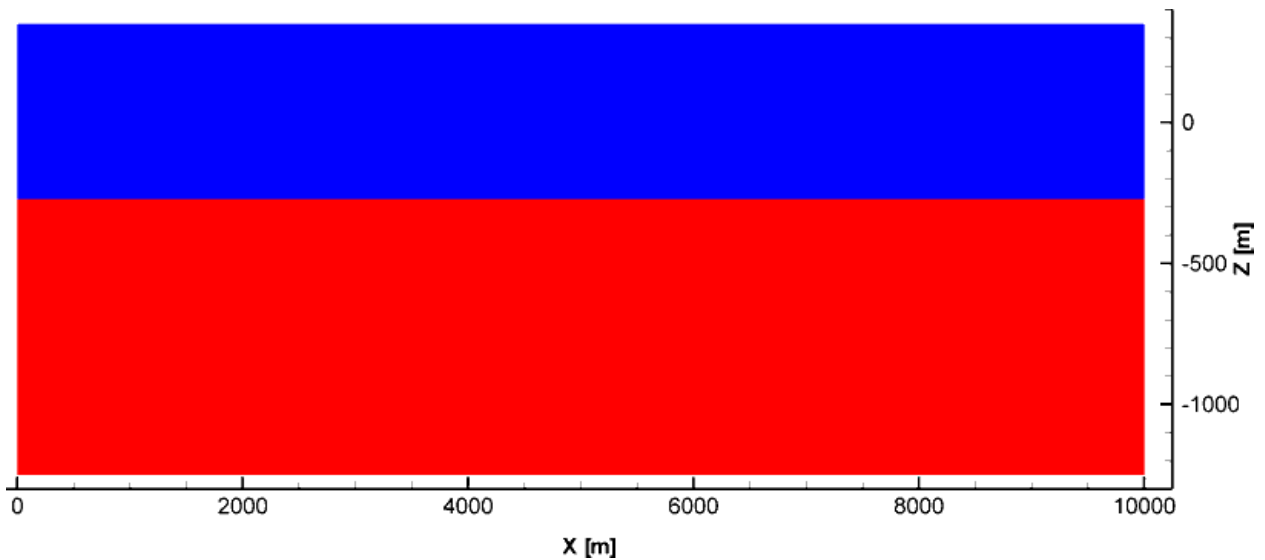


**Figure 29: Initial relative brine concentration**

Figure 32, it is shown that the change in groundwater flow due to the change in fluid density is not significant in the recharge area but upward velocity in the discharge area becomes smaller with higher fluid density, as illustrated by the reduction in velocity vector magnitude near the top right corner. The results imply that brine can retard migration of contaminants released in the brine region to the surface discharge areas.

Figure 33 shows the change in streamlines with different values of maximum brine density. The results show that the brine region behaves similar to a diffraction zone (a low permeability zone) and the groundwater recharged into the system flows through the shallower region as the maximum fluid density increases.

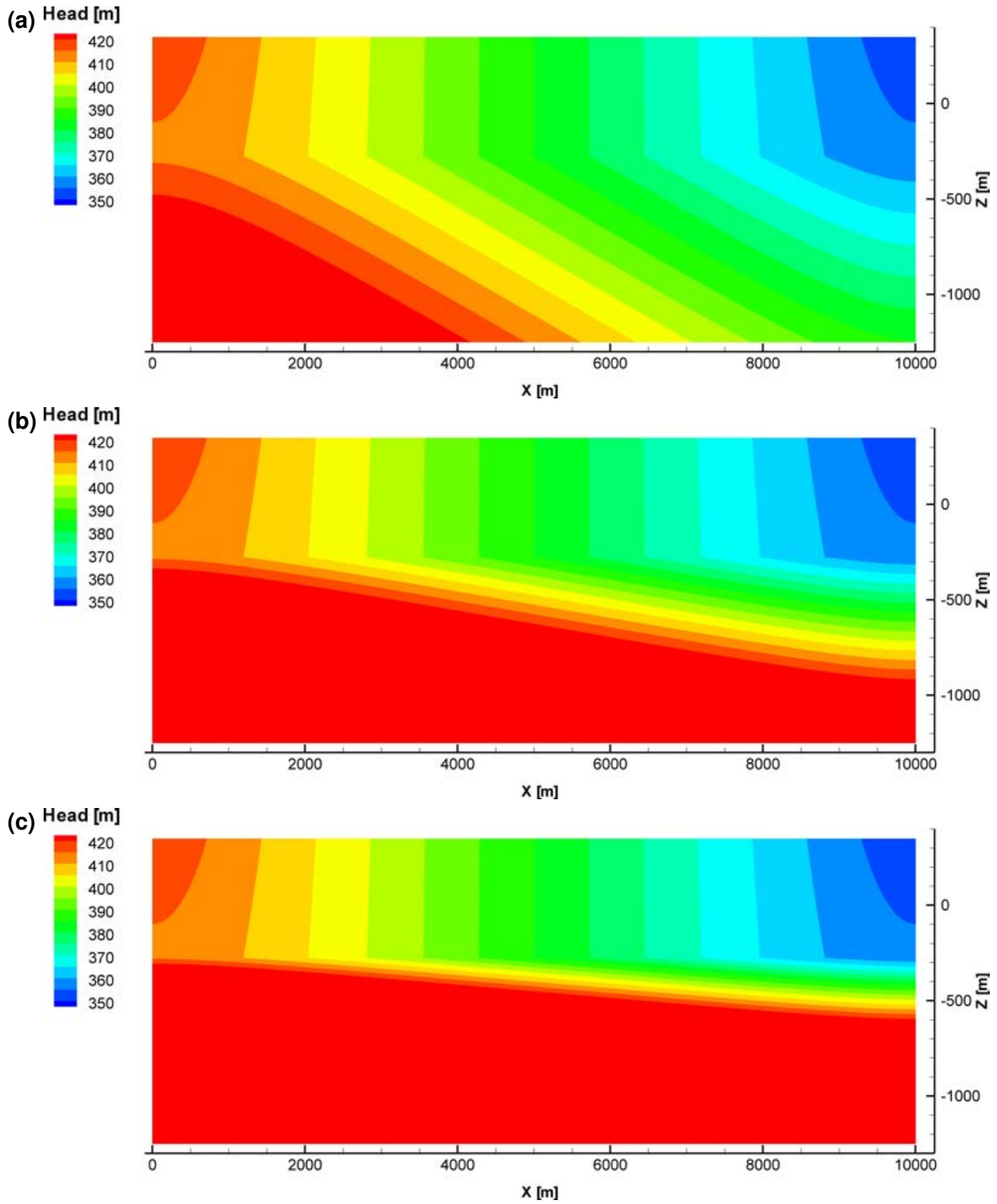


Figure 30: Illustrative initial equivalent freshwater head for a relative brine density of: (a) 1.03, (b) 1.1, and (c) 1.2

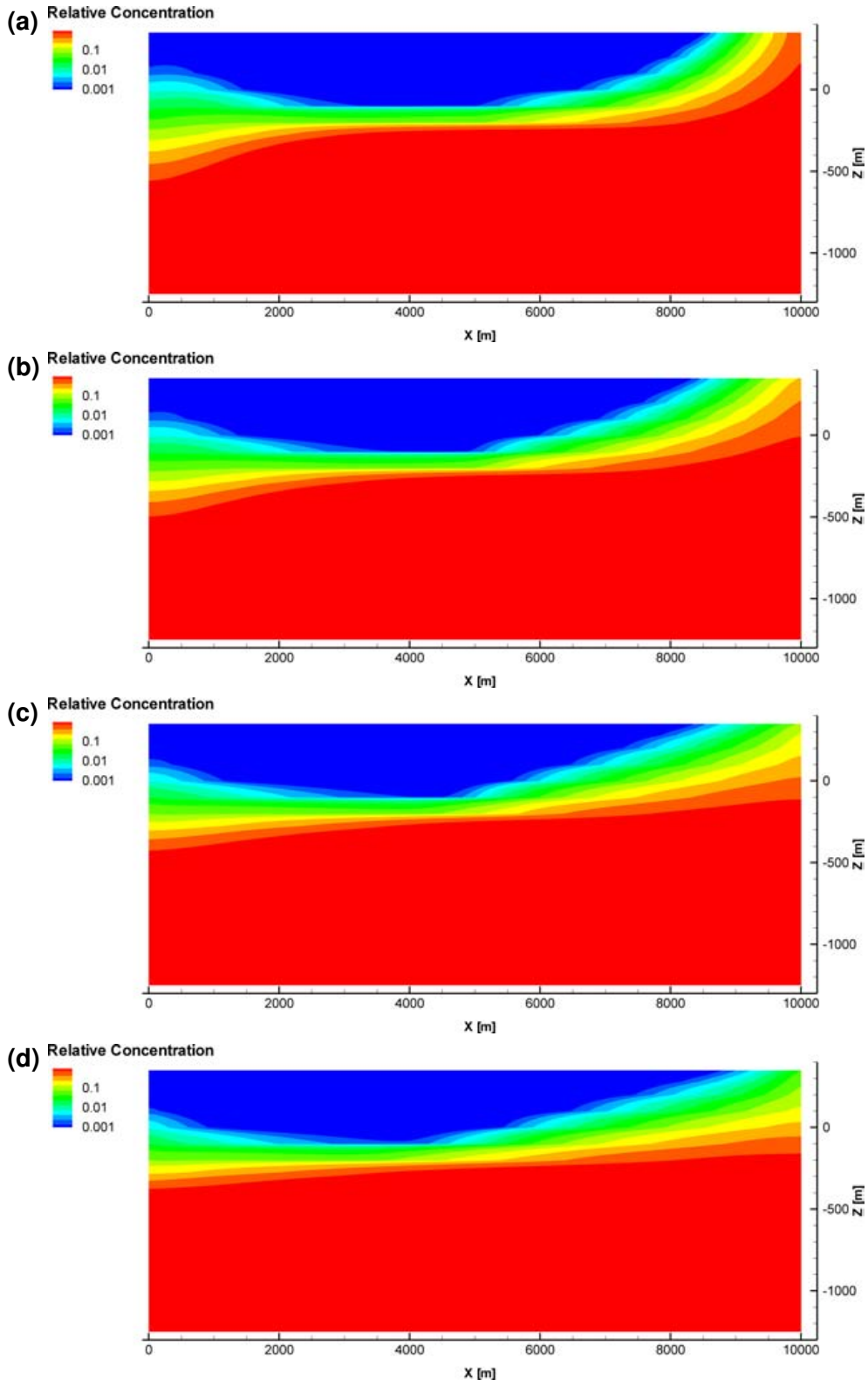


Figure 31: Relative brine concentration at 20 000 years for relative brine densities of: (a) 1.0, (b) 1.03, (c) 1.1, and (d) 1.2

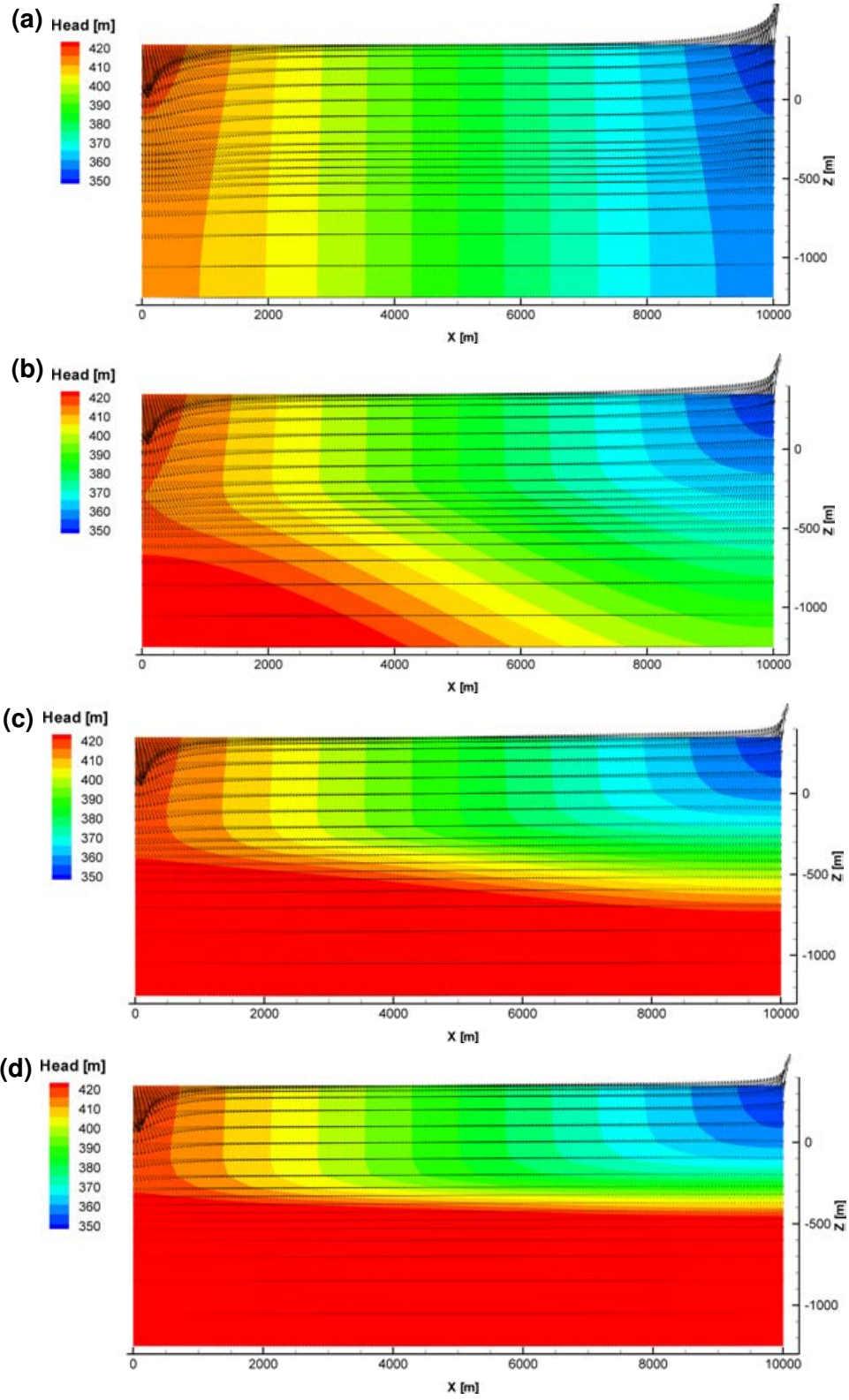


Figure 32: Linear velocity at 20 000 years for relative brine densities of: (a) 1.0, (b) 1.03, (c) 1.1, and (d) 1.2

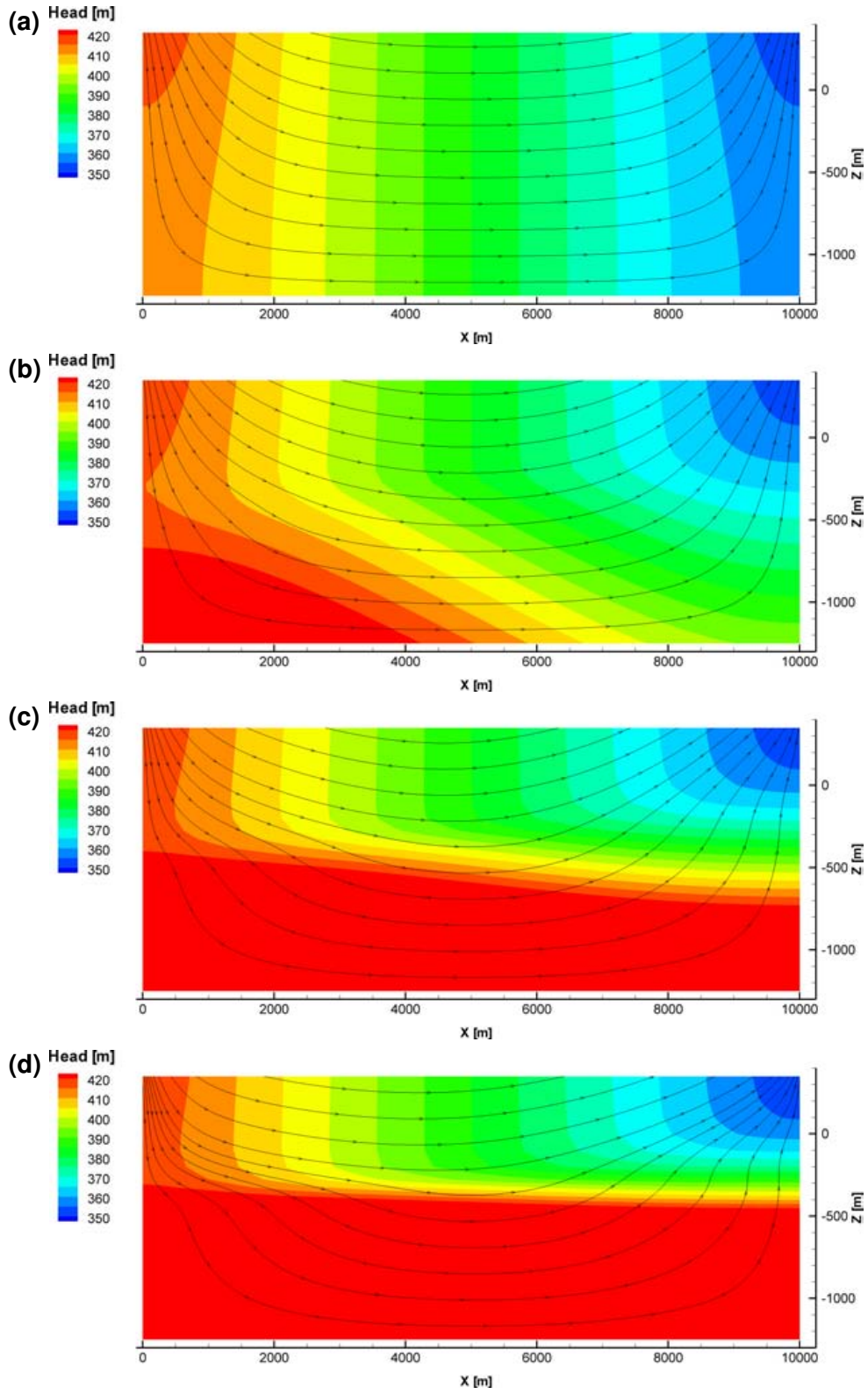
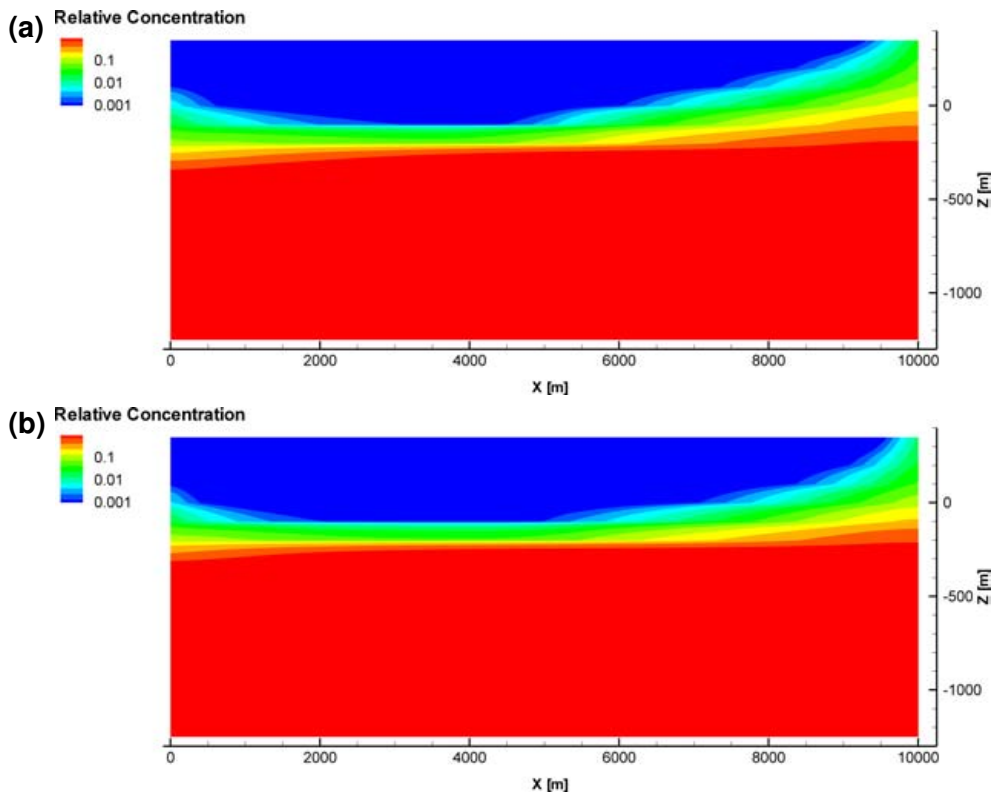


Figure 33: Streamlines at 20 000 years for relative brine densities of: (a) 1.0, (b) 1.03, (c) 1.1, and (d) 1.2

Density-dependent flow and transport were simulated when the maximum fluid viscosity was assumed to be two or four times larger than fresh water. Figure 34 shows the relative concentration distribution when the maximum density of fluid was set to be 1.2 with a maximum relative viscosity of 2.0 or 4.0. The results indicate that increasing maximum viscosity can retard the migration of brine at depth. Velocity and streamline distributions also show that a change in fluid viscosity values causes the brine region to be more stagnant (Figure 35 and Figure 36). Although the figures for a maximum relative viscosity of 2.0 or 4.0 look similar, the differences are noted if one carefully examines the top right portion of the relevant figures. The concentration contours are slightly elevated in the 2.0 relative viscosity case, when compared to the case with a relative viscosity of 4.0



**Figure 34: Relative brine concentration at 20 000 years for a relative brine density of 1.2 and with maximum relative viscosities of: (a) 2.0, and (b) 4.0**

Alternatively, the distribution of the magnitude of linear fluid velocity is presented to demonstrate the effects of brine density and viscosity on the distribution of stagnant areas (see Figure 37 and Figure 38). The results show that stagnant areas (blueish colours) become bigger as the maximum density increases. It is worth noting that density variations affect only the vertical component of groundwater flow; although horizontal flow is dominant in the mid-region of the domain, linear velocity in the mid-region decreases significantly with increasing density. Increasing viscosity due to the presence of brine also significantly retards groundwater flow especially in the mid-region but the influence is relatively minor below recharge or discharge areas.

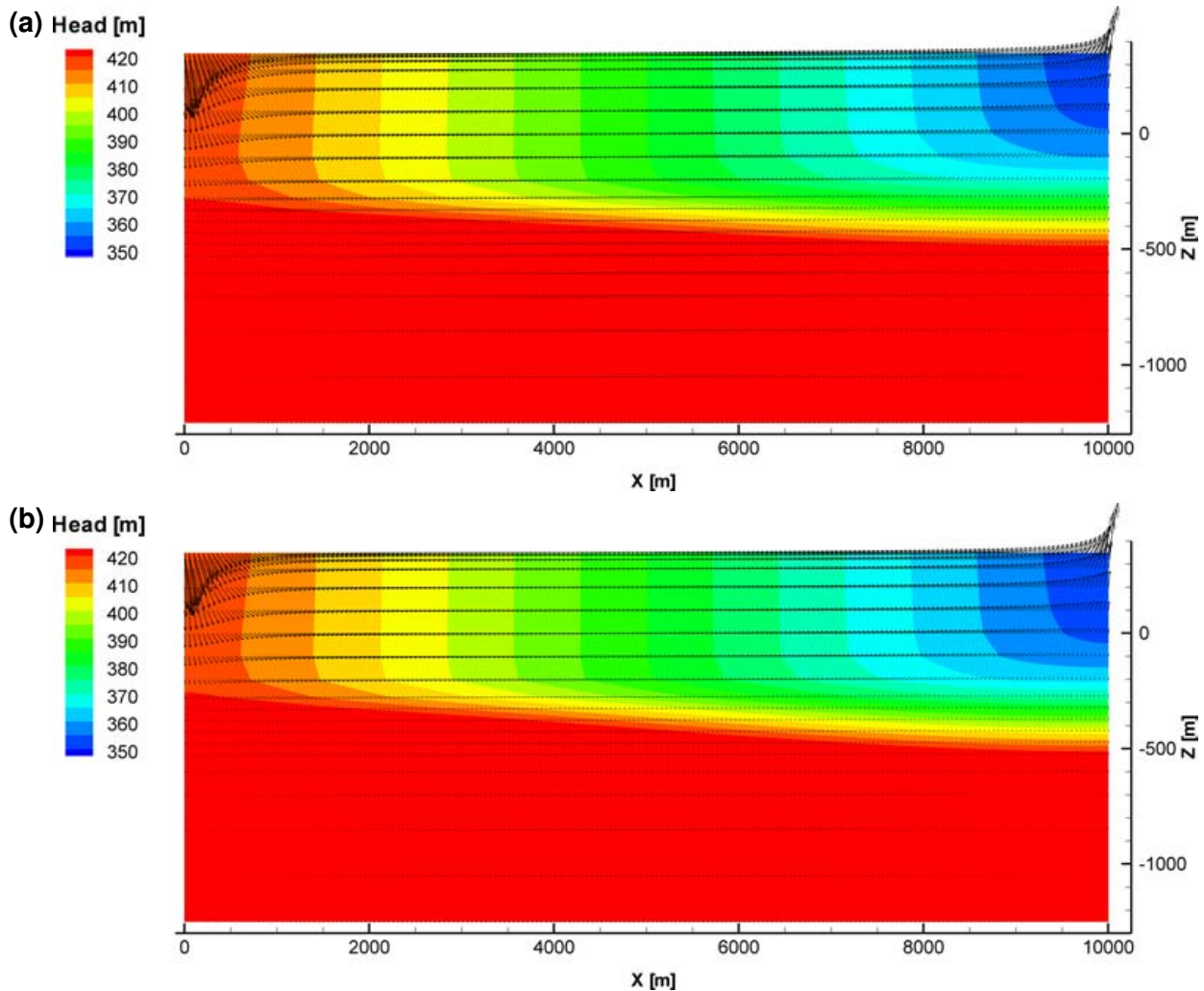


**Figure 35: Linear velocity at 20 000 years for a relative brine density of 1.2 and with maximum relative viscosities of: (a) 2.0, and (b) 4.0**

### 4.3.3 Brine Distribution and Groundwater Flow in the Sub-Regional Domain

Brine distribution was simulated within the sub-regional domain. With given initial and boundary conditions described in Section 4.3.1, density-dependent flow was simulated for 20 000 years. As a reference case, brine distribution was simulated without density and viscosity changes (Figure 39). Note that the brine migrates in a steady groundwater flow field if the variation in density and viscosity is not considered.

Figure 39 shows that although brine initially located below  $-250$  masl moves upwards through fracture zones, the concentration is negligible near ground surface except in major fracture zones as shown in Figure 40.

Figure 41 shows the distribution of relative brine concentration for different values for maximum brine density. The results show that as the maximum brine density increases, the relative brine

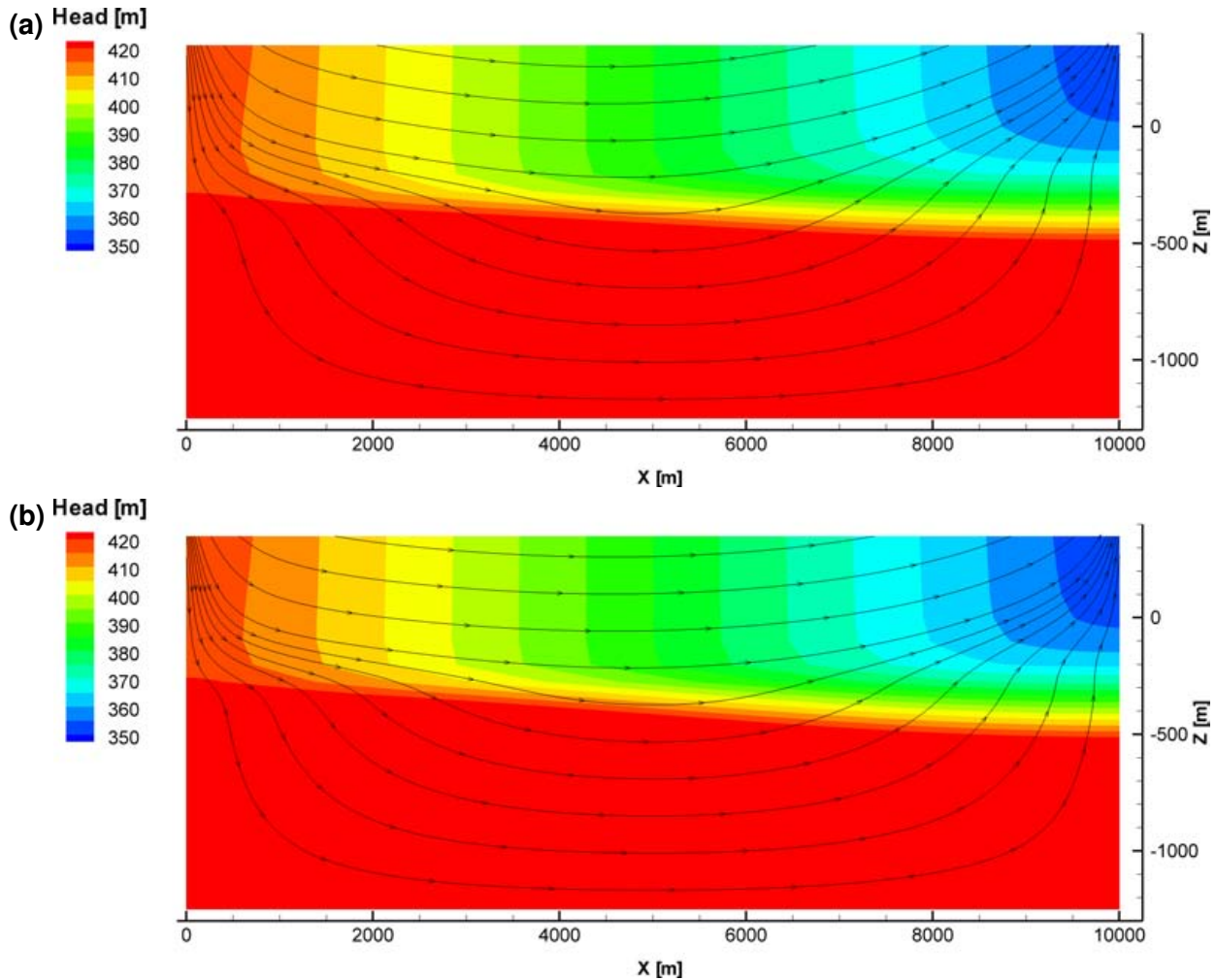


**Figure 36: Streamlines at 20 000 years for a relative brine density of 1.2 and with maximum relative viscosities of: (a) 2.0, and (b) 4.0**

concentration becomes smaller in permeable fracture zones as upward migration of brine is restricted by gravity.

The groundwater flow system can be influenced by the brine distribution as shown in the illustrative cross-section example of Section 4.3.2. Figure 42 shows the total Darcy flux in the domain for different values for maximum brine density. Although Darcy flux becomes smaller as the density increases, the effect is not significant because the fluxes are much more influenced by the vertical distribution of permeability and the location of fracture zones.

In order to closely examine the brine effects on groundwater flow, a vertical cross section was selected to plot the brine concentration and the Darcy flux vector in the matrix (Figure 43). This cross-section is the same as the X–Z cross-section shown in Figure 42. In Figure 43, Darcy flux was plotted only in the region below sea level to remove the relatively larger vectors near ground surface. The results indicate that the vertical component of the Darcy flux vector becomes smaller as the brine density increases for both upward and downward cases and the change in

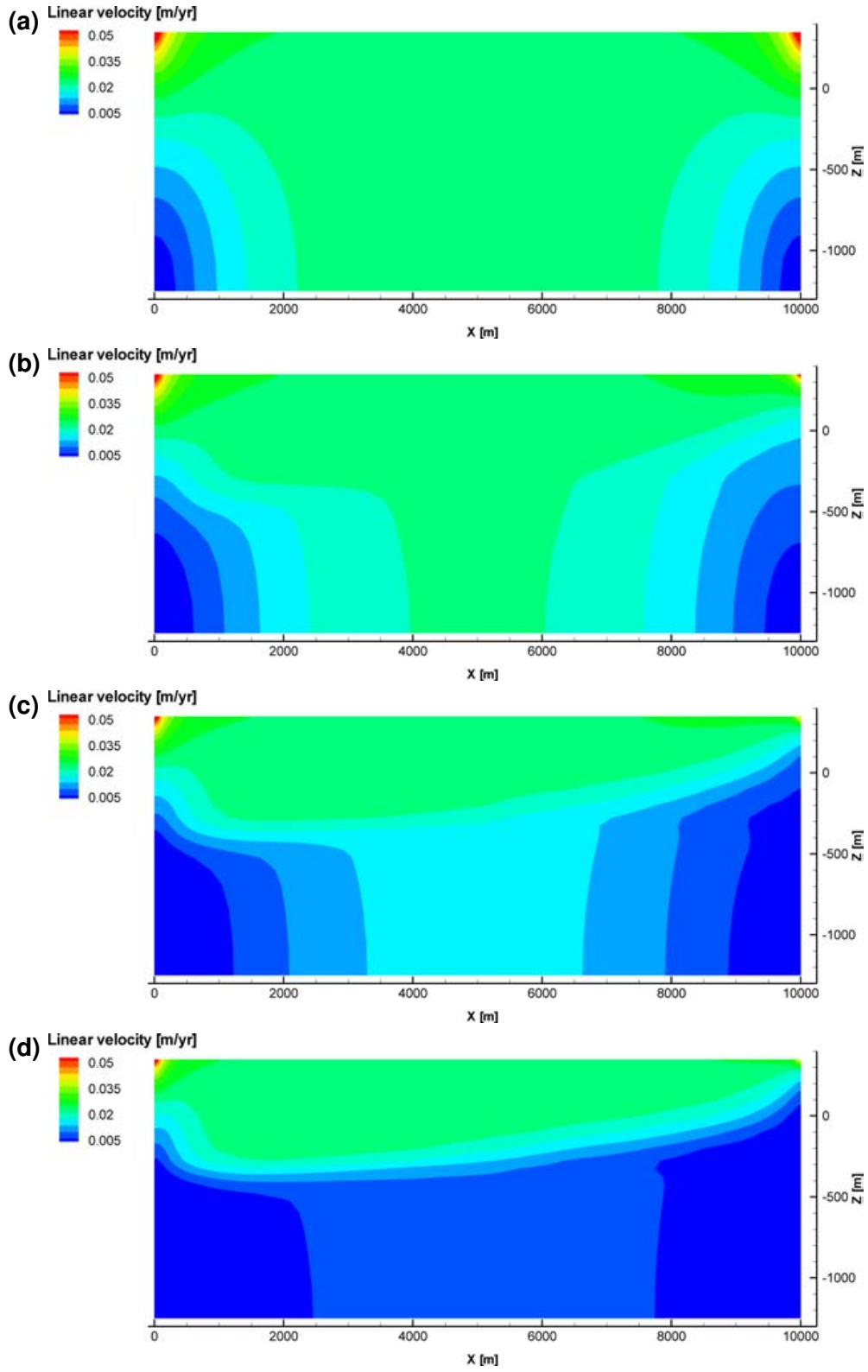


Figure 37: Magnitude of linear fluid velocity at 20 000 years for maximum relative brine densities of: (a) 1.0, (b) 1.03, (c) 1.1, and (d) 1.2

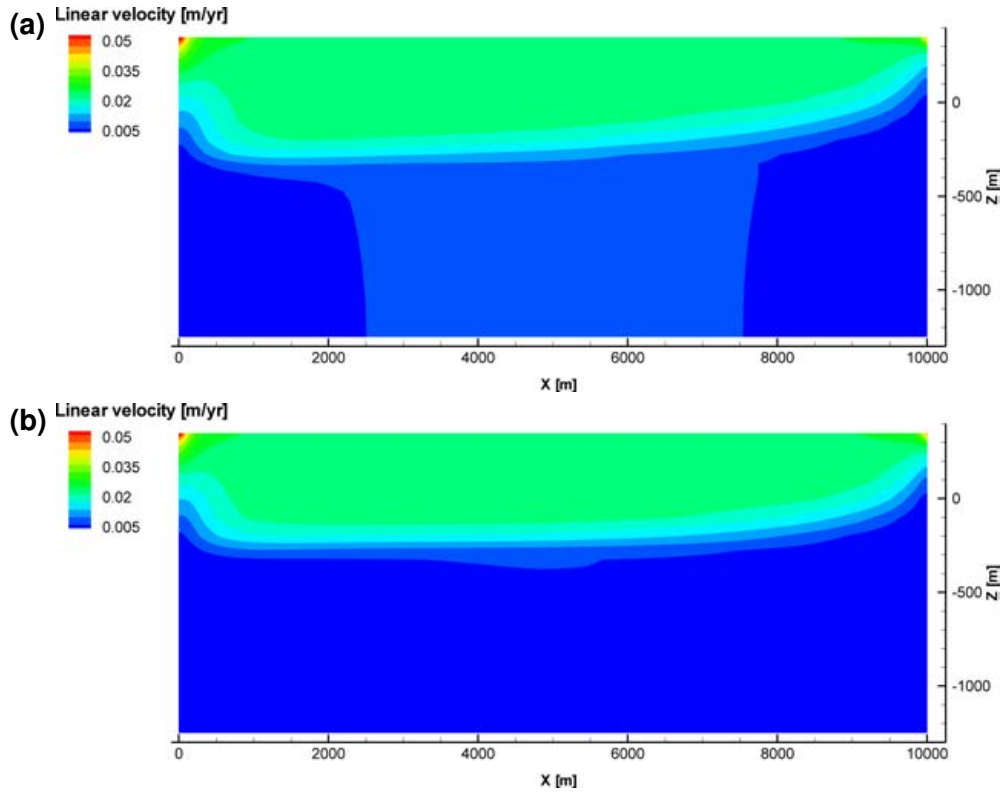


Figure 38: Magnitude of linear fluid velocity at 20 000 years for a relative brine density of 1.2 and with maximum relative viscosities of: (a) 2.0, and (b) 4.0

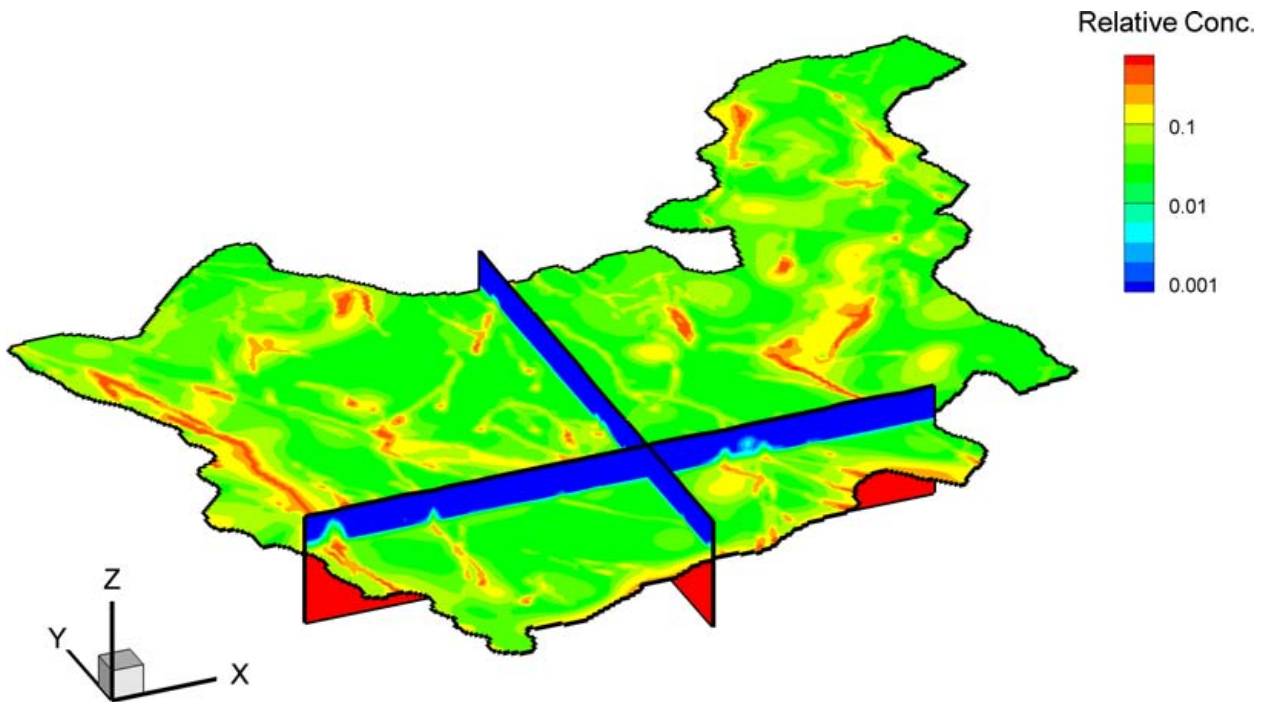
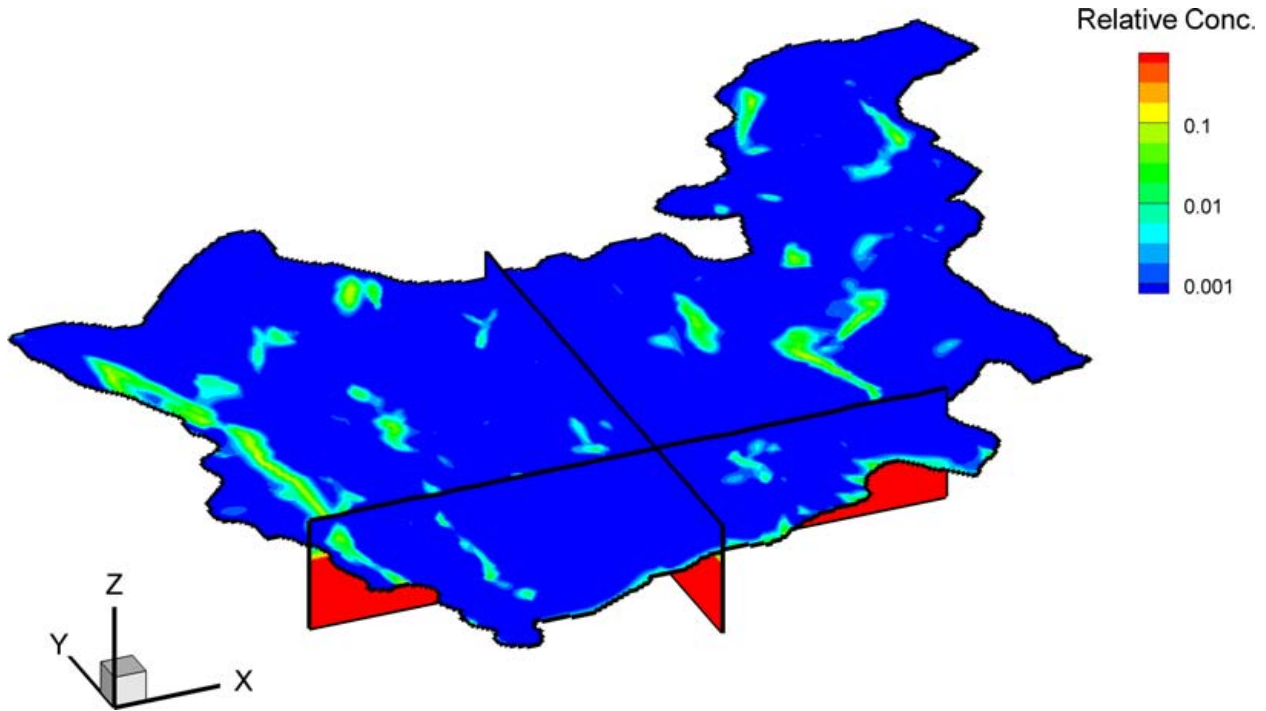


Figure 39: Relative brine concentration without density and viscosity effects. Plane view at -200 masl



**Figure 40: Relative brine concentration without density and viscosity effects. Plane view at 0 masl**

flux vectors restricts the vertical migration of brine to a discharge area. It is important to note that the change in vertical flux vectors in the recharge or discharge areas, as a result of density effects, also influences the flow in the brine region below because of the reduced amount of water needed to flow from the brine region.

#### 4.4 LONG-TERM CLIMATE CHANGE

The effects of long-term climate change (e.g., permafrost) on the groundwater flow system are investigated by modifying the permeability of rock within the permafrost zone, and by changing the surface boundary conditions to reflect a glacial scenario as developed in Section 3.2. Plots of permafrost depth and ice load, expressed as equivalent metres of water, are shown in Figure 44 for the NN2008 glaciation scenario provided by the University of Toronto's Glacial Systems Model (GSM) (Peltier, 2003b). Permafrost exists for nearly the entire simulation period of 121 000 years before present, except for approximately the most recent 10 000 years (see Figure 44a). Three glaciation events were predicted to occur over the sub-regional domain as shown in Figure 44b.

Zero flux Neumann boundary conditions were used for the lateral and bottom surfaces of the model domain. A Dirichlet boundary condition was applied as described in Section 3.2. The ice loading was assumed to be entirely applied as a piezometric head equivalent to the normal stress imposed by the ice sheet upon the domain. This approach neglects the fact that the bedrock will carry a significant portion of the imposed normal stress, due to the fact that rock is less compressible than water. Although FRAC3DVS does not account for hydro-mechanical effects,

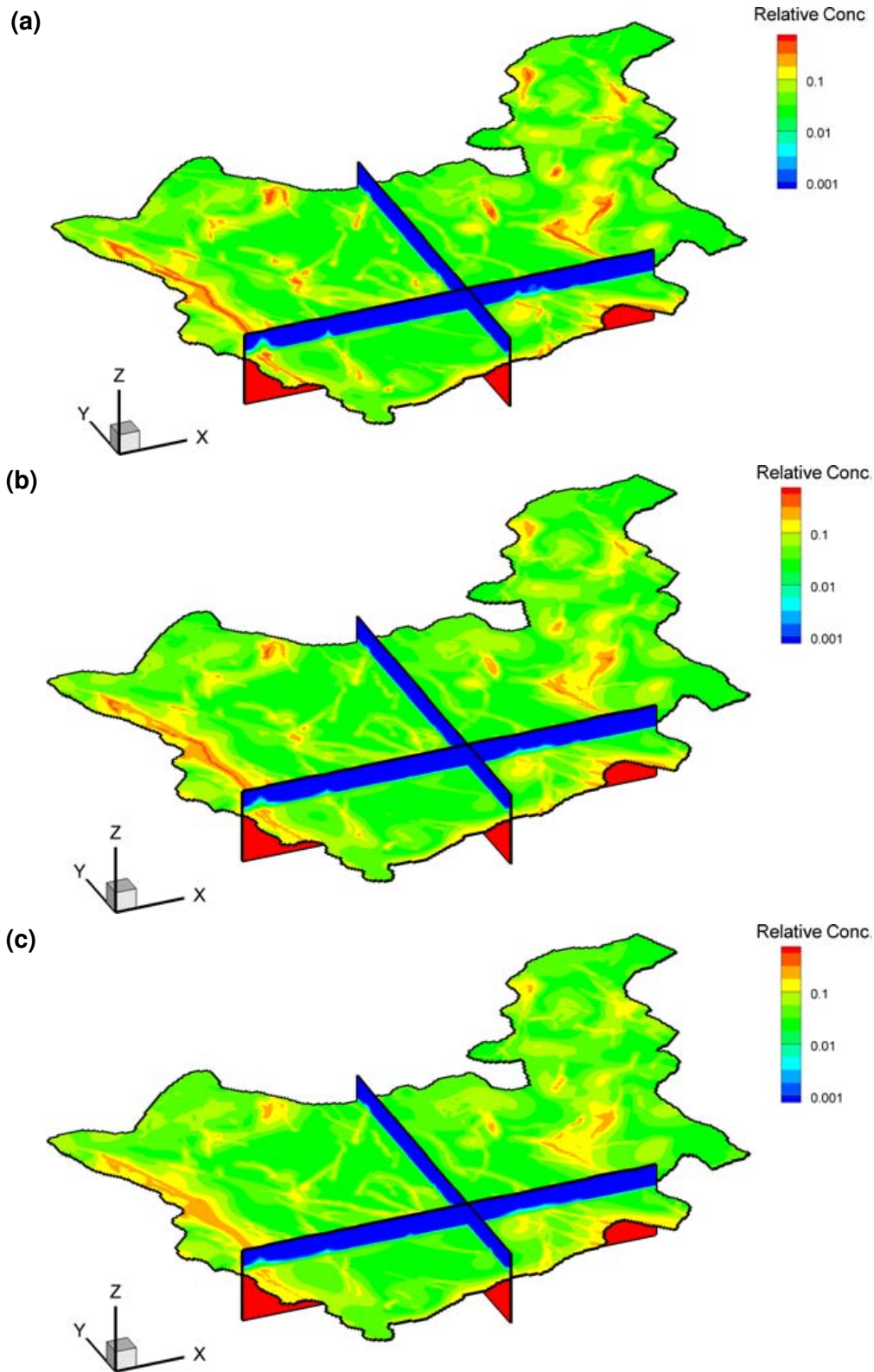


Figure 41: Relative brine concentration at 20 000 years for maximum relative brine densities of: (a) 1.03, (b) 1.1, and (c) 1.2. Plane view at -200 masl

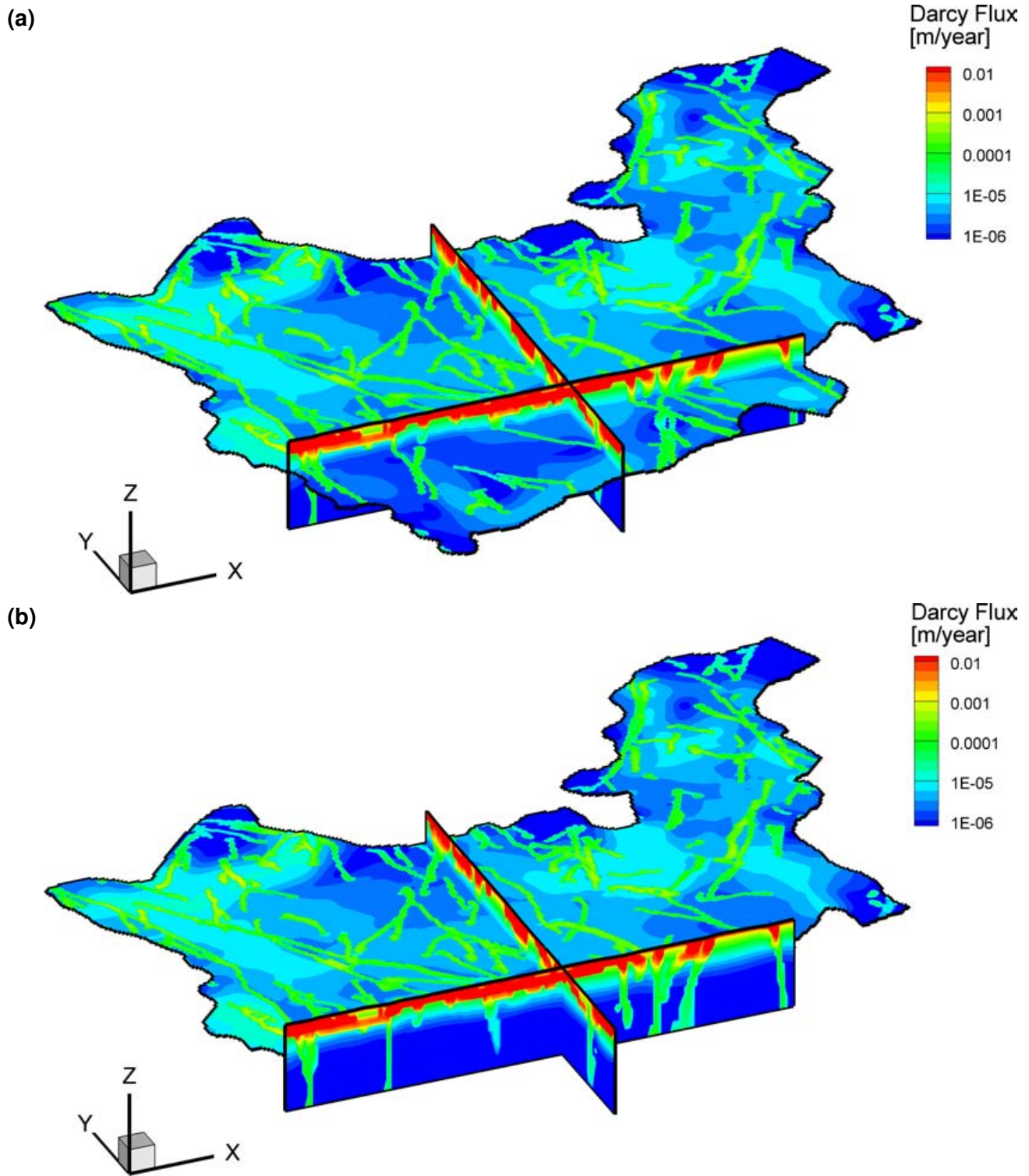
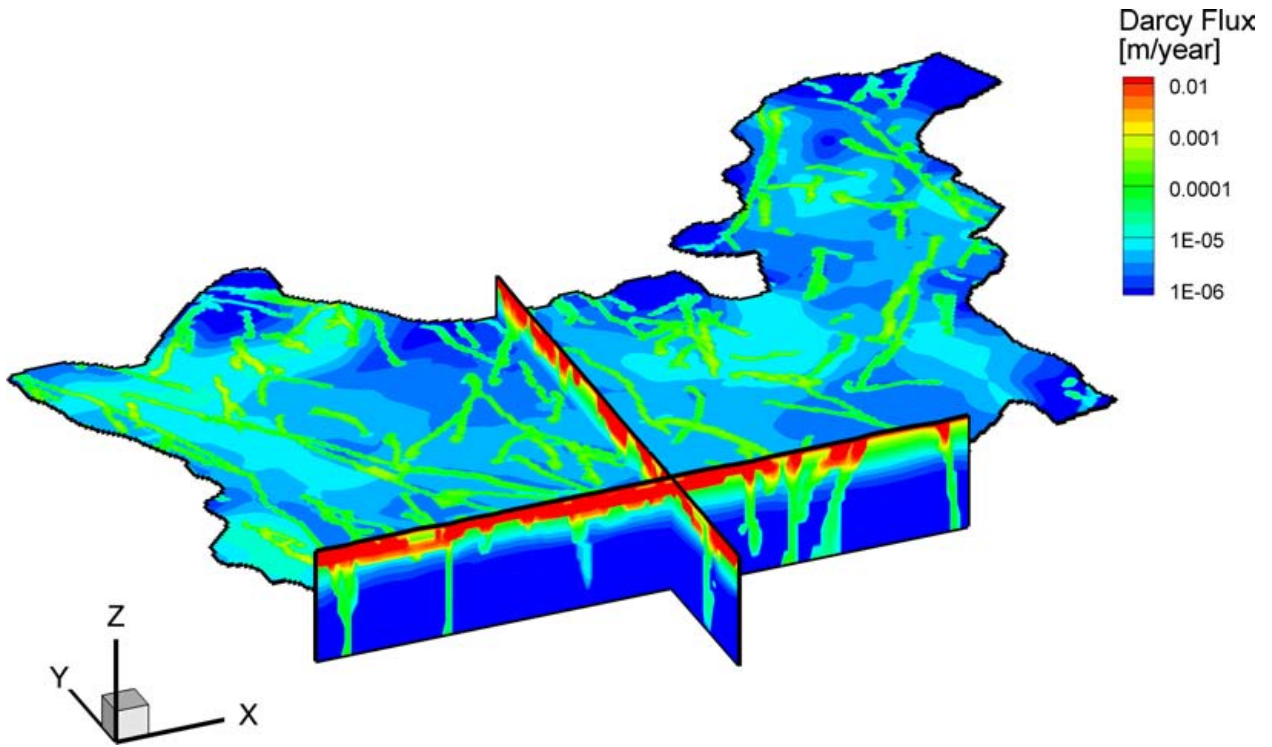


Figure 42: Darcy flux distribution at 20 000 years for maximum relative brine densities of: (a) 1.0, (b) 1.03, (c) 1.1, and (d) 1.2. Plane view at  $-200$  masl

(c)



(d)

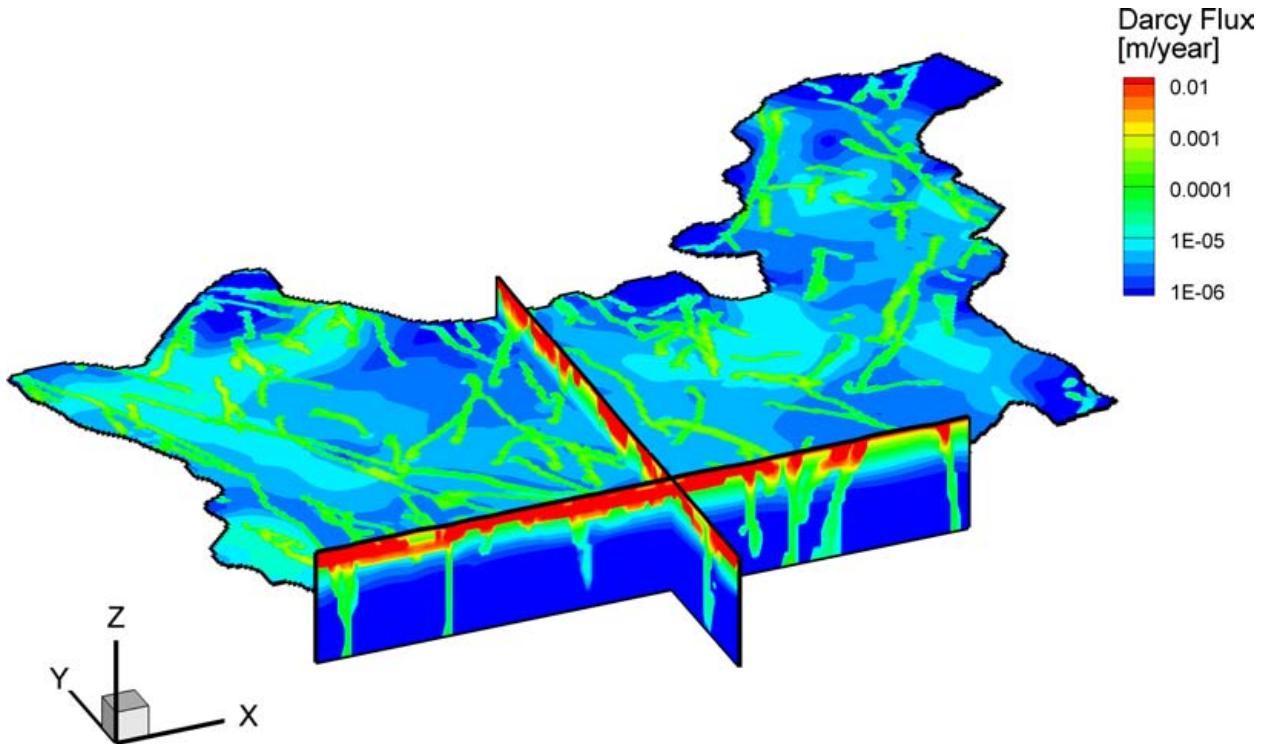
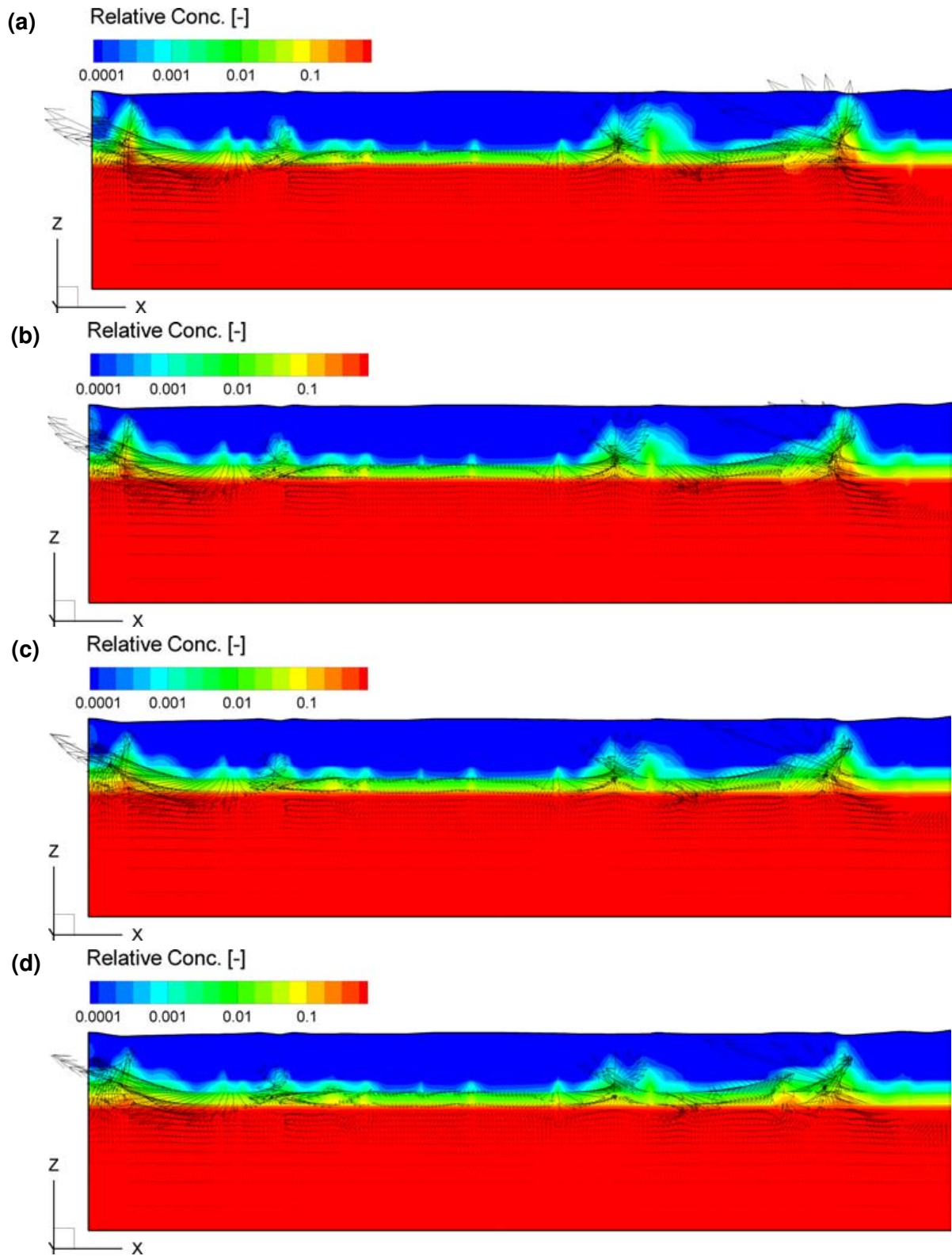
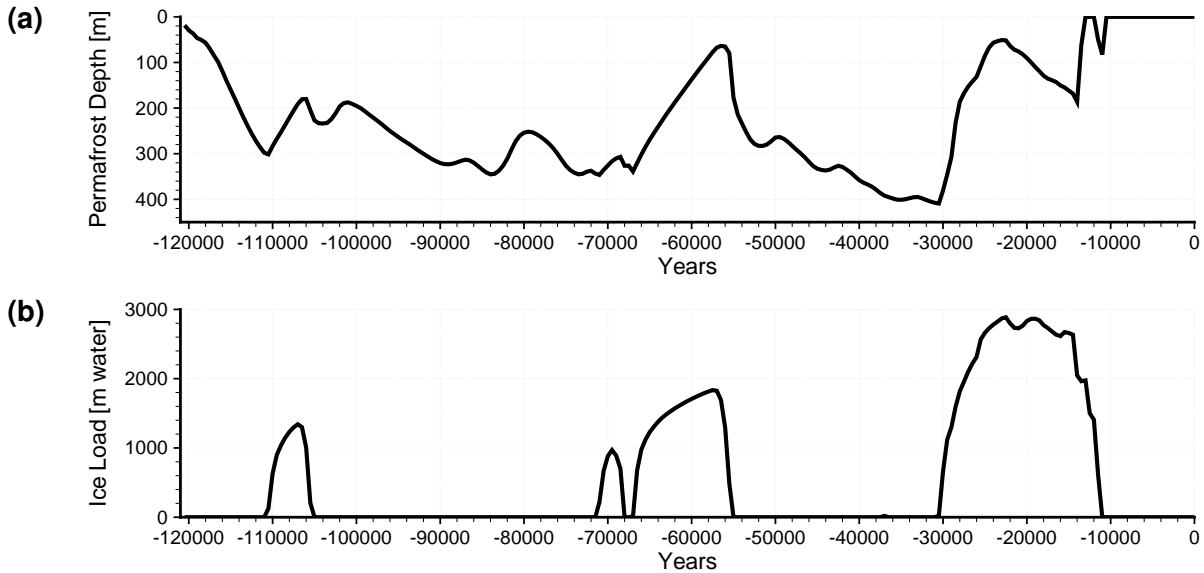


Figure 42: (continued) Darcy flux distribution at 20 000 years for maximum relative brine densities of: (a) 1.0, (b) 1.03, (c) 1.1, and (d) 1.2. Plane view at  $-200$  masl



**Figure 43: Darcy velocity vectors along with relative brine concentration in a cross section of the sub-regional domain at 20 000 years for maximum relative brine densities of: (a) 1.0, (b) 1.03, (c) 1.1, and (d) 1.2**



**Figure 44: Time series plots of (a) permafrost depth, and (b) ice load in equivalent metres of water for climate simulation NN2008 (cold-based glaciation)**

this analysis does demonstrate the behaviour of deep groundwater flow systems subjected to permafrost conditions and glacial loading events at ground surface and provides a basis to qualitatively understand the magnitude and time rate-of-change of flow in response to ice-sheet advance and retreat.

Matrix properties for solute transport include a longitudinal dispersivity of 50 m, a transverse horizontal dispersivity of 5 m and a transverse vertical dispersivity of 0.5 m. A free solution diffusion coefficient of  $7.258 \times 10^{-3} \text{ m}^2/\text{yr}$  was also applied. A matrix bulk density of  $2642.05 \text{ kg/m}^3$  ( $2650 \text{ kg/m}^3 \times (1 - 0.003)$ ) is used. Fracture hydraulic conductivity is set to  $1.0 \times 10^{-6} \text{ m/s}$ , porosity to 0.1, and thickness to 1 m throughout the modelling domain. Salinity is not included in these climate simulations.

Similarly, Peltier (2006) has provided an alternate climate simulation, NN2778. This climate scenario differs from NN2008 (cold-based glaciation) in that the base of the glacier is unfrozen for significant periods of time representing a warm-based glaciation. Both permafrost depth and ice load specific to the sub-regional modelling domain are plotted in Figure 45. Although the GSM simulations are North-American continent in scale, the results plotted in Figure 45 are specific to the sub-regional modelling domain.

#### 4.4.1 Simulation Results

A north-south cross-section through the domain with piezometric heads at 12 000 years before present is shown in Figure 46. At this point in time, the last glacial episode is retreating, thereby reducing the ice loading. However, due to the lower permeabilities at depth, the higher pressures from the prior ice loads remain at depth. Higher permeability features such as fractures are able to dissipate excess pore pressures quicker than the rock matrix. Two arbitrary locations are

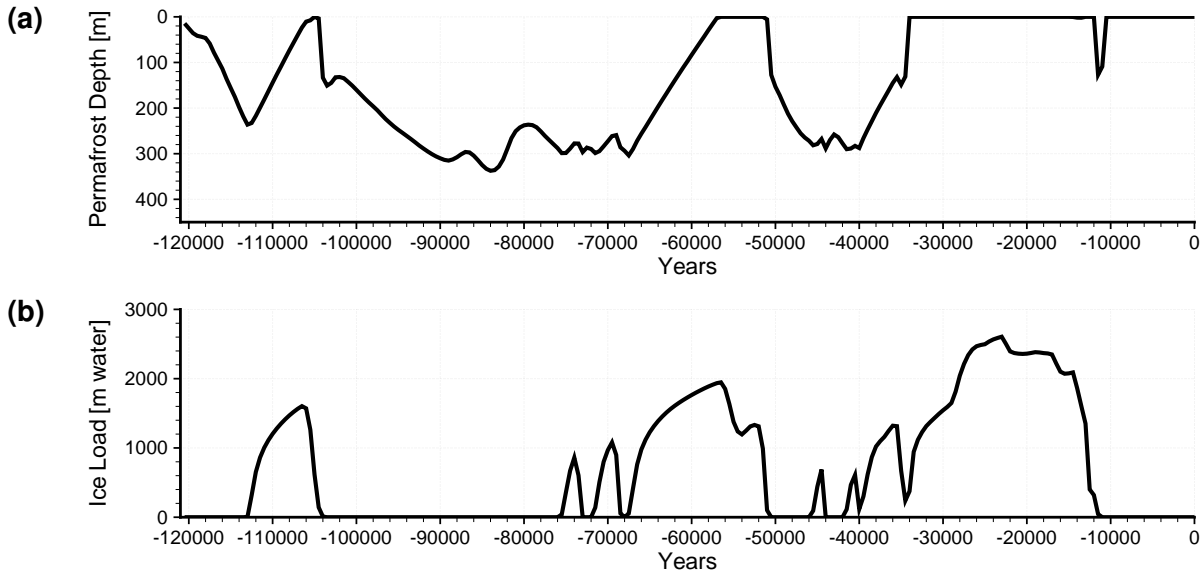


**Figure 45: Time series plots of (a) permafrost depth, and (b) ice load in equivalent metres of water for climate simulation NN2778 (warm-based glaciation)**

highlighted on Figure 46: a red dot within the rock matrix, and a green dot within a fracture. Vertical Darcy velocities at these locations are plotted in Figure 47 for NN2008. The vertical Darcy fluxes are also plotted for simulation NN2778 as shown in Figure 48

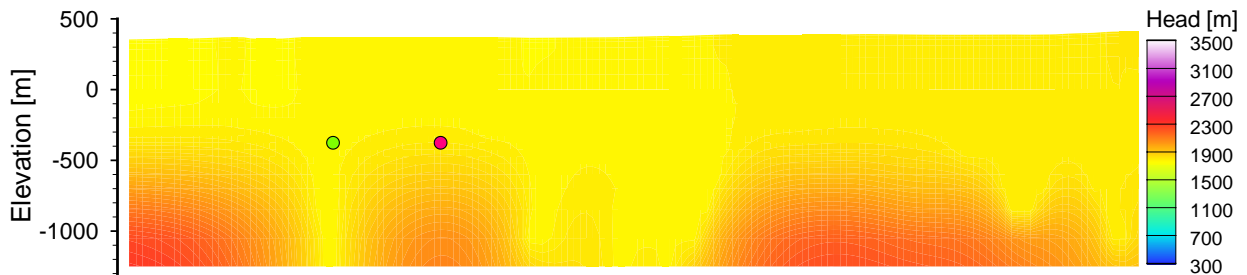


**Figure 46: Piezometric heads for north-south cross-section at 12 000 years before present. The red dot represents a location in the rock matrix, while the green dot represents a location within a fracture.**

Both Figure 47 and Figure 48 show that the vertical Darcy velocities in both the rock matrix and a fracture can be both downwards (negative) and upwards (positive), depending on whether the ice load at ground surface is increasing or decreasing, respectively. The vertical Darcy velocities in the fractures are much larger than in the rock matrix and can vary by approximately 5 orders of magnitude. It is interesting to note that the Darcy velocities for the matrix and fracture are very similar in shape when permafrost is present in the near surface. However, when no permafrost is present, the vertical Darcy velocity in the fracture is strongly influenced by topographic gradients

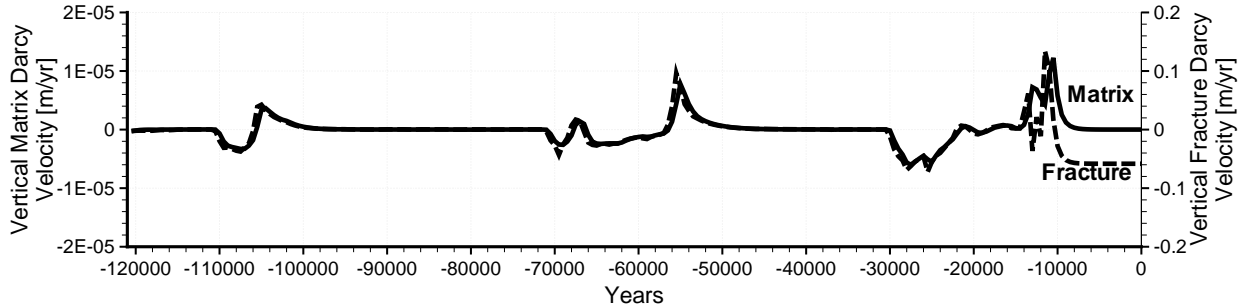


**Figure 47: Vertical Darcy velocities within the rock matrix and a fracture as indicated in Figure 46, for climate simulation NN2008 (cold-based glaciation)**

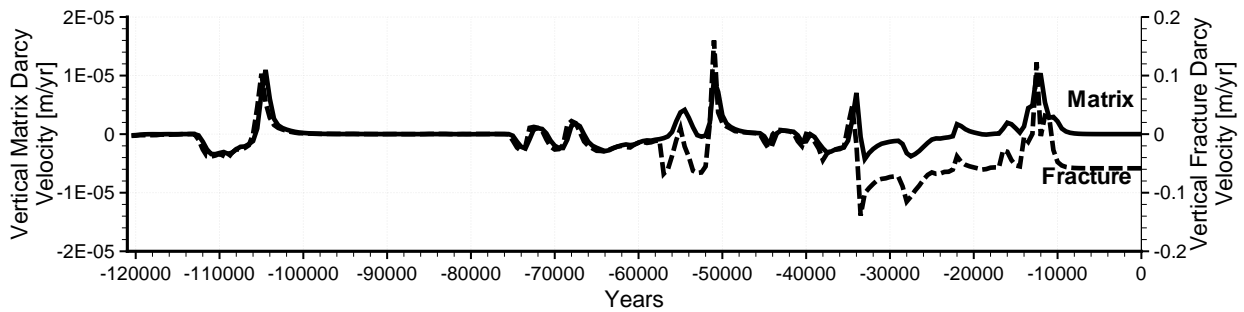


**Figure 48: Vertical Darcy velocities within the rock matrix and a fracture as indicated in Figure 46, for climate simulation NN2778 (warm-based glaciation)**

since it is well connected to the near surface flow system. The presence of permafrost inhibits this connection and the fracture responds in a similar manner to the surrounding rock matrix.

Concern has been expressed regarding the ability of oxygenated recharge waters penetrating to great depths during and following a glaciation event. To analyze this situation, a unit load of concentration was applied at the surface nodes of the numerical model. Recharge occurring during the 121 000 year simulation is thereby tagged with a tracer of unit concentration. Mean life expectancy could not be used since it is only applicable to steady-state simulations. Plotting an iso-surface representing 5% recharge water (a concentration of 0.05) can provide an indication of the depth to which recharge waters can migrate. A plot of the 5% iso-surfaces for the NN2008 and NN2778 climate simulations is shown in Figure 49.

As can be clearly seen, the blue iso-surface representing NN2778, the warm-based glaciation scenario, is barely visible as the red iso-surface for NN2008 is above it. This indicates that the warm-based glacier scenario leads to greater penetration of recharge waters to depth. A different plot showing the intersection of both iso-surfaces with numerous east-west and north-south trending cross-sections is shown in Figure 50.

Figure 50 clearly shows that the depth of recharge water penetration for NN2778 is greater than for NN2008. Depth of recharge water penetration is greater within fractures than the matrix. This

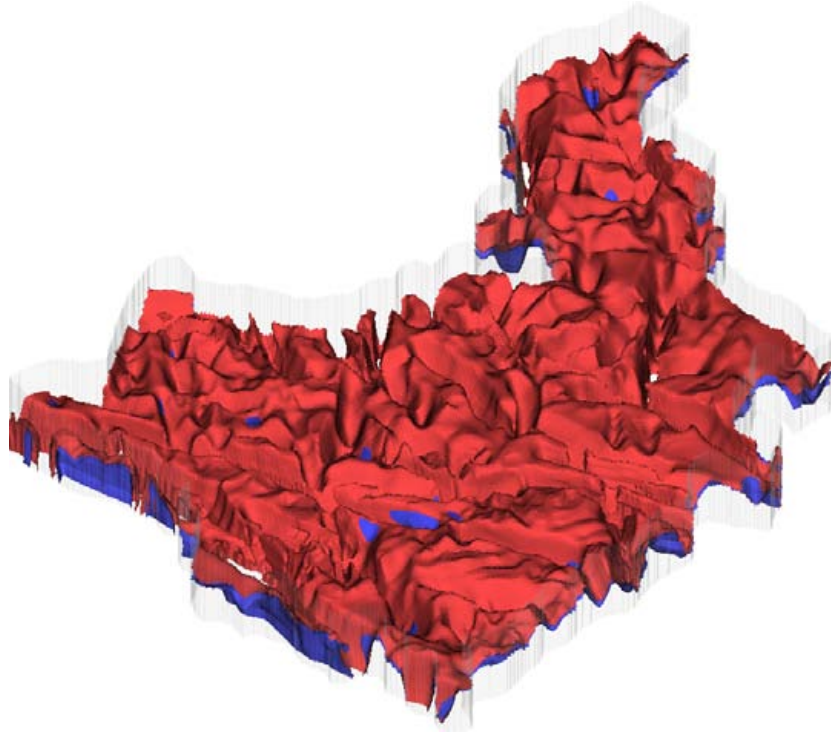


**Figure 49: Iso-surface of 5% recharge water at the end of a 121 000 year simulation for the NN2008 climate simulation (red iso-surface) and for the NN2778 climate simulation (blue iso-surface)**

fact is also prevalent in comparing Figure 48 to Figure 47 as the duration of downward velocity in the fracture is also greater for NN2778 than for NN2008. Some fractures permit the 5% recharge water to penetrate to the bottom of the modelling domain, while the 5% recharge water penetrates the matrix to approximately 500–600 m depth for the NN2008 scenario and 100–200 m deeper than NN2008 for the NN2778 scenario. It should be mentioned that the depths of penetration are accentuated by the translation of ice thickness into hydraulic head for the boundary conditions.

## **4.5 LIFETIME EXPECTANCY**

### **4.5.1 Illustrative Examples**

In this section, the utility and the applicability of the concepts of lifetime expectancy and backward-in-time transport for optimal location of subsurface waste repositories are illustrated with a set of numerical examples. We focus specifically on the effects of fracture network geometry on lifetime expectancy, as a preliminary study for the application of this approach to the Canadian Shield sub-regional environment.

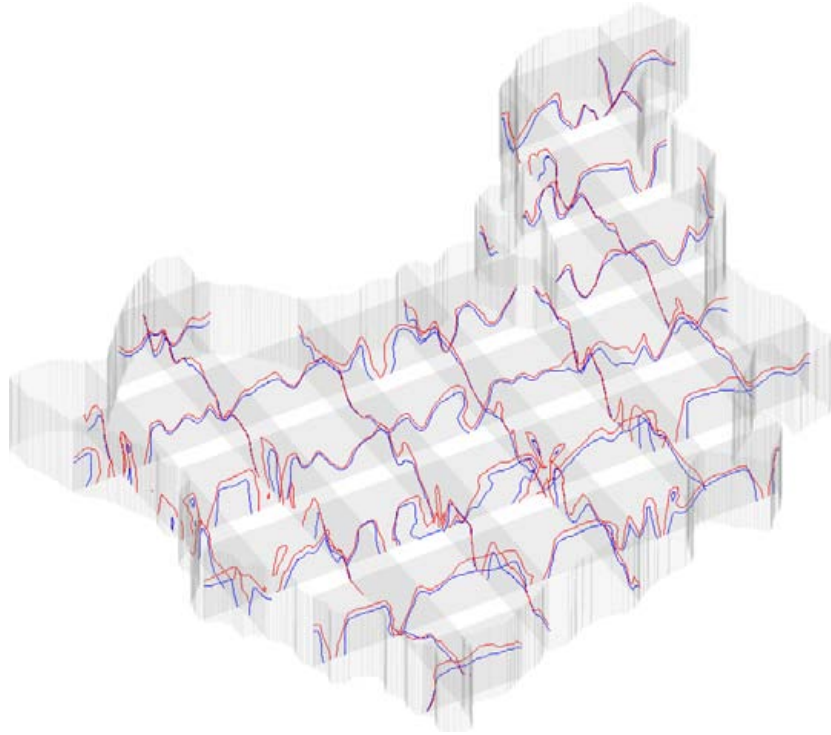


Figure 50: East-west and north-south trending fences showing 5% recharge water at the end of a 121 000 year simulation for the NN2008 climate simulation (red lines) and for the NN2778 climate simulation (blue lines)

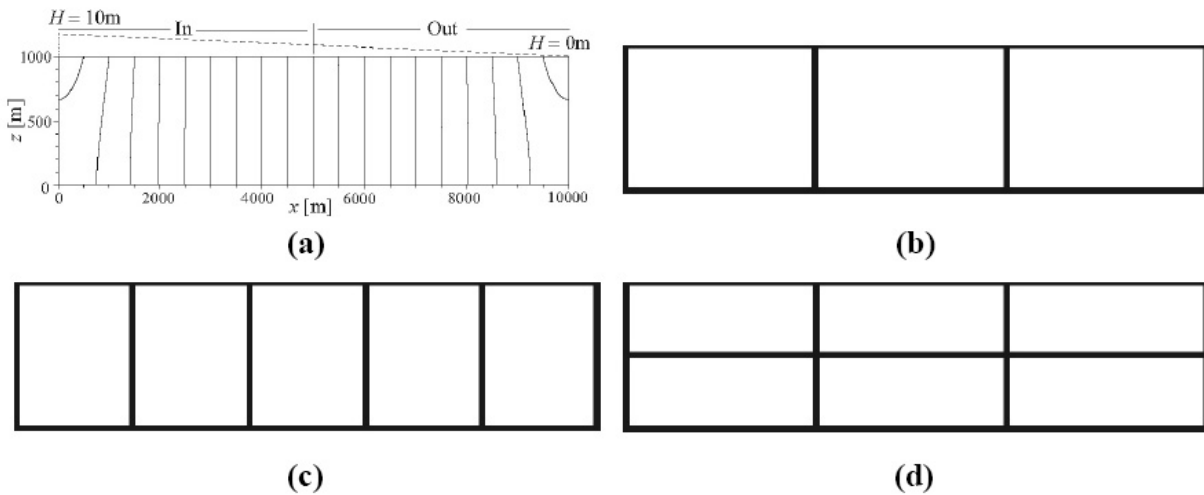
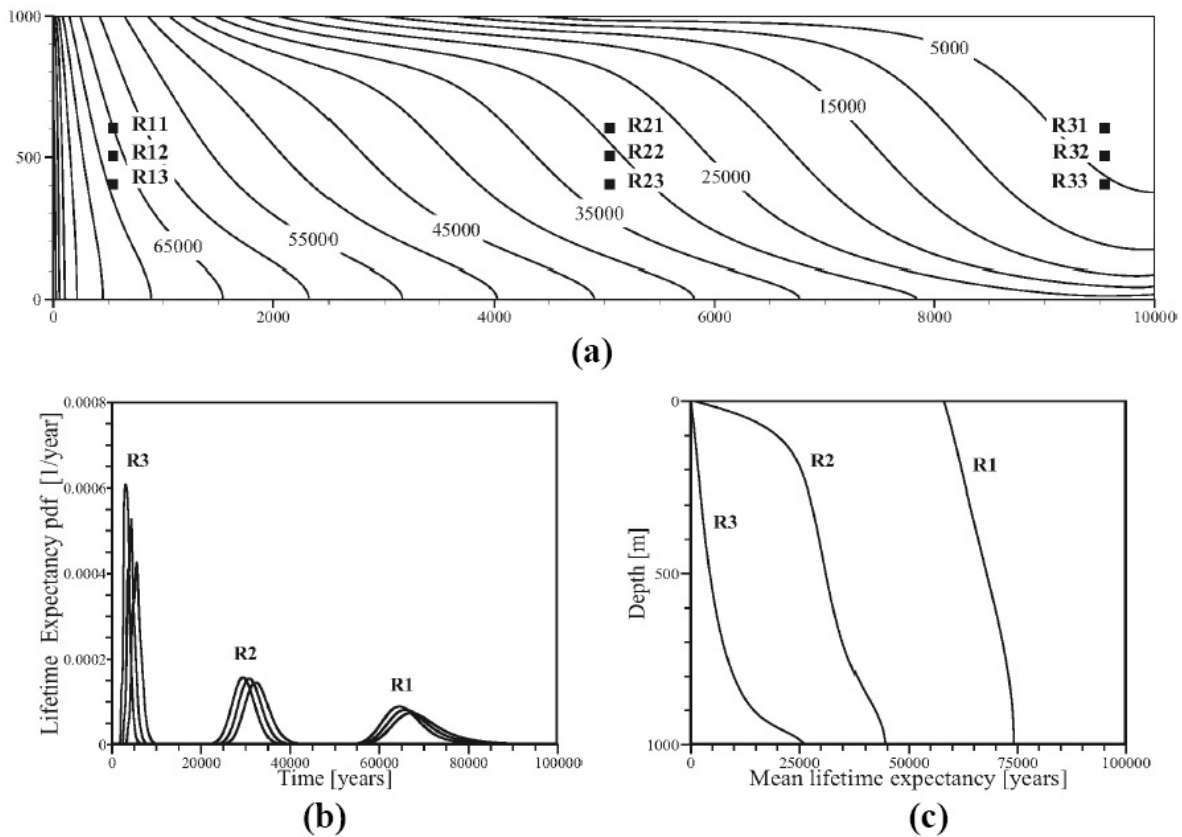


Figure 51: Schematics of the vertical cross-sections used to model mean and probability density for lifetime expectancy: (a) hydraulic head distribution in a homogeneous matrix system under given flow boundary conditions; (b)-(d) variation cases with different fracture networks (thick lines).

#### 4.5.1.1 Model Layout and Proof-of-Concept

Four sets of different fracture network geometries are considered in a two-dimensional, 10 km wide and 1 km deep, cross-sectional domain (Figure 51). The domain is discretized using 10 m square rectangular elements. For the illustrative schematic of fractured porous media, the fracture domain is assumed to be more permeable and have a higher porosity than the matrix domain. Flow and transport properties are homogeneous, with the fracture domain having a hydraulic conductivity of  $10^{-3}$  m/s, porosity of 0.3, dispersivity of 10 m, and free solution diffusion coefficient of  $2.3 \times 10^{-9}$  m<sup>2</sup>/s, and the matrix domain having a isotropic hydraulic conductivity of  $10^{-6}$  m/s, porosity of 0.2, and longitudinal and transverse dispersivities of 10 m and 1 m respectively. Decay and retardation are excluded for simplification and clarity. A specified hydraulic head boundary condition is imposed at the top of the domain, to derive a steady flow from top left to top right as shown in Figure 51a.



**Figure 52: Lifetime expectancy solutions for the case in Figure 51. (a) Mean lifetime expectancy distribution in years, (b) lifetime expectancy probability density at nine observation points in (a), and (c) vertical logs of mean lifetime expectancy passing through the observation points.**

As a first step, mean lifetime expectancy is computed throughout the whole domain for the homogeneous matrix system (Figure 52a). The result was obtained by solving the steady state backward-in-time mean lifetime expectancy Equation (36), and is equivalent to solving the forward transport Equation (29), or its first moment form, a number of times using a Dirac input at each nodal upstream point. The result in Figure 52a can easily be understood from the flow field in Figure 51a: mean lifetime expectancy gets shorter as any point becomes closer to the top right exit boundary because one can expect a short travel time to the exit boundary if a source is near the exit boundary, while travel time is longer for the bottom left corner of the domain (up to 100 000 years). With this result in mind, one might conclude that the bottom left corner would be the safest location for hosting a repository in terms of the longest average expected travel time to the biosphere.

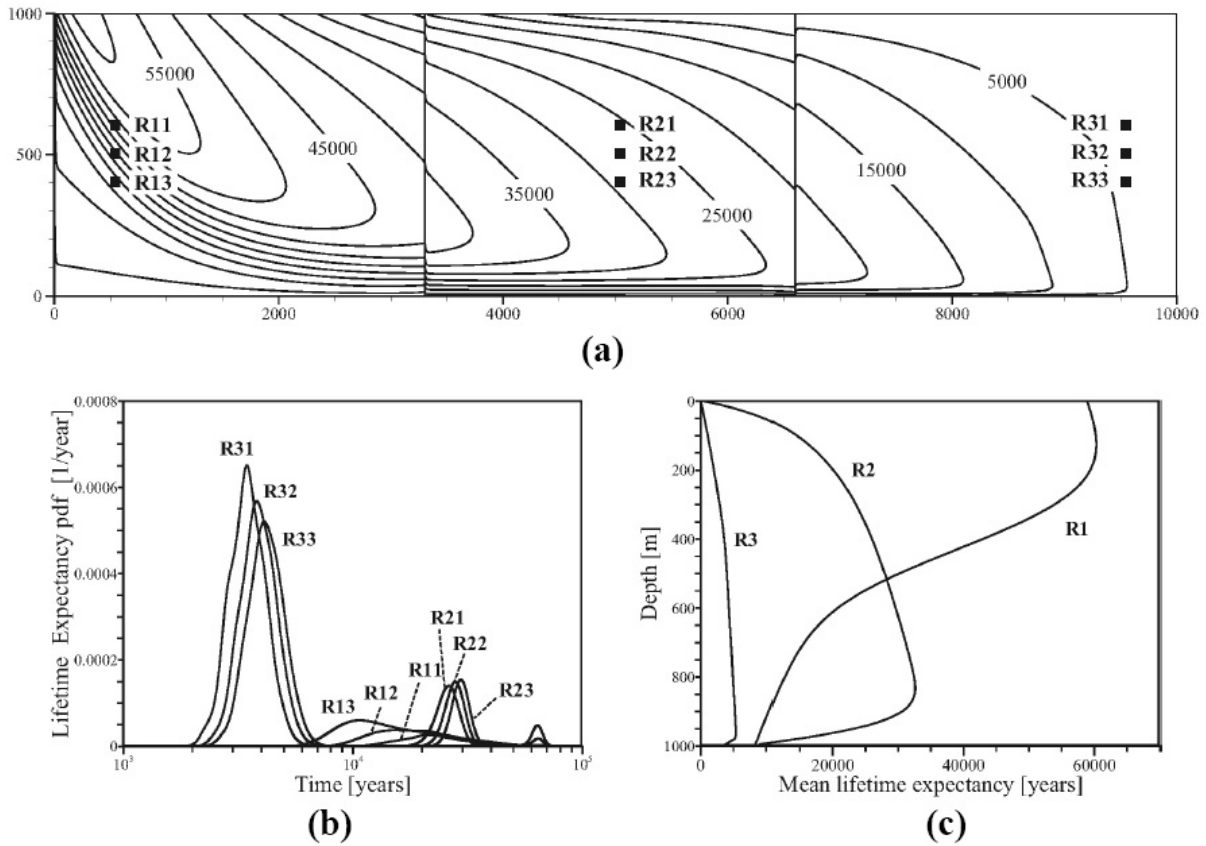
Figure 52b shows nine probability density functions for lifetime expectancy at the observation points R11-R33 in Figure 52a. Since the probability density for lifetime expectancy accounts for the temporal probabilistic distribution for lifetime expectancy, travel time from one point within the domain to the exit boundary could vary significantly, depending on the flow field and hydro-dispersive properties of the medium. For this specific example, water molecules at the observation point, for example R22, will reach the top of the domain (biosphere) in about 30 000 years on average, but it could be 5000 years earlier or later as shown in Figure 52b. Note that as lifetime expectancy becomes longer, it tends to spread wider as in classical transport theory.

Figure 52c shows vertical profiles of mean lifetime expectancy through the observation points R11-R13 (R1), R21-R23 (R2), and R31-R33 (R3). The results show that the expected travel time is longer as a source becomes deeper. Interestingly, the three vertical profiles in Figure 52c behave in different ways due to their different locations in the flow field. For the profile across R1, mean lifetime expectancy linearly increases with depth, while it increases quickly down to 100 m depth for the profile across R2 and it increases relatively slowly down to 900 m depth for R3.

#### 4.5.1.2 Effects of Fracture Zone Geometry

In order to investigate the influence of fracture zone geometry on lifetime expectancy in fractured porous media, three sets of fracture network geometries were embedded in the matrix system. First we consider the case with one horizontal fracture zone at the bottom and four evenly spaced vertical fracture zones (Figure 51b) and then the cases with different numbers of vertical and horizontal fracture zones (Figure 51b and Figure 51c).

For the case in Figure 51b, mean lifetime expectancy in the matrix domain varies up to about 60 000 years along the recharge area at the upper left corner and contours tend to be refracted across fracture zones due to a higher flow rate in the discontinuities (Figure 53a). The main difference between Figure 52a and Figure 53a lies in the mean lifetime expectancy near the bottom horizontal fracture zone, where mean lifetime expectancy becomes smaller (e.g., see the 5000 year contour). Computed probability density functions of lifetime expectancy from nine observation points (Figure 54b) indicate that lifetime expectancy becomes much smaller over the domain compared to the results in Figure 52b, because fracture zones act as a “short cut” to the biosphere. Not surprisingly, the probability density for R1 has notable multiple peaks due to multiple distinct flow paths to the discharge area along the fracture zones. It is worth noting that first peaks for R1 come earlier than peaks for R2 because the observation points R1 are located



**Figure 53: Lifetime expectancy solutions for the case in Figure 51b. (a) Mean lifetime expectancy distribution in years, (b) lifetime expectancy probability density at nine observation points in (a), and (c) vertical logs of mean lifetime expectancy passing through the observation points.**

closer to fracture zones. The mean lifetime expectancy for R1 ranges from about 20 000 years for R13 to 45 000 years for R11, as attested to by the strong gradient in mean lifetime expectancy in the neighbourhood of R1 (Figure 53a), even though the first peaks will appear between 10 000 and 20 000 years. This discrepancy is important in the context of risk or safety in hosting repositories because a life expectancy PDF can be multi-modal, having two or more peaks representing the likelihood of travel time to the biosphere. The mean or some weighted average of the life expectancy PDF may not be sufficient to represent the travel time, and hence risk. In this case, it would be best or more prudent to choose the shorter travel time, even though the mean travel time is greater. Due to the existence of the bottom fracture zone, mean lifetime expectancy decreases near the bottom of the domain (Figure 53c). A rapid decrease in mean lifetime expectancy along R1 could be explained by downward flow in the matrix block, compared to lateral or upward directional flow in other blocks.

Figure 54 shows the results for mean lifetime expectancy and the corresponding PDFs when the number of vertical or horizontal fracture zones is increased (Figure 51c and Figure 51d). For Figure 54a and Figure 54b, lifetime expectancy is smaller than in the previous case (Figure 53),

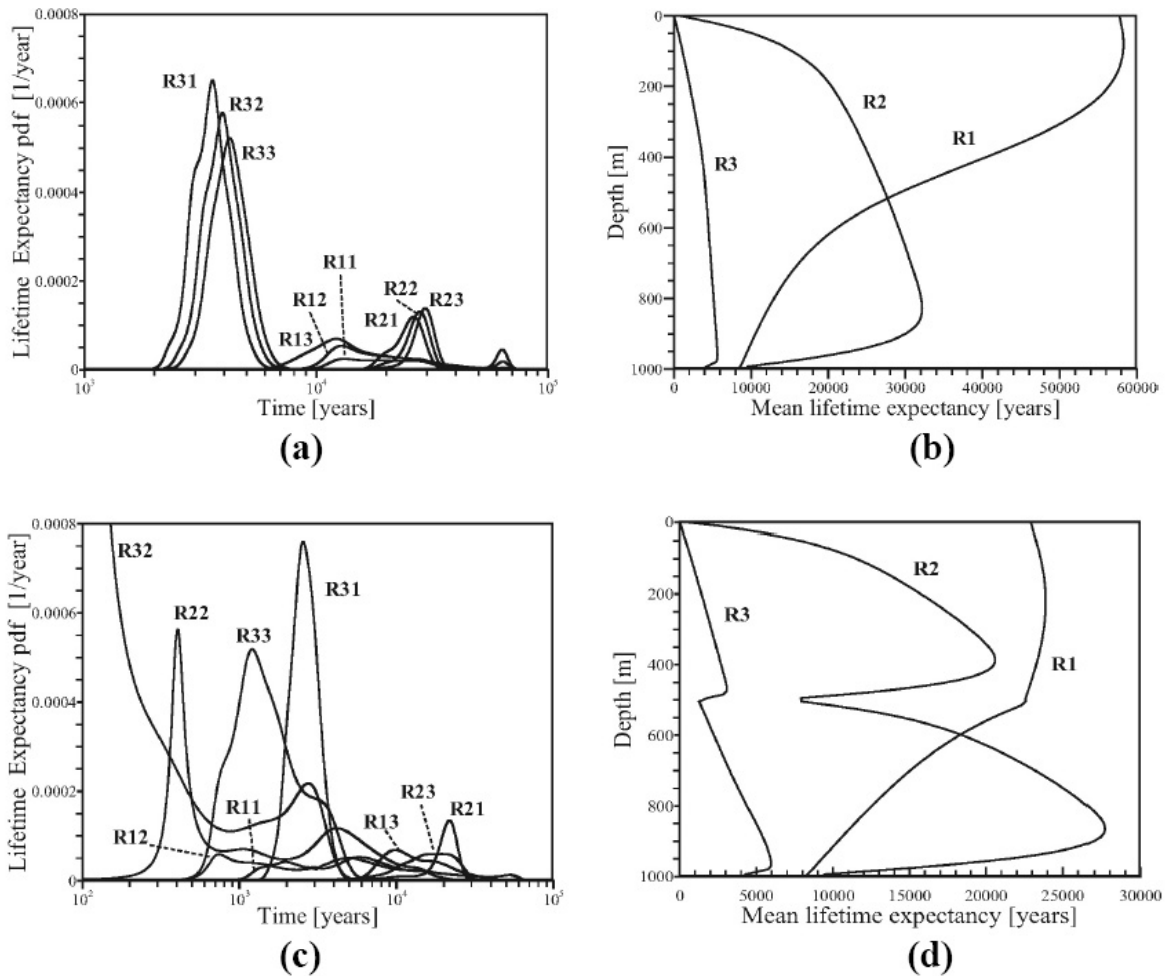


**Figure 54: Lifetime expectancy solutions for different fracture network geometries. (a) and (c) show lifetime expectancy probability density at nine observation points for Figure 51c and Figure 51d, respectively. (b) and (d) are vertical logs of mean lifetime expectancy passing through the observation points for Figure 51c and Figure 51d**

although the general tendency in the distribution does not change significantly as the distance from the observation points to the nearest fracture zones does not change significantly. Note again that the points in R2 could represent more suitable repository locations than in R1, regarding the first arrival times. This result could be contradictory to the suggestion that a repository could be best hosted in the recharge area by Tóth and Sheng (1996). When a horizontal fracture zone is added in the middle of the domain (Figure 51d), the nine observation points become significantly closer to a fracture zone (R12, R22, and R32 are now located on the fracture zone). The mean lifetime expectancy distribution shows that the additional fracture zone could shorten the lifetime expectancy values to less than one half of their original values for most of the domain (Figure 54c and Figure 54d). The lifetime expectancy PDFs for R12, R22, and R32 shows multiple peaks and significant tailing due to matrix diffusion. It should be noted that a repository would not knowingly be placed in or near a fracture zone.

Analyses of lifetime expectancy for the illustrative examples indicate that one can expect shorter lifetime expectancy near horizontal fracture zones, and that, as a matter of fact, depth is not necessarily a secure factor in ensuring safety in fractured porous media. In addition, the comparison between the mean and PDF solutions in lifetime expectancy leads to the suggestion that multiple pathways reactive transport systems such as fractured porous media require more careful analyses.

#### **4.5.2 Mean Lifetime Expectancy - Sub-Regional Domain**

Mean lifetime expectancy (MLE) was computed throughout the sub-regional domain following the theory described in Section 3.3.3 (Figure 55). In Figure 55, MLE generally increases at deeper locations, ranging from less than one hundred years near ground surface to greater than 10 million years at depth; it is the least at major fracture zones; and it becomes greater as one moves from fracture zones towards the middle of matrix blocks. It is worth noting that MLE could be less than 100 years, as represented by the blue contours, near ground surface. This is mostly associated with discharge areas but can occur in recharge areas as well since local flow/dispersion is a key factor for MLE.

Figure 56 shows the distribution of MLE for four horizontal slices at different depths. At an elevation of 100 masl (approximately 270 m below ground surface), MLE could be less than 1000 years in major fracture zones but for most of the horizontal slice, it ranges from  $10^4$  to  $10^6$  years; at an elevation of -100 masl (approximately 470 m below ground surface), MLE becomes larger than  $10^4$  years even within fracture zones; at an elevation of -300 masl (approximately 670 m below ground surface), MLE becomes greater than  $10^6$  years for most areas except within major fracture zones; and finally, MLE becomes greater than 10 million years for deeper areas. MLE captures the impact of diffusion and hydromechanical dispersion, while advective particle tracking does not.

Figure 57 shows an isosurface for  $MLE = 10^6$  years in the sub-region: MLE is greater than  $10^6$  years below the isosurface and this region is relatively more suitable than the upper region for locating a repository. In Figure 57, depression of the isosurface is mostly due to major sub-vertical fracture zones distributed across the domain, which act as preferential pathways from the deep sub-surface, reducing MLE in their vicinity.

Figure 58 shows frequency plots for MLE at four different elevations across the sub-region. The results show that MLE is strongly influenced by depth as MLE at an elevation of -500 masl increased by three orders of magnitude compared to that at an elevation of 100 masl. Figure 58 also shows that the MLE distributions (in log-scale) become narrower as depth increases, indicating less variation with increasing depth.

In order to compare MLE distributions at different elevations, cumulative frequency plots were generated for various elevations (Figure 59). It is clear in Figure 59 that MLE increases with depth and its range becomes narrower. The results imply that with sparser and less permeable fracture zones, expected groundwater travel time from depth to the biosphere increases with less uncertainty.

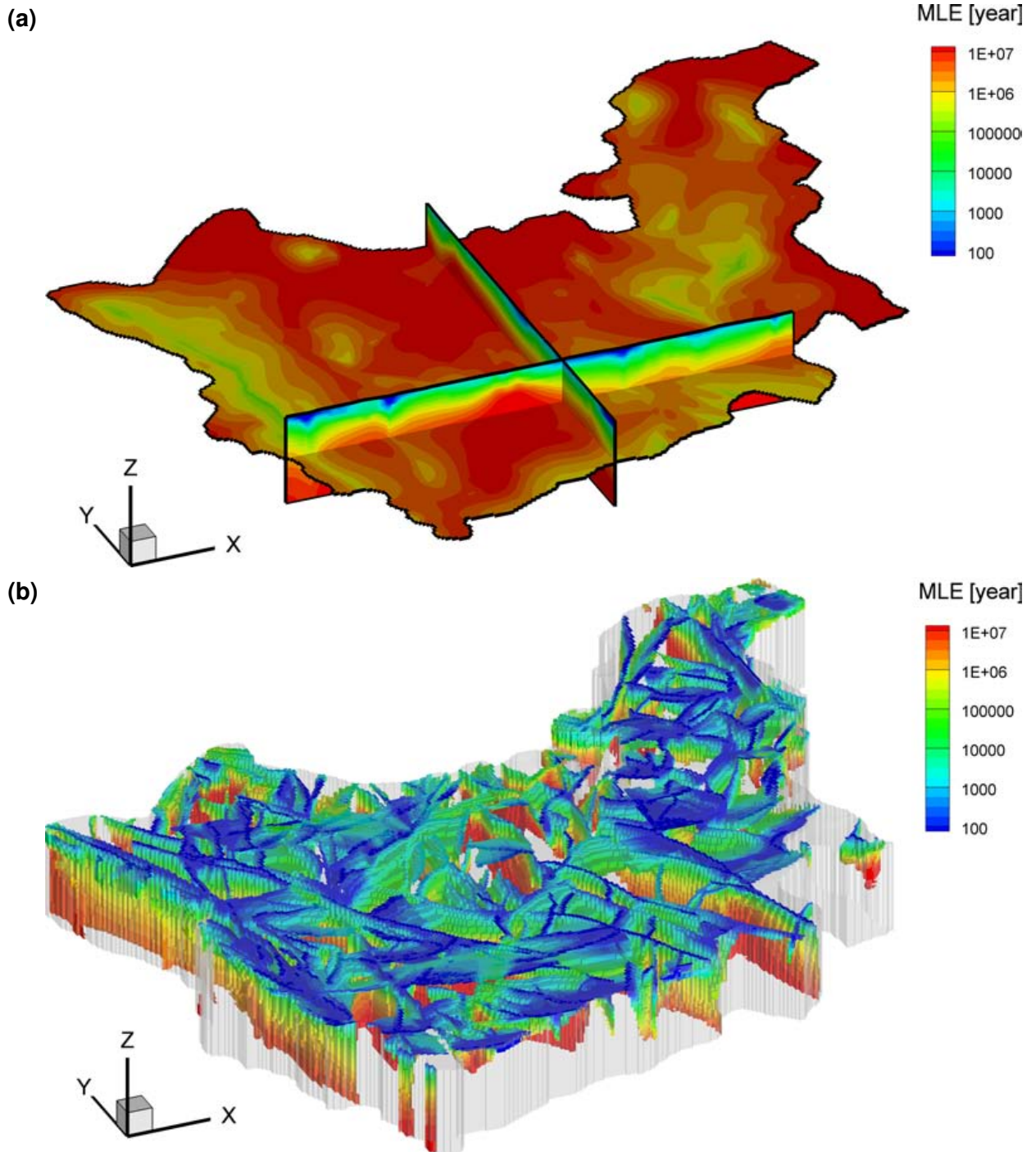


Figure 55: Mean lifetime expectancy distribution in (a) matrix, and (b) fracture domains. Plane view at  $-415$  masl

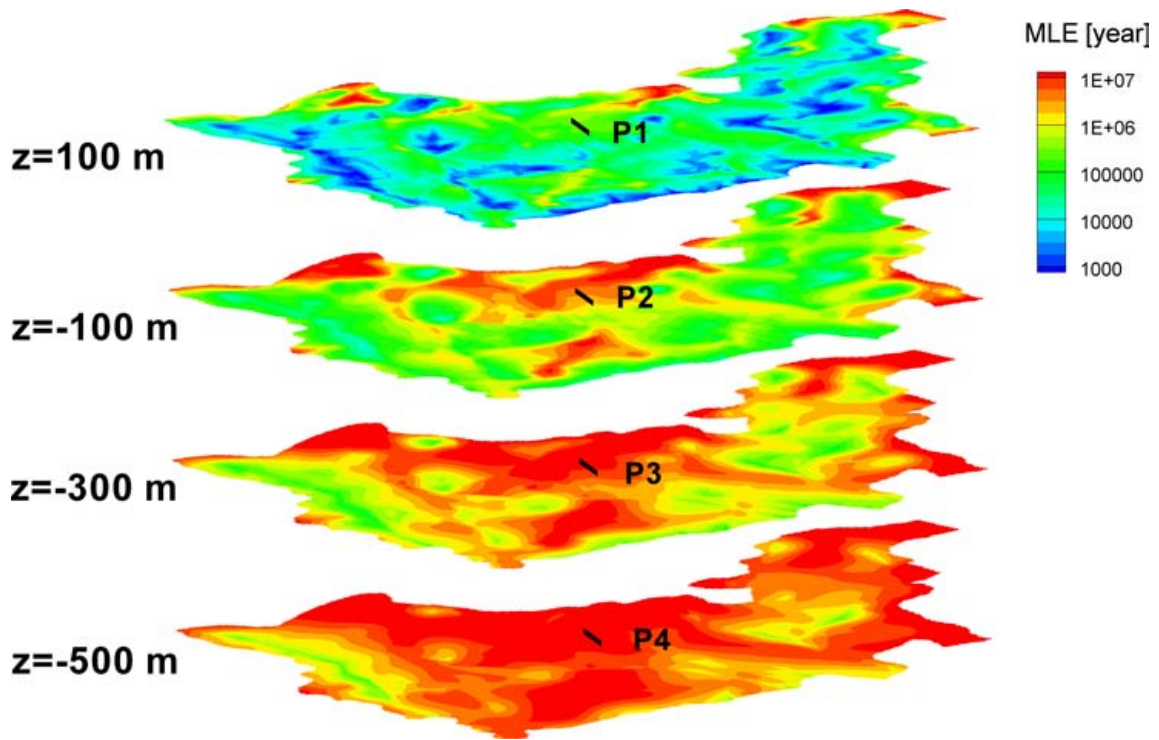


Figure 56: Mean lifetime expectancy at four different elevations in the sub-region

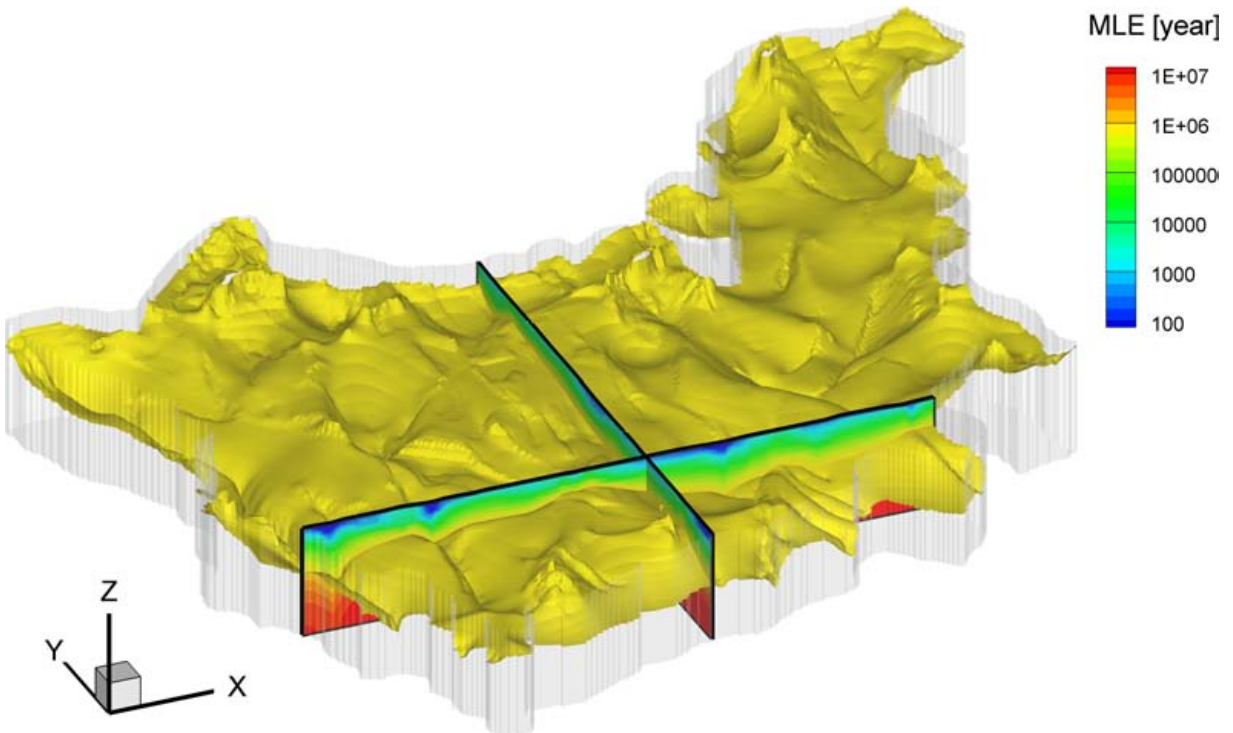


Figure 57: Isosurface for  $10^6$  years of mean lifetime expectancy

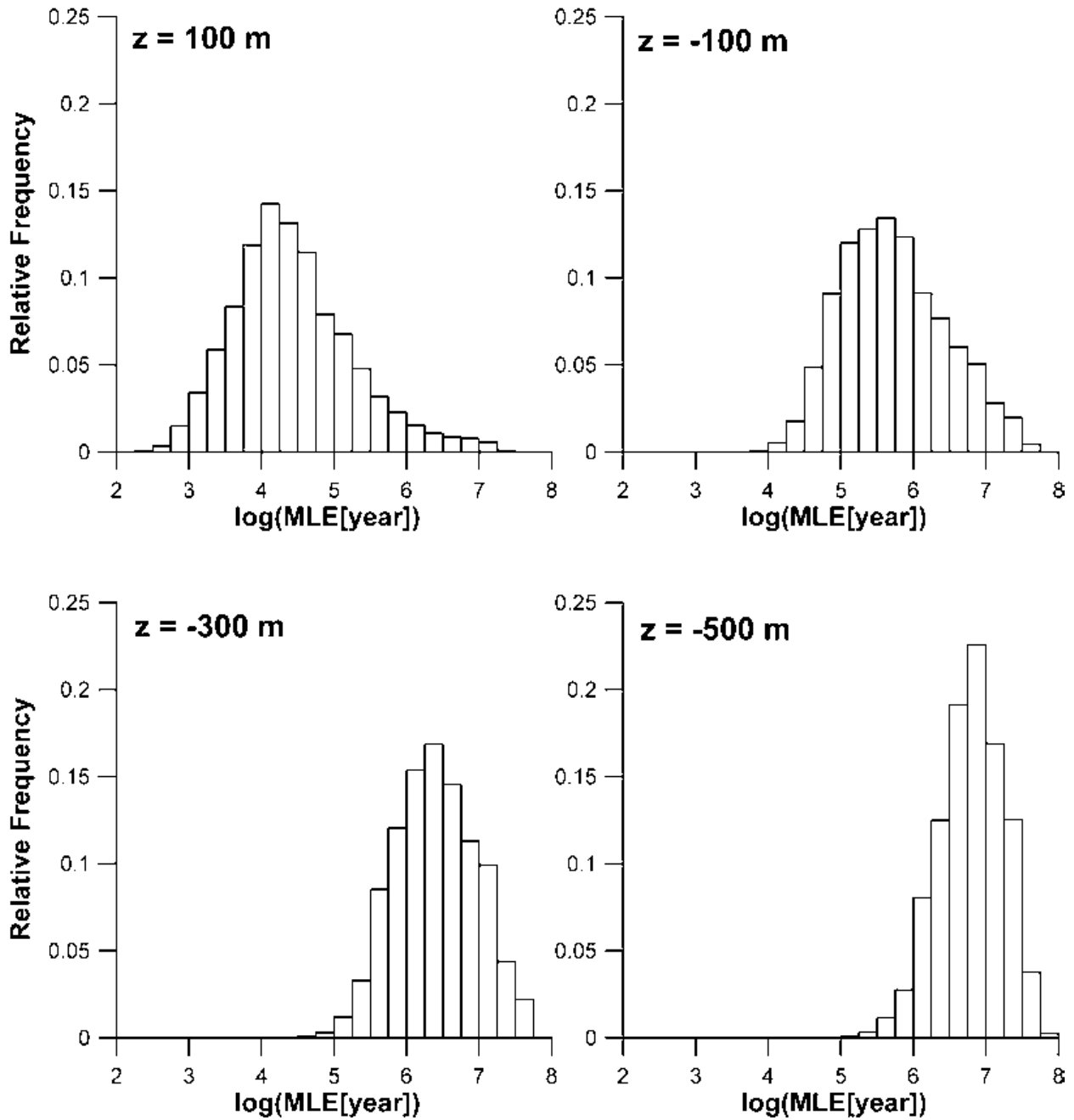
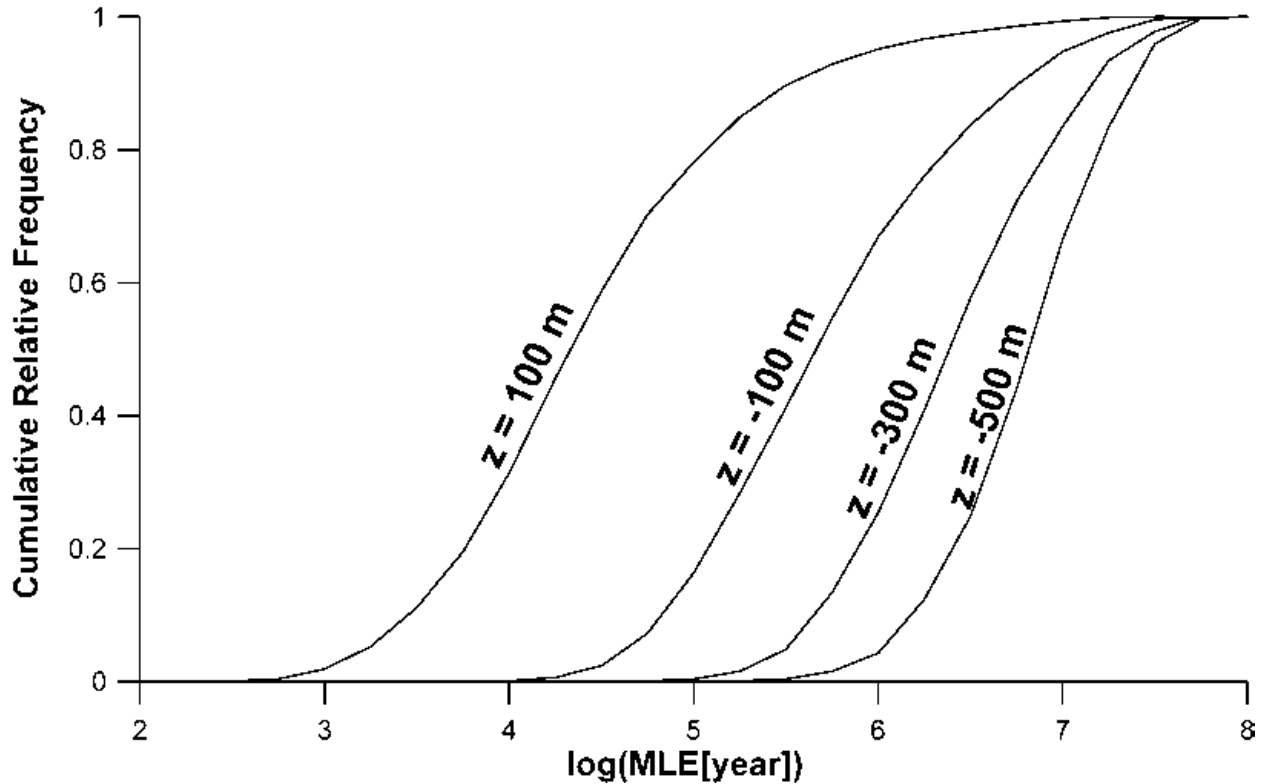


Figure 58: Frequency plots for mean lifetime expectancy at four different elevations

#### 4.5.3 Probability Density for Lifetime Expectancy - Sub-Regional Domain

MLE is the first temporal moment of lifetime expectancy probability, and thus, a greater MLE does not always guarantee the least dose, or the later arrival of contaminants at the biosphere, as the averaged travel time of contaminants can be much greater than either first or peak arrivals in multiple pathway reactive systems, even though it might indicate so. It was clearly demonstrated in Section 4.5.1, with illustrative fractured porous media, that it is more desirable to compute the



**Figure 59: Cumulative frequency plots for mean lifetime expectancy at four different elevations**

probability density function for lifetime expectancy, in order to completely analyze the suitability of a location to host a subsurface repository. It is possible to compute the probability density for lifetime expectancy for any given volume or for any union of volume subsets with a given release function (see Equation (37)). Figure 56 shows four specific repository locations at different depths to compute PDFs of lifetime expectancy: P1 at  $z = 100$  masl, P2 at  $z = -100$  masl, P3 at  $z = -300$  masl, and P4 at  $z = -500$  masl. Each location has an approximate size of  $(\Delta x, \Delta y, \Delta z) = (100 \text{ m}, 1 \text{ km}, 100 \text{ m})$ . For the given locations, the mean of lifetime expectancy was calculated to be between 100 000 and 1 000 000 years for P1 and P2, but peak mass flux arrival times for P1 and P2, based on Equation (37), were earlier than the calculated MLE values: approximately 30 000 and 150 000 years for P1 and P2, respectively as shown in Figure 60. For the deeper release points P3 and P4, mass flux computed from the source locations was negligible for 2 million years of simulation time, as can be expected from MLE solutions which are greater than  $10^7$  years. This result implies that strong tailing for transport in fractured porous media due to multiple pathways and matrix diffusion could make a significant difference between the first temporal moment and the peak arrival time, even though a greater MLE would still be an indicator of later water molecule arrival. The risk associated with potential subsurface repositories needs to be analyzed for the given safety criteria, ideally with transient simulations and the PDFs of lifetime expectancy instead of MLE.

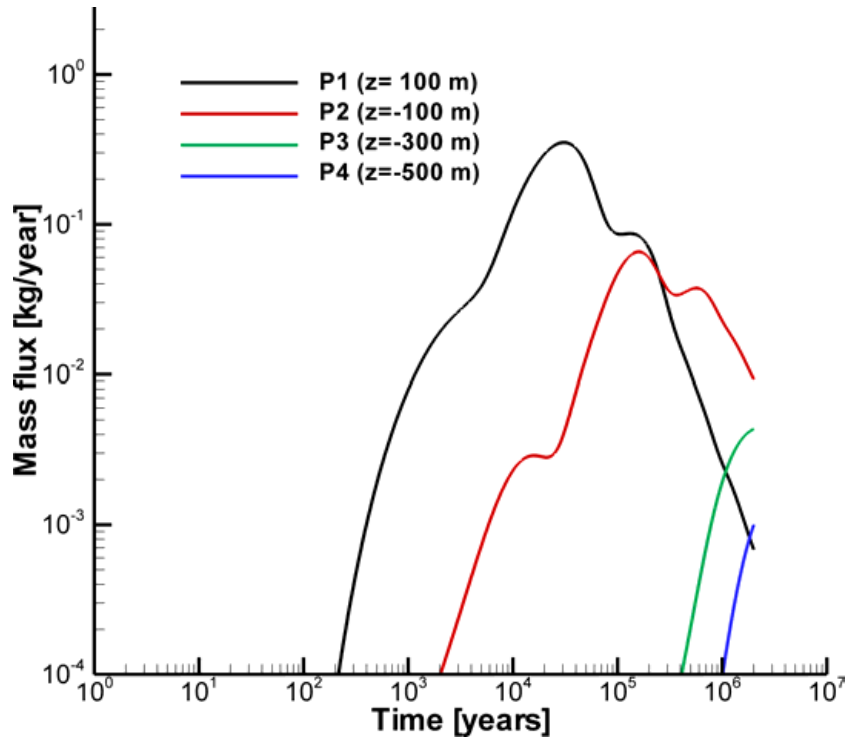


Figure 60: Mass flux to biosphere from sources at four different elevations

#### 4.5.4 Effects of Shield Brine - Sub-Regional Domain

As shown in Section 4.3, Shield brine can retard upward groundwater flow and may influence lifetime expectancy and the performance of deep subsurface repositories. In this section, the effects of Shield brines on mean lifetime expectancy (MLE) distributions are examined. MLE distributions are computed by using the flow field simulated with different maximum brine density values discussed in Section 4.3.

For illustrative purposes, flow fields and brine distributions for the vertical cross-sectional examples in Section 4.3.2 were utilized to obtain the MLE distribution (Figure 61). The results in Figure 61 clearly demonstrate that as Shield brines become denser, MLE increases in the brine region. Figure 61 also shows that MLE contour lines become more horizontal in the brine region as density increases, indicating that the depth-dependency of MLE becomes stronger in more hydraulically stagnant regions.

MLE was computed in the sub-regional domain by using the groundwater flow fields obtained from the density-dependent flow and transport simulations in Section 4.3 (Figure 62). The results show that MLE generally increases with less variation at deeper locations as brines become denser. This can be seen by comparing the  $z = -500$  masl elevation of Figure 62a and Figure 62d, where the higher density of Figure 62d results in greater MLE, than similar locations in Figure 62a. Similar trends can be seen when comparing the various sub-figures (varying density) of Figure 62 at similar elevations.

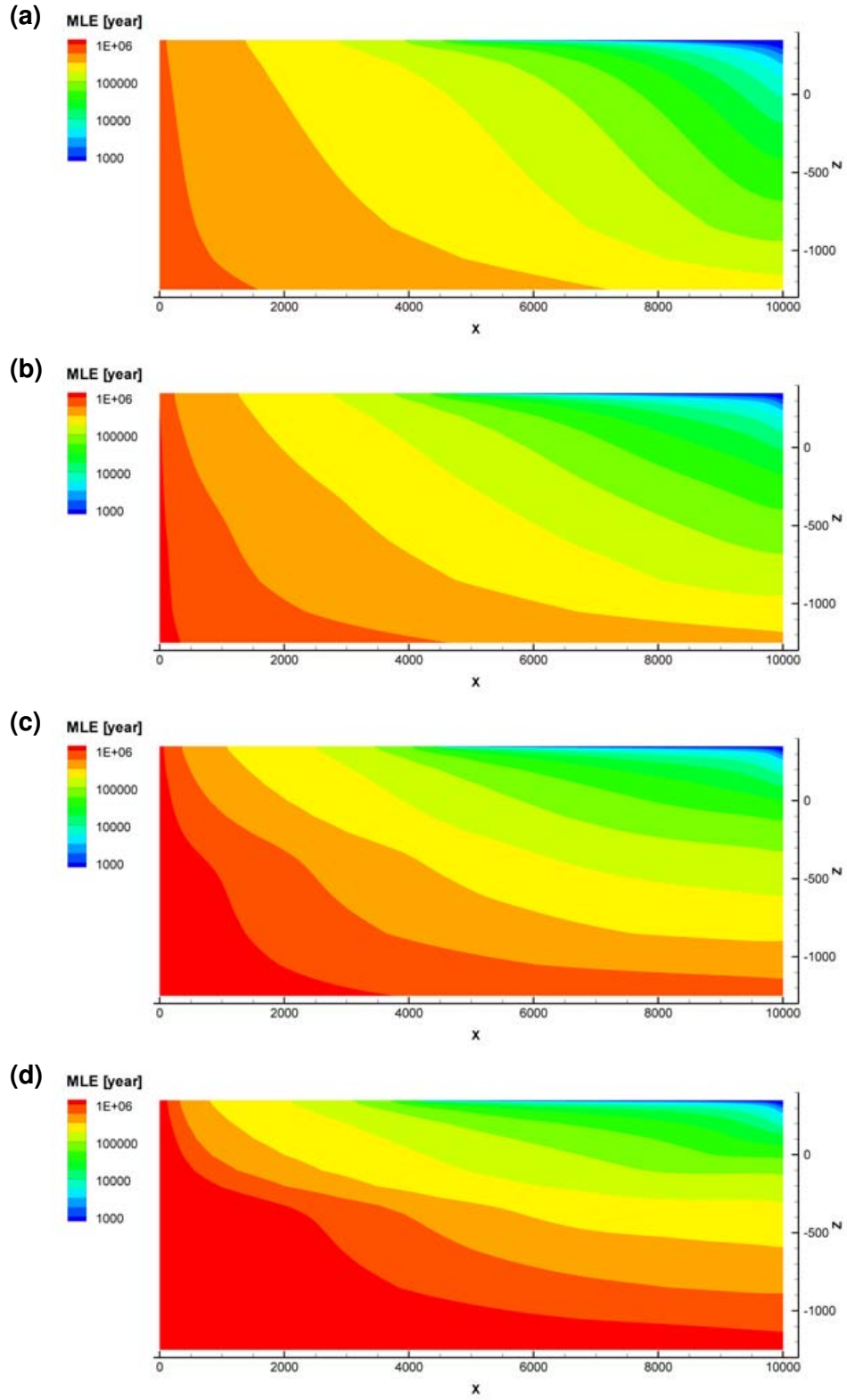


Figure 61: Mean lifetime expectancy distributions for maximum relative brine densities of: (a) 1.0, (b) 1.03, (c) 1.1, and (d) 1.2

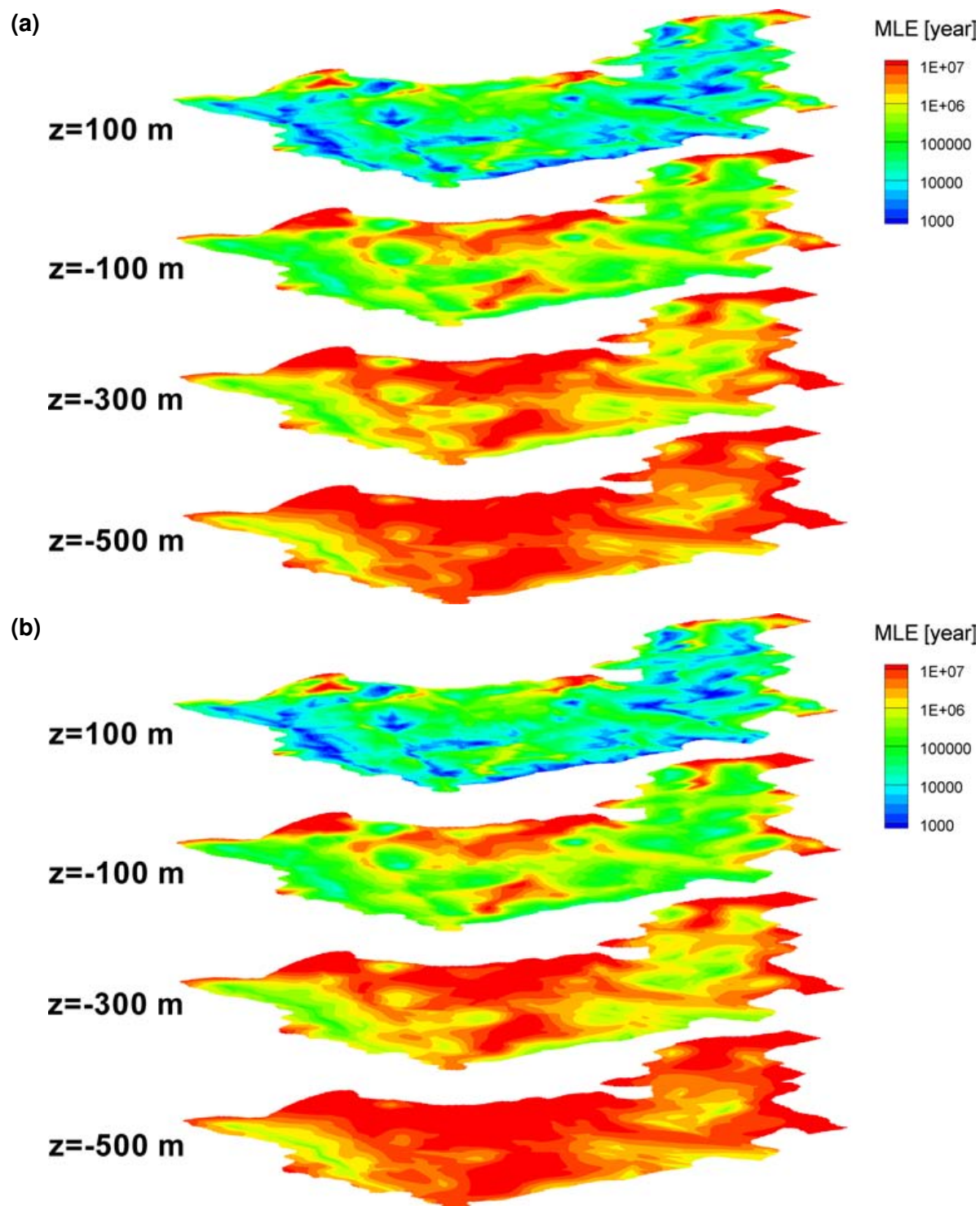


Figure 62: Mean lifetime expectancy at four elevations in the sub-region with maximum relative brine density of: (a) 1.0, (b) 1.03, (c) 1.1, and (d) 1.2

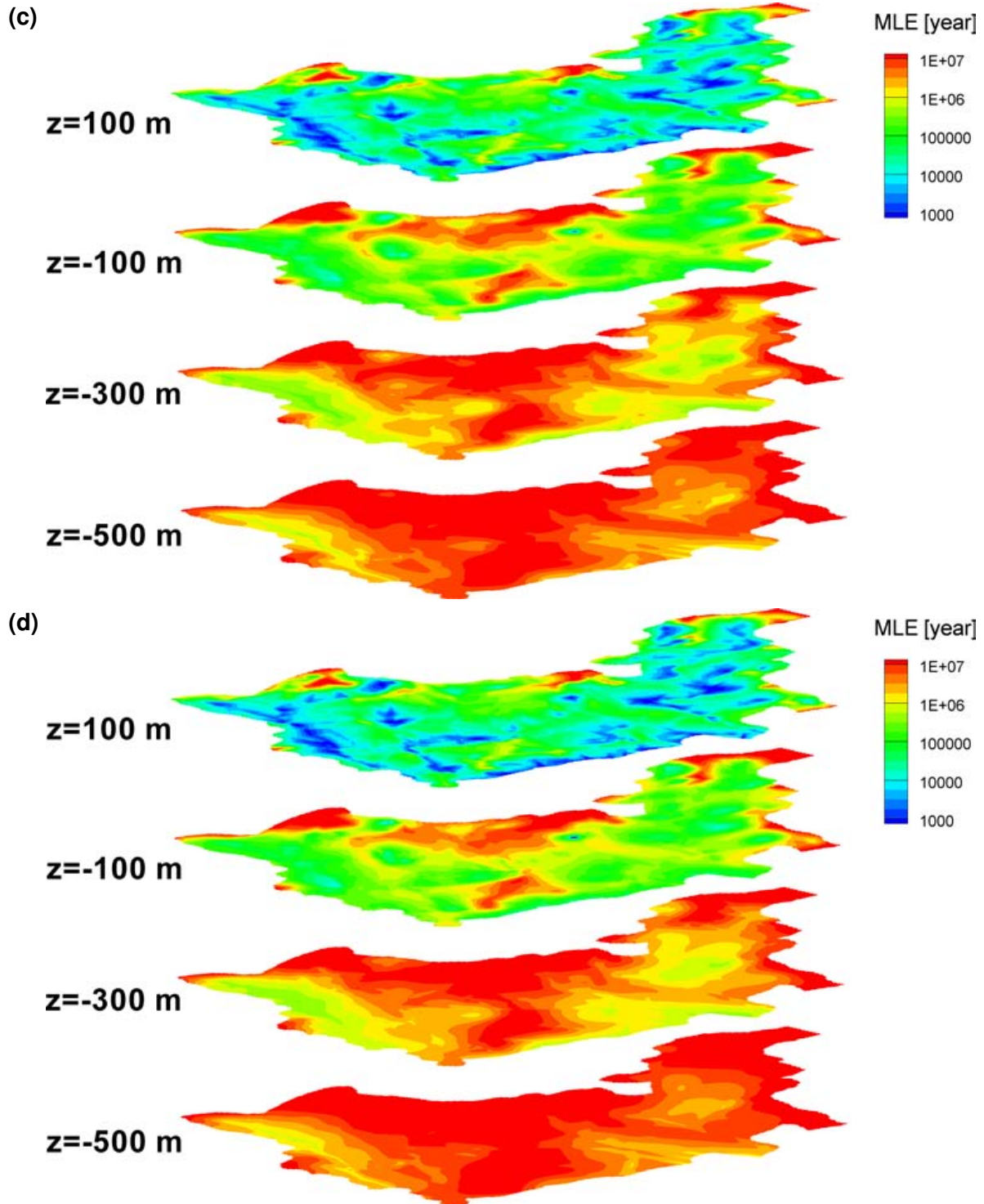


Figure 62: (continued) Mean lifetime expectancy at four elevations in the sub-region with maximum relative brine density of: (a) 1.0, (b) 1.03, (c) 1.1, and (d) 1.2

In Figure 63, an isosurface for  $MLE = 10^6$  years was compared for the cases with and without density effects. The results clearly show that the MLE isosurface with dense brine undulates less than the MLE isosurface without brine effects.

Cumulative frequency plots for MLE with and without density effects are compared in Figure 64. In the shallow elevations, brine effects are negligible but dense brine at deeper locations influences the leading edges of cumulative frequency distributions (smaller MLE in hydraulically more active regions). The aggregate effect of density is to shift the MLE cumulative frequency plots to the right, especially for elevations which contain brine, thereby increasing MLE at that horizon.

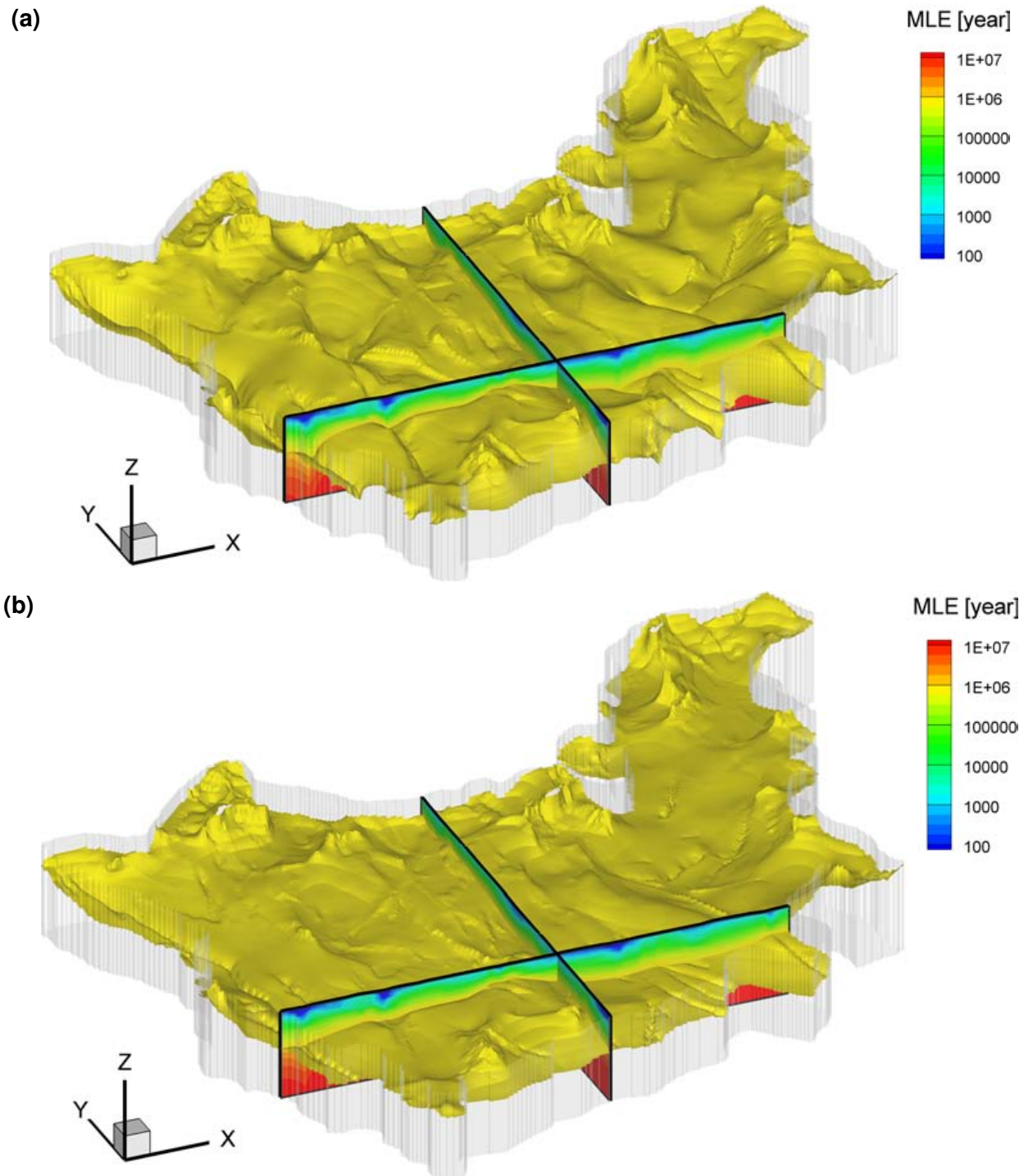


Figure 63: Isosurface for  $10^6$  years of mean lifetime expectancy in the sub-region with maximum relative brine density of: (a) 1.0, and (b) 1.2

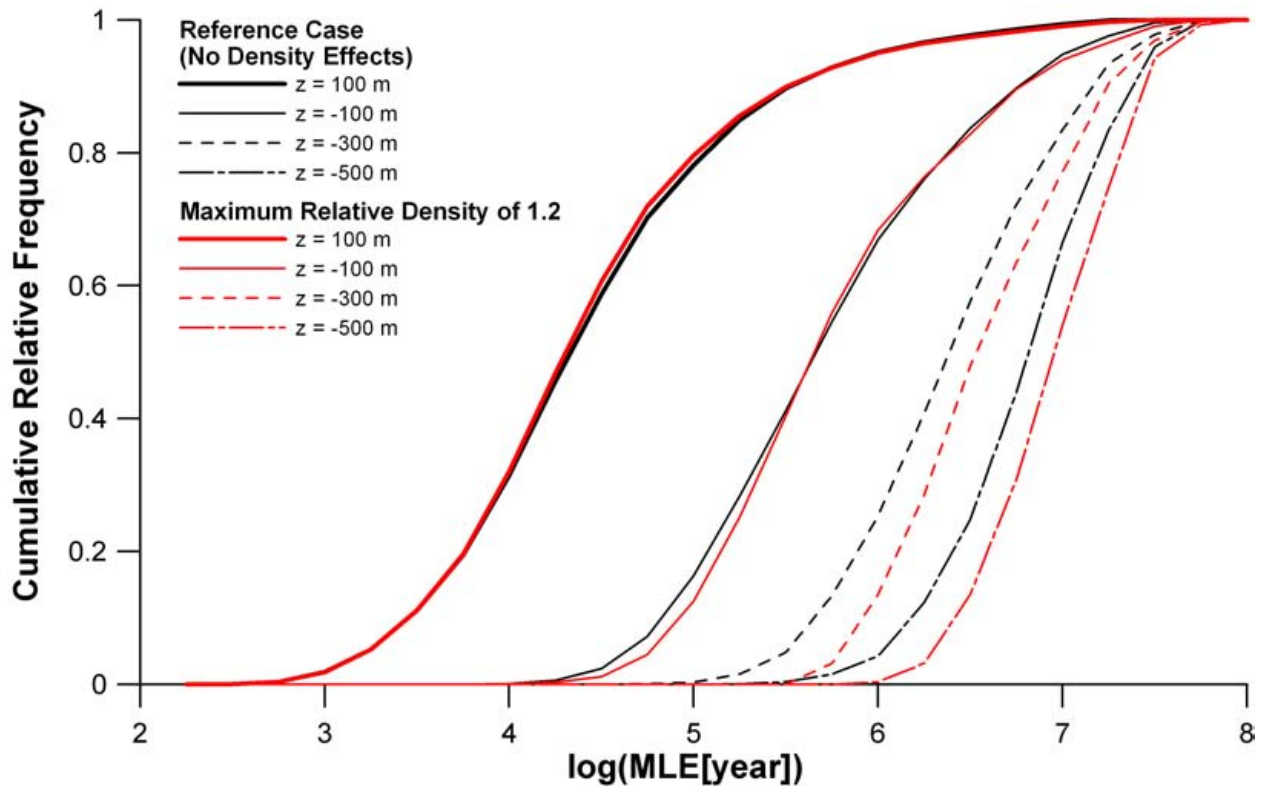


Figure 64: Comparison of cumulative frequency plots for mean lifetime expectancy at four different elevations in the sub-region with (red lines) and without brine effects (black lines)

## 5. SUB-REGIONAL MODEL UNCERTAINTY AND SENSITIVITY ANALYSIS

### 5.1 PARAMETER UNCERTAINTY

It was shown in Chapter 4 that fluid flow and lifetime expectancy can be strongly influenced by the presence of fracture zones. However, it is unlikely that the hydraulic properties of the fracture zones can be completely characterized and thus they, at best, can be characterized statistically to a certain degree (see Chapter 2). In this section, the effects of uncertainties in fracture zone permeability, porosity, and width distributions on groundwater flow and lifetime expectancy are discussed.

#### 5.1.1 Fracture Zone Permeability

Based on the distribution of fracture zone permeability with depth observed at the WRA and Finnish sites (see Figure 7), a statistical model was developed to describe the relationship between fracture zone permeability and depth (see Section 2.5). In order to investigate the effects of fracture zone permeability distributions on a sub-regional groundwater flow system, fluid flow and mean lifetime expectancy were simulated for three different permeability-depth relationships: uniform permeability, deterministic decrease of permeability with depth, and statistical decrease of permeability with depth.

In Figure 11, it was shown that most of the measured fracture zone permeability values range from  $10^{-12} \text{ m}^2$  to  $10^{-15} \text{ m}^2$  at ground surface, decreasing by two to three orders of magnitude at approximately 600 m below ground surface, and become statistically homogeneous, with a range from  $10^{-13} \text{ m}^2$  to  $10^{-18} \text{ m}^2$  at depth. Using the median (50<sup>th</sup> percentile in Figure 11), the permeability is approximately  $10^{-13} \text{ m}^2$  near ground surface, mildly decreases to 200 m below ground surface, rapidly decreases by about three orders of magnitude to 500 m below ground surface, and stabilizes at  $10^{-16} \text{ m}^2$  for the remaining depth to 1600 m. This median relationship between fracture zone permeability and depth (Figure 21) was utilized for the reference simulations in Chapter 4.

In order to compare the case of a uniform fracture permeability ( $k_F$ ) to the reference case, a uniform constant  $k_F$  value of  $10^{-13} \text{ m}^2$  (average  $k_F$  at ground surface) was applied throughout the domain to simulate groundwater flow and mean lifetime expectancy. The resulting Darcy flux and MLE distributions at four different elevations are plotted in Figure 65. Compared to the results from the reference case in Figure 25 and Figure 56, the Darcy flux increased mostly in the fractures, while mean lifetime expectancy decreased both in the fractures and the matrix due to higher  $k_F$  values at depth.

Comparison of the frequency distribution of MLE at four different elevations in Figure 66 to the results in Figure 58 clearly shows the effects of higher  $k_F$  values at depth: MLE distributions shift toward smaller values at all elevations. As the fracture zone permeability contrast with the matrix increases, the MLE frequency plot can become bimodal (see the results at the elevation of -500 masl).

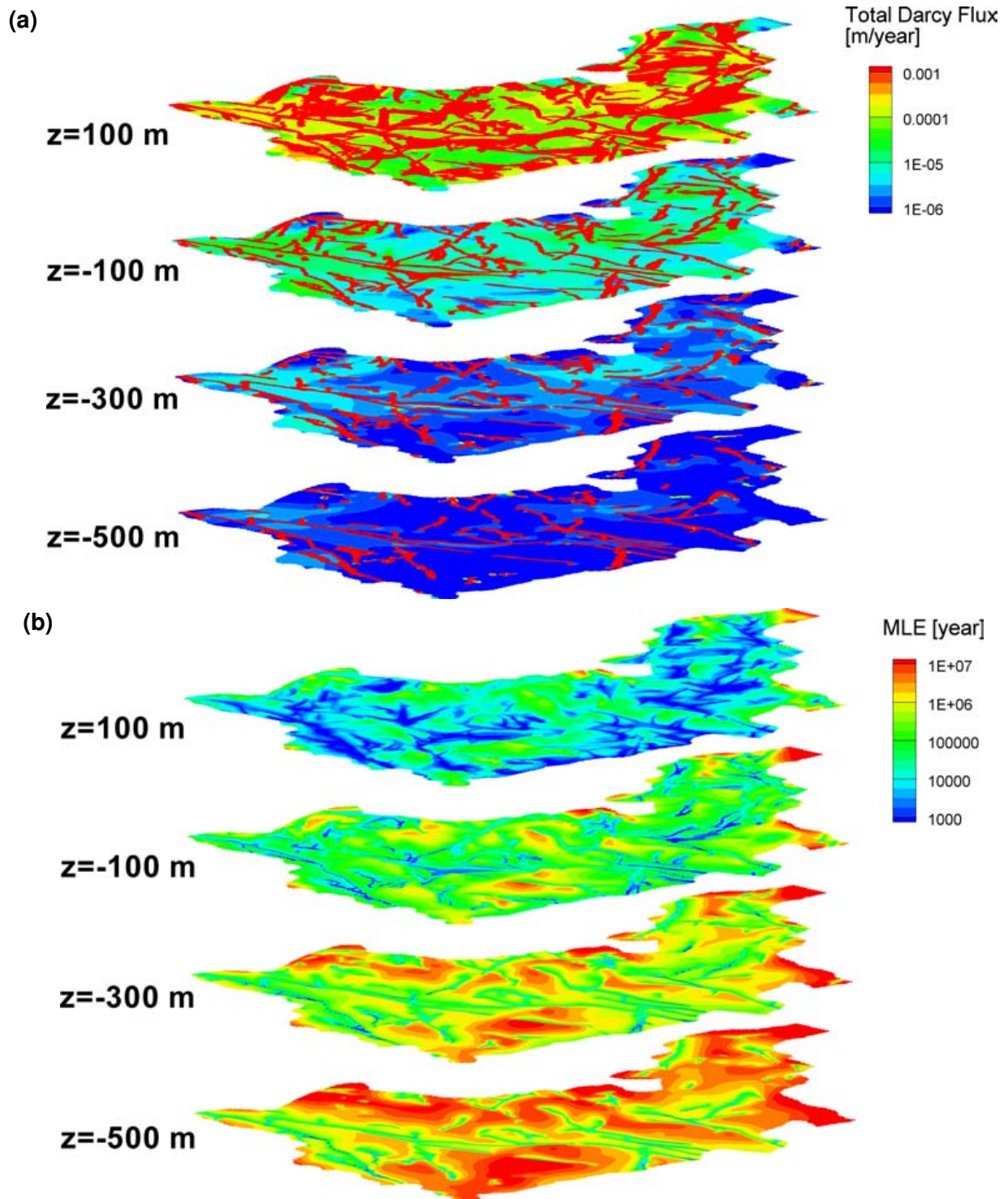
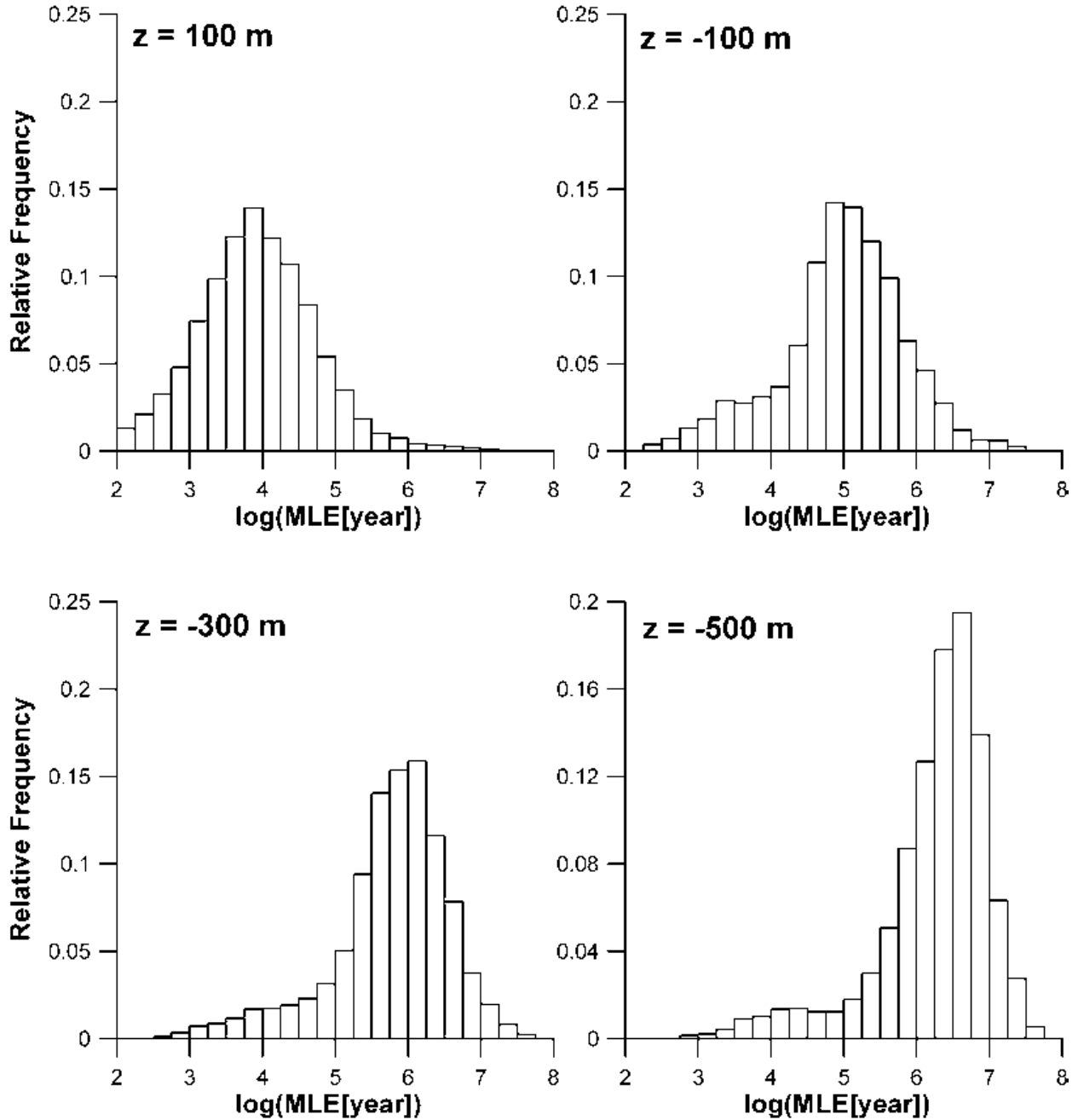


Figure 65: Darcy flux (a) and MLE distributions (b) for  $k_F = 10^{-13} \text{ m}^2$



**Figure 66: Frequency plots for mean lifetime expectancy at four different elevations for  $k_F = 10^{-13} \text{ m}^2$**

In Figure 67, cumulative frequencies for MLE values at four elevations are compared for the reference case and a constant  $k_F$  case. The results indicate that decreasing MLE in fracture zones (stronger leading edges) is accompanied by a decrease of MLE in the matrix.

In order to compare the effects of different  $k_F$  values, three uniform  $k_F$  values were considered for flow and transport simulations:  $10^{-12} \text{ m}^2$ ,  $10^{-14} \text{ m}^2$ , and  $10^{-16} \text{ m}^2$ . Figure 68, Figure 69, and

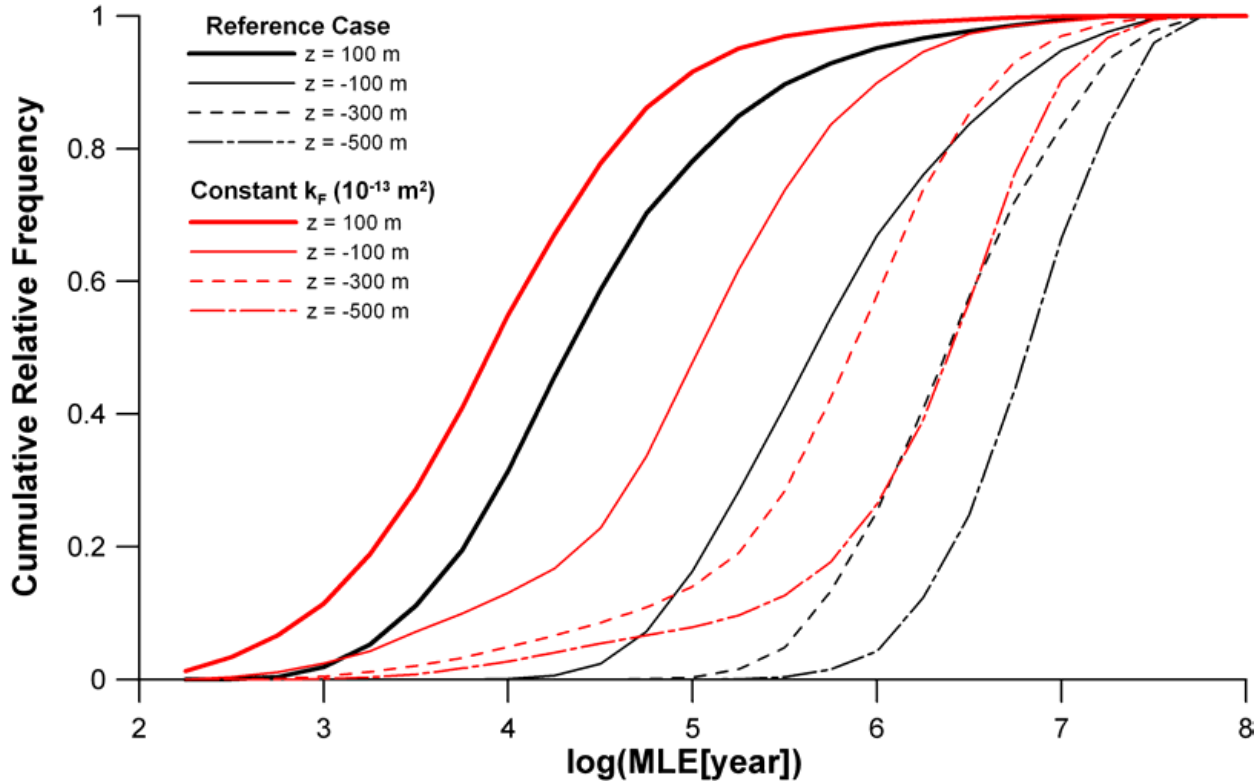


**Figure 67: Comparison of cumulative frequency plots for mean lifetime expectancy at four different elevations: Reference case (black lines) and  $k_F = 10^{-13} \text{ m}^2$  (red lines)**

Figure 70 shows Darcy flux and mean lifetime expectancy distributions for three constant  $k_F$  values. The results show that the Darcy flux near fracture zones becomes smaller as  $k_F$  decreases but the change is relatively minor in the matrix. However, mean lifetime expectancy can be orders of magnitude smaller with higher  $k_F$  values both in the fracture zones and in the matrix.

Cumulative frequencies for MLE values at four elevations are compared for the cases with various uniform  $k_F$  values. Figure 71 shows that the result for  $k_F = 10^{-14} \text{ m}^2$  is most comparable to the result from the reference case at an elevation of 100 masl but for other elevations, the results for  $k_F = 10^{-16} \text{ m}^2$  are most similar to the results for the reference case. We recall that average fracture permeability is about  $10^{-16} \text{ m}^2$  from 500 m below ground surface and it is about  $10^{-14} \text{ m}^2$  at an elevation of 100 masl (Figure 11). The results suggest that mean lifetime expectancy at depth is strongly influenced by changes in fracture zone permeability, but the effects of higher fracture permeability values near surface is relatively minor for MLE values at depth. The factor that appears more important is the permeability of the fracture zone at depth, compared to the variation of permeability in the fracture from near surface to depth.

As shown in Section 2.5, fracture zone permeability is highly variable at any depth and the deterministic average decreasing trend may not be sufficient to capture the characteristics in the observed  $k_F$  distribution in Figure 7. In order to incorporate the observed  $k_F$  distribution with depth in the simulations, the probabilistic model developed in Section 2.5 (Figure 11) was

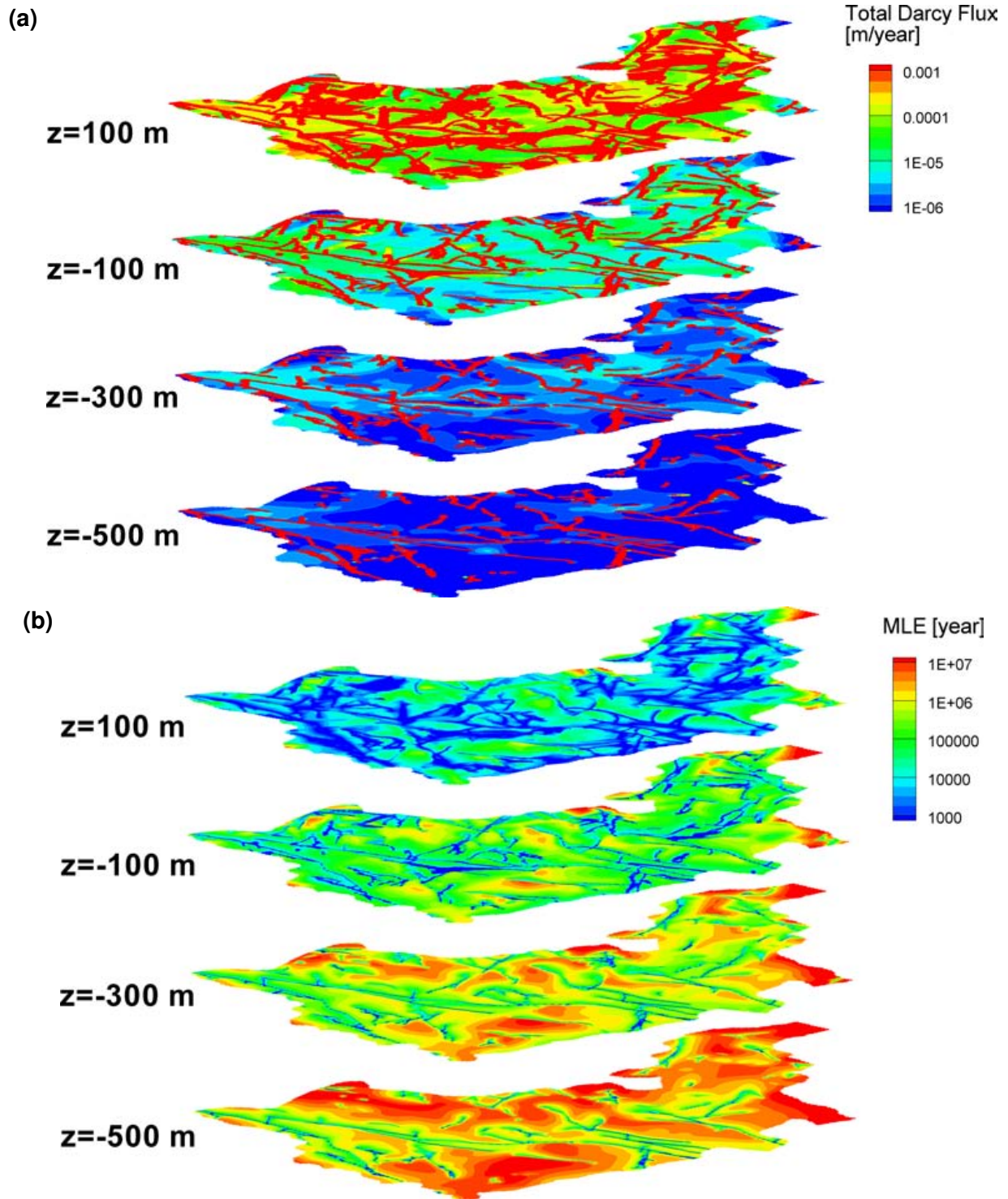


Figure 68: Darcy flux and MLE distributions for  $k_F = 10^{-12} \text{ m}^2$

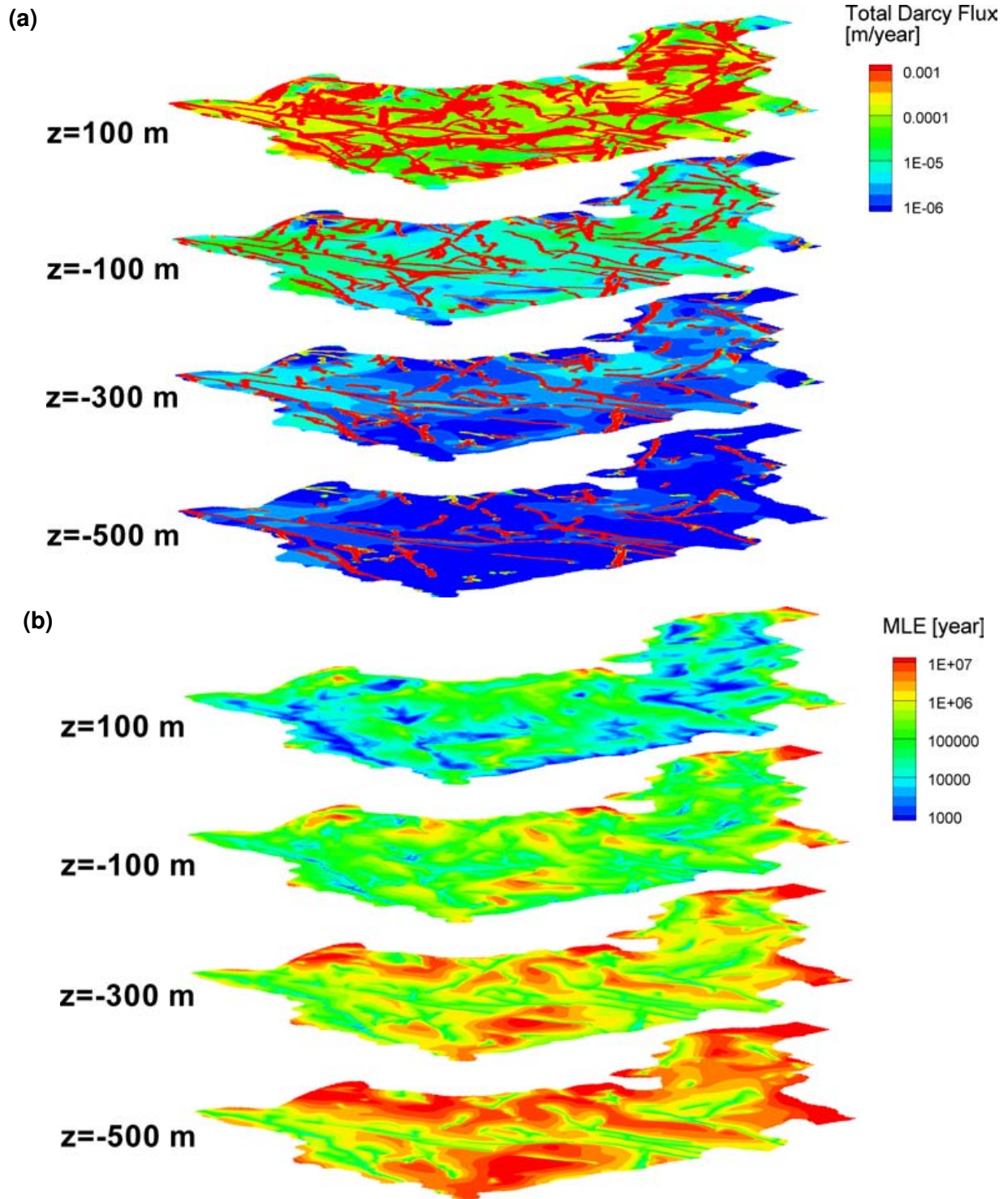


Figure 69: Darcy flux and MLE distributions for  $k_F = 10^{-14} \text{ m}^2$

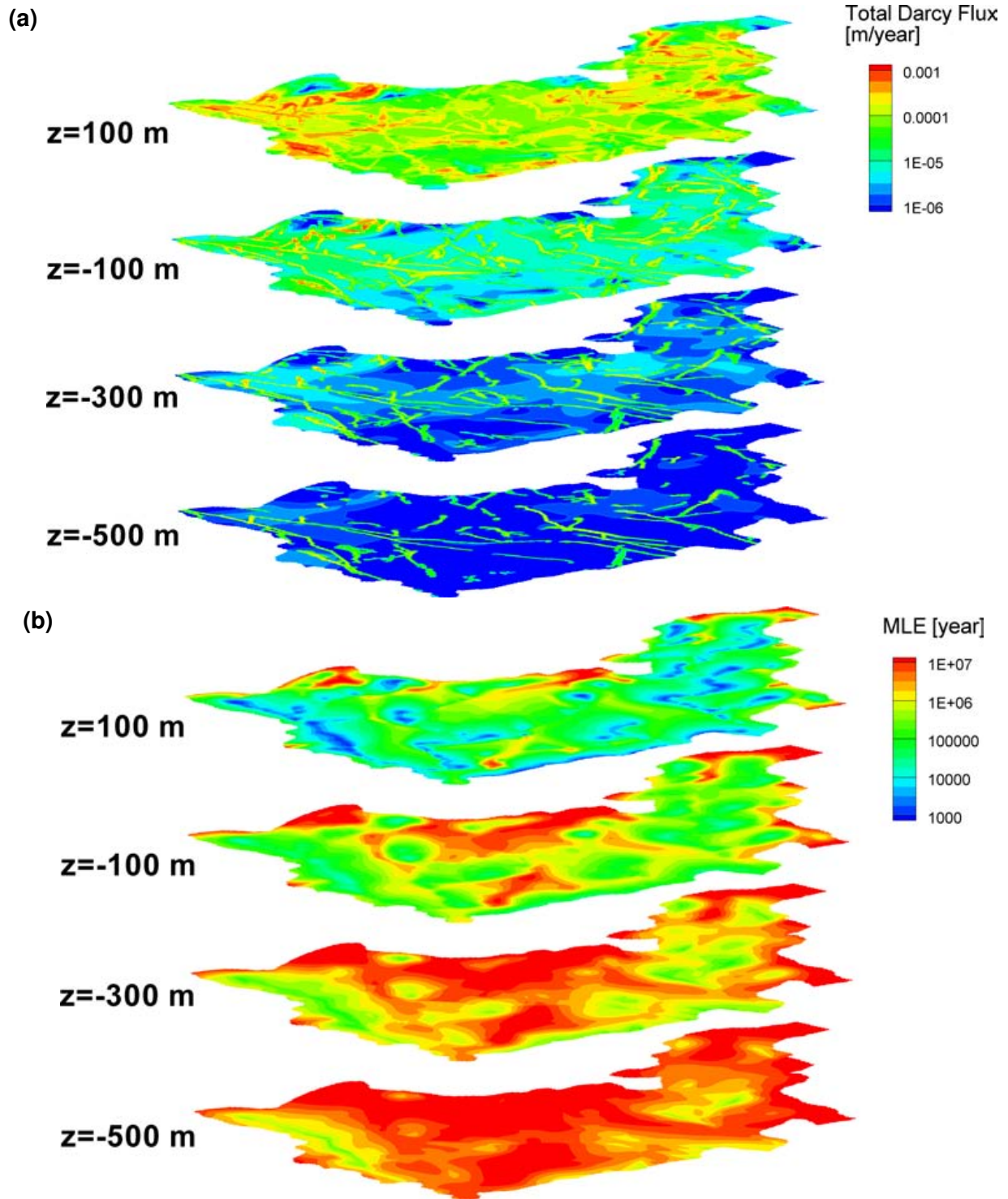
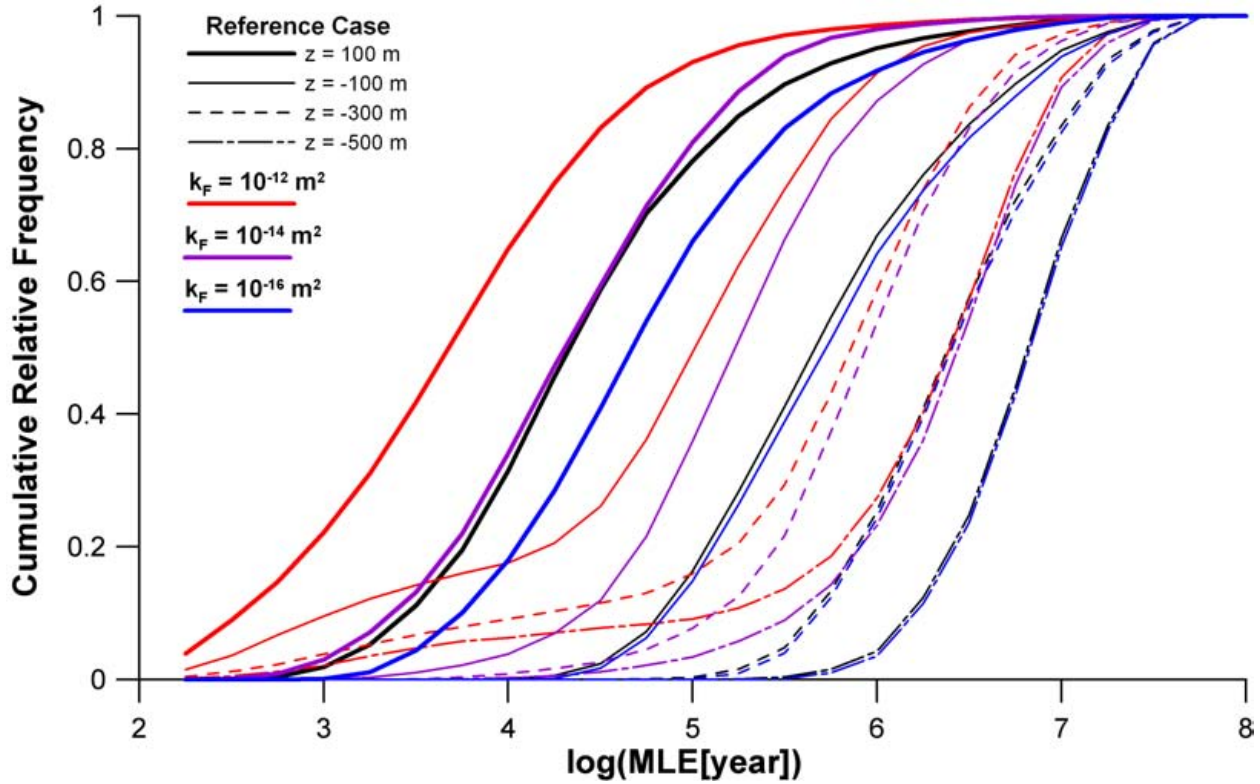


Figure 70: Darcy flux and MLE distributions for  $k_F = 10^{-16} \text{ m}^2$



**Figure 71: Comparison of cumulative frequency plots for mean lifetime expectancy at four different elevations: Reference case (black lines), and  $k_F = 10^{-12} \text{ m}^2$  (red lines),  $k_F = 10^{-14} \text{ m}^2$  (purple lines), and  $k_F = 10^{-16} \text{ m}^2$  (blue lines)**

adapted to assign a different relationship between  $k_F$  and depth for each fracture zone. Each fracture zone follows an  $i^{\text{th}}$  percentile trend for  $k_F$  with a randomly generated  $i$  (see Section 2.5 for detail). Darcy flux and MLE distributions with a probabilistic  $k_F$  model are shown in Figure 72. The results are, in general, comparable to the results for the reference case, but in some major fracture zones, Darcy flux increases while MLE decreases at depth due to the presence of more permeable fracture zones.

In Figure 73, cumulative frequencies for MLE values at four elevations are compared for the reference case and for the case with the probabilistic  $k_F$  distribution. Overall, the effects of a variable  $k_F$  were not significant because the probability of a fracture zone having an extremely high-permeability was not sufficient in this case.

In conclusion, the effects of fracture zone permeability on flow and transport in the sub-regional domain are significant and the fracture zone permeability observed near ground surface, if assumed to be representative throughout the entire depth of the model, can significantly overestimate fluid flow and MLE in both fracture zones and the adjacent matrix. The influence of the variability in fracture zone permeability was minor for the sub-regional domain, but it could become significant if the probability of having extremely high permeability fracture zones at depth increases compared to the model in Figure 11.

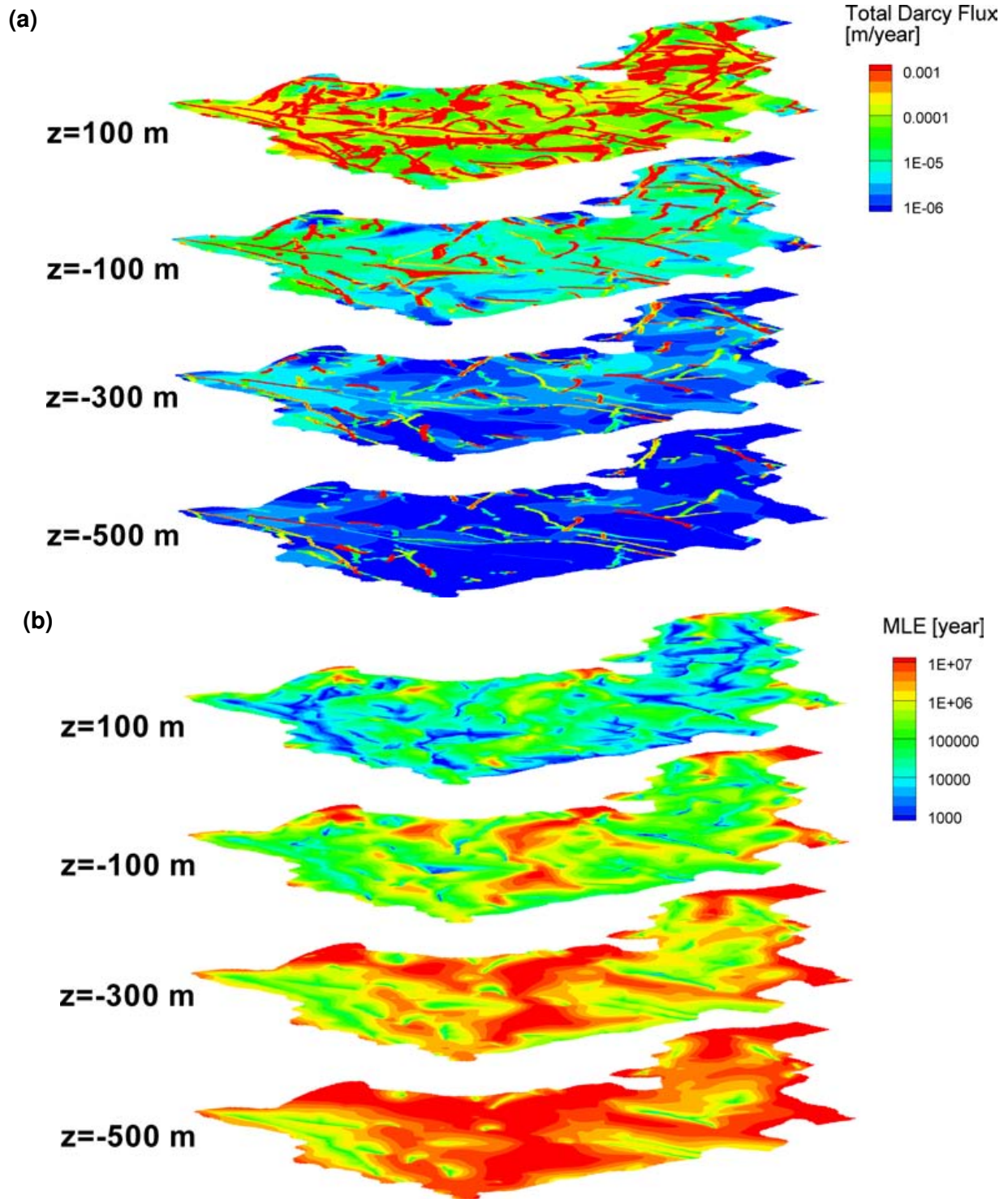
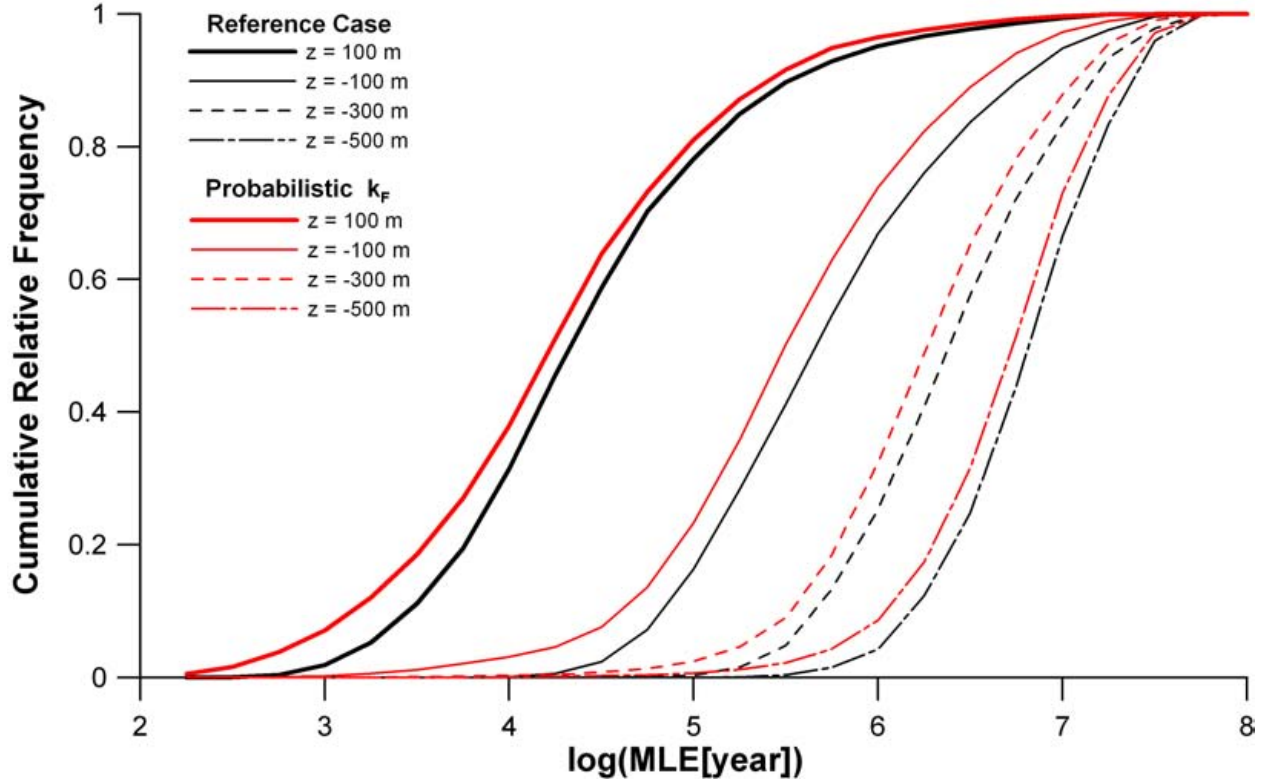


Figure 72: Darcy flux and MLE distributions with probabilistic  $k_F$  and depth relationship



**Figure 73: Comparison of cumulative frequency plots for mean lifetime expectancy at four different elevations: Reference case (black lines) and a probabilistic  $k_F$  distribution (red lines)**

### 5.1.2 Fracture Zone Porosity

Bulk porosity in a fracture zone ( $\phi_F^{bulk}$ ) can be represented as a function of fracture zone permeability ( $k_F$ ) with a set of assumptions as presented in Equation (10) where bulk porosity increases as a fracture zone becomes more permeable and its lower limit is given by matrix porosity (0.3% for the sub-regional domain). With a fracture frequency of  $10 \text{ m}^{-1}$ , porosity ranged from 0.32% to 0.56% for the permeability values in the reference case ( $10^{-13} \text{ m}^2 - 10^{-16} \text{ m}^2$ ). Although the fracture zone porosity change is not significant for a given permeability and porosity relationship, it can be higher in some fracture zones, depending on their origin. In order to investigate the effects of fracture zone porosity on fluid flow and solute transport in the sub-region, MLE was simulated with constant  $\phi_F^{bulk}$  values of 0.3% and 3% (as lower and upper limits), but using the same  $k_F$  as the reference case (Figure 74). Note that porosity does not influence fluid flux, however, it does affect fluid velocity. The results in Figure 74 show that the effects of a change in fracture zone porosity on MLE distribution is relatively minor both in fracture zones and matrix domain. It was shown in Section 3.3.5 that MLE in a fracture zone ( $E_f$ ) is given as  $z/2bq_f(n_mL + 2bn_f)$  and if the fluid volume in the matrix is much larger than the volume in the fracture ( $n_mL \gg 2bn_f$ ), then the influence of fracture zone porosity ( $n_f$ ) on lifetime expectancy is negligible for a given Darcy flux  $q_f$ . MLE in the matrix domain is determined by the effective diffusion coefficient and the MLE distribution in the fracture zones (see Equation (39)), and thus, the influence of fracture zone porosity on MLE within the matrix is insignificant in this case.

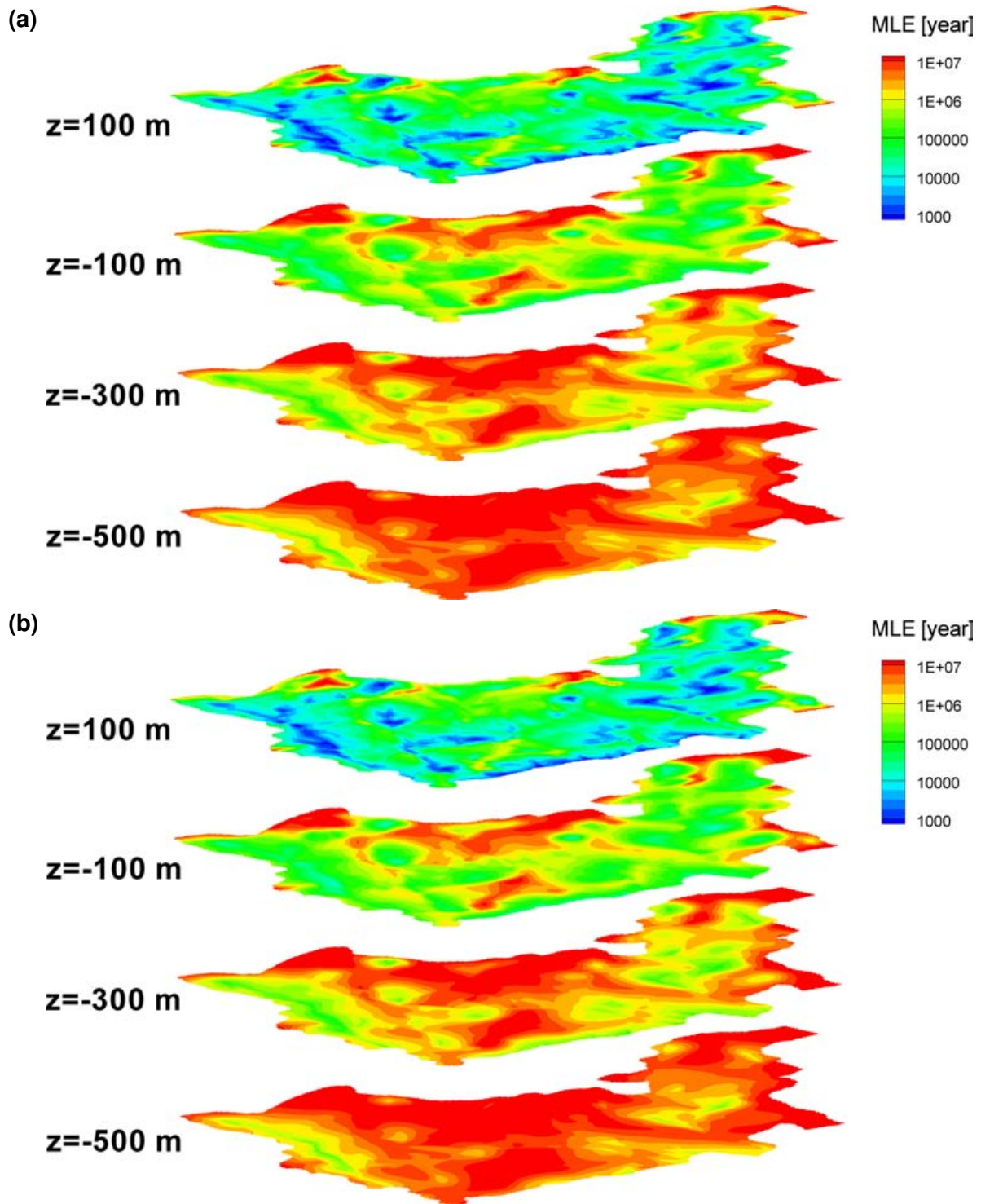


Figure 74: MLE distributions for constant fracture zone porosity of (a) 0.3%, and (b) 3%

Comparison of cumulative frequencies for MLE values at four elevations confirms that fracture zone porosity is insignificant for MLE at all depths (Figure 75).

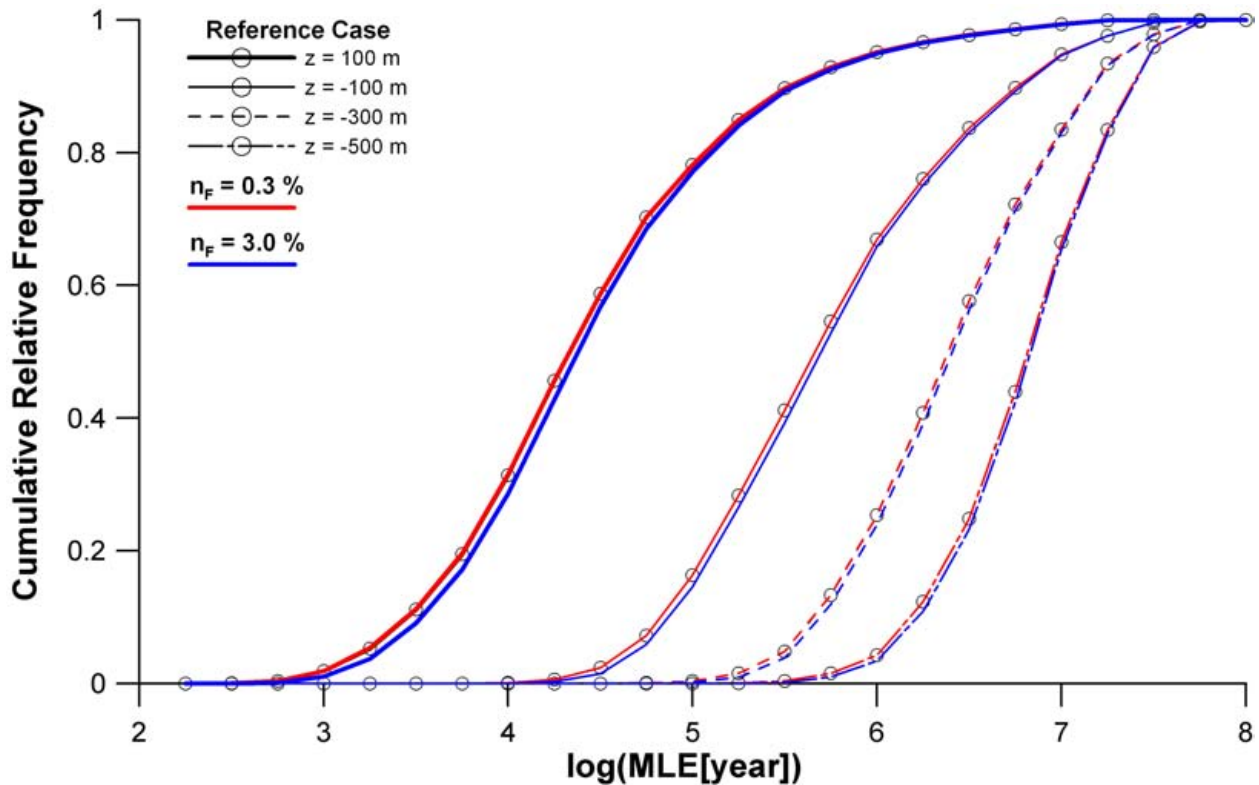


Figure 75: Comparison of cumulative frequency plots for mean lifetime expectancy at four different elevations: Reference case (circles), and uniform fracture zone porosity ( $n_F$ ) of 0.3% (red lines) and 3.0% (blue lines)

In conclusion, the effects of fracture zone porosity on MLE distribution in the sub-region are negligible compared to the effects of fracture zone permeability since the fluid volume in the matrix is much larger than that in the fracture zones. Fracture zone porosity can be an important factor only when the volume fraction of fracture zones is comparable to the matrix volume fraction.

### 5.1.3 Fracture Zone Width

Fracture zone width observed at the WRA follows a log-normal distribution (Figure 15), with a mean and standard deviation of 3.27 m and 0.483 m, respectively. This distribution was used in the reference case as illustrated in Figure 23. Uniform fracture zone widths of 1 m and 10 m, as two end member cases, were used to check the sensitivity on flow and transport, keeping other parameters the same as the reference case. Comparing the results in Figure 76 and Figure 77 shows that an increase in uniform fracture zone width from 1 m to 10 m can reduce the lifetime expectancy in fracture zones and influence the MLE distribution in the matrix blocks, because an

increase in fracture zone width by an order of magnitude has a similar influence as an order of magnitude increase in fracture zone permeability and volume fraction.

Comparison of cumulative frequencies shows that MLE at all depths can be influenced by a change in fracture zone width (Figure 78).

In conclusion, fracture zone width, in general, is a significant factor for MLE distribution as it can increase or decrease transmissivity of fracture zones. However, since fracture zone width was observed to vary only within an order of magnitude at the WRA site (as a typical Canadian Shield environment), the effects of fracture zone width variability on the MLE is relatively less significant in the sub-region, as compared to the effects of variability in fracture zone permeability.

#### 5.1.4 Diffusion and Tortuosity

Hydrodynamic dispersion includes molecular diffusion and mechanical dispersion as defined by Bear (1988) and presented in Equation (20). Diffusive flux of solute ( $q_{diff}$ ) in saturated porous media follows Fick's law as:

$$(q_{diff})_i = \phi \tau D_{free} \delta_{ij} \frac{\partial C}{\partial x_j} = \phi D_e \delta_{ij} \frac{\partial C}{\partial x_j} \quad (48)$$

where  $D_e$  is the effective diffusion coefficient defined as  $\tau D_{free}$ . The free solution diffusion coefficient  $D_{free}$  is assumed to be constant for a given solute species and the tortuosity is a medium property, representing the ratio of diffusion paths in a porous medium to those paths in free solution.

Diffusion is considered to be a relatively slower process compared to advection and mechanical dispersion in hydraulically active environments. However, in deep subsurface crystalline environments such as in the Canadian Shield, groundwater flow is extremely slow and thus long-term transport is likely to be diffusion-dominated.

In order to investigate the effects of diffusion, mean lifetime expectancy was simulated in the sub-region, by increasing or decreasing the effective diffusion coefficient by an order of magnitude. In the reference simulation,  $D_e$  was assumed to be about  $2.3 \times 10^{-10} \text{ m}^2/\text{sec}$  or  $D_{free} = 2.0 \text{ cm}^2/\text{day}$  with  $\tau = 0.1$ . Compared to the results for the reference case in Figure 56, the influence of increased tortuosity was remarkable, as shown in Figure 79: at shallower depths, the effects of increased effective diffusion was relatively insignificant as the transport is dominated by advection and mechanical dispersion, while at deeper elevations ( $z < -100 \text{ m}$ ), the MLE decreases notably and becomes more uniform, and fracture zones are less noticeable, because diffusion is the dominant transport process.

To further illustrate the effect of different tortuosities, and hence, effective diffusion coefficients on the sub-region, cumulative frequencies for MLE values at four elevations are shown in Figure 80, comparing the reference case and the cases with different tortuosity values. It is clear that the effects of lowering tortuosity (e.g.,  $\tau = 0.01$ ) on MLE distributions is relatively insignificant, but higher tortuosity has a significant influence on MLE distributions at greater depths: (1) more uniform MLE at depth with less variation characterized by steeper, narrower curves; and (2) a general decrease in MLE, particularly at greater depths.

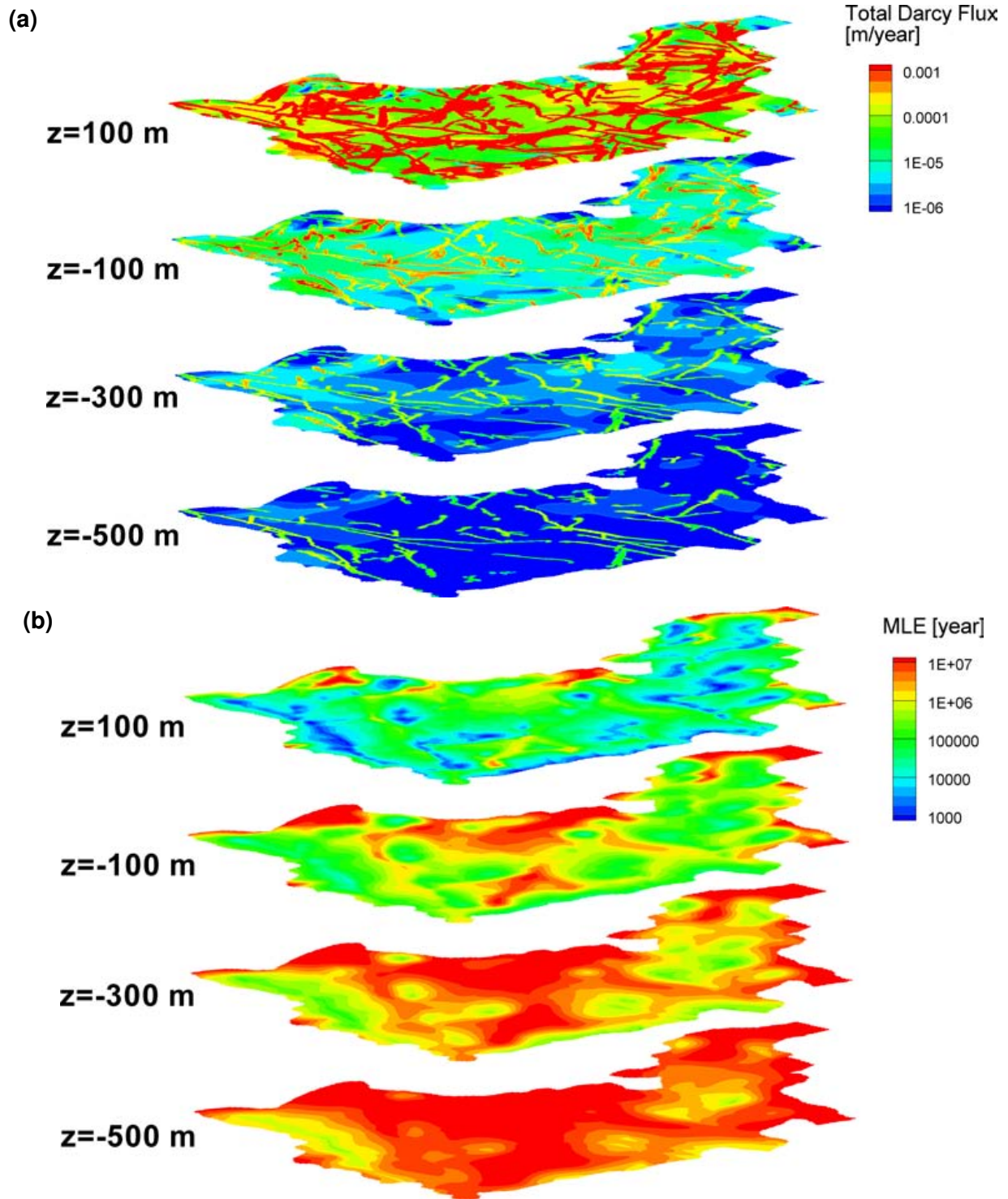


Figure 76: Darcy flux and MLE distributions for a fracture zone width of 1 m

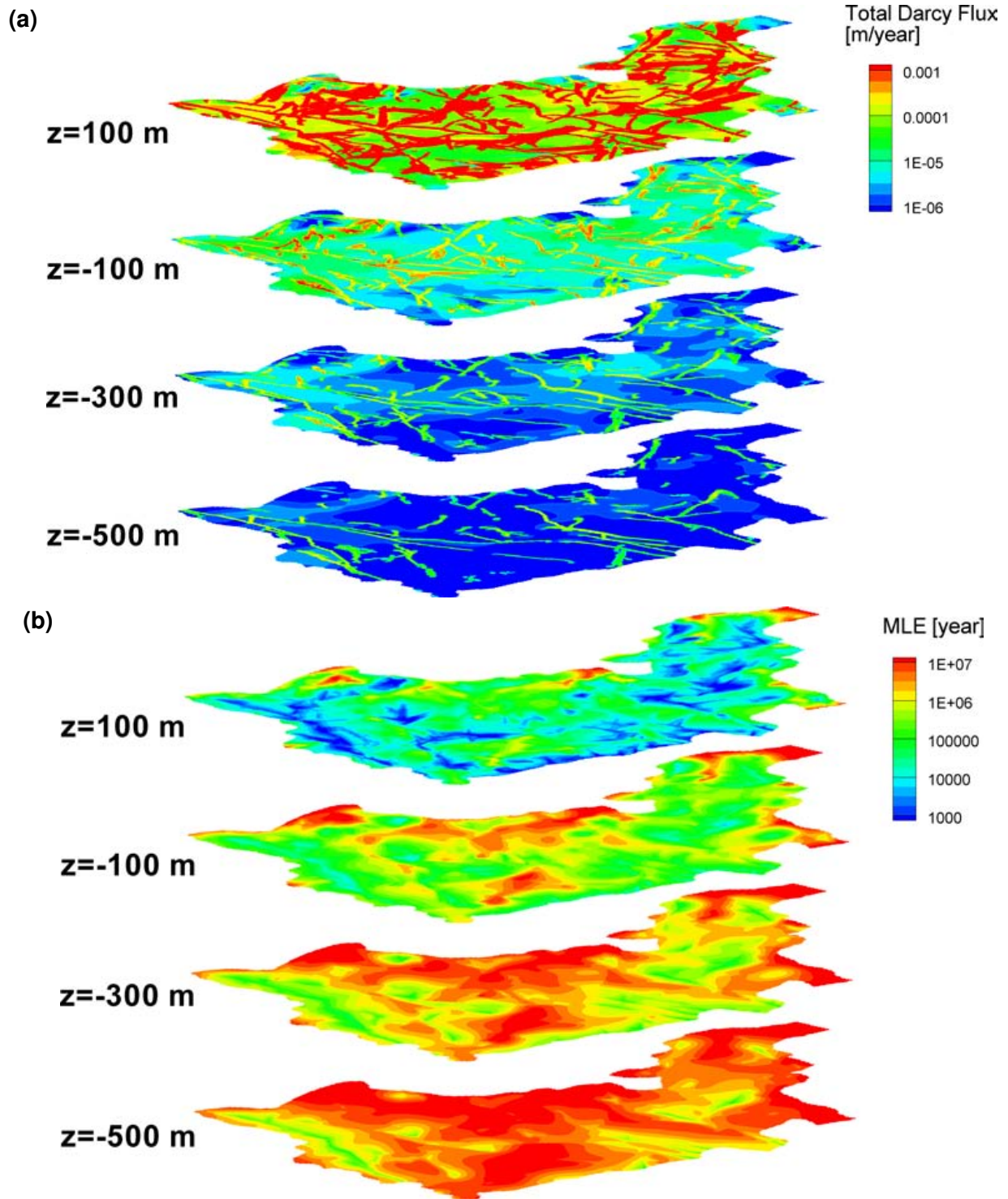
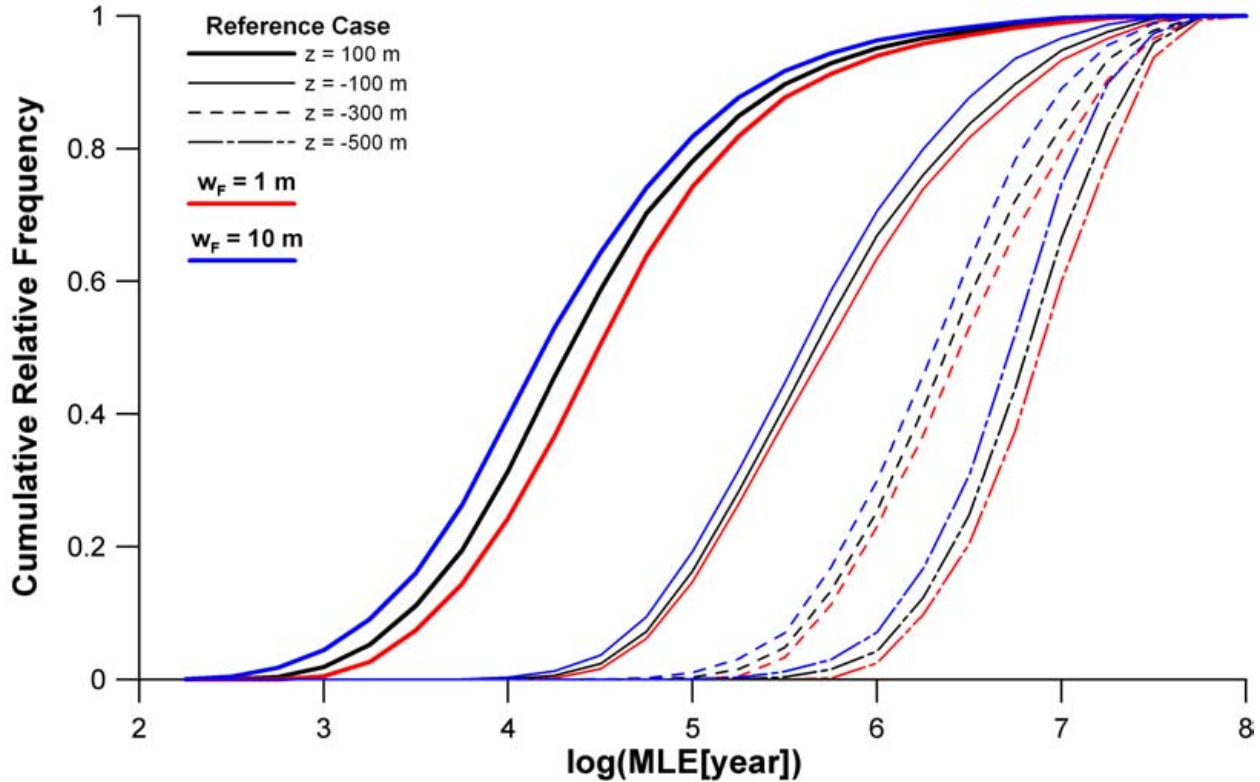


Figure 77: Darcy flux and MLE distributions for a fracture zone width of 10 m



**Figure 78: Comparison of cumulative frequency plots for mean lifetime expectancy at four different elevations: Reference case (black lines) and uniform fracture zone widths ( $w_F$ ) of 1 m (red lines) and 10 m (blue lines)**

When the diffusion path has a directional preference and is anisotropic, the scalar  $\tau$  in Equation (48) can be replaced by a tortuosity tensor  $\tau_{ij}$ . As shown in Figure 80, solute transport is diffusion-dominant in deep crystalline rock settings; as such, effective diffusion characteristics need to be better understood than for shallower, hydraulically active regions.

## 5.2 FRACTURE ZONE NETWORK GEOMETRY

Srivastava (2002) developed a discrete fracture network model, which provides geostatistical tools for the probabilistic simulation of the propagation of surface lineaments to depth in order to build geologically and geomechanically plausible fracture networks that honour the type of information typically available from a non-invasive Site Characterization stage. The model utilizes such information as the surface expression of some of the fractures, which manifest themselves as lineaments on aerial photographs and remote sensing images, statistics on fracture density and length distributions, general structural geology principles that describe the down-dip behaviour of fractures, and truncation rules that come from regional tectonic considerations and geology. When applied to the sub-regional domain, additional surface lineaments were created to account for the extension of existing major lineaments, and to increase the fracture density in areas where overburden cover would have obscured the surface lineaments or where aerial photographs had weak contrast.

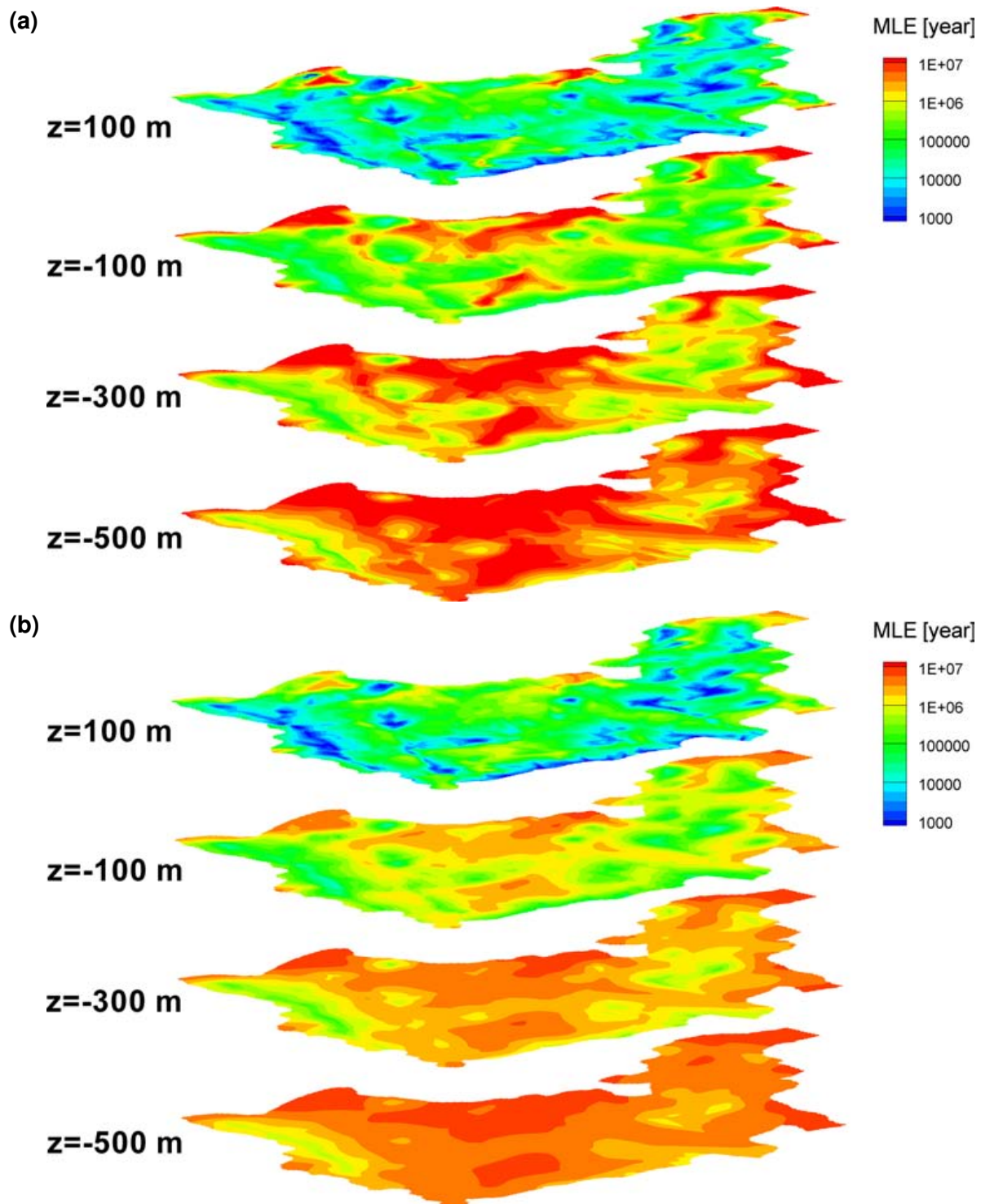
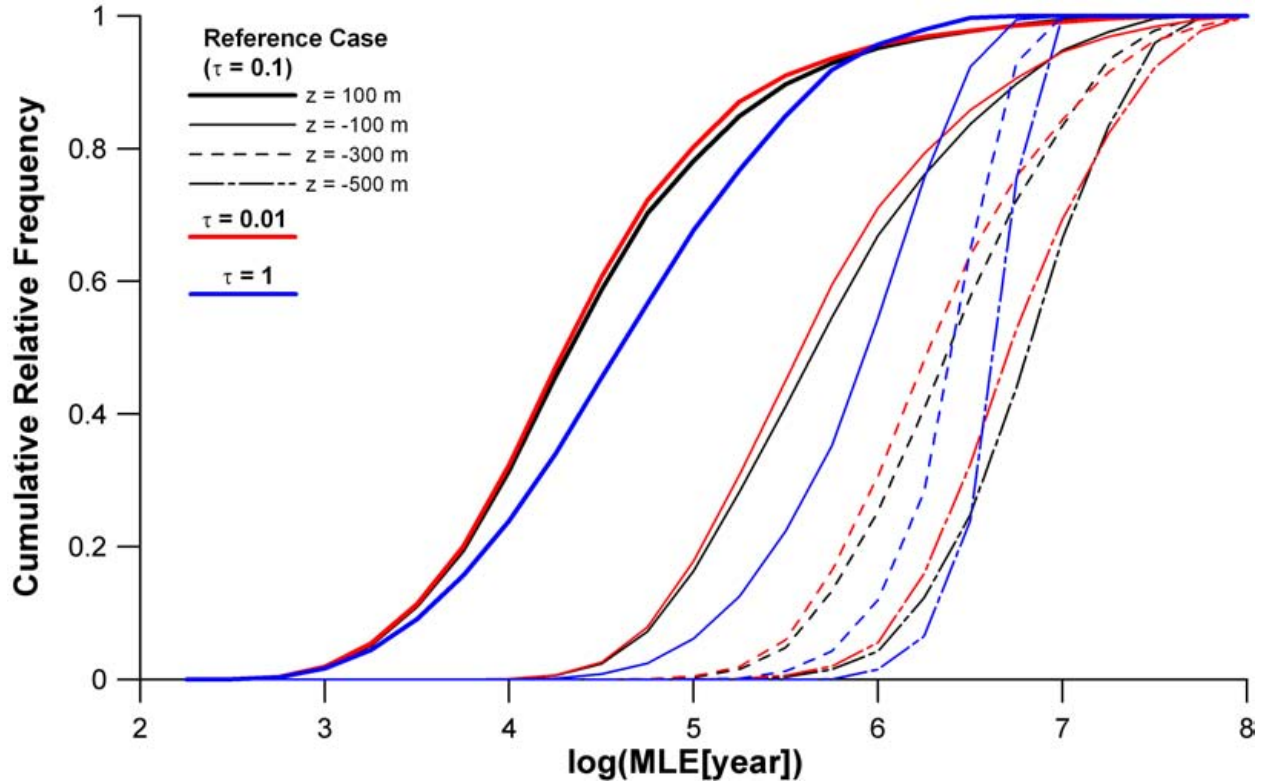


Figure 79: MLE Distributions for Different Tortuosity Values of (a) 0.01 and (b) 1



**Figure 80: Comparison of cumulative frequency plots for mean lifetime expectancy at four different depths: Reference case (black lines) and tortuosity values of 0.01 (red lines) and 1.0 (blue lines)**

The curve-planar fracture networks, developed by Srivastava (2002), were mapped onto orthogonal faces of brick elements as permeable two-dimensional planes (Therrien et al., 2004). Fracture planes mapped onto elemental faces can accommodate both the dip and orientation of original curve-planar fractures in the scale under consideration, despite their stepped nature (Sykes et al., 2004).

The fracture zone network model developed by Srivastava (2002) utilizes statistical tools for downward propagation of surface lineaments according to geological and geomechanical principles. Due to its probabilistic nature, an infinite number of equally probable fracture zone networks can be generated for given surface lineaments. In addition, a certain number of random surface features are generated to accommodate a given fracture density, resulting in generated subsurface fracture zone geometries that reflect greater uncertainty.

In this study, 100 equally probable fracture zone networks were used to analyze the statistics and uncertainty in groundwater flow and solute transport associated with the uncertainty in fracture zone geometry.

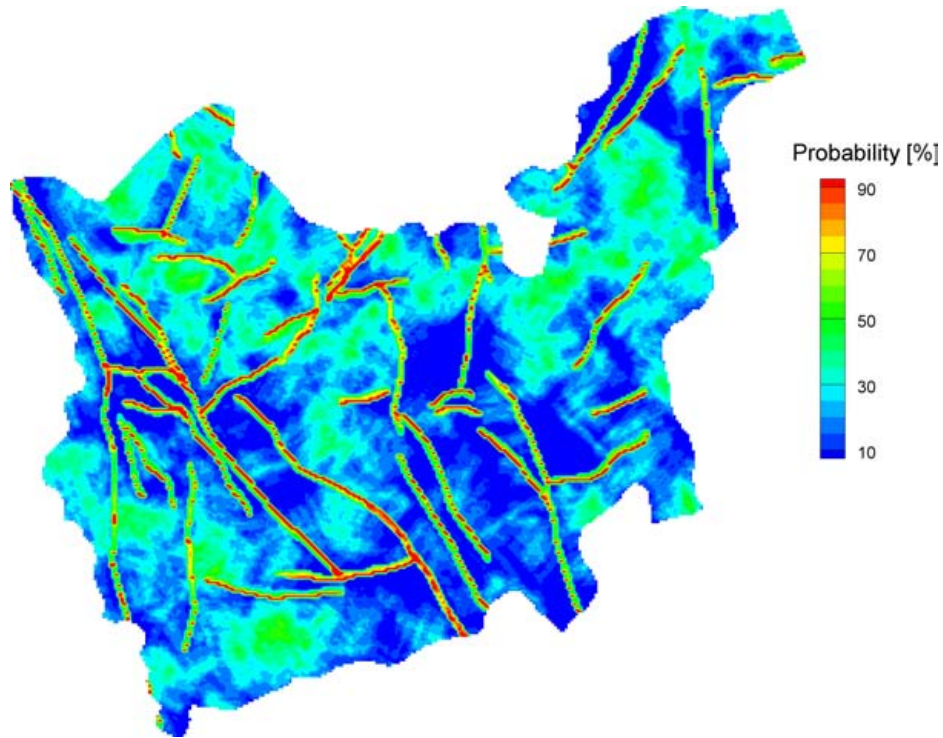


**Figure 81: Fracture zone probability at ground surface**

### 5.2.1 Probabilistic Characteristics

The existence and location of a fracture zone is inevitably uncertain at depth, even though the model can honour surface observations and incorporate geological and geomechanical principles for downward propagation of surface lineaments. As fracture zones either observed or generated at the ground surface propagate to the subsurface, the probability of a given point belonging to a fracture zone (fracture zone probability,  $Pr_F$ ) itself propagates from ground surface to depth (see Figure 81 and Figure 82).

The results show that major fracture zones observed at ground surface are propagated to the bottom of the domain with a slight probabilistic variation in their dip-angles, but most intermediate fracture zones generated from surface lineaments typically propagate downward only a few hundred metres, to an elevation near sea level (see Figure 83). The existence of a fracture zone at a certain point follows a binomial distribution with a mean of  $Pr_F$  and a variance of  $Pr_F(1 - Pr_F)$  and thus, the geometrical uncertainty is maximized when  $Pr_F = 0.5$  (green in Figure 81, Figure 82, and Figure 83) and minimized when  $Pr_F$  approaches 0 or 1 (blue and red in Figure 81, Figure 82, and Figure 83). Geometrical uncertainty increases due to the randomly generated intermediate fracture zones near ground surface, but at depth, a greater proportion of the uncertainty originates from the probabilistic propagation of fracture zones to depth and the uncertainty is therefore greatest near major fracture zones.

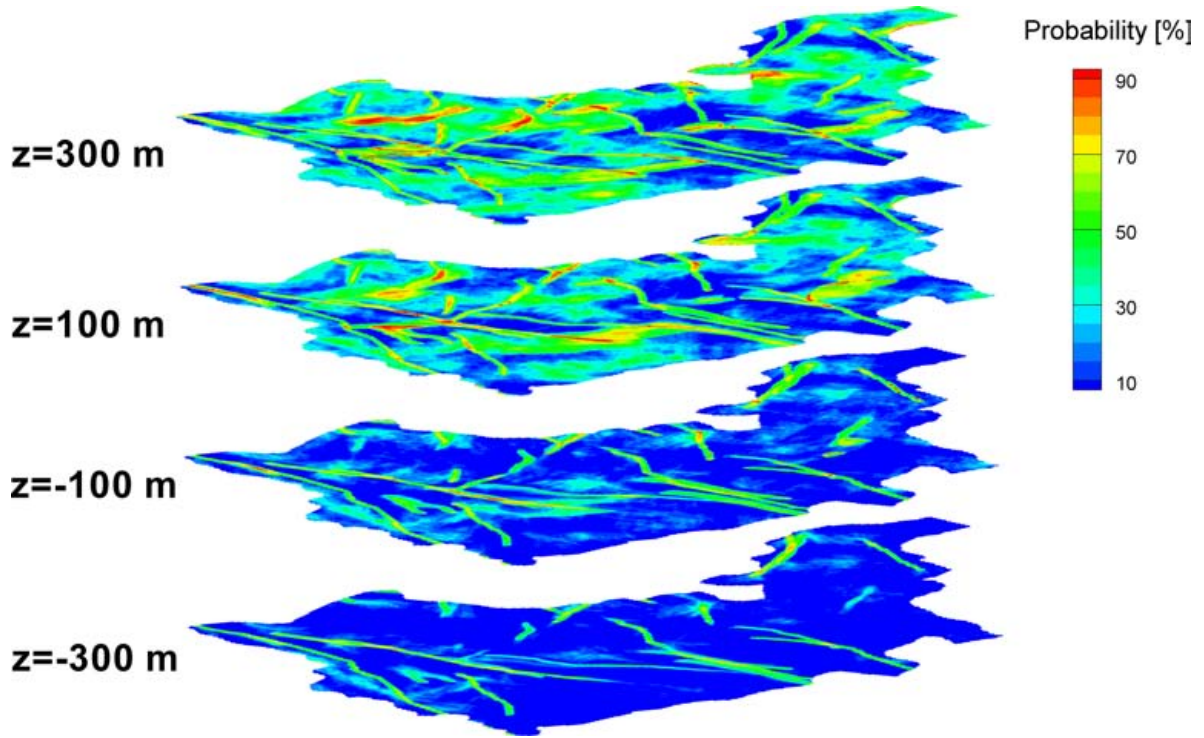


Figure 82: Propagation of fracture zone probability with depth

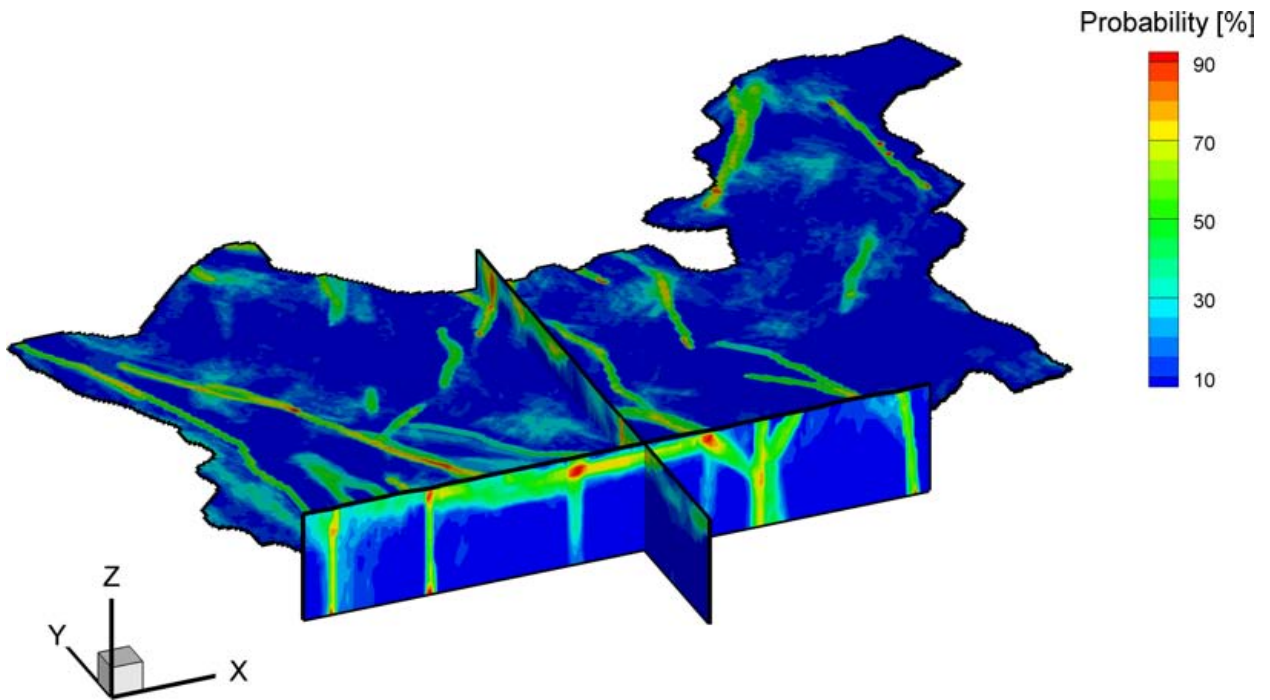


Figure 83: Fracture zone probability in the subsurface. Plane elevation at  $-200\text{ masl}$

## 5.2.2 Effects on Groundwater Flow

Steady-state groundwater flow was simulated for 100 fracture zone network realizations with the same fracture zone hydraulic properties and boundary conditions used in the reference simulation discussed in Section 4.1. With 100 simulations, 100 head values at each node and 100 Darcy flux values in each element were obtained. Statistical properties for 100 values at nodes and elements can be calculated using parametric or non-parametric methods. For example, arithmetic or geometric mean and standard deviation are parametric statistics while median, midrange, or quartiles are non-parametric statistics. These various statistical measures are investigated to determine which measures best characterize the model output of interest.

Figure 84 shows the distribution of mean and standard deviation for 100 head values at each node computed for 100 fracture zone network realizations. Mean head distribution in Figure 84a is similar to the result obtained from a single realization (Figure 24) and scattering from the mean is not significant because the mean ranges from 350 m to 420 m and the deviation is less than 1 m for most of the domain.

Figure 85 shows the distribution of median and quartile deviations for the same data used for Figure 84. As most head values are distributed near the mean value, median and quartile deviation distributions are similar to mean and standard deviation distributions.

Four different representative statistics for 100 Darcy flux values in each element are computed and compared at four different elevations: arithmetic and geometric means, median, and midrange (Figure 86). Note that the median statistic is least dependent on outliers and the midrange is most dependent on them. The results indicate that all four representative statistics have similar values but the midrange differs to a greater extent than the other statistics, possibly due to mild outliers. The midrange is also a more robust estimator since it is the average of Q1 and Q3, comprising two non-parametric estimators.

Variation or uncertainty of the representative statistics can be measured by standard deviation, quartile deviation, or half-range (Figure 87). Similar to representative statistics, quartile deviation is least dependent on outliers and half-range is most influenced by outliers. Figure 87d shows that half-range is more uniformly distributed in depth than the other statistics, as the highest flux values at each node could be more uniform. The results indicate that the standard deviation in log-scale is independent from the magnitude of the flux value and is less dependent on depth, while the other variational measures are strongly dependent on depth since the flux decreases with depth.

Measures of variation such as standard deviation or quartile deviation are strongly dependent on the magnitude of the representative statistics. Coefficient of variation or quartile variation coefficient are scale-independent and measures the relative degree of scattering. Figure 88 shows the distribution of these two relative uncertainty measures. The results indicate that the relative uncertainty is higher at shallower depth and becomes highest near major fracture zones at any depth. This can be compared to Figure 82 which shows the probability of fracture zone intersection. The quartile coefficient of variation is preferred since it is non-parametric and is a more robust estimator of the variance as compared to using parametric statistics, which require that the data are distributed according to a particular probability density function.

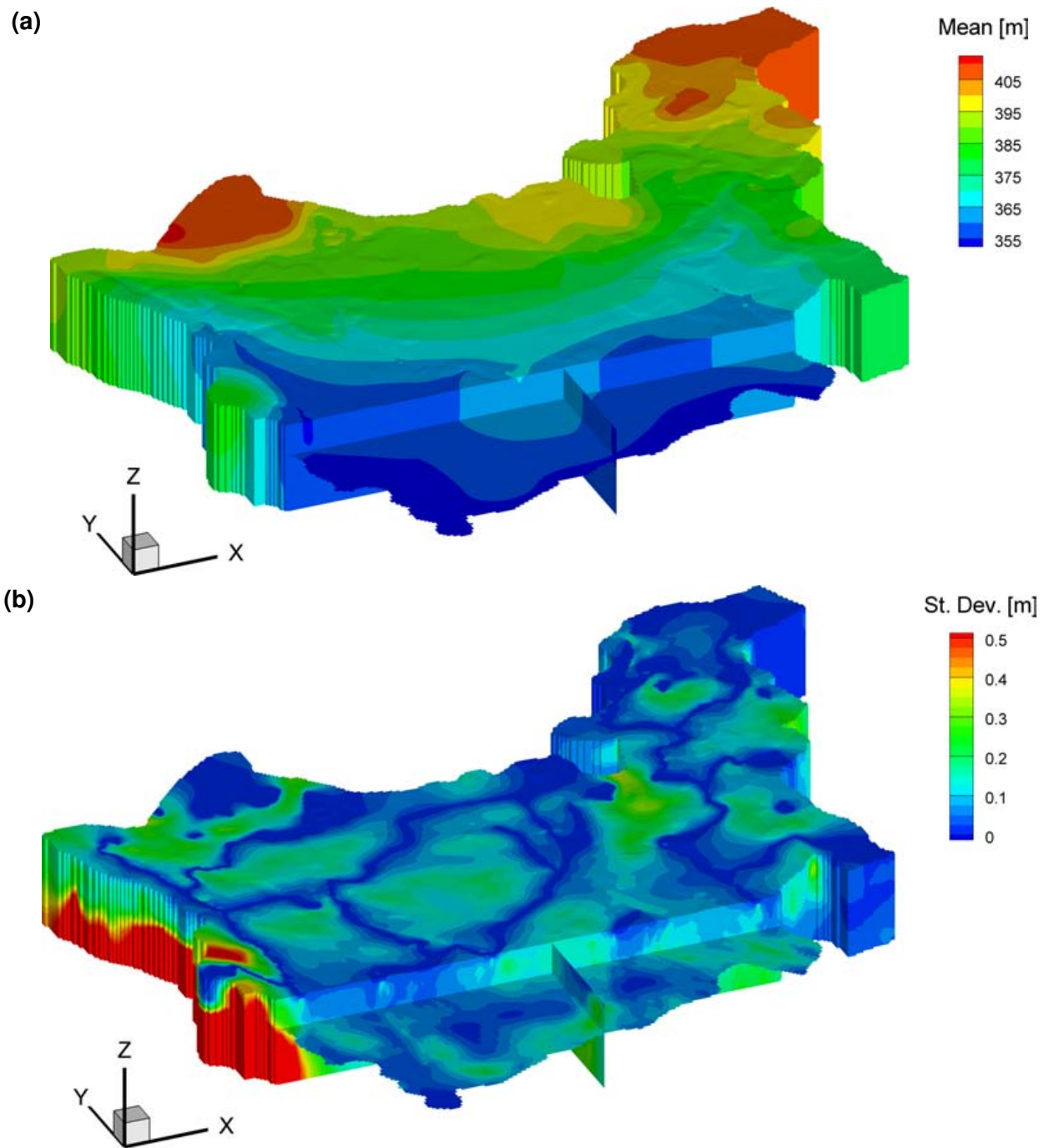


Figure 84: Distribution of (a) mean, and (b) standard deviation for 100 head values at each node computed for 100 fracture zone network realizations

### 5.2.3 Effects on Lifetime Expectancy

Mean lifetime expectancy (MLE) was computed for 100 fracture zone network realizations using the flow fields from the previous section. Different statistics for representative value, degree of scattering, and worst case value were computed for 100 MLE values at each node.

Figure 89 shows the distributions of four different representative statistics for MLE at each node. The results indicate that all four representative values are similar to each other and also similar to the result obtained for realization 1 (Figure 56). Similar distributions of the MLE from a single realization and the average MLE from multiple realizations indicate that the stochastic field may be ergodic at depth.

Figure 90 shows the distribution of the degree of scattering or uncertainty in the representative values in terms of standard deviation, quartile range, and half-range. Similar to the analysis in Darcy flux, half-range is more uniformly distributed at each depth than other statistics, as the smallest MLE values at each node could be more uniform and the standard deviation in log-scale is less dependent on depth, while the other variational measures are strongly dependent on depth as MLE increases with depth.

Figure 91 shows the normalized degree of scattering for the coefficient of variation and quartile variation coefficient. The results indicate that the relative uncertainty is more uniform but greater at shallower depths and becomes greatest near major fracture zones at all depths.

For safety analysis, a worst case needs to be considered to ensure that the risk is minimal. In parametric statistics, the 2.5 percentage point or  $z_{2.5} = \mu - 2\sigma$  can be used for a worst case estimate, to ensure that 97.5% of the sample is greater than  $z_{2.5}$ . Figure 92 shows the distribution of the 2.5 percentage point for MLE. The results show that the 2.5 percentage point values are much smaller than mean values at shallower depth and near major fracture zones where the coefficient of variation is greater. Note that the coefficient of variation,  $\sigma/\mu$ , is more important than the standard deviation for  $z_{2.5}$  as the relative magnitude of  $\sigma$  to  $\mu$  determines the confidence interval for  $\mu$ .

In non-parametric order statistics, minimum, 5<sup>th</sup> percentile, and  $Q2 - 2QD$  can be utilized for worst case estimates. A minimum is the same as  $MD - 2HR$  and first percentile for 100 samples in this study. Figure 93 shows the distribution of three non-parametric worst case estimates for MLE.

The results indicate that the distribution of the 2.5 percentage point in a linear scale is more irregular as the MLE distribution deviates the greatest amount from a normal distribution. Except for the percentage point in a linear scale, distribution of all other worst case estimates are similar to each other, but  $Q2 - 2QD$  is smaller than the others near fracture zones where the quartile deviation is relatively greater.

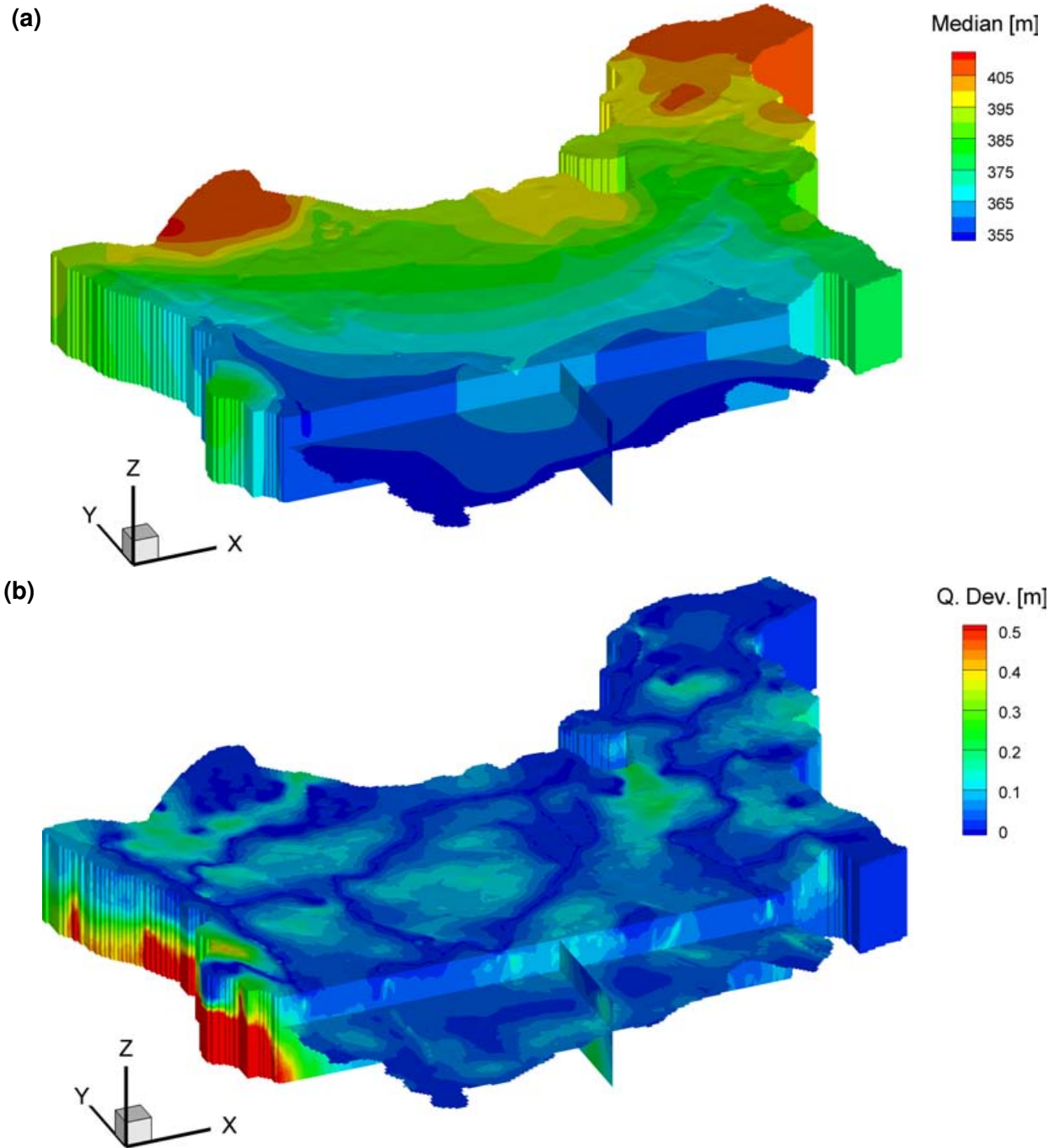


Figure 85: Distribution of (a) median, and (b) quartile deviation for 100 head values at each node computed for 100 fracture zone network realizations

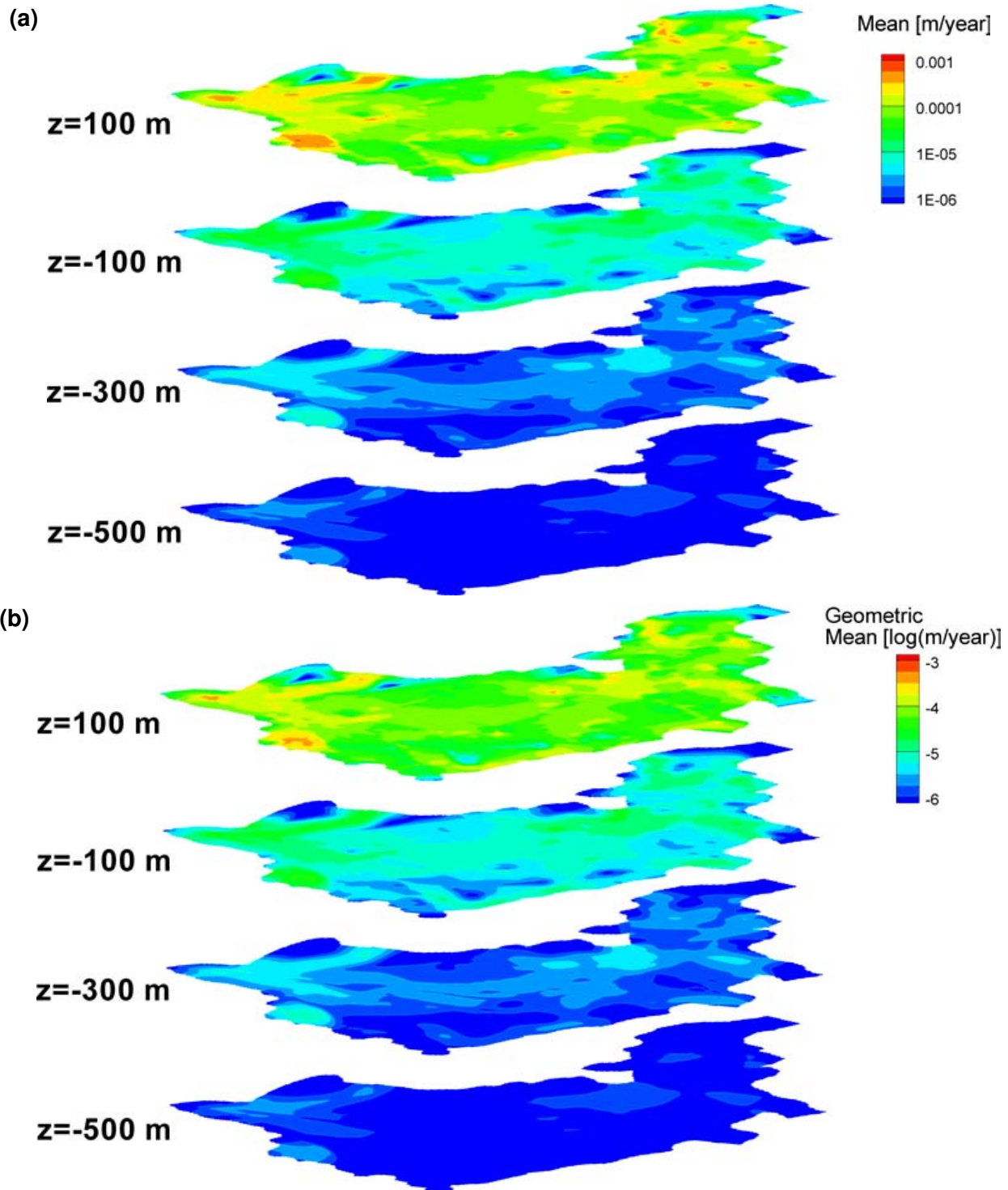


Figure 86: Four representative statistics for 100 Darcy flux values at each element computed for 100 fracture zone realizations: (a) arithmetic mean, (b) geometric mean, (c) median, and (d) midrange

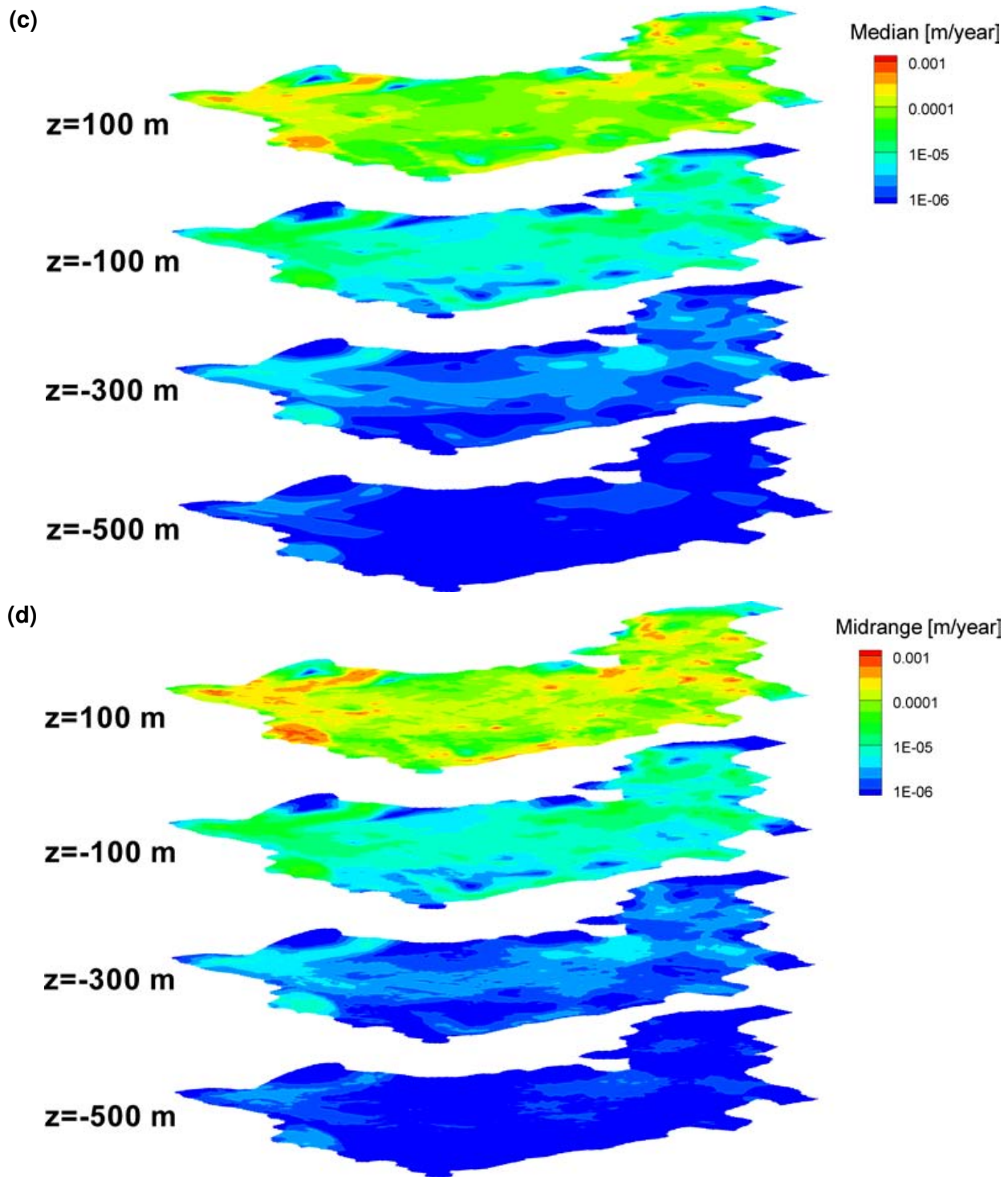


Figure 86: (continued) Four representative statistics for 100 Darcy flux values at each element computed for 100 fracture zone realizations: (a) arithmetic mean, (b) geometric mean, (c) median, and (d) midrange

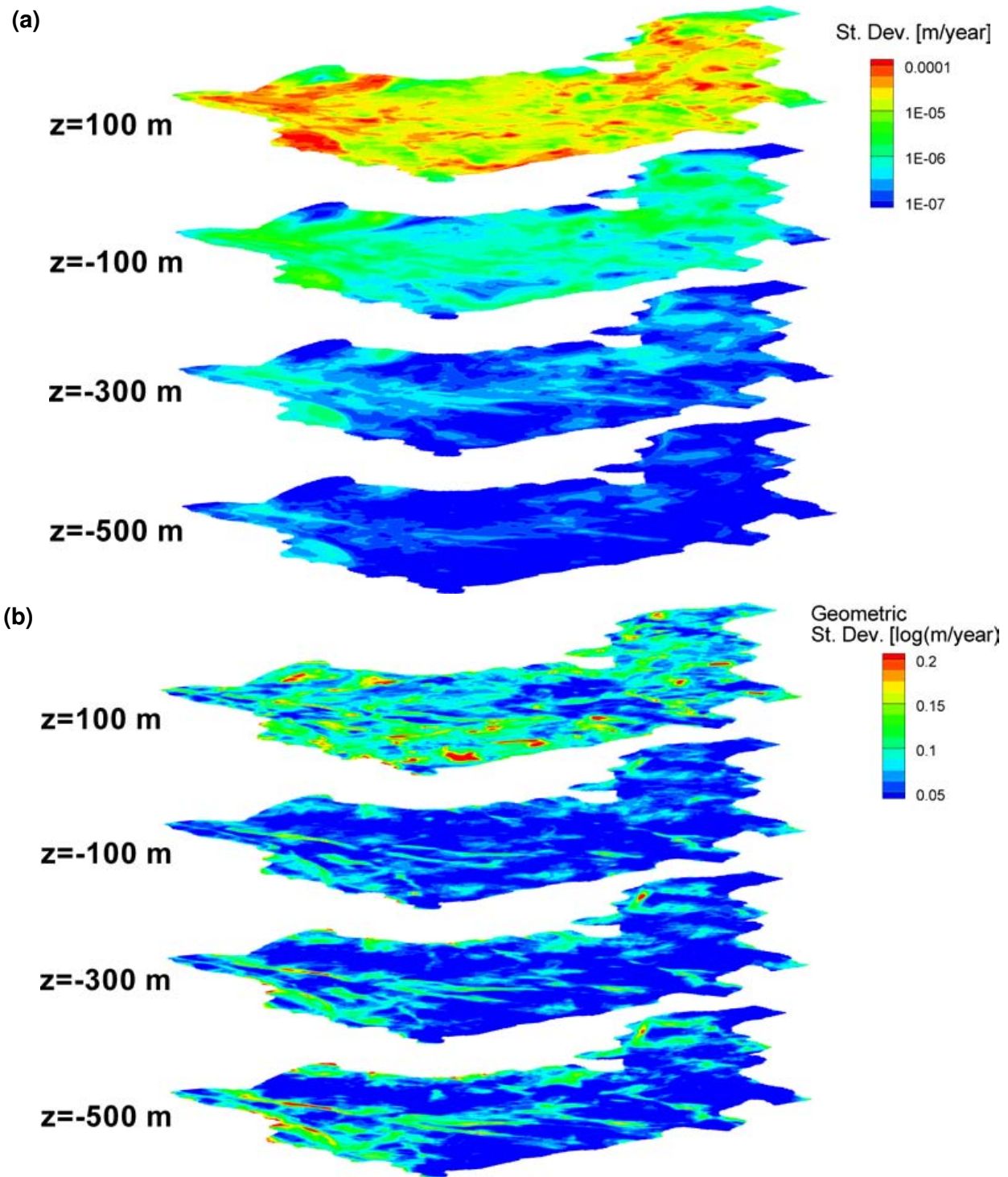


Figure 87: Four different measures for uncertainty in representative statistics for Darcy flux: standard deviations in (a) linear and (b) log-scale, (c) quartile deviation, and (d) half-range

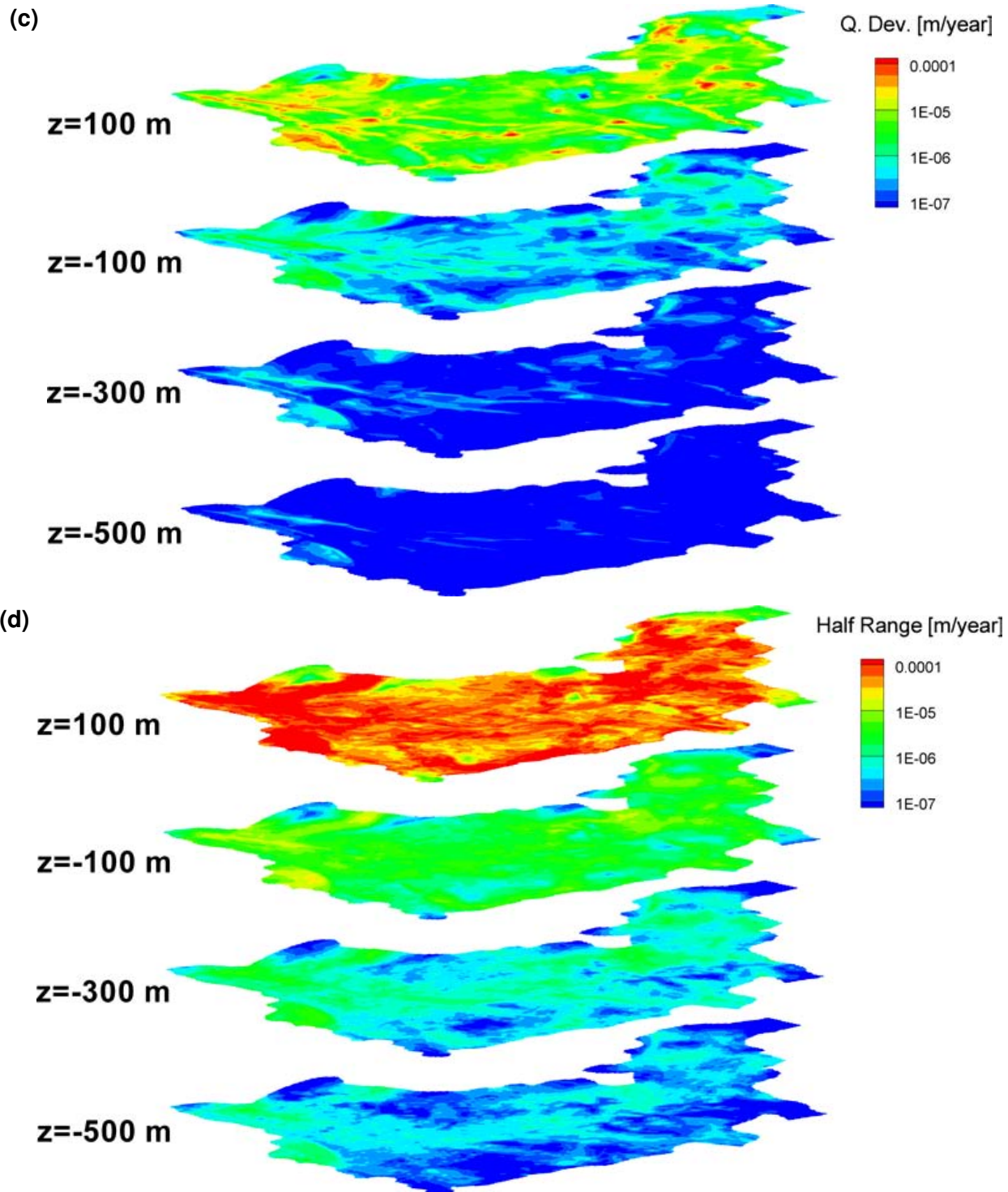


Figure 87: (continued) Four different measures for uncertainty in representative statistics for Darcy flux: standard deviations in (a) linear and (b) log-scale, (c) quartile deviation, and (d) half-range

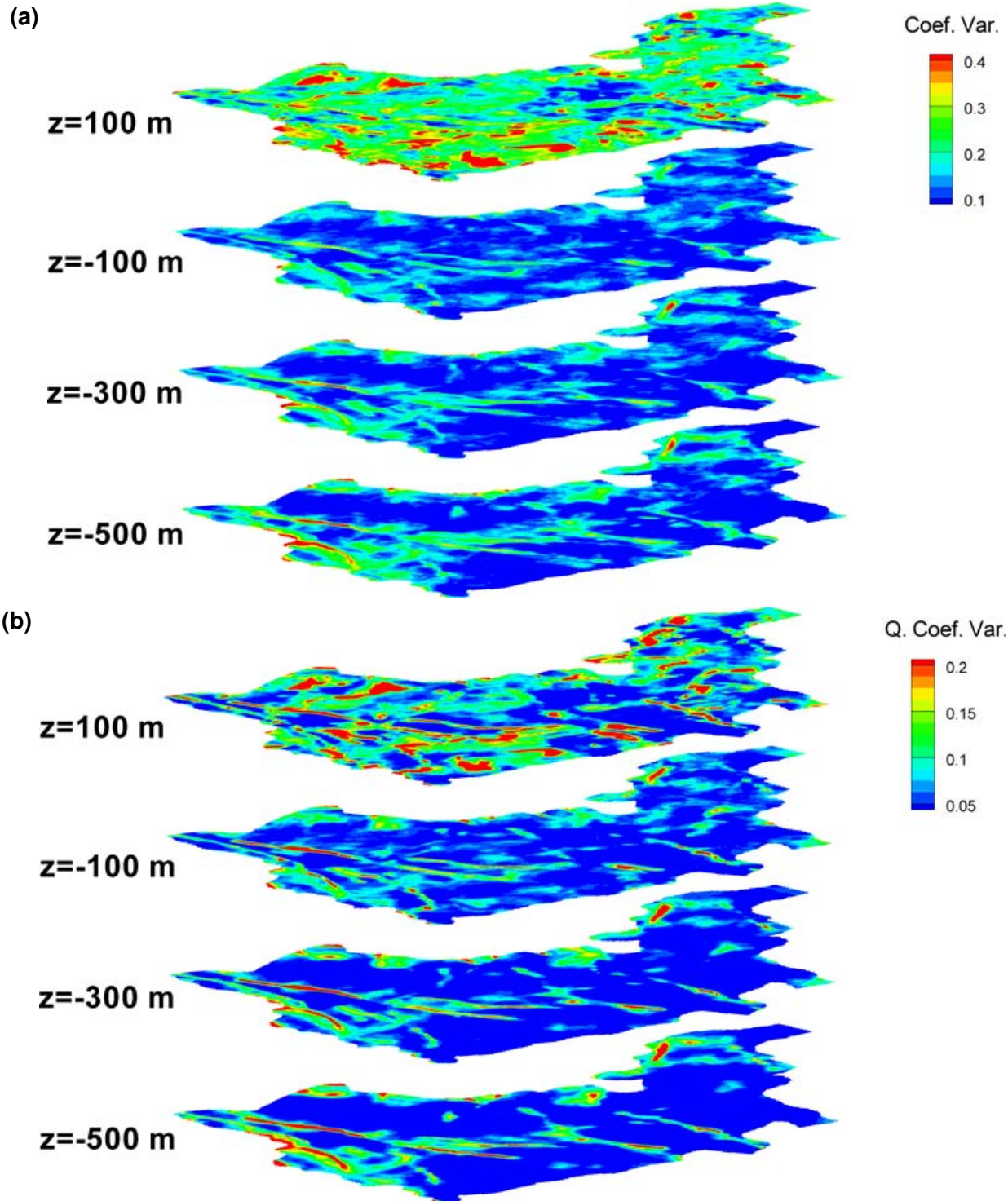


Figure 88: Measures for relative uncertainty in representative statistics for Darcy flux: (a) coefficient of variation, and (b) quartile coefficient of variation

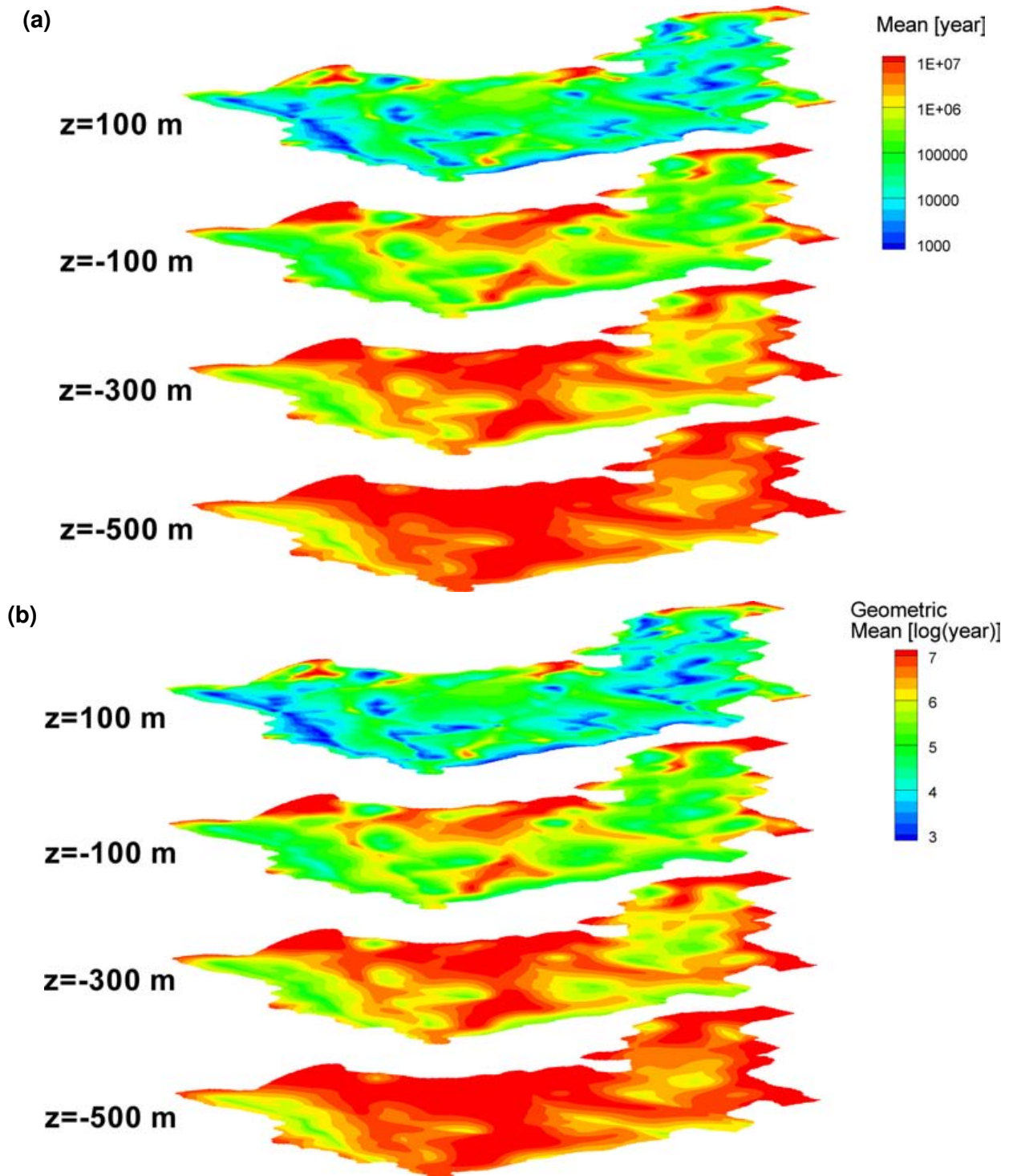


Figure 89: Representative statistics for mean lifetime expectancy computed for 100 fracture zone realizations: (a) arithmetic mean, (b) geometric mean, (c) median, and (d) midrange

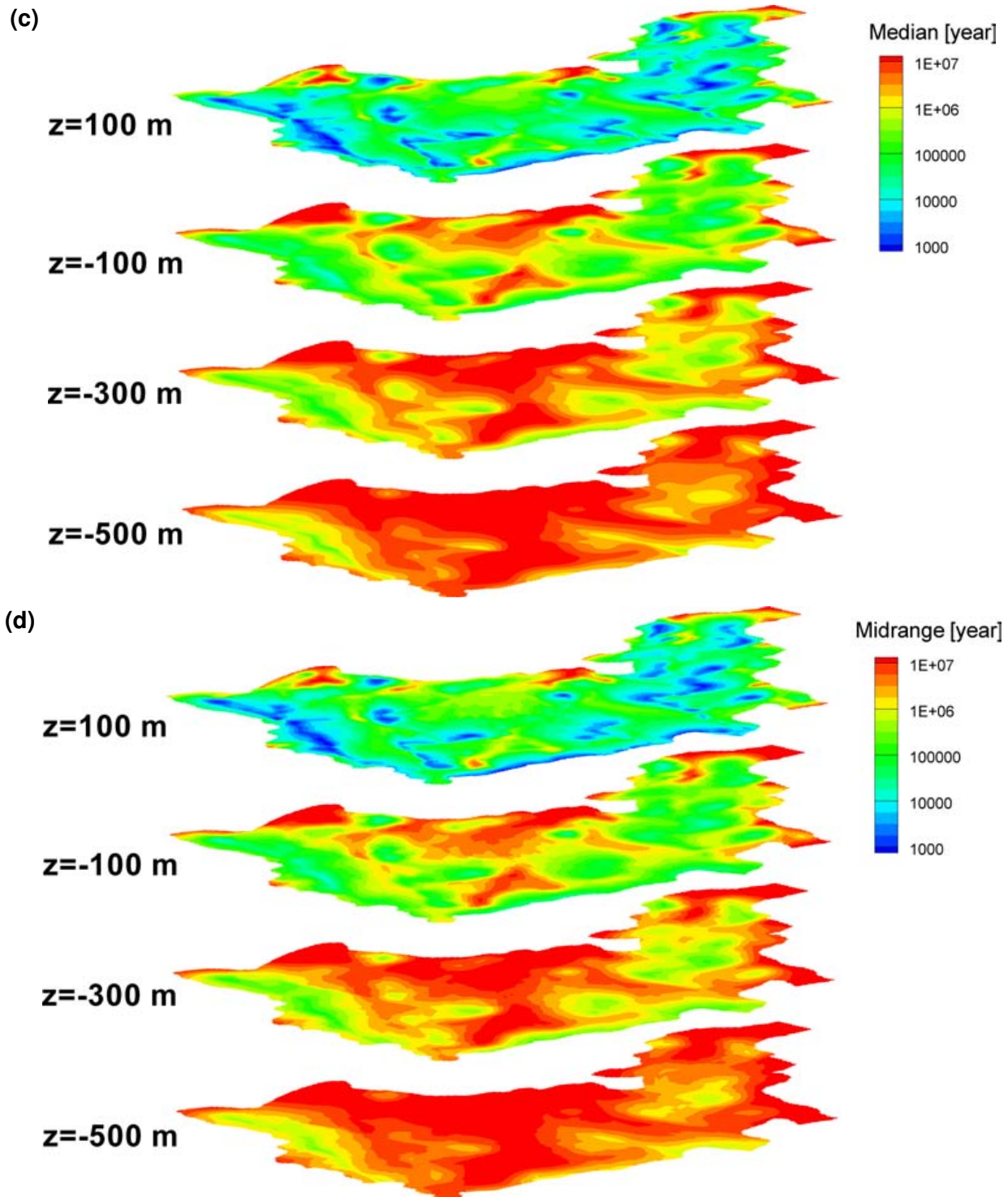


Figure 89: (continued) Representative statistics for mean lifetime expectancy computed for 100 fracture zone realizations: (a) arithmetic mean, (b) geometric mean, (c) median, and (d) midrange

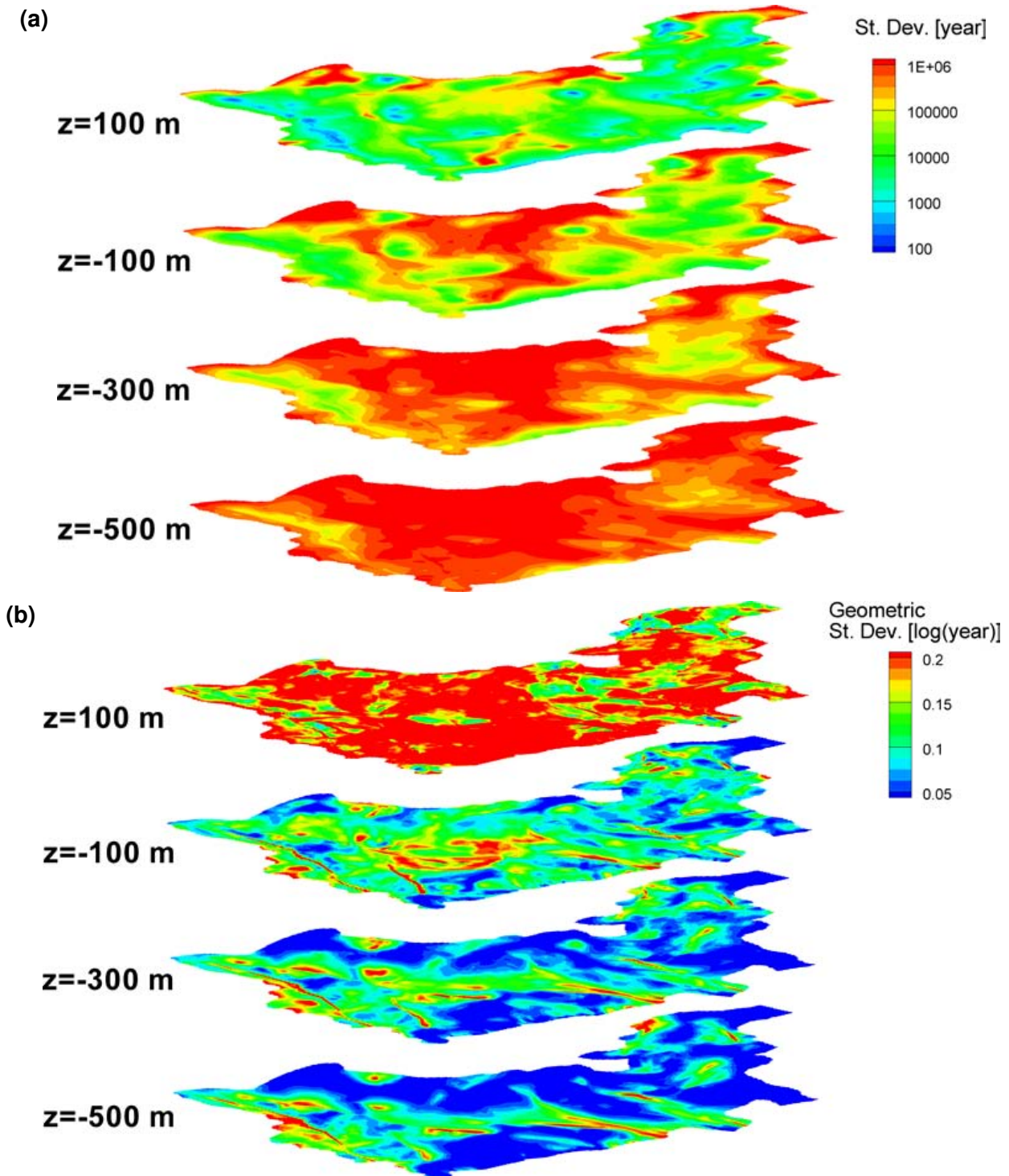


Figure 90: Degree of scattering in representative statistics for mean lifetime expectancy: standard deviations in (a) linear and (b) log-scale, (c) quartile deviation, and (d) half-range

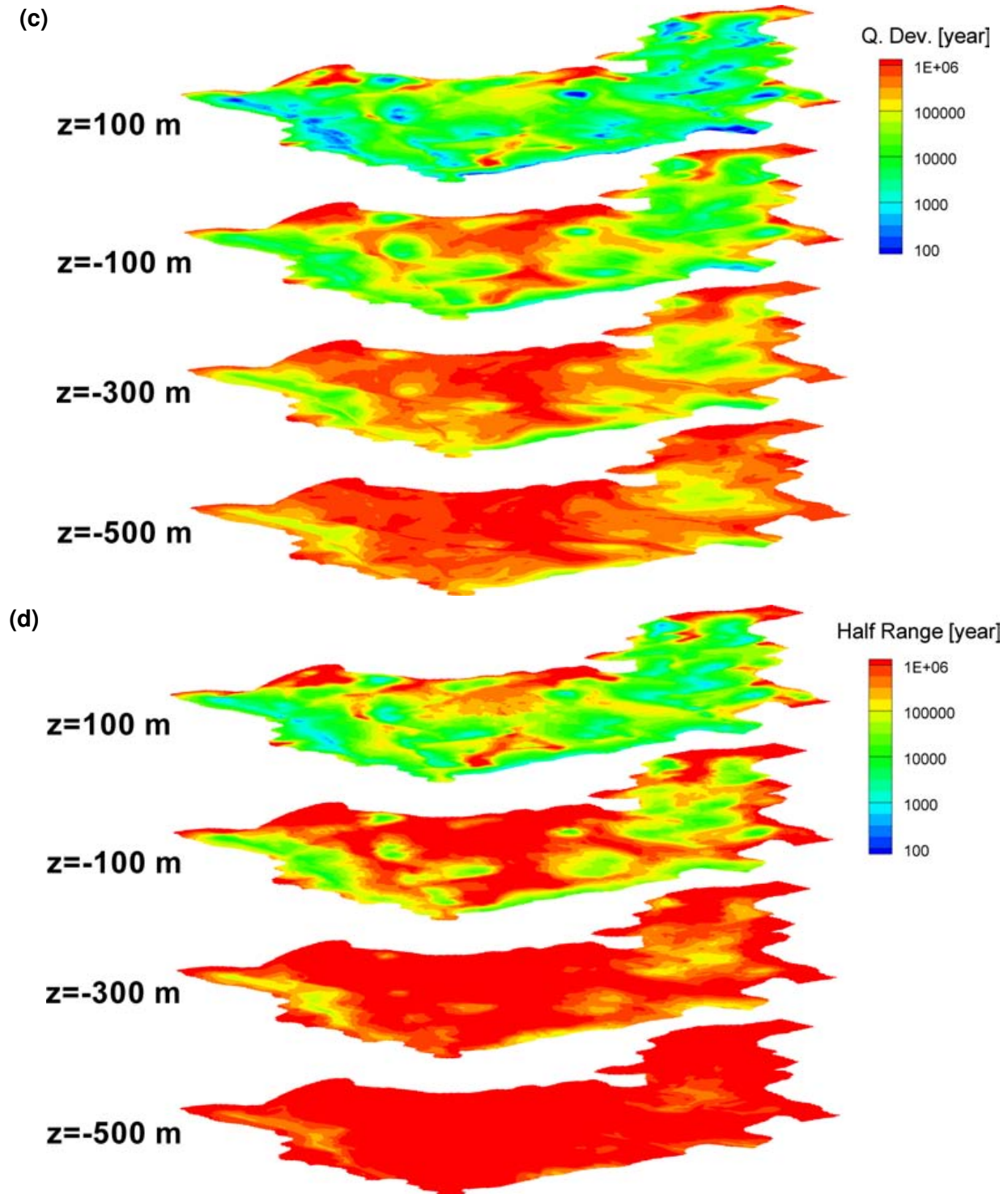


Figure 90: (continued) Degree of scattering in representative statistics for mean lifetime expectancy: standard deviations in (a) linear and (b) log-scale, (c) quartile deviation, and (d) half-range

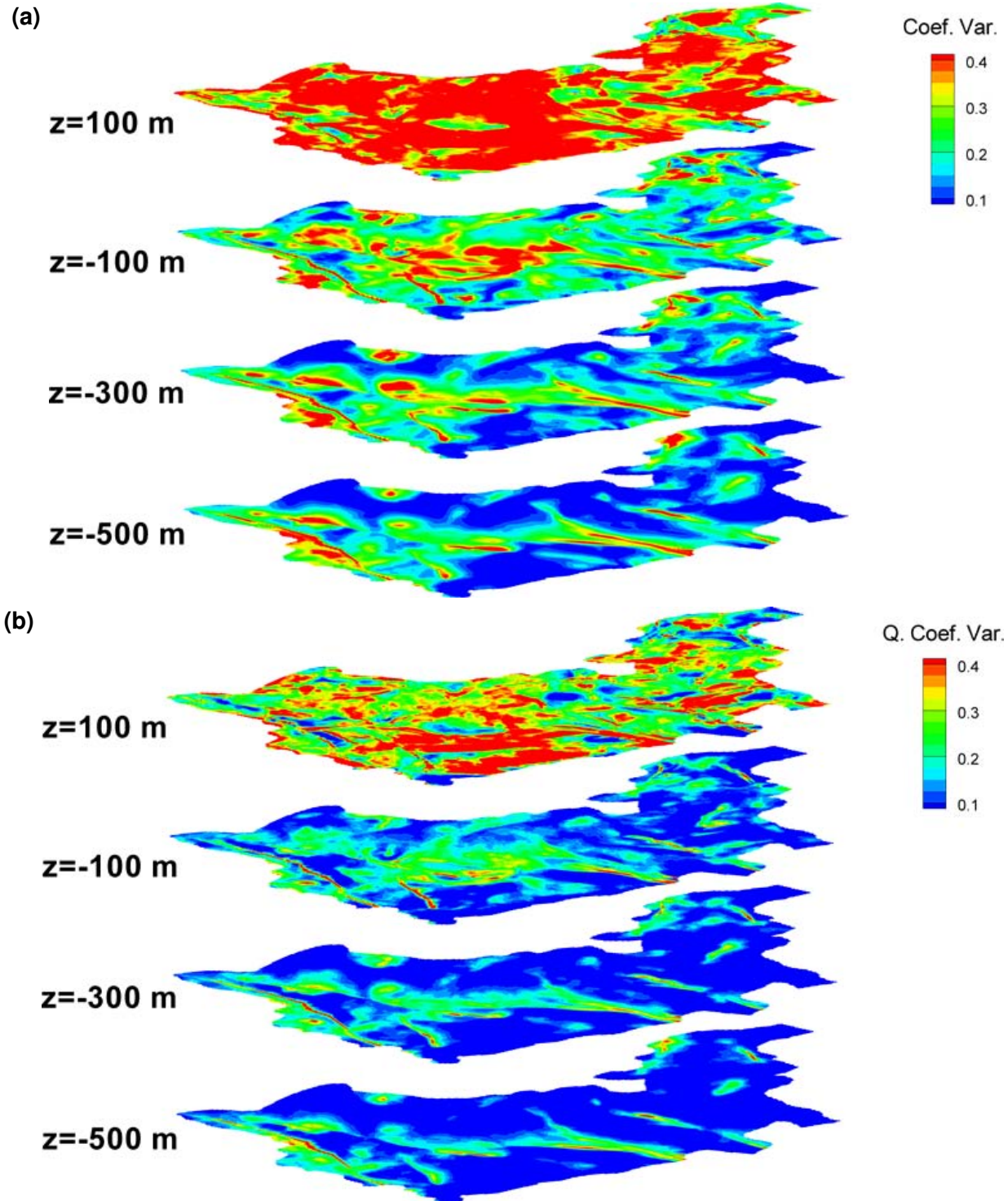


Figure 91: Measures for relative uncertainty in representative statistics for mean lifetime expectancy: (a) coefficient of variation, and (b) quartile coefficient of variation

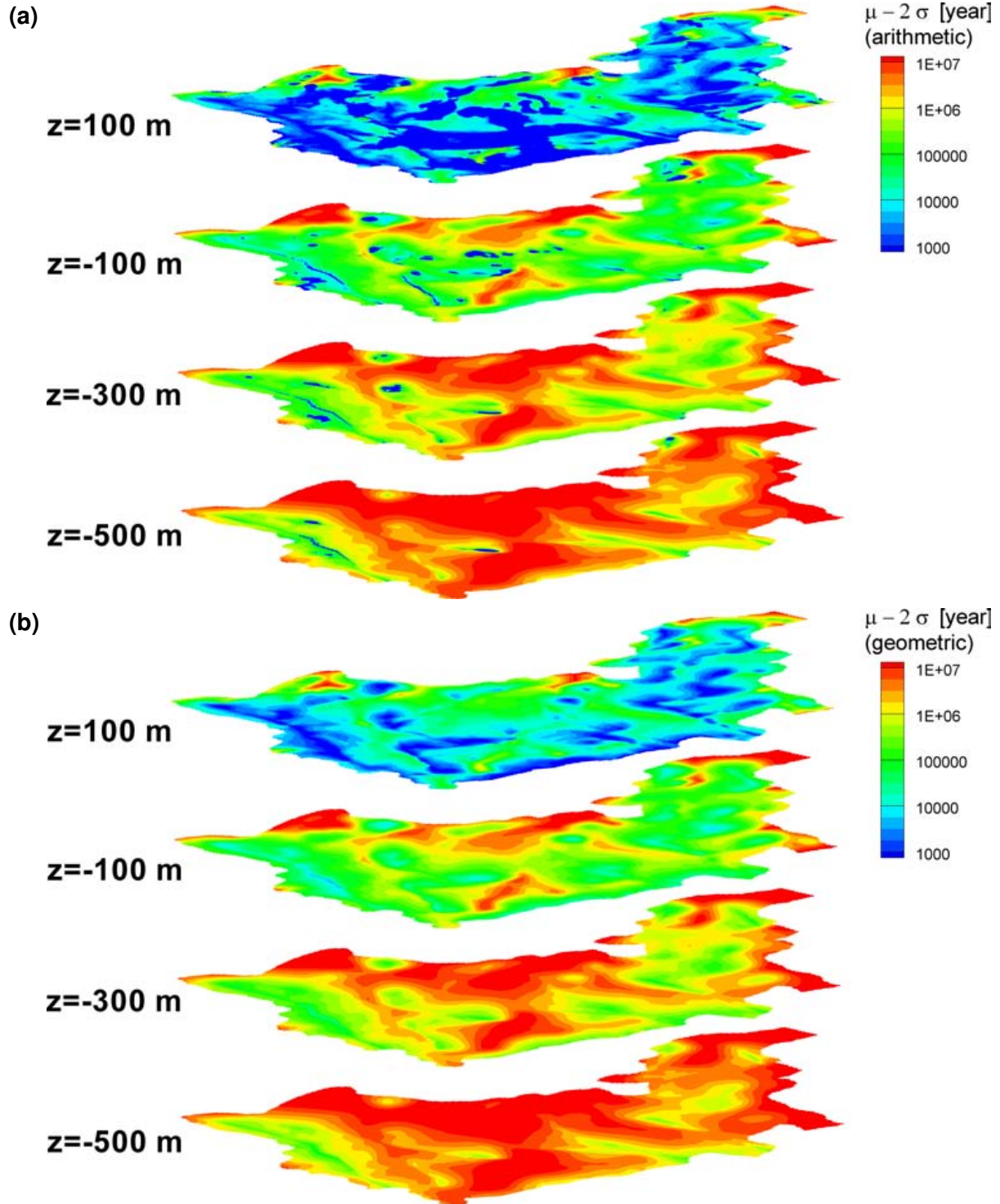


Figure 92: Worst case estimates for mean lifetime expectancy in terms of 2.5 percentage points in (a) linear and (b) log-scale

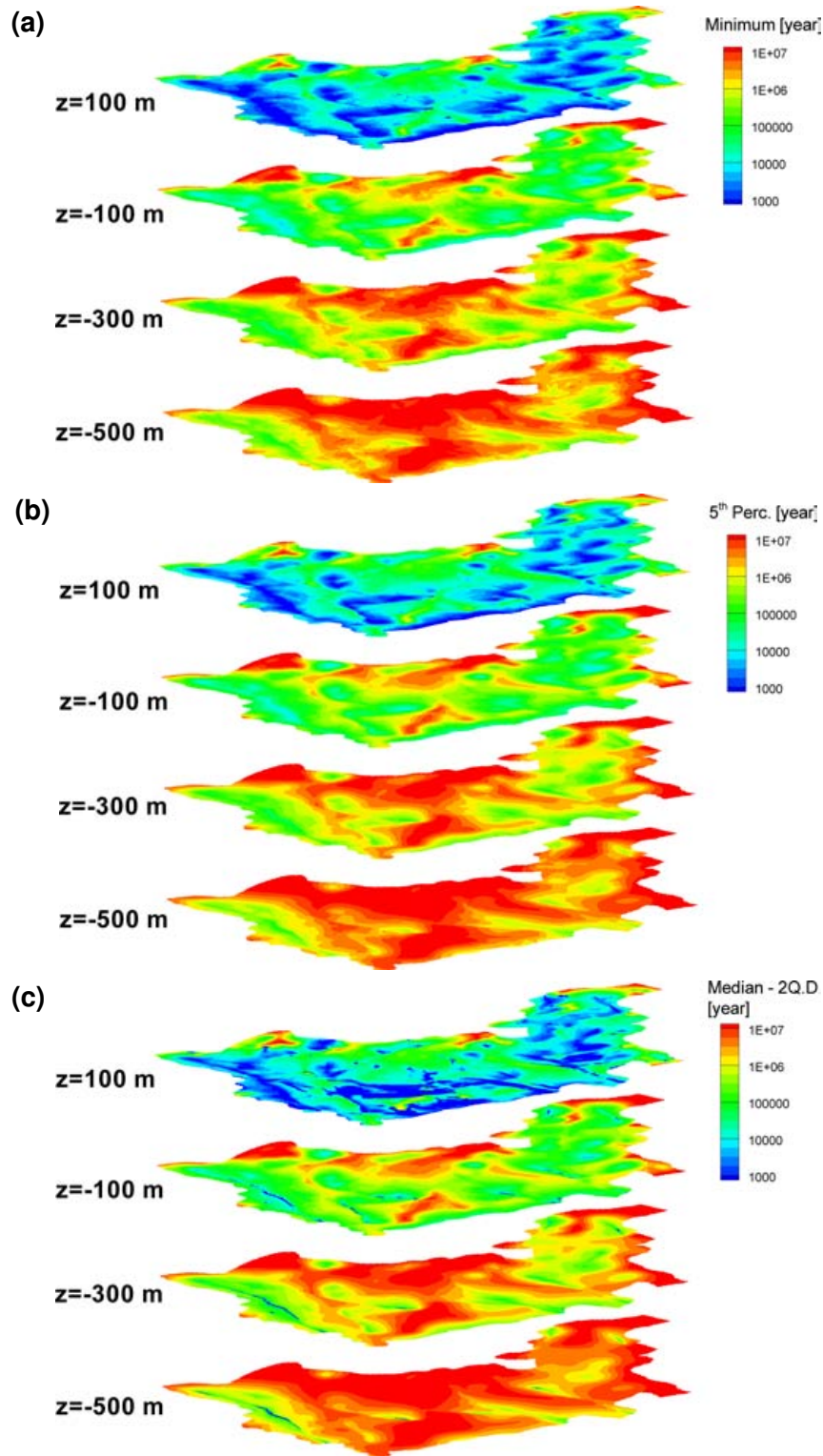


Figure 93: Worst case estimates for mean lifetime expectancy in terms of (a) minimum, (b) 5<sup>th</sup> percentile, and (c)  $Q2 - 2QD$

## 6. SUMMARY AND CONCLUSIONS

The Phase-II sub-regional model presented in this report is an improvement upon the Phase-I model developed in Sykes et al. (2004). Surface boundary conditions were changed from fixed head at all nodes to fixed head only at water features. Recharge was then applied at a rate of 1.0 mm/year. This approach avoids digital elevation model (DEM) artifacts, allows discharge to occur coincident with known rivers, lakes, and wetlands, and reduces short-circuiting of water in surface and near surface grid blocks and fracture elements. Reduced short-circuiting improves solute transport, age, and mean life expectancy simulation times in FRAC3DVS.

A statistical model of fracture permeability was developed, providing a depth varying probability density function (PDF). The inversion of this PDF can be used in a stochastic Monte Carlo sense to develop spatially varying and correlated fracture zone permeability fields. Percentile depth permeability fields were applied in this study. Fracture zone porosity can also be calculated from fracture zone permeability. A PDF for fracture zone width was developed based on data obtained at the Whiteshell Research Area.

Mean life expectancy (MLE) has been shown to be an excellent performance measure in determining the most relevant and dominant geosphere parameters and processes that would be relevant to the long-term safety of a deep geological repository in a fractured, crystalline rock setting characteristic of the Canadian Shield. Mean life expectancy represents the average time for any subsurface location to discharge to the biosphere, while honouring both advective and diffusive dispersion processes (unlike particle tracking which can only honour advection). Life expectancy is characterized by a probability density function; its mean may not represent earliest arrival or least dose, and hence, must be used with this caveat in mind.

The presence of brines at depth plays an important role in determining the characteristics of deep flow systems and can impact the safety of a deep geological repository from the perspective of retarding the migration of contaminants released in the brine region. Denser pore fluids at depth essentially reduce the topographic gradient (and driving forces) by requiring a greater energy potential to displace them. As deep pore fluid density increases, the shallow zone accommodates higher fluxes, while fluxes at depth decrease. Increasing fluid viscosity has a similar effect, namely increasing the resistance to fluid flow at depth. This increased flow resistance leads to decreased linear velocities at depth, as clearly shown for the illustrative example in Figure 37 and Figure 38.

Although the illustrative example neglects permeability variations to highlight the impact of denser fluids at depth, a similar conclusion can be drawn for the sub-regional domain. Increased pore fluid density tends to reduce the ability of deep fluids to migrate to discharge areas, and is evidenced by reduced vertical flux vectors below discharge and recharge areas. For the sub-regional domain, mean life expectancy increases with increasing brine density at depth as shown in Figure 64. It should be noted that the presence of brines at depth have a greater influence on the MLE of fluids in fractures than they do on fluids in the matrix.

MLE was used to assess the impact of fracture zone permeability on travel time. Decreasing fracture permeability can significantly increase MLE by several orders of magnitude as shown in Figure 71. The effects of fracture zone permeability assumptions on flow and transport are significant. The fracture zone permeability observed near ground surface, if assigned to fracture

zones at depth, can significantly overestimate the risk associated with a subsurface repository location by reducing the MLE, even in the adjacent matrix domain. Statistical variability in fracture zone permeability had a minor effect on the sub-regional domain, but it could become significant as the probability of encountering an extremely high permeability fracture zone at depth increases.

The effects of fracture zone porosity on MLE distributions in the sub-regional domain are negligible as compared to the effects of fracture zone permeability, since the fluid volume in the matrix is much greater than that in the fracture zones. Fracture zone porosity can be an important factor only when the volume fraction of fracture zones is comparable to the matrix volume fraction.

Fracture zone width, in general, is a significant factor for MLE distributions as it can increase or decrease the transmissivity of fracture zones, since fracture transmissivity is the product of permeability and width. However, as fracture zone width was observed to vary within an order of magnitude at the WRA site (typical of a Canadian Shield environment), the effects of fracture zone width on MLE may be relatively less significant in the sub-regional domain, as compared to the effects of fracture zone permeability.

The mean and standard deviation were calculated for 100 head values at each node computed for 100 fracture network realizations. The mean head distribution is similar to the results obtained from a single realization and scattering from the mean is not significant. The median and quartile deviation were also determined for 100 head values at each node, computed from 100 fracture network realizations. As most head values are distributed near the mean, median and quartile distributions are similar to the mean and standard deviations.

MLE was computed for 100 fracture zone network realizations and different statistics for representative value, degree of scattering and worst case value were computed. The arithmetic mean, geometric mean, median and midrange have similar distributions. The uncertainty in the representative value was measured by the standard deviation, quartile range and half-range. The results indicate that the half-range is more uniformly distributed than the other statistics.

In terms of the cold-based (NN2008) and warm-based (NN2778) climate simulations, recharge waters are able to penetrate deeper in the warm-based simulation. This is primarily due to the absence of permafrost below the ice-sheet in NN2778. In the case of NN2008, freezing temperatures are present below the ice-sheet for a much longer time, thereby resulting in greater permafrost, which seals the near surface and greatly reduces, by several orders of magnitude, the hydraulic connection with the fracture zone network.

It should be noted that these simulation results were undertaken without accounting for fluid density, or hydromechanical effects associated with ice-sheet loading and unloading. Therefore, the results should be viewed with this caveat in mind.

## REFERENCES

- Adams, J.J. and S. Bachu. 2002. Equations of state for basin geofluids: Algorithm review and intercomparison for brines. *Geofluids* 2(4), 257–271.
- Andričević, R., J. Daniels, and R. Jacobson. 1994. Radionuclide migration using travel time transport approach and its application in risk analysis. *J Hydrol* 163, 125–145.
- Arnold, L. 1974. *Stochastic Differential Equations: Theory and Applications*. John Wiley, New York.
- Bear, J. 1988. *Dynamics of Fluids in Porous Media*. Dover edition. Dover Publications Inc.
- Chen, M., M. Bai, and J.C. Roegiers. 1999. Permeability tensors of anisotropic fracture networks. *Mathematical Geology* 31(4), 355–373.
- Cornaton, F. 2003. Deterministic models of groundwater age, life expectancy and transit time distributions in advective-dispersive systems. Ph.D. thesis, University of Neuchâtel, Switzerland.
- Cornaton, F. and P. Perrochet. 2006a. Groundwater age, life expectancy and transit time distributions in advective–dispersive systems: 1. Generalized reservoir theory. *Advances in Water Resources* 29(9), 1267–1291.
- Cornaton, F. and P. Perrochet. 2006b. Groundwater age, life expectancy and transit time distributions in advective–dispersive systems: 2. Reservoir theory for sub-drainage basins. *Advances in Water Resources* 29(9), 1292–1305.
- Cotesta, L. and P. Kaiser. 2004. Application of virtual reality and the development of advanced visualization tools for site characterization: Moderately Fractured Rock Experiment (Phase II). Ontario Power Generation, Nuclear Waste Management Division, Supporting Technical Report 06819-REP-01300-10079-R00. Toronto, Canada.
- Frape, S.K., R.L. Stotler, T. Rusheeniemi, L. Ahonen, M. Paananen, and M.Y. Hobbs. 2004. Hydrogeochemistry of groundwaters at and below the base of the permafrost at Lupin: Report of Phase II. Ontario Power Generation, Nuclear Waste Management Division, Supporting Technical Report 06819-REP-01300-10047-R00. Toronto, Canada.
- Frind, E.O. 1982. Simulation of long-term transient density-dependent transport in groundwater. *Advances in Water Resources* 5, 73–88.
- Garabedian, P.R. 1964. *Partial Differential Equations*. John Wiley, New York.
- Gardiner, C.W. 1983. *Handbook of Stochastic Methods for Physics, Chemistry and Natural Sciences*. Springer, Berlin.
- Gascoyne, M., J. McMurray, and R. Ejeckham. 2004. Paleohydrogeologic case study of the Whiteshell Research Area. Ontario Power Generation, Nuclear Waste Management Division, Technical Report 06819-REP-01200-10121-R00. Toronto, Canada.

- Hellä, P., E. Tammisto, and H. Ahokas. 2004. Hydraulically conductive fractures and their properties in boreholes KR4 and KR7-KR10 at Olkiluoto site. Posiva Oy, Working Report 2004-21. Olkiluoto, Finland.
- Kolmogorov, A.N. 1931. Über die analytischen methoden in der wahrscheinlichkeitsrechnung. *Math Anal* 104, 415–458.
- LaBolle, E.M., J. Quastel, and G.E. Fogg. 1998. Diffusion theory for transport in porous media: Transition-probability densities of diffusion processes corresponding to advection–dispersion equations. *Water Resour Res* 34(7), 1685–1693.
- LaBolle, E.M., J. Quastel, G.E. Fogg, and J. Gravner. 2000. Diffusion processes in composite porous media and their numerical integration by random-walks: Generalized stochastic differential equations with discontinuous coefficients. *Water Resour Res* 36(3), 651–662.
- Neupauer, R. and J.L. Wilson. 1999. Adjoint method for obtaining backward-in-time location and travel time probabilities of a conservative groundwater contaminant. *Water Resour Res* 35(11), 3389–3398.
- Neuzil, C.E. 2003. Hydromechanical coupling in geologic processes. *Hydrogeology Journal* 11(1), 41–83.
- Peltier, W.R. 2002. A design basis glacier scenario. Ontario Power Generation, Nuclear Waste Management Division, Technical Report 06819-REP-01200-10069-R00. Toronto, Canada.
- Peltier, W.R. 2003a. Long-term climate change – glaciation. Ontario Power Generation, Nuclear Waste Management Division, Technical Report 06819-REP-01200-10113-R00. Toronto, Canada.
- Peltier, W.R. 2003b. Personal communication.
- Peltier, W.R. 2006. Boundary conditions data sets for spent fuel repository performance assessment. Ontario Power Generation, Nuclear Waste Management Division, Technical Report 06819-REP-01200-10154-R00. Toronto, Canada.
- Rubin, Y. 2003. *Applied Stochastic Hydrology*. Oxford University Press, New York.
- Snow, D.T. 1968. Rock fracture spacings, openings, and porosities. *Journal of the Soil Mechanics and Foundations Division* 94(1), 73–91.
- Snow, D.T. 1969. Anisotropic permeability of fractured media. *Water Resources Research* 5(6), 1273–1289.
- Spivakovskaya, D., A.W. Heemik, G.N. Milstein, and J.G.M. Schoenmakers. 2005. Simulation of the transport of particles in coastal waters using forward and reverse time diffusion. *Adv Water Res* 28, 927–938.
- Srivastava, R.M. 2002. The discrete fracture network model in the local scale flow system for the Third Case Study. Ontario Power Generation, Nuclear Waste Management Division, Supporting Technical Report 06819-REP-01300-10061-R00. Toronto, Canada.

- Stevenson, D.R., A. Brown, C.C. Davison, M. Gascoyne, R.G. McGregor, D.U. Ophori, N.W. Scheier, F. Stanchell, G.A. Thorne, and D.K. Tomsons. 1996. A revised conceptual hydrogeologic model of a crystalline rock environment, Whiteshell Research Area, southeastern Manitoba, Canada. Atomic Energy of Canada Limited, Whiteshell Laboratories, Technical Report AECL-11331, COG-95-271. Pinawa, Manitoba, Canada.
- Sudicky, E.A. and E.O. Frind. 1982. Contaminant transport in fractured porous media: Analytic solutions for a system of parallel fractures. *Water Resources Research* 18(6), 1634–1642.
- Sykes, J.F., S.D. Normani, and E.A. Sudicky. 2003. Regional scale groundwater flow in a Canadian Shield setting. Ontario Power Generation, Nuclear Waste Management Division, Technical Report 06819-REP-01200-10114-R00. Toronto, Canada.
- Sykes, J.F., S.D. Normani, E.A. Sudicky, and R.G. McLaren. 2004. Sub-regional scale groundwater flow within an irregular discretely fractured Canadian Shield setting. Ontario Power Generation, Nuclear Waste Management Division, Technical Report 06819-REP-01200-10133-R00. Toronto, Canada.
- Therrien, R., E.A. Sudicky, and R.G. McLaren. 2004. FRAC3DVS: An Efficient Simulator for Three-dimensional, Saturated-Unsaturated Groundwater Flow and Density-dependent, Chain-Decay Solute Transport in Porous, Discretely-Fractured Porous or Dual-porosity Formations. User's Guide. Groundwater Simulations Group, University of Waterloo, Waterloo, Ontario, Canada.
- Tóth, J. and G. Sheng. 1996. Enhancing safety of nuclear waste disposal by exploiting regional groundwater flow: The recharge area concept. *Hydrogeology Journal* 4(4), 4–25.
- Uffink, G.J.M. 1989. Application of the Kolmogorovs backward equation in random walk simulation of groundwater contaminant transport. *In* *Contaminant Transport in Groundwater* (H.E. Kobus and W. Kinzelbach, eds.). Balkema, Rotterdam, 283–298.
- Vahtinen, T., H. Ahokas, E. Heikkinen, P. Hellä, J. Nummela, P. Saksä, E. Tammisto, S. Paulamäki, M. Paananen, K. Front, and A. Kärki. 2003. Bedrock model of the Olkiluoto site. Version 2003/1. Posiva Oy, Working Report 2003-43. Olkiluoto, Finland.
- Van Kooten, J.J.A. 1995. An asymptotic method for predicting the contamination of a pumping well. *Adv Water Res* 18(5), 295313.
- Weissmann, G.S., Y. Zhang, E. LaBolle, and G.E. Fogg. 2002. Dispersion of groundwater age in an alluvial aquifer system. *Water Resour Res* 38(10), 1198–1211.
- Wilson, J.L. and J. Liu. 1997. Field validation of the backward-in-time advection dispersion theory. *In* *Proceedings of the 1996 HSRC/WERC Joint Conference on the Environment* (L.E. Erickson, D.L. Tillison, S.C. Grant, and J.P. McDonald, eds.). Great Plains/Rocky Mountain Hazardous Substance Research Center, Kansas State University, Manhattan, Kansas.

**APPENDIX A – FORWARD AND BACKWARD ADVECTION-DISPERSION EQUATIONS  
EQUIVALENT TO STOCHASTIC DIFFERENTIAL EQUATIONS**

**CONTENTS**

	<b><u>Page</u></b>
A.1 DERIVATION . . . . .	119
A.2 REFERENCES . . . . .	122



## A.1 DERIVATION

The position of a particle  $X_{x_0, t_0}(t)$ , that was released at time  $t_0$  at  $X_{x_0, t_0}(t_0) = x_0$  is described by the following Itô stochastic differential equation (SDE):

$$dX_i = a_i(t, X)dt + \sigma_{ij}(t, X)dW_j(t) \quad (\text{A.1})$$

where  $a_i$  is a vector function,  $\sigma_{ij}$  is a matrix function related to the dispersion tensor, and  $W_j$  is a vector-valued Brownian motion process. The term  $\sigma_{ij}(t, X)dW_j(t)$  accounts for the stochastic displacement due to dispersion, and the  $W_j$ 's are independent Wiener processes (Gardiner, 1983). The transition density  $p(x, t | x_0, t_0)$  to find a particle at position  $x$  at time  $t$ , given that it was released at time  $t_0$  at position  $x_0$ , can be obtained by solving the Fokker-Planck equation (FPE):

$$\frac{\partial p}{\partial t} = -\frac{\partial a_i p}{\partial x_i} + \frac{\partial^2 b_{ij} p}{\partial x_i \partial x_j} \quad (\text{A.2})$$

Note that Equation (A.2) is formulated according to Langevin's formulation (Langevin, 1908) of the FPE. The terms  $a_i = a_i(x, t)$  and  $b_{ij} = b_{ij}(x, t) = \sigma_{ik}\sigma_{jk}$  denote the drift vector and noise tensor, respectively. The solution of the FPE is subject to the initial condition  $p(x, t_0 | x_0, t_0) = \delta(x - x_0)$  and any appropriate boundary condition (Gardiner, 1983). Defining  $a_i$  and  $b_{ij}$  according to:

$$a_i = v_i + \frac{\partial b_{ij}}{\partial x_j} \quad (\text{A.3a})$$

$$b_{ij} = D_{ij} \quad (\text{A.3b})$$

where the  $v_i$ 's are the components of pore velocity and  $D_{ij}$ 's are the entries of the dispersion tensor. One can show that Equation (A.2) becomes equivalent to the following classical forward advection-dispersion equation (ADE):

$$\frac{\partial p}{\partial t} = -\frac{\partial}{\partial x_i}(v_i p) + \frac{\partial}{\partial x_i} D_{ij} \frac{\partial p}{\partial x_j} \quad (\text{A.4})$$

This result implies that the particle model Equation (A.1) with  $a_i$  and  $b_{ij}$  defined as in Equation (A.3) is exactly consistent with the ADE. Consequently, a particle concentration that is obtained by simulating the SDE for many different particles is an approximation of the solution of Equation (A.2). Considering the FPE, we replace the variable  $p(x, t)$  with  $\phi(x)C(x, t)$ , where  $\phi$  is porosity, or mobile water content, and where  $C$  is the solute resident concentration. In this case, the equivalence between the FPE and the forward ADE is given by specifying the drift vector and the noise tensor as:

$$a_i(x, t) = v_i(x, t) + \phi(x)^{-1} \frac{\partial}{\partial x_j} (\phi(x)b_{ij}(x, t)) \quad (\text{A.5a})$$

$$b_{ij}(x, t) = D_{ij}(x, t) \quad (\text{A.5b})$$

The equivalent ADE is then given by:

$$\frac{\partial \phi C}{\partial t} = -\frac{\partial}{\partial x_i}(q_i C) + \frac{\partial}{\partial x_i} \phi D_{ij} \frac{\partial C}{\partial x_j} \quad (\text{A.6})$$

where  $q_i = \phi v_i$  is the water flux vector. Note that linear reaction processes such as decay and linear equilibrium adsorption can be incorporated by replacing the parameters  $q_i$  and  $D_{ij}$  by their retarded values  $q_i^r = q_i/R$  and  $D_{ij}^r = D_{ij}/R$ , where  $R$  is the retardation factor, and by adding a decay term in the right-hand sides of Equation (A.2) and Equation (A.6):

$$\frac{\partial p}{\partial t} = -\frac{\partial a_i p}{\partial x_i} + \frac{\partial^2 b_{ij} p}{\partial x_i \partial x_j} - \lambda p \quad (\text{A.7})$$

$$\frac{\partial \phi RC}{\partial t} = -\frac{\partial}{\partial x_i} (q_i C) + \frac{\partial}{\partial x_i} \phi D_{ij} \frac{\partial C}{\partial x_j} - \phi R \lambda C \quad (\text{A.8})$$

where  $\lambda$  is the decay constant. In this case, the equivalence between the FPE and the ADE is obtained by adding the term to the right-hand side of Equation (A.2).

The backward equation as given by Kolmogorov (1931) can be formalized as follows:

$$\frac{\partial p}{\partial t} = -a_i \frac{\partial p}{\partial x_i} - b_{ij} \frac{\partial^2 p}{\partial x_i \partial x_j} \quad (\text{A.9})$$

Equation (A.9) is the formal adjoint model of the FPE (Garabedian, 1964; Arnold, 1974), and can be transformed into the following formulation:

$$\frac{\partial p}{\partial t} = -\left[ a_i - \frac{\partial b_{ij}}{\partial x_j} \right] \frac{\partial p}{\partial x_i} - \frac{\partial^2 b_{ij} p}{\partial x_i \partial x_j} + \frac{\partial}{\partial x_i} \left( p \frac{\partial b_{ij}}{\partial x_j} \right) \quad (\text{A.10})$$

We consider the case of a steady-state divergence-free velocity field, which can be expressed by  $\partial v_i / \partial x_i = 0$ . Combining this condition with Equation (A.5), we obtain:

$$\frac{\partial}{\partial x_i} \left( a_i - \frac{\partial b_{ij}}{\partial x_j} \right) = 0 \quad (\text{A.11})$$

Consequently, one can write

$$\frac{\partial}{\partial x_i} \left[ \left( a_i - \frac{\partial b_{ij}}{\partial x_j} \right) p \right] = \left( a_i - \frac{\partial b_{ij}}{\partial x_j} \right) \frac{\partial p}{\partial x_i} \quad (\text{A.12})$$

Using Equation (A.12) to modify Equation (A.10), and reversing time,  $\tau = t_0 - t$ , yields:

$$\frac{\partial p}{\partial \tau} = -\frac{\partial a_i^* p}{\partial x_i} + \frac{\partial^2 b_{ij} p}{\partial x_i \partial x_j} \quad (\text{A.13})$$

where  $a_i^*$  and  $b_{ij}$  are given by:

$$a_i^* = -v_i + \frac{\partial b_{ij}}{\partial x_j} \quad (\text{A.14a})$$

$$b_{ij} = D_{ij} \quad (\text{A.14b})$$

Equation (A.13) has the form of a forward equation, showing that the FPE and the BKE are equivalent to each other. Only the drift coefficient differs from its original definition: velocity presents a reversed sign to handle the backward-in-time evolution. Using the definitions of Equation (A.14), the BKE formulated according to Equation (A.13) becomes:

$$\frac{\partial \rho}{\partial \tau} = \frac{\partial}{\partial x_i} (v_i \rho) + \frac{\partial}{\partial x_i} D_{ij} \frac{\partial \rho}{\partial x_j} \quad (\text{A.15})$$

Equation (A.15) corresponds to the backward advection-dispersion equation (BADE) equivalent to the BKE. Finally, by specifying

$$a_i^*(x) = -v_i(x) + \phi(x)^{-1} \frac{\partial}{\partial x_j} (\phi(x) b_{ij}(x)) \quad (\text{A.16a})$$

$$b_{ij}(x) = D_{ij}(x) \quad (\text{A.16b})$$

and by letting  $\rho = \phi g$  in Equation (A.13), one obtains:

$$\frac{\partial \phi g}{\partial \tau} = \frac{\partial}{\partial x_i} (q_i g) + \frac{\partial}{\partial x_i} \phi D_{ij} \frac{\partial g}{\partial x_j} \quad (\text{A.17})$$

Like with the forward equation, linear equilibrium adsorption and decay can be incorporated into the backward models by replacing  $q_i$  and  $D_{ij}$  by their retarded values:

$$\frac{\partial \rho}{\partial \tau} = -\frac{\partial a_i^* \rho}{\partial x_i} + \frac{\partial^2 b_{ij} \rho}{\partial x_i \partial x_j} - \lambda \rho \quad (\text{A.18})$$

$$\frac{\partial \phi R g}{\partial \tau} = \frac{\partial}{\partial x_i} (q_i g) + \frac{\partial}{\partial x_i} \phi D_{ij} \frac{\partial g}{\partial x_j} - \phi R \lambda g \quad (\text{A.19})$$

## A.2 REFERENCES

Arnold, L. 1974. Stochastic Differential Equations: Theory and Applications. John Wiley, New York.

Garabedian, P.R. 1964. Partial Differential Equations. John Wiley, New York.

Gardiner, C.W. 1983. Handbook of Stochastic Methods for Physics, Chemistry and Natural Sciences. Springer, Berlin.

Kolmogorov, A.N. 1931. Über die analytischen methoden in der wahrscheinlichkeitsrechnung. Math Anal 104, 415–458.

Langevin, P. 1908. Sur la théorie du mouvement brownien. Comptes Rendus de l'Académie des Sciences 146, 530–533.